The Dissertation Committee for Peng Wang Certifies that this is the approved version of the following dissertation:

THEORETICAL AND NUMERICAL STUDY ON ADHESIVE INTERACTIONS BETWEEN GRAPHENE AND SUBSTRATE

Committee:

Rui Huang, Supervisor

Kenneth M. Liechti

Chad M. Landis

Krishnaswa Ravi-Chandar

Pengyu Ren

THEORETICAL AND NUMERICAL STUDY ON ADHESIVE INTERACTIONS BETWEEN GRAPHENE AND SUBSTRATE

by

Peng Wang

Dissertation

Presented to the Faculty of the Graduate School of

The University of Texas at Austin

in Partial Fulfillment

of the Requirements

for the Degree of

Doctor of Philosophy

The University of Texas at Austin

May 2018

Dedication

To my parents and teachers

Acknowledgements

I would like to express my sincere appreciation to my advisor, Professor Rui Huang, for his invaluable guidance for this work. His inspiring discussions, insightful ideas, broad knowledge, careful thinking and persistent encouragement are of vital help to my Ph. D. career. I am grateful to Professor Kenneth M. Liechti for his beneficial suggestions and advices to my research. Without his broad and practical experience on experimental side, this work would have not been possible. I would like to thank Professor Chad M. Landis and K. Ravi-Chandar for their extensive and thorough discussions during my presentations. I would like to thank Professor Pengyu Ren for his professional knowledge and great suggestions in molecular dynamics simulations.

I acknowledge the Texas Advanced Computing Center (TACC) at the University of Texas at Austin for providing HPC resources that have contributed to the research results reported within this dissertation.

I would like to express my earnest gratitude to Dr. Wei Gao, who is a former member in our research group and currently an assistant professor at University of Texas at San Antonio, for his great help to my research. His insightful ideas and excellent research results lay the foundation for this work. I would like to extend my appreciation to the members in our research group and other collaborators. I would like to thank Dr. Zhiyi Cao, for his collaboration in blister test experiment. I am grateful to Professor Nanshu Lu' research group, including Daniel A. Sanchez and Zhaohe Dai, for the great work in the liquid-filled blisters of 2D crystals. I want to thank Dr. Dong Yan for his collaboration in buckling of graphene on substrate. I would like to acknowledge Dr.

Seung Ryul Na, Dr. Chenglin Wu and Tianhao Yang for their helps and discussions in the group meetings.

I want to thank all my friends, Jiachuan He, Chenglin Yang, Dr. Dongjie Jiang, Dr. Shixuan Yang, Shutao Qiao, Liu Wang and many others who made my life easier and colorful in Austin.

Finally, I would like to thank my parents for their endless love and unconditional support to every decision I have made in my life.

THEORETICAL AND NUMERICAL STUDY ON ADHESIVE INTERACTIONS BETWEEN GRAPHENE AND SUBSTRATE

Peng Wang, Ph. D.

The University of Texas at Austin, 2018

Supervisor: Rui Huang

This dissertation presents a set of theoretical and numerical studies on adhesive interactions between monolayer graphene membranes and their substrates. Both continuum mechanics models and molecular dynamics simulations are developed to investigate deformation of graphene membranes depending on the adhesive interactions with the substrates. First, a numerical study on snap transitions of gas-filled graphene blisters is presented, based on a continuum model combining a nonlinear plate theory with a nonlinear traction–separation relation. The numerical results may be used in conjunction with experiments for quantitative characterization of the interfacial properties of graphene and other two-dimensional (2D) membrane materials.

Next, a statistical mechanics analysis on thermal rippling of monolayer graphene supported on a rigid substrate is presented and compared with molecular dynamics simulations to reveal the entropic effects of thermal rippling on van der Waals interactions between graphene and the substrate. While the amplitude of thermal rippling is reduced by the adhesive interactions, the entropic contribution of thermal rippling leads to an effective repulsion, thus reducing the effective adhesion. Moreover, the effect of a biaxial pre-strain in graphene is considered, and a buckling instability is predicted at a critical compressive strain that depends on both the temperature and the adhesive

interactions. This motivates a systematic study on morphological transitions of monolayer graphene on a substrate under uniaxial compressive strain, from rippling to wrinkling/buckling and to folding.

The presence of water at the interface has significant influence on the adhesive interactions between graphene and its substrate. Molecular dynamics simulations are performed to study the interactions between graphene and a wet substrate that is covered by a thin layer of water. Four stages of the traction-separation relations are identified and they are analyzed approximately by simple continuum models. When the thickness of water layer is below 1 nm, the water molecules form discrete monolayer or bilayer structures, leading to different traction-separation behaviors. Finally, with a finite number of water molecules trapped between a monolayer graphene and its substrate, water-filled graphene blisters form spontaneously. Based on molecular dynamics simulations and a simple theoretical model, the work of adhesion for the graphene/substrate interface may be estimated by measuring the aspect ratios of the graphene blisters. Unlike gas-filled graphene blisters in previous studies, the shape and size of the water-filled graphene blister depend on the wetting properties of graphene and the substrate. The results on wet adhesion and water-filled blisters can be readily extended to other 2D materials.

Table of Contents

List of Tables xii

List of Figures xiii

Chapter 1 Introduction 1

1.1. GRAPHENE AND 2D MATERIALS 1

1.2. ELASTIC PROPERTIES OF GRAPHENE 2

1.3 INTERFACIAL PROPERTIES OF GRAPHENE 8

1.3.1 Experiments 8

1.3.2 Theoretical studies 11

1.4 RESEARCH SCOPE 15

Chapter 2 Snap transitions of graphene blisters 17

2.1 INTRODUCTION 17

2.2 A CONTINUUM MODEL FOR GRAPHENE BLISTERS 20

2.2.1 General formulation 20

2.2.2 Axisymmetric formulation 23

2.3 ANALYTICAL METHODS 25

2.3.1 A linear solution for graphene bubble blisters 25

2.3.2 A membrane solution for graphene bubble blisters 27

2.3.3 A membrane analysis for center-island graphene blisters 27

2.4 NUMERICAL METHOD 28

2.5 GRAPHENE BUBBLE BLISTERS 32

2.5.1 Nano-bubble blisters 32

2.5.2 Micro-bubble blisters 36

2.6 CENTER-ISLAND GRAPHENE BLISTERS 41

2.7 CENTER-HOLE GRAPHENE BLISTERS 46

2.8 SUMMARY 52

Chapter 3 Thermal rippling of graphene on substrate 54
3.1 Introduction 54
3.2 A Continuum statistical mechanics analysis 56
3.3 Molecular dynamics simulation 72
3.4 Results and discussion 75
3.5 Summary 81

Chapter 4 Buckling of monolayer graphene on a substrate 82
4.1 Introduction 82
4.2 Analytical predictions 83
4.2.1 Sinusoidal wrinkling 83
4.2.2 Localized buckling 86
4.2.3 Buckling transitions 87
4.3 Molecular Dynamics Simulations 90
4.4 Results and Discussion 91
4.4.1 Buckling height and width 91
4.4.2 Folding 94
4.4.3 Effect of h_0 97
4.4.4 Effect of temperature 98
4.5 Summary 101

Chapter 5 Wet adhesion of graphene 102
5.1 Introduction 102
5.2 Molecular dynamics simulation 103
5.3 Force fields 108
5.3.1 Water model 108
5.3.2 Interaction between water and substrate 110
5.3.3 Interaction between water and graphene 111
5.4 Modified nucleation theory 112
5.5 Full separation 120
5.5.1 Spherical-cap cavitation 121
5.5.2 Parallel ridge capillary bridging 123

5.5.3 Island capillary bridging 124
5.6 RESULTS AND DISCUSSION 126
5.6.1 Effect of relaxation time 126
5.6.2 Effect of water contact angle of graphene 127
5.6.3 Effect of the thickness of water film 130
5.6.4 Discrete layered water structures 133
5.6.5 Comparison 140
5.7 SUMMARY 144
Chapter 6 Liquid-filled graphene blisters 145
6.1 INTRODUCTION 145
6.2 MOLECULAR DYNAMICS SIMULATION 146
6.3 A SIMPLE MEMBRANE ANALYSIS 149
6.3.1 Aspect ratio of bubble 149
6.3.2 Pressure inside bubble 151
6.4 RESULTS AND DISCUSSION 151
6.4.1 Aspect ratio of bubbles 151
6.4.2 Pressure inside bubble 153
6.4.3 Breakdown of the continuum model 154
6.4.4 Profile of bubble 156
6.5 APPLICATIONS OF 2D MATERIAL BLISTERS 158
6.6 SUMMARY 160
Chapter 7 Conclusions 162
7.1 SUMMARY 162
7.2 FUTURE WORK 164
References 167
Vita 179

List of Tables

Table 1.1: Linearly elastic properties of monolayer graphene predicted by first principles and empirical potential based calculations.....4

Table 5.1: The ε_{CO} parameters and corresponding water contact angles for graphene used in the MD simulations in Chapter 5.....110

Table 5.2: The number of water molecules N and corresponding initial thickness of water film t_w after relaxation for MD simulations with in-plane dimension $L \sim 10$ nm and $\theta_g = 60°$. 132

Table 5.3: The adhesion energy between graphene membrane and bulk water for different water contact angle of graphene θ_g. 143

List of Figures

Figure 1.1: (a) Schematic of the constant *N* blister test before pressurization, and (b) after pressurization and delamination. (c) Atomic force microscope line scans through the center of a pressurized graphene blister at varying pressure differences. (d) AFM image (upper) and schematic (lower) of a pressurized graphene membrane in the island blister test before and (e) after snap-off. (f) AFM line scan through the center of a pressurized graphene membrane in the island blister test. Source: Figures adapted from: (a-c) [27], (d-e) [28], and (f) [29].....3

Figure 1.2: A representative configuration for the thermal rippling of graphene in atomistic Monte Carlo simulations [49]. 6

Figure 1.3: (a) Normalized potential energy as a function of separation and (b) normalized traction-separation relation for van der Waals interactions between graphene and substrate.....13

Figure 1.4: Interfacial blisters between 2D crystals and their supporting substrates [86]. (a) Tapping mode AFM image of liquid filled blisters between highly ordered pyrolytic graphite and SiO_2. (b) A closer look at two monolayer regions from the blue dashed region of (a). (c) Height profile of each blister by curve fitting a parabolic function. (d) Aspect ratio of blisters for different interfaces. 14

Figure 2.1: Three types of graphene blisters: (a) a circular bubble blister with radius *a* and height *h*; (b) a center-island blister; (c) a center-hole blister. .19

Figure 2.2: Shape functions for graphene bubble blisters. 26

Figure 2.3: Pressure versus height for a nanoscale graphene bubble blister (a = 10 nm), showing the snap transitions from A to B and from C to D. The dotted line is the unstable branch from A to C. The linear solution and the approximate membrane solution are shown as dashed lines for comparison. 31

Figure 2.4: Snap transitions of a nanoscale graphene bubble blister (a = 10 nm): (a) Snap-through of the deflection profile from A to B at $p = 243$ MPa; (b) Distributions of the van der Waals force at A and B; (c) Snap-back of the deflection profile from C to D at $p = 142$ MPa; (d) Distributions of the van der Waals force at C and D. The points A-D refer to those marked in Figure 2.3. 33

Figure 2.5: Comparison of the approximate two-state solution by energy minimization with the numerical solution for the pressure-height curve of a graphene bubble blister (a = 10 nm). 34

Figure 2.6: (a) Pressure versus height for a microscale graphene bubble blister (a = 1.5 μm). (b) Pressure-height in a log-log plot. (c) Pressure versus volume for the micro-bubble blister. 37

Figure 2.7: Evolution of deflection profile for a microscale graphene bubble blister (a = 1.5 μm): (a-b) for increasing pressure along branch I (stable), with (b) showing the deflection near the edge; (c-e) for decreasing pressure along the unstable branch, with (c) showing the deflection near the center and (d) showing the deflection near the edge; (f) for increasing pressure along branch II (stable). 38

Figure 2.8: Phase diagrams for graphene bubble blisters. (a) Pressure versus radius; (b) Height versus radius. 41

Figure 2.9: (a) Central height versus pressure and (b) Volume versus pressure for a center-island graphene blister (a = 1.5 μm and b = 0.25 μm). 42

Figure 2.10: Deflection profiles of a center-island graphene blister (a = 1.5 μm and b = 0.25 μm). (a) Donut-like profiles (stable branch I); (b-c) Delamination and popping (unstable branch); (d) Dome-like profiles (stable branch II). 43

Figure 2.11: Snap-back transition for a center-island graphene blister (a = 1.5 μm and b = 0.25 μm): (a) Critical pressure and (b) Pull-in distance. The analytical solutions from Liu *et al.* [28] are shown for comparison. 45

Figure 2.12: Critical pressure for snap-through transition of a center-island graphene blister (a = 1.5 μm and b = 0.25 μm), as a function of the adhesion energy Γ_0. The predictions by the membrane analysis and the analytical model in Boddeti *et al.* [29] are shown in comparison with the numerical results (symbols). 46

Figure 2.13: (a) Pressure-volume curve for a center-hole graphene blister (a = 1.5 μm and b = 0.25 μm). The dashed lines correspond to the ideal gas law, $pV = NkT$, with different values of N as indicated (T = 300 K). (b) Deflection profiles for increasing number of gas molecules. The dashed lines correspond to the critical points B and C in (a).....48

Figure 2.14: (a) Central height, (b) pressure, and (c) the change of radius for a center-hole graphene blister (a = 1.5 μm and b = 0.25 μm). Dashed lines show the predictions by the approximate membrane analysis. 48

Figure 2.15: Calculated delamination resistance curves for a center-hole graphene blister (a = 1.5 μm and b = 0.25 μm) using two different formulas based on the approximate membrane analysis. 49

Figure 2.16: Pressure-volume curves, (a) for unstable growth of a center-hole graphene blister (d = 1.0 μm) and (b) for stable growth with d = 0.01 μm, both under N-control. The dashed lines correspond to the ideal gas law with different values of N as indicated (T = 300 K).....52

Figure 3.1: Thermal rippling of graphene on a rigid substrate by MD simulation (Γ_0 = 0.242 J/m^2, h_0 = 0.316 nm, ε_0 = 0, and T = 1000 K): a top-view snapshot with color contour for the height and a deflection profile along a line.....57

Figure 3.2: (a) Predicted normal traction as a function of temperature at different average separations, $\bar{z} = 1$, 1.01, 1.02, and 1.05 (symbols by summation and lines by integral approximation); (b) Predicted traction-separation relations at different temperatures, in comparison with the relation at T = 0 K (dashed line). Parameters: D = 1.4 eV, Γ_0 = 0.242 J/m^2, h_0 = 0.316 nm, η = 0.11, and ε_0 = 0. 65

Figure 3.3: (a) Predicted equilibrium average separation as a function of temperature, with an unstable branch for the critical separation (dashed lines); (b) Predicted out-of-plane coefficient of thermal expansion as a function of temperature.....66

Figure 3.4: (a) Predicted RMS amplitude of thermal rippling as a function of temperature. (b) Normalized adhesion energy as a function of temperature due to the effect of thermal rippling. 67

Figure 3.5: Effects of pre-strain by the statistical mechanics analysis (with parameters: E^* = 403 N/m, D = 1.4 eV, Γ_0 = 0.242 J/m^2, h_0 = 0.316 nm, η = 0.11). (a) Traction-separation relations at T = 300 K with different pre-strains as indicated. The dashed line is the traction-separation relation at T = 0 K, independent of the pre-strain. (b) Equilibrium average separation, with a critical strain at each temperature. (c) RMS amplitude of thermal rippling. (d) Critical strain versus temperature (a stability phase diagram). 69

Figure 3.6: (a) Predicted rippling stress as a function of pre-strain; (b) Comparison of the average in-plane stresses at 1000 K with and without rippling.72

Figure 3.7: Comparison between theoretical predictions and MD (ε_0 = 0): (a) RMS amplitude of thermal rippling as a function of temperature for different η. (b) Equilibrium average separation as a function of temperature. (c) Average interaction energy between graphene and substrate. (d) Average in-plane stress in graphene (dashed line for the case of no rippling). All symbols are from MD simulations and lines by the theoretical predictions.....77

Figure 3.8: Effects of pre-strain by MD (Γ_0 = 0.242 J/m^2, h_0 = 0.316 nm, and η = 0.11). (a) RMS amplitude of thermal rippling as a function of strain at different temperatures. (b) Equilibrium average separation as a function of strain. (c) Average interaction energy between graphene and substrate. (d) Average in-plane stress in graphene. All symbols are from MD simulations and lines by the theoretical predictions.....79

Figure 3.9: Buckling of a substrate-supported graphene by MD simulation at 300 K with a biaxial pre-strain of -0.02. The side length of the graphene membrane as shown is about 20 nm, and the interfacial properties are: Γ_0 = 0.242 J/m^2 and h_0 = 0.316 nm.....80

Figure 4.1: (a) Wrinkling profile of top view (Top) and cross-sectional view (Bottom) from MD simulation for a square graphene membrane with length and width around 20 nm under compressive strain ε_0 = 0.025 at T = 1 K and the interfacial properties Γ_0 = 0.242 J/m^2 and h_0 = 6 nm. (b) Buckling profile of top view (Top) and cross-sectional view (Bottom) from MD simulation for a square graphene membrane with length and width around 20 nm under compressive strain ε_0 = 0.1 at T = 1 K and the interfacial properties Γ_0 = 0.242 J/m^2 and h_0 = 0.316 nm. Cross-sectional profile is extracted by a line scan at the middle of graphene membrane.....85

Figure 4.2: Potential energies for flat, wrinkled and buckled graphene at various strain level. The initial length of graphene is 20 nm and the adhesion energy Γ_0 is 0.242 J/m^2. The wrinkle energies are calculated for both h_0 = 0.316 nm and h_0 = 6 nm.....87

Figure 4.3: (a) RMS amplitude for h_0 = 0.316 nm indicating flat to buckling transition. (b) RMS amplitude for h_0 = 6 nm indicating flat to wrinkling transition. 89

Figure 4.4: (a) Normalized buckle height and (b) normalized buckle width as a function of normalized compressive displacement Δ/l_b for different adhesion energy Γ_0 (l_b). Here we use $h_0 = 0.316$ nm, $L = 20$ nm and $W = 5$ nm. All symbols are from MD simulations and dashed lines by the buckling analysis. 92

Figure 4.5: (a) Normalized buckle height and (b) normalized buckle width as a function of normalized compressive displacement Δ/l_b for different length of graphene membrane L. Here we use $h_0 = 0.316$ nm, $W = 5$ nm and $\Gamma_0 = 0.242$ J/m^2. All symbols are from MD simulations and dashed lines by buckling analysis. 92

Figure 4.6: (a) Normalized buckle height and (b) normalized buckle width as a function of normalized compressive displacement Δ/l_b for $\Gamma_0 = 2.42 \times 10^{-3}$ J/m^2. (c) Buckling profiles of graphene membrane for different compressive displacement from MD simulation. Here we use $h_0 = 0.316$ nm, $L = 80$ nm and $W = 5$ nm. All symbols are from MD simulations and dashed lines by buckling analysis. 94

Figure 4.7: Profiles of graphene membrane under different compressive displacement from MD simulation with $L = 10$ nm, $W = 5$ nm, $h_0 = 0.316$ nm and adhesion energy $\Gamma_0 = 0.242$ J/m^2. 95

Figure 4.8: (a) Normalized RMS amplitude, (b) normalized buckle height and (c) normalized buckle width as a function of normalized compressive displacement Δ/l_b for different equilibrium separation h_0. (d) Buckling profiles of graphene membrane under the same compression $\Delta = 2$ nm for different equilibrium separation h_0. Here we use $L = 20$ nm, $W = 5$ nm and $\Gamma_0 = 0.242$ J/m^2. All symbols are from MD simulations and dashed lines by buckling analysis. The dotted line in (a) are calculated by wrinkling analysis. 96

Figure 4.9: (a) Normalized RMS amplitude, (b) normalized buckle height and (c) normalized buckle width as a function of normalized compressive displacement Δ/l_b for different temperature T. (d) Buckling profiles of graphene membrane under the same compression $\Delta = 1$ nm for different temperature T. Here we use $L = 20$ nm, $W = 5$ nm, $h_0 = 0.316$ nm and $\Gamma_0 = 0.242$ J/m^2. All symbols are from MD simulations and dashed lines by buckling analysis. 99

Figure 4.10: Critical pre-strain for the onset of buckling versus temperature T (a stability phase diagram) from both MD simulations and statistical harmonic analysis.....100

Figure 5.1: MD simulation of a graphene membrane on wet substrate with 14580 water molecules (t_w = 4.19 nm). The water contact angles are 60°and 5° for graphene and the substrate, respectively.(a) A side view snapshot after relaxation, showing the water molecules (oxygen in red and hydrogen in white) between graphene (carbon in gray) and the substrate surface (blue line). (b) Cavity surface at d = 1.12 nm, constructed by the alpha-shape method [167] with a virtual probe sphere of radius 0.4 nm using OVITO [168]. (c) Calculated traction separation relation, subjected to a loading-unloading cycle at T = 300 K.....105

Figure 5.2: (a) A snapshot of a water droplet on a substrate surface with N = 900 and ε_{OS} = 0.08 eV, where the contact angle is around 40°. (b) Water contact angle of substrate as a function of ε_{OS} 109

Figure 5.3: (a) A snapshot of a water droplet on graphene with N = 1000 and ε_{CO} = 6.0 meV, where the contact angle is around 60°. (b) Water contact angle of graphene as a function of ε_{CO} by MD simulations.....111

Figure 5.4: A schematic illustration for a cavity with a spherical cap shape in water without penetrating the substrate. The radius of the cavity is R and the water contact angle of graphene is θ_g. 115

Figure 5.5: Prediction of traction-separation relation and cavitation by a modified nucleation theory: (a) Traction-separation relation diagram, in comparison with MD simulation (filled symbols). (b) Free energy function under different separation d. (c) Cavity radius as a function of separation, in comparison with MD simulation (filled symbols). (d) Nucleation rate for cavitation and de-cavitation. The dashed lines in (a) and (c) are the unstable branches. The vertical lines in (a) and (c) indicate the transition (from A to B) at the critical strain. 117

Figure 5.6: Full traction separation relation from both MD simulation and continuum model. The initial thickness of water film t_w is 4.19 nm and the water contact angle of graphene membrane θ_g is 60°. 121

Figure 5.7: Cross section of a water bridging between graphene and substrate, comparing the continuum model (red lines) with MD simulation (t_w = 4.19 nm, θ_g = 60° and σ = 24.2 MPa). 123

Figure 5.8: Traction-separation relation by MD simulations with different relaxation times (t_w = 4.19 nm and θ_g = 60°). 126

Figure 5.9: Traction-separation relation by MD simulations and analytical prediction with different water contact angle of graphene θ_g (t_w = 4.19 nm). (a) Full traction-separation diagram by MD simulations. (b) Zoom in of (a) near the cavitation point. (c) Traction-separation relation and (d) radius of cavity predicted by the modified nucleation theory, with the vertical dashed lines for onset of cavitation. 129

Figure 5.10: Traction-separation relation by MD simulations and analytical prediction with different thicknesses of water film (θ_g = 60°). (a) Full traction-separation diagram by MD simulations. (b) Zoom in of (a) near the cavitation point. (c) Traction-separation relation and (d) radius of cavity predicted by the modified nucleation theory, with the vertical dashed lines for onset of cavitation. 130

Figure 5.11: Side view snapshots (top) and top view snapshots (bottom) of (a) monolayer water structure with N = 1156 and (b) bilayer water structure with N = 2312 from MD simulations with water contact angle of graphene θ_g = 60°. Top view snapshots of water layers are shown by removing graphene on top of them. 133

Figure 5.12: Traction-separation relation from both MD simulation and analytical prediction for monolayer water. Top view snapshots at critical points from MD simulation are inserted. The water contact angle of graphene membrane θ_g is 60°. The blue dashed line and green dotted line are predicted by analytical monolayer and bilayer model, respectively.135

Figure 5.13: Traction-separation relation of (a) monolayer water structure and (b) bilayer water structure for different water contact angles. 139

Figure 5.14: Interface spacings at graphene/water interface a^{gw} and water/substrate interface a^{ws} from MD simulations (all dots) for monolayer water structure at different temperatures. The dashed lines are equilibrium interlayer separations predicted by theoretical model at T = 0 K. ..139

Figure 5.15: (a) Strength, (b) initial stiffness, (c) adhesion energy and (d) interaction range of the traction-separation relation for graphene on wet substrate. All symbols are from MD simulations and dashed lines represent the graphene/substrate system without any water (dry adhesion). 143

Figure 6.1: MD simulation of a graphene bubble with 2700 water molecules. The adhesion energy $\Gamma_0 = 0.242$ J/m^2, while the water contact angles are 60° and 40° for graphene and the substrate, respectively. (a) A top view snapshot of the bubble, with color contour for the z-position of the carbon atoms in graphene; (b) A height profile along a line scan (dashed line in (a)) across the bubble; (c) A cross-sectional view of the bubble, showing the water molecules (oxygen in red and hydrogen in white) between graphene (carbon in gray) and the substrate surface (blue line). 147

Figure 6.2: Analytical solution and MD simulations of water-filled blisters. Comparing simulation results (circular markers) with our simplified model assuming frictionless, sliding interface. The deviations, especially under small height or aspect ratio, are attributed to the size limitation of MD, which can induce discrete behaviors. The inset figure demonstrates how the shape of the blister changes for different values of the work of adhesion. 152

Figure 6.3: Normalized pressure for different aspect ratio h/a. The dots represent result from MD simulations while the dashed lines represent three types of analytical solutions. 153

Figure 6.4: (a) The height of graphene blister as a function of the number of water molecules, predicted by the continuum model for $\Gamma_0 = 0.1$ J/m^2 and 0.242 J/m^2, where the dashed line indicates the critical height for the continuum model. (b) The breakdown limit for the continuum model, in terms of the adhesion energy Γ_0 and the number of water molecules N with the water contact angles being 60° and 40° for graphene and the substrate, respectively. 154

Figure 6.5: Blister aspect ratio for different numbers of water molecules, for (a) $\Gamma_0 =$ 0.242 J/m^2 and (b) 0.1 J/m^2 with water contact angles being 60° and 40° for graphene and the substrate, respectively. The dashed line is predicted by the continuum model. The breakdown of the continuum model is predicted at $N = 1690$ for $\Gamma_0 = 0.242$ J/m^2 (dotted vertical line in (a)) and $N = 7640$ for $\Gamma_0 = 0.1$ J/m^2. 156

Figure 6.6: Height profiles of the bubble with $N = 2700$ for different adhesion energies from 0.1 J/m^2 to 0.5 J/m^2. Dots represent carbon atoms. The height profile with $N = 300$ and $\Gamma_0 = 0.1$ J/m^2 was added to show the monolayer structure. 158

Chapter 1 Introduction

1.1. GRAPHENE AND 2D MATERIALS

Graphene, consisting of a single layer of carbon atoms arranged in a hexagonal lattice, is the basic structural element of many other allotropes of carbon. It can be wrapped up into 0D fullerenes, rolled into 1D nanotubes or stacked into 3D graphite. In 2004, Novoselov and Geim [1] first used the "scotch-tape" method to mechanically exfoliate graphite multiple times to produce monolayer and multilayer graphene in a simple and cheap way. Since then, substantial research has shown that graphene has exceptional electronic, mechanical, and thermal properties. It is the strongest material ever tested, efficiently conducts heat and electricity, and is nearly transparent. In 2010, the Nobel Prize in Physics was awarded to Novoselov and Geim "for groundbreaking experiments regarding two-dimensional material graphene".

Geim and Novoselov's "scotch-tape" method is simple but inefficient for large-scale production. The graphene flakes produced by this method were small in size and irregular in shape [2]. To obtain larger areas of graphene, Ruoff and his co-workers [3] pioneered the method of growing graphene on thin copper foil by chemical vapor deposition (CVD), which allows graphene to be synthesized in an easily scalable manner. Tao *et al*. [4] developed a two-step CVD process to control the grain size of graphene grown on silicon wafers. Other metals, such as nickel [5-7], ruthenium [8, 9], palladium [10], platinum [11] and silicon nitride [12], have also been used as seed layers to grow graphene via CVD.

Experiments have observed extraordinary electronic, mechanical, thermal and optical properties of graphene membrane. In 2005, Zhang *et al*. [13] observed the quantum Hall effect and Berry's phase in graphene, which laid the foundation for discovery of extraordinary electronic properties of graphene. The electron mobility in

suspended graphene was found to be exceptionally high, as demonstrated by several measurements, ranging in values from 10^5 $cm^2 V^{-1} s^{-1}$ near room temperature [14, 15] to 10^7 cm^2 V^{-1} s^{-1} at liquid helium temperatures [16]. The mobilities in graphene are, however, very sensitive to the supporting substrate [17]. Graphene was reported to behave as an n-type semiconductor after being doped by nitrogen [18, 19]. An extremely high thermal conductivity was measured by Balandin *et al*. [20] using Raman spectroscopy, suggesting that graphene might be suitable for heat management in electronic applications. Graphene displays a universal optical conductivity [21, 22] and a tunable interband optical response [23, 24], making graphene suitable for various photonic applications.

In addition to graphene, many other 2D materials have also been discovered, such as transition metal-dichalcogenides (TMDs, e.g., MoS2), hexagonal boron-nitride (h-BN), and black phosphorous or phosphorene. The family of 2D materials offers a full spectrum of physical properties, from conducting graphene to semiconducting MoS_2 and to insulating h-BN. Moreover, the 2D crystal structures render a unique combination of mechanical properties, with high in-plane stiffness and strength but extremely low flexural rigidity. Together, the 2D materials are promising for a wide range of applications [25, 26].

1.2. ELASTIC PROPERTIES OF GRAPHENE

Similar to thin membranes, graphene may be deformed by in-plane stretching or by bending out-of-plane. As a result, the elastic properties include both in-plane moduli and bending stiffness, which have been measured in experiments and predicted by theoretical methods from first principles to continuum modeling.

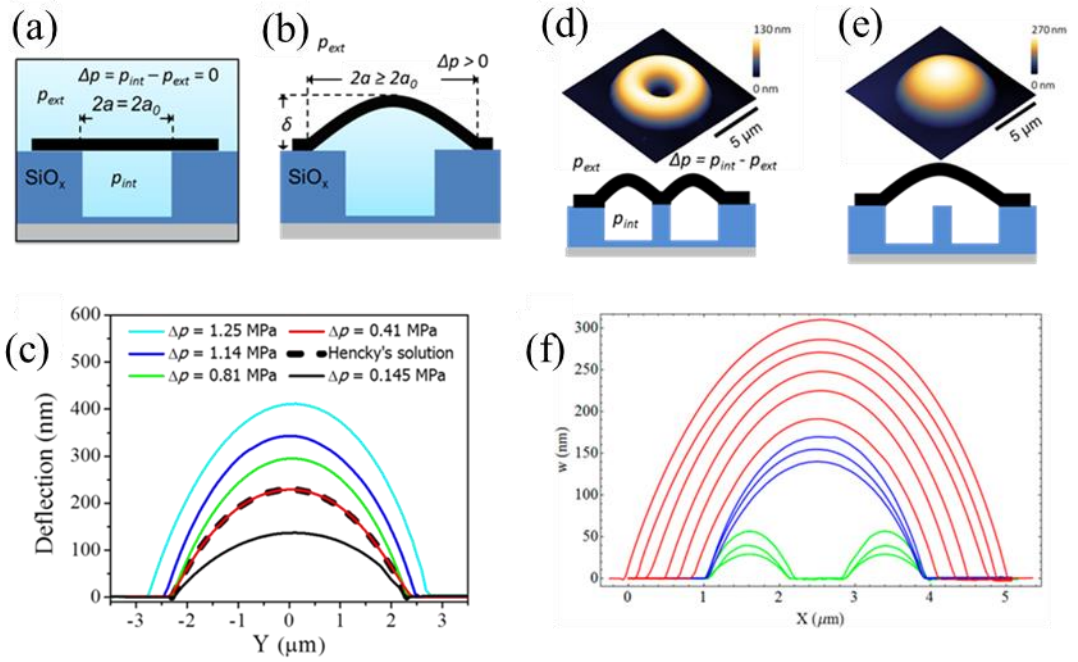

Figure 1.1: (a) Schematic of the constant *N* blister test before pressurization, and (b) after pressurization and delamination. (c) Atomic force microscope line scans through the center of a pressurized graphene blister at varying pressure differences. (d) AFM image (upper) and schematic (lower) of a pressurized graphene membrane in the island blister test before and (e) after snap-off. (f) AFM line scan through the center of a pressurized graphene membrane in the island blister test. Source: Figures adapted from: (a-c) [27], (d-e) [28], and (f) [29].

A direct measurement of elastic properties of monolayer graphene was first reported by Lee *et al.* [30] from nanoindentation experiments of suspended monolayer graphene membranes. By using an atomic force microscope (AFM), they obtained a 2D Young's modulus of 340 N/m and a breaking strength of 42 N/m. The elastic properties of 2D materials can also be measured by pressurized blister tests or bulge tests (see Figure 1.1), a common method for thin film materials [31], due to its remarkable gas and liquid impermeability. Koenig *et al.* [27] conducted a series of blister tests and obtained an elastic moduli of 347 N/m for monolayer graphene membrane. In both the AFM-based

nanoindentation and pressurized blister experiments, the effect of bending modulus of the 2D materials is often considered to be negligible in the mechanics model. However, direct measurement of the bending modulus has been challenging for monolayer graphene. The value often quoted for the bending modulus of monolayer graphene (~1.2 eV) was estimated from the phonon spectrum of bulk graphite [32].

Method	2D Young's modulus E_{2D} (N/m)	Poisson's ratio ν	Biaxial modulus (N/m)	Bending modulus D_m (eV)	Gaussian modulus D_G (eV)
DFT [33]	345	0.149	406	1.49	–
DFT [34]	348	0.169	419	–	–
DF-TB [35]	–	–	–	1.61	-0.7
DFT [36]	–	–	–	1.44	-1.52
REBO-1 [37]	236	0.412	401	0.83	–
REBO-2 [38]	243	0.397	403	1.41	–
AIREBO [39]	279	0.357	434	1.56	–
REBO-LB [40]	349	0.132	402	–	–
LCBOPII [41]	343	0.156	406	~1.1	–

Table 1.1: Linearly elastic properties of monolayer graphene predicted by first principles and empirical potential based calculations.

The elastic properties of pristine graphene have been well predicted by first principles based calculations [33, 34, 42]. When subjected to small in-plane deformation, graphene demonstrates isotropic and linear elasticity with a 2D Young's modulus (E_{2D}) and Poisson's ratio (ν) as listed in Table 1.1 [43]. The predicted 2D Young's moduli are in good agreement with the measured values [30]. In addition to first principle calculations, Molecular dynamics (MD) simulations are often used to investigate the

elastic behavior of graphene. The accuracy of MD simulations highly depends on parametrization of the empirical potentials that describe the atomic interactions. Several versions of reactive empirical bond-order (REBO) potentials have been commonly used in MD simulations of graphene and carbon nanotubes (CNTs) [37-39]. Unfortunately, these potentials were not parameterized to yield accurate elastic properties of graphene [44, 45]. As listed in Table 1.1, the 2D Young's moduli and Poisson's ratios obtained by the REBO potentials are considerably different from the values predicted by first-principles calculations, although the biaxial moduli ($\frac{E_{2D}}{1-\nu}$) are in good agreement. A few other potentials have also been used for graphene, and their predictions of the linear elastic properties are listed in Table 1.1 for comparison.

Due to the extremely low flexural stiffness of graphene, the flexural deformation of graphene is commonly observed in the form of rippling, wrinkling, and folding. A general continuum mechanics formulation was proposed to describe the coupled in-plane and flexural deformation of monolayer graphene [46]. Under relatively small in-plane deformation and moderately large out-of-plane deflection, the general formulation reduces to a form similar to the nonlinear von-Karman plate theory with two elastic bending moduli [47], one for the mean curvature and the other for the Gaussian curvature. Unlike classical plate theory, the bending moduli of monolayer graphene are not directly related to the in-plane Young's modulus and Poisson's ratio. Instead, they are independent properties resulting from multibody interactions among carbon atoms in a monolayer [33, 35, 36, 44, 45, 48]. As listed in Table 1.1, the bending modulus of graphene associated with mean curvature (D_m) can be well predicted by the second-generation REBO potential [38], which includes atomic interactions up to the third nearest neighbors via bond angle and dihedral angle effects. On the other hand, the

bending modulus associated with Gaussian curvature (D_G) has received less attention, for which the two reported values differ by more than a factor of two [35, 36].

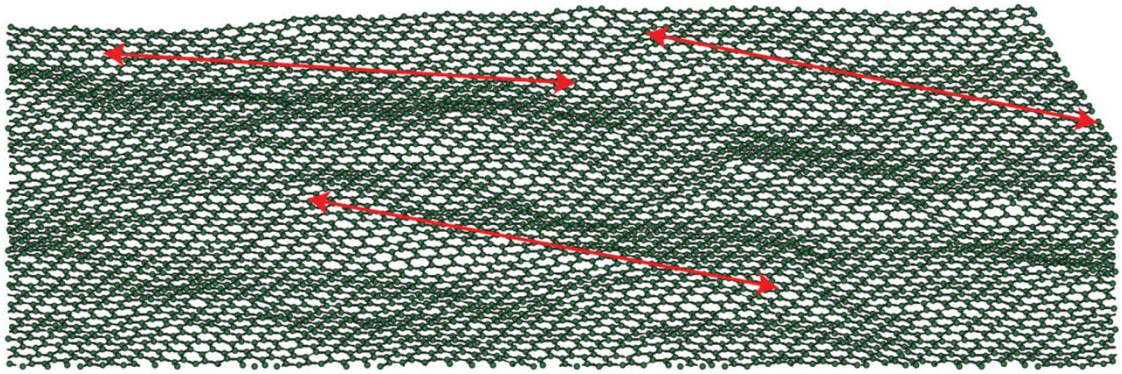

Figure 1.2: A representative configuration for the thermal rippling of graphene in atomistic Monte Carlo simulations [49].

Although the basic elastic properties of graphene have been reasonably understood based on first principles, the effects of finite temperature on the elastic properties have not been fully established. It is well known that a graphene monolayer is not perfectly flat at a finite temperature, as illustrated in Figure 1.2. Experimental observations have found that suspended graphene membranes often display spontaneous ripples [2, 50, 51]. The inevitable thermal rippling may have profound effects on thermomechanical properties of graphene, including thermal expansion and temperature-dependent elastic modulus [52, 53]. MD simulations by Zhao and Aluru [54] predicted that Young's modulus of graphene does not vary significantly with temperature up to about 1200 K, beyond which graphene becomes more compliant. On the other hand, by atomistic Monte Carlo (MC) simulations, Zakharchenko *et al.* [55] predicted a non-monotonic behavior of the shear modulus of graphene with a maximum at about 900 K, while Chen and Chrzan [56] predicted a monotonic decrease of the elastic modulus of graphene with temperature up to 4000 K. More recently, Los *et al.* [57] predicted a power

law scaling of the in-plane elastic modulus, which decreases with increasing membrane size at a finite temperature. Another manifestation of thermal rippling is the reduction of the projected area, which has been suggested as the cause of the negative in-plane thermal expansion of graphene [55, 56]. Based on density function theory (DFT) calculations and a quasiharmonic approximation, Mounet and Marzari [58] predicted negative in-plane thermal expansion for graphite and graphene, which was attributed to the lowest transversal acoustic (ZA) phonon modes (also called bending modes). Negative thermal expansion of graphene was also predicted by a nonequilibrium Green's function approach [59] and ab initio molecular dynamics (AIMD) simulations [60]. By statistical mechanics and MD simulations, Gao and Huang [53] found that the thermal rippling was responsible for the effectively negative in-plane thermal expansion of graphene at relatively low temperatures, while a transition to positive thermal expansion is predicted as the anharmonic interactions suppress the rippling effect at high temperatures.

More recently, Blees *et al.* [61] measured the spring constant of a graphene cantilever structure by using the photon pressure from an infrared laser, based on which the bending modulus of monolayer graphene was inferred (using an elementary mechanics model). They also measured thermal fluctuations of the graphene cantilevers to determine the spring constants based on the equipartition theorem of classical statistical mechanics. Both methods yielded a surprisingly high bending modulus for monolayer graphene, on the order of $10^3 - 10^4$ eV. They attributed the obtained high bending modulus to the effects of ripples (both static and thermal) in the graphene membranes, which suggested a strong size dependence for the bending modulus of graphene at finite temperatures. Based on a variational perturbation method, a nonlinear statistical mechanics analysis of thermal fluctuations of elastic sheets such as graphene

was conducted to evaluate the effective bending stiffness at finite temperatures [62], which demonstrated how an elastic sheet becomes effectively stiffer (for bending) at larger sizes.

1.3 INTERFACIAL PROPERTIES OF GRAPHENE

Surface forces play a significant role as graphene membranes are being transferred and integrated into microelectronics, MEMS and NEMS devices and composite materials. In addition, graphene can conform more closely to a substrate surface than conventional materials due to its high flexibility [63], providing a great opportunity to study short-range interactions like van der Waals or Casimir forces. Thus it is essential to understand and characterize the interfacial properties between graphene and substrates.

1.3.1 Experiments

Experimental works on graphene adhesion have mainly focused on the measurement of adhesion energies between graphene and various substrates. The majority of adhesion measurements have been made using blister and laminated beam fracture experiments. Zong *et al*. [64] trapped nanoparticles at graphene-silicon interface acting as point wedges to support axisymmetric blisters and reported an adhesion energy of 0.151 J/m^2 by measuring the particle height and blister radius using a scanning electron microscope. Applying a pressurized blister with fixed number of gas molecules trapped in the micro-chamber for mechanically exfoliated graphene on SiO_2, Koenig *et al*. [27] measured the adhesion energy of 0.45 J/m^2 for monolayer graphene and 0.31 J/m^2 for samples containing two to five graphene layers. Boddeti *et al.* [65] carried out similar blister experiments and obtained a lower average adhesion energy of 0.24 J/m^2

for the graphene/SiO_2 interfaces. Recently, utilizing similar mechanical blister test configuration, Lloyd *et al.* [66] observed adhesion hysteresis during inflation and deflation of pressurized MoS_2 bubbles, and estimated the work of separation of MoS_2 membranes from a SiO_x substrate to be 220 mJ/m^2 and the work of adhesion to be 42 mJ/m^2, calling for further study on the adhesion hysteresis. A variation of the standard blister test 1the pressure difference increases, the graphene snaps off the inner post and then at a higher pressure, begins delamination from the outer edge as in the standard blister test. Boddeti *et al.* [29] utilized the pressure at snap-off to measure the adhesion energy of 0.24 J/m^2 for graphene on SiO_2 substrate. The time reversal of this experiment is to keep the outside pressure fixed and let the internal pressure decrease slowly as gas diffuses out of the micro cavity. This results in a decreasing height of the blister and a pull-in instability (snap-back) at a critical height [28, 67]. Liu *et al.* [28] found the pull-in instability took place at separation of 10−20 nm and follow an inverse fourth power traction-separation relation, which is consistent with van der Waals interactions. A numerical study on the snap transitions is presented in Chapter 2 of this dissertation to establish the relationship between van der Waals interactions and measurable quantities.

Larger scale blister tests on CVD graphene that had been transferred to copper and silicon were conducted by Cao *et al.* [68]. Following transfer, the graphene was reinforced by an epoxy layer and separated from the substrates under volume-controlled pressurization. Measurements of the blister profile as a function of pressure allowed the adhesion energies to be extracted from mechanics models of a thin membrane or plate, depending on the thickness of the composite film specimen (graphene and epoxy) [47]. The adhesion energies were commensurate with the values obtained with exfoliated, single crystal graphene by Bunch's group [27, 29, 65].

Blister tests are inherently mixed mode in nature with both normal and shear tractions at the interface near the crack front [69]. By varying the thickness of the backing layers in their blister tests, Cao *et al.* [70] showed that the interfacial toughness between graphene and both substrates (Cu and Si) had a strong dependence on the fracture mode-mix. In the absence of plasticity effects, the most likely explanation of this effect is asperity locking [71] due to the surface roughness of the substrates.

Another common fracture test, the double cantilever beam (DCB), has also been utilized to measure the interfacial properties between graphene and substrate. By bonding silicon backing layers to both sides of the graphene-coated copper foil with epoxy and applying loads on the backing layers, Na *et al*. [72] reported a selective delamination along different interfaces depending on the separation rate. The separation energies associated with delamination along the graphene/copper foil and graphene/epoxy interfaces were 6 and 3.4 J/m^2, respectively. Selective delamination has also been observed for graphene-coated copper films on silicon wafers [73, 74]. In this case, Yoon *et al*. [73] reported the adhesion energy of large-area monolayer graphene to be 0.72 J/m^2. In the experiments by Na *et al.* [74], higher separation rates led to delamination along the silicon/copper interface at 1.7 J/m^2 compared to 1.5 J/m^2 for delamination along the graphene/copper interface at lower separation rates.

Nanoindentation experiments have also been widely used for adhesion measurements. Using a combined SEM/AFM/STM technique, Ishigami *et al.* [75] showed that structural corrugations of the graphene sheet partially conform to the underlying silicon oxide substrate and estimated the adhesion energy between graphene and SiO_2 to be 0.096 J/m^2. Jiang and Zhu [76] used AFM in the force spectroscopy mode to measure the adhesion force between graphene and spherical tip, and reported adhesion energies of monolayer graphene to SiO_2 and Cu tips as 0.46 and 0.75 J/m^2, respectively.

On the other hand, displacement-controlled nanoindentation experiments was used by Suk *et al.* [77] to compare the force profiles for a diamond tip indenting mono-, bi- and trilayer graphene membranes that had been transferred onto silicon oxide substrates. The measured force profiles were compared with finite element method (FEM) based numerical simulations that accounted for the interactions between the probe and the target surfaces as well as between graphene and silicon oxide. The traction-separation relations that were required to bring the numerical and experimental force profiles into agreement suggested that both van der Waals and capillary forces were at play.

In general, the processes of adhesion and separation can be described by interfacial traction-separation relations (TSRs) as in cohesive zone modeling of nonlinear fracture mechanics [78, 79]. The TSR of an interface provides a functional form of the interaction during fracture, with which the interfacial strength and the range of interactions can be determined in addition to the adhesion energy or fracture toughness of the interface. Recently, Na *et al.* [80] reported measurements of the TSRs between wet-transferred, CVD grown graphene and the native oxide surface of silicon substrates by combining the DCB experiments with interferometry measurements. The deduced TSRs exhibited a much longer range (greater than 100 nm) than those normally associated with van der Waals forces. Similar to the displacement-controlled nanoindentation measurements [77], the TSRs suggest that interaction mechanisms other than van der Waals forces should be considered for adhesion of graphene and other 2D materials.

1.3.2 Theoretical studies

Theoretical studies of interactions between graphene and substrates have mainly focused on van der Waals interactions. By DFT Rudenko *et al*. [81] studied the

morphology effect on graphene/mica interactions and found the mica-graphene binding is mainly of van der Waals nature by assuming electroneutrality for both surfaces. Gao *et al.* [82] investigated the interfacial adhesion between graphene and SiO_2 by DFT with dispersion correction and concluded that van der Waals interaction is the predominated mechanism at the interface, with an adhesion energy of ~0.3 J/m^2 and an equilibrium separation of ~0.3 nm. Such interactions can be included in MD simulations using the empirical Lennard-Jones (LJ) potential for pairwise particle-particle interactions. By summing up the energy between carbon atoms of graphene and all atoms in the substrate, a generic form of the van der Waals interaction potential energy function (per unit area) between a flat monolayer graphene and a flat substrate surface can be written as [83]

$$V(z) = \Gamma_0 \left[\frac{1}{2} \left(\frac{h_0}{z} \right)^9 - \frac{3}{2} \left(\frac{h_0}{z} \right)^3 \right], \tag{1.1}$$

where z is the separation distance between graphene and the substrate surface, Γ_0 is the adhesion energy (per unit area), and h_0 is the equilibrium separation, as shown in Figure 1.3a. By taking the first derivative of the interaction energy in Eq. (1.1) with respect to z, the van der Waals force (per unit area, positive for attraction) between graphene and substrate can be obtained as

$$\sigma_{vdW}(z) = \frac{9\Gamma_0}{2h_0} \left[\left(\frac{h_0}{z} \right)^4 - \left(\frac{h_0}{z} \right)^{10} \right], \tag{1.2}$$

as shown in Figure 1.3b. Such a traction-separation relation has been used to model adhesion and delamination of graphene at much larger scales such as graphene bubbles and blisters [28, 29, 67, 84]. The van der Waals force σ_{vdW} is zero at the equilibrium separation ($z = h_0$) and reaches a maximum, $\sigma_{vdW}^{\max} = 1.466\Gamma_0 / h_0$, at $z = 1.165 h_0$. The peak traction, often called the interfacial (tensile) strength, is directly related to the two basic parameters: Γ_0 and h_0. The initial stiffness at the equilibrium separation is

$k_0 = 27\Gamma_0/h_0^2$. The range of vdW interactions typically extends to a few times of the equilibrium separation, although the pull-in instability observed in the island blister test indicated much longer ranges (up to 10 - 20 nm) [28].

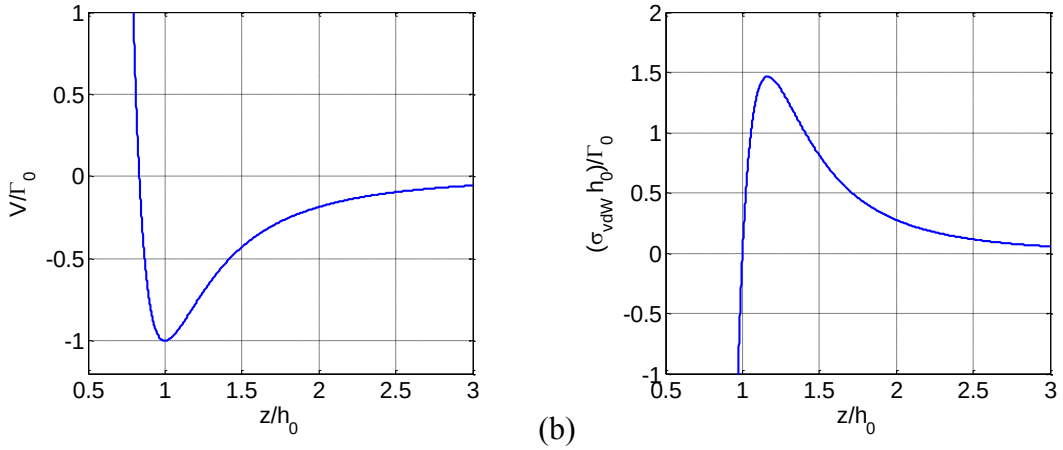

Figure 1.3: (a) Normalized potential energy as a function of separation and (b) normalized traction-separation relation for van der Waals interactions between graphene and substrate.

The continuum model was also used to predict the morphological corrugation of substrate–supported graphene, where the monolayer membrane could be fully conformal, partly conformal or non-conformal to the substrate surface depending on the surface roughness and the adhesive interactions [83]. Moreover, the effective adhesion energy was found to depend on the surface roughness and corresponding graphene morphology [85], which led to apparently lower adhesion energy for multilayered graphene [27]. As discussed in Section 1.2, thermal rippling is inevitable for freestanding graphene. When placed on a solid substrate, the adhesive interactions between graphene and the substrate could considerably suppress thermal rippling. Meanwhile, the statistical nature of thermal rippling would introduce an entropic effect on the graphene–substrate interactions. A

statistical mechanics analysis is presented along with MD simulations in Chapter 3 of this dissertation to predict the entropic effect of thermal rippling.

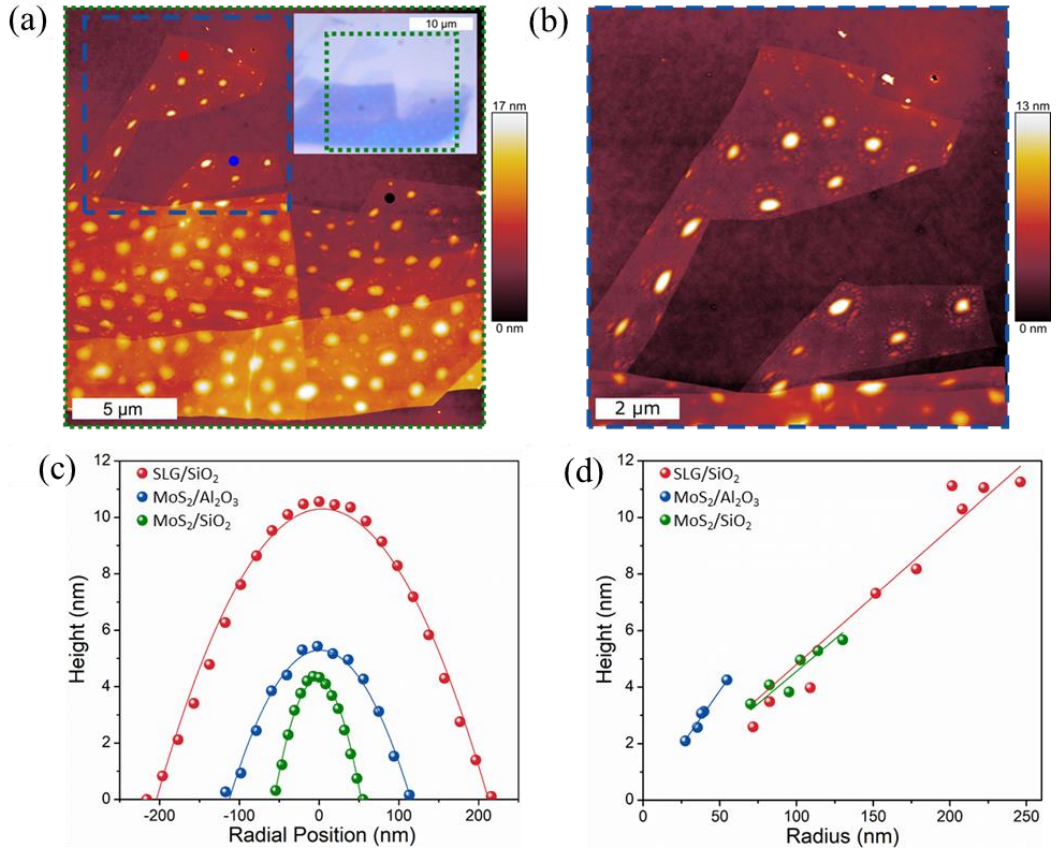

Figure 1.4: Interfacial blisters between 2D crystals and their supporting substrates [86]. (a) Tapping mode AFM image of liquid filled blisters between highly ordered pyrolytic graphite and SiO_2. (b) A closer look at two monolayer regions from the blue dashed region of (a). (c) Height profile of each blister by curve fitting a parabolic function. (d) Aspect ratio of blisters for different interfaces.

Since water is inevitably present for experiments conducted in ambient environments, the effects of water on the interfacial properties have been investigated. Gao *et al.* [87] performed MD simulations to study the traction-separation behaviors for wet adhesion of graphene on amorphous silicon oxide covered by a thin layer of water [87]. Compared to van der Waals interactions for dry adhesion of graphene, a smaller

work of separation, a lower maximum traction but a longer interaction range were predicted with morphological evolution of water from cavitation to capillary bridging. More interestingly, Xu *et al.* [88] observed water adlayers grew epitaxially at graphene/mica interfaces in a layer-by-layer fashion, with submonolayers and second adlayers appearing ice-like while thicker layers appearing liquidlike. In addition, formation of 'square ice' locked between two graphene sheets at room temperature was reported by Algara-Siller *et al.* [89], which was also verified by MD simulations. It is also suspected that water molecules trapped at the interface between graphene and its substrate lead to spontaneous formation of graphene nanoblisters (see Figure 1.4), which can be measured to estimate the work of adhesion for the interface [86]. A systematic study on the wet adhesion of graphene is presented in Chapter 5 of this dissertation, followed by a study on liquid-filled graphene blisters in Chapter 6.

1.4 RESEARCH SCOPE

This dissertation presents a set of theoretical and numerical studies on adhesive interactions between monolayer graphene membranes and their substrates. Both continuum mechanics models and molecular dynamics (MD) simulations are developed to investigate deformation of graphene membranes depending on the adhesive interactions with the substrates, including gas-filled and liquid-filled graphene blisters, rippling, wrinkling, buckling and folding of graphene. The remainder of the dissertation is organized as follows.

Chapter 2 presents a numerical study on snap transitions of gas-filled graphene blisters. A continuum model is adopted combining a nonlinear plate theory for monolayer graphene with a nonlinear traction–separation relation for van der Waals interactions. The

numerical results may be used in conjunction with experiments for quantitative characterization of the interfacial properties of graphene and other two-dimensional (2D) membrane materials.

In Chapter 3, we present a statistical mechanics analysis on thermal rippling of monolayer graphene supported on a rigid substrate, assuming a generic form of van der Waals interactions between graphene and substrate at T = 0 K. The rippling amplitude, the equilibrium average separation, and the average interaction energy are predicted simultaneously and compared with MD simulations. Moreover, a rippling to buckling transition is predicted at a critical compressive strain that depends on both the temperature and the adhesive interactions.

Motivated by the predicted buckling transition in Chapter 3, we present a systematic study on morphological transitions of monolayer graphene on a substrate under uniaxial compression, from rippling to wrinkling/buckling and to folding in Chapter 4.

Chapter 5 considers the effects of water at the interface. MD simulations are preformed to study wet adhesion of graphene with a thin layer of water at the interface, from a few nanometers to below 1 nm. The effect of water contact angle of graphene on the traction-separation relation is investigated.

In Chapter 6, molecular dynamics simulations and a simple theoretical model are presented to investigate liquid-filled graphene blisters, with a finite number of water molecules trapped between a monolayer graphene and its substrate. The relation between the work of adhesion for the graphene/substrate interface and the aspect ratios of the graphene blisters are established.

Finally, Chapter 7 concludes the dissertation with an outlook on future study.

Chapter 2 Snap transitions of graphene blisters[1]

2.1 INTRODUCTION

Pressurized blister tests are commonly used to measure mechanical and adhesion properties of thin films and coatings [90-93]. Several types of blister tests have been developed, including the standard blister test, island blister test, constrained blister test and peninsula blister test. Recently, similar blister tests have been applied to measure interfacial properties of graphene [27, 64, 65, 68]. Using a center-island blister configuration, Liu *et al.* [28] observed pull-in instability of graphene membranes at ~10 nm separation. Although such a separation is considerably larger than typical ranges of van der Waals forces, it was found to be consistent with a theoretical model assuming long-range van der Waals interactions. In a subsequent study, Boddeti *et al.* [29] reported switchable shapes of graphene blisters using the same blister configuration. In this chapter, we show by a numerical analysis that both the pull-in instability and the switchable blister shapes are results of snap transitions, a structural instability modulated by adhesive interactions. Moreover, it is suggested that such a blister test may be used to determine the two key parameters of van der Waals interactions between graphene and its substrate, including the adhesion energy and the equilibrium separation (as a length scale). The latter is typically less than 1 nm and thus difficult to determine by other experimental methods.

Besides specifically designed graphene blister tests, graphene bubble blisters are often observed when graphene membranes are placed on top of solid substrates [94, 95]. Such graphene bubble blisters may form during transfer or growth processes with trapped

[1] The content in this chapter was published in P. Wang, K.M. Liechti, and R. Huang, *Snap transitions of pressurized graphene blisters.* Journal of Applied Mechanics, 2016. **83**(7): p. 071002. Wang did the numerical simulation and wrote the paper. Liechti and Huang reviewed and revised the paper.

gas or hydrocarbon residuals between the graphene membranes and the substrates since graphene is impermeable to most gases [96]. Irradiation of energetic protons or exposure to hydrofluoric acid (HF) and water (H_2O) vapors for etching could also cause formation of graphene bubble blisters due to accumulation of the chemically released gas from the substrate [94, 97]. The observed graphene bubble blisters have diameters ranging from tens of nanometers to tens of microns, with a variety of shapes (circular, triangular, and diamond). Use of graphene nano-bubbles has been suggested as a viable method for strain engineering to manipulate the electronic properties of graphene [98-101]. Microscale graphene bubble blisters have been used to study the Raman spectrum of graphene under biaxial strain [102]. In a previous study [103], analytical methods were developed to deduce the interfacial adhesion energy from measurements of the bubble blister size (height and radius). Subsequently, a more accurate solution was obtained by a numerical method, in comparison with the analytical solutions and molecular dynamics simulations [47]. The effect of van der Waals interactions was considered and a snap-back behavior was predicted for the graphene bubble blisters when the pressure difference drops to a critical level, similar to the pull-in instability observed for the center-island blisters [28]. In this chapter, we consider both the graphene bubble blisters and the center-island blisters, with a focus on the snap transitions. Such snap transitions depend on the nonlinear interactions between graphene and its substrate, which may be exploited to experimentally characterize the adhesive properties of graphene and other thin membrane materials.

The remainder of this chapter is organized as follows. Section 2.2 presents a continuum model combining a nonlinear plate theory for monolayer graphene and an analytical model for van der Waals interactions. Section 2.3 describes a numerical method to solve the nonlinear problem with snap transitions. Three types of blister

configurations are then considered (Figure 2.1): graphene bubble blisters in Section 2.4, center-island blisters in Section 2.5, and center-hole blisters in Section 2.6. The results are summarized in Section 2.7.

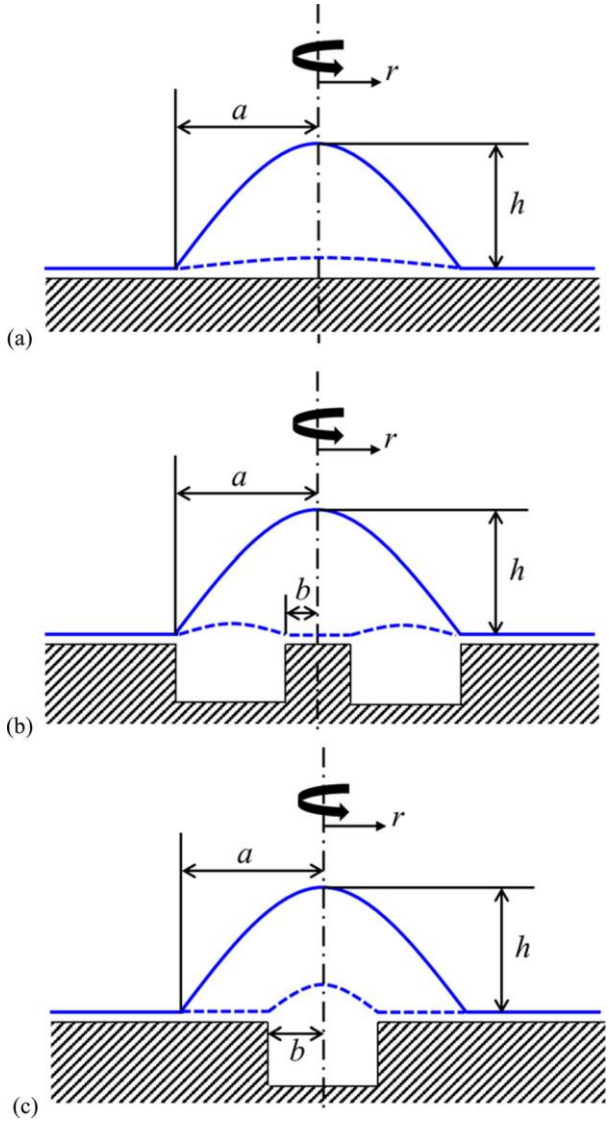

Figure 2.1: Three types of graphene blisters: (a) a circular bubble blister with radius a and height h; (b) a center-island blister; (c) a center-hole blister.

2.2 A CONTINUUM MODEL FOR GRAPHENE BLISTERS

In this chapter we consider three types of axisymmetric graphene blisters as illustrated in Figure 2.1. The circular bubble blister has a radius a and height h (Figure 2.1a). As the pressure inside the bubble changes, the height changes and may snap back to a nearly flat state due to the adhesive interaction with the substrate. The radius is assumed to be fixed and the graphene outside the blister ($r > a$) is assumed to bond perfectly with the substrate. For the center-island blister (Figure 2.1b), the substrate underneath the blister has been removed in the annular region ($b < r < a$), leaving behind a circular island at the center. As a result, the adhesive interaction is limited to the center region of the membrane ($r < b$). In this case, the snap transitions could occur between a dome-shaped blister and a donut-shaped with a flat center region. Finally, for the center-hole blister (Figure 2.1c), the substrate has been removed in the center region ($r < b$) so that the adhesive interaction is limited to the annular region ($a > r > b$). This is the standard blister test configuration, which can have either stable or unstable growth of the blister radius by delamination. In all cases, we model the graphene as a continuum membrane and employ an analytical formula for the adhesive interaction, whereas the substrate is assumed to be rigid.

2.2.1 General formulation

The mechanical behavior of a graphene monolayer can be described by a mixed continuum mechanics formulation mapping a two-dimensional (2D) plane to a surface in the three-dimensional (3D) space [44, 46]. The general kinematics of deformation is described by an in-plane Green-Lagrange strain tensor and a curvature tensor, both defined with respect to a reference state in 2D (i.e., the ground state of graphene). Under the assumption of relatively small deformation but with moderately large deflection, the in-plane strain and curvature are approximately

$$\varepsilon_{ij} = \frac{1}{2}\left(\frac{\partial u_i}{\partial x_j} + \frac{\partial u_j}{\partial x_i} + \frac{\partial w}{\partial x_i}\frac{\partial w}{\partial x_j} \right) \tag{2.1}$$

and

$$\kappa_{ij} = \frac{\partial^2 w}{\partial x_i \partial x_j}, \tag{2.2}$$

where the Latin subscripts (*i* or *j*) take values 1 or 2 for the in-plane coordinates, u_1 and u_2 are the in-plane displacements, and *w* is the lateral deflection.

The elastic property of graphene is nonlinear and anisotropic in general [30, 34]. Under the condition of small deformation, it is taken approximately as linear and transversely isotropic. In this case, a strain energy density function can be written as

$$\Phi = \Phi_\varepsilon(\boldsymbol{\varepsilon}) + \Phi_\kappa(\boldsymbol{\kappa}), \tag{2.3}$$

where $\Phi_\varepsilon(\boldsymbol{\varepsilon})$ is the strain energy due to in-plane strain and $\Phi_\kappa(\boldsymbol{\kappa})$ is due to curvature; both are measured per unit area of the graphene monolayer at the ground state, with the unit J/m^2 as opposed to J/m^3 for a 3D solid.

The linear elastic strain energy density function due to the in-plane strain is

$$\Phi_\varepsilon = \frac{E_{2D}}{2(1+\nu)}\left(\varepsilon_{ij}\varepsilon_{ij} + \frac{\nu}{1-\nu}\varepsilon_{ii}\varepsilon_{jj} \right) = \frac{1}{2} N_{ij}\varepsilon_{ij}, \tag{2.4}$$

where N_{ij} is the in-plane membrane force (or 2D stress):

$$N_{ij} = \frac{\partial \Phi_\varepsilon}{\partial \varepsilon_{ij}} = \frac{E_{2D}}{1+\nu}\left(\varepsilon_{ij} + \frac{\nu}{1-\nu}\varepsilon_{kk}\delta_{ij} \right). \tag{2.5}$$

Here we have used the 2D Young's modulus E_{2D} and Poisson's ratio ν defined under the condition of uniaxial stress [34, 104]. The summation convention is implied for the repeated subscripts, and δ_{ij} is the Kronecker delta.

The strain energy density due to curvature can be written as a function of the two invariants of the curvature tensor [105]

$$\Phi_\kappa = \frac{1}{2} D I_\kappa^2 - D_G II_\kappa = \frac{D - D_G}{2}\kappa_{ii}\kappa_{jj} + \frac{D_G}{2}\kappa_{ij}\kappa_{ij}, \tag{2.6}$$

where the invariants $I_\kappa = \kappa_{ii}$ and $II_\kappa = \left(\kappa_{ii}\kappa_{jj} - \kappa_{ij}\kappa_{ij}\right)/2$, D and D_G are the two bending moduli corresponding to the mean curvature ($\kappa_m = \kappa_{ii}/2$) and the Gaussian curvature ($\kappa_G = II_\kappa$), respectively. The bending and twisting moments are then obtained as the work conjugates with respect to the curvature components

$$M_{ij} = \frac{\partial \Phi_\kappa}{\partial \kappa_{ij}} = \left(D - D_G\right)\kappa_{kk}\delta_{ij} + D_G\kappa_{ij}. \tag{2.7}$$

Unlike classical plate theory [106], the bending moduli of monolayer graphene are not directly related to the in-plane Young's modulus and Poisson's ratio. Instead, they are determined from atomistic modeling as independent properties [33, 35, 44, 45, 48]. As discussed in a previous study [48], the physical origin of the bending moduli of the monolayer graphene is fundamentally different from those in classical plate theory.

With the strain energy density functions, the equilibrium equations and boundary conditions can be developed by the principle of virtual displacements, similar to classical plate theory [106]. The in-plane force equilibrium requires that (assuming no body force)

$$\frac{\partial N_{ij}}{\partial x_j} = 0 \tag{2.8}$$

and moment equilibrium requires that

$$\frac{\partial^2 M_{ij}}{\partial x_i \partial x_j} - N_{ij}\frac{\partial^2 w}{\partial x_i \partial x_j} = q, \tag{2.9}$$

where q is the lateral loading intensity (e.g., pressure). Substitution of Eq. (2.7) into Eq. (2.9) leads to

$$D\nabla^4 w - N_{ij}\frac{\partial^2 w}{\partial x_i \partial x_j} = q. \tag{2.10}$$

Therefore, under the condition of small in-plane strain and moderately large deflection, a set of nonlinear equations can be used to describe the mechanical behavior of monolayer graphene, which closely resemble the von Karman equations for an

isotropic elastic thin plate [106]. The only notable difference lies in the bending moduli of graphene. In particular, we note that it is unnecessary to define a thickness for the graphene monolayer in the 2D continuum formulation. The four basic elastic properties of monolayer graphene have been determined by first-principle calculations and atomistic modeling, as listed in Table 1.1. Note that the ratio between the two bending moduli of graphene is $D_G/D = 0.435$ [35], not $(1 - \nu)$ as in classical plate theory. Here we use the material properties obtained from first-principle density functional theory (DFT) calculations [33]: $E_{2D} = 345$ N/m, $\nu = 0.149$ and $D = 1.5$ eV.

2.2.2 Axisymmetric formulation

Consider a circular graphene membrane subjected to axisymmetric loading. The displacements expressed in polar coordinates are: $u_r = u(r)$, $u_\theta = 0$, and $w = w(r)$. The corresponding in-plane strain components are

$$\varepsilon_r = \frac{du}{dr} + \frac{1}{2}\left(\frac{dw}{dr}\right)^2, \tag{2.11}$$

$$\varepsilon_\theta = \frac{u}{r}, \tag{2.12}$$

and $\varepsilon_{r\theta} = 0$. The curvature components are

$$\kappa_r = \frac{d^2 w}{dr^2}, \tag{2.13}$$

$$\kappa_\theta = \frac{1}{r}\frac{dw}{dr}, \tag{2.14}$$

and $\kappa_{r\theta} = 0$.

From Eq. (2.5), the radial and circumferential membrane forces are

$$N_r = \frac{E_{2D}}{1-\nu^2}\left(\frac{du}{dr} + \nu\frac{u}{r} + \frac{1}{2}\left(\frac{dw}{dr}\right)^2\right) \tag{2.15}$$

and

$$N_\theta = \frac{E_{2D}}{1-\nu^2}\left(\nu\frac{du}{dr}+\frac{u}{r}+\frac{\nu}{2}\left(\frac{dw}{dr}\right)^2\right). \tag{2.16}$$

The in-plane force equilibrium equation in (2.8) reduces to

$$\frac{dN_r}{dr}+\frac{N_r-N_\theta}{r}=0. \tag{2.17}$$

Substitution of Eq. (2.15) and Eq. (2.16) into Eq. (2.17) leads to a nonlinear displacement equation

$$\frac{d^2u}{dr^2}+\frac{1}{r}\frac{du}{dr}-\frac{u}{r^2}=-\frac{1-\nu}{2r}\left(\frac{dw}{dr}\right)^2-\frac{dw}{dr}\frac{d^2w}{dr^2}. \tag{2.18}$$

From Eq. (2.7), the bending moments are

$$M_r = D\frac{d^2w}{dr^2}+\left(D-D_G\right)\frac{1}{r}\frac{dw}{dr} \tag{2.19}$$

and

$$M_\theta = \left(D-D_G\right)\frac{d^2w}{dr^2}+\frac{D}{r}\frac{dw}{dr}. \tag{2.20}$$

The moment equilibrium equation in (2.10) is integrated once with respect to *r*, yielding another nonlinear displacement equation

$$D\left(\frac{d^3w}{dr^3}+\frac{1}{r}\frac{d^2w}{dr^2}-\frac{1}{r^2}\frac{dw}{dr}\right)-\frac{E_{2D}}{1-\nu^2}\frac{dw}{dr}\left(\frac{du}{dr}+\nu\frac{u}{r}+\frac{1}{2}\left(\frac{dw}{dr}\right)^2\right)=\frac{1}{r}\int_0^r qr\,dr. \tag{2.21}$$

Therefore, the axisymmetric problem is to solve the two nonlinear equations in (2.18) and (2.21) with prescribed boundary conditions at the edge ($r = a$).

Previous studies have noted that the graphene membrane is often subject to a pre-tension [27, 28, 65], and the blister behavior depends sensitively on the pre-tension. The effect of pre-tension (T_0) can be taken into account by including an additional term, $-T_0\frac{dw}{dr}$, on the left hand side of Eq. (2.21). In the present study, we assume zero pre-tension ($T_0 = 0$).

In the present study, the lateral load intensity q consists of a constant pressure p (or pressure difference if the outer pressure is considered) and the van der Waals (vdW) force between graphene and the substrate, i.e., $q = p - \sigma_{vdW}$, where $\sigma_{vdW} > 0$ for attractive force. The formula for van der Waals force is obtained by replacing the separation distance z with $\mathrm{w} + \mathrm{h}_0$ in Eq. (1.2). The value adhesion energy Γ_0 between graphene and substrate is varied between 0.05 and 1.0 J/m^2, as the typical range for the adhesion energy from both experiments and theoretical calculations [27, 64, 65, 68, 73, 75, 80, 82, 86, 107]. For the equilibrium separation h_0, direct measurements are difficult and typical values from 0.3 to 1.0 nm were estimated from indirect measurements and DFT calculations [75, 82, 108, 109]. In this chapter, we take $\mathrm{h}_0 = 0.6$ nm and $\Gamma_0 = 0.1$ J/m^2 unless specified otherwise.

2.3 Analytical Methods

Similar to previous studies [47, 103], several approximate solutions for graphene blisters were developed here for comparison with the numerical results.

2.3.1 A linear solution for graphene bubble blisters

For very small deflection, we linearize the van der Waals force in Eq. (1.2) as

$$\sigma_{vdW} \approx k_s w, \tag{2.22}$$

where $k_s = 27\Gamma_0 / h_0^2$ is the initial stiffness. Moreover, the equilibrium equations are linearized to recover the linear plate equation for the deflection,

$$\frac{D}{r}\frac{d}{dr}\left(r\frac{d^3 w}{dr^3} + \frac{d^2 w}{dr^2} - \frac{1}{r}\frac{dw}{dr} \right) = p - k_s w, \tag{2.23}$$

which is identical to the problem of a linear plate resting on an elastic foundation. Solving (2.23), the deflection profile is obtained as

$$w(r) = \frac{p}{k_s} N_1(r), \tag{2.24}$$

where the shape function is

$$N_1(r) = 1 - \frac{\xi_2 J_1(\xi_2 a) J_0(\xi_1 r) - \xi_1 J_1(\xi_1 a) J_0(\xi_2 r)}{\xi_2 J_1(\xi_2 a) J_0(\xi_1 a) - \xi_1 J_1(\xi_1 a) J_0(\xi_2 a)}, \tag{2.25}$$

with $\xi_1 = \frac{\sqrt{2}(1+i)}{2}\left(\frac{k_s}{D}\right)^{1/4}$ and $\xi_2 = \frac{\sqrt{2}(1-i)}{2}\left(\frac{k_s}{D}\right)^{1/4}$. A length scale for the shape function emerges: $L_1 = (D/k_s)^{1/4}$, which is about 0.4 nm for monolayer graphene. As shown in Figure 2.2, this shape function is a constant except in the annular region near the edge of the blister. In this case, the shape of the blister is pancake-like and the central height depends on the pressure linearly as: $h = p/k_s$. Hence, the initial slope of the pressure-height curve (Figure 2.3) is directly related to the stiffness of van der Waals interactions.

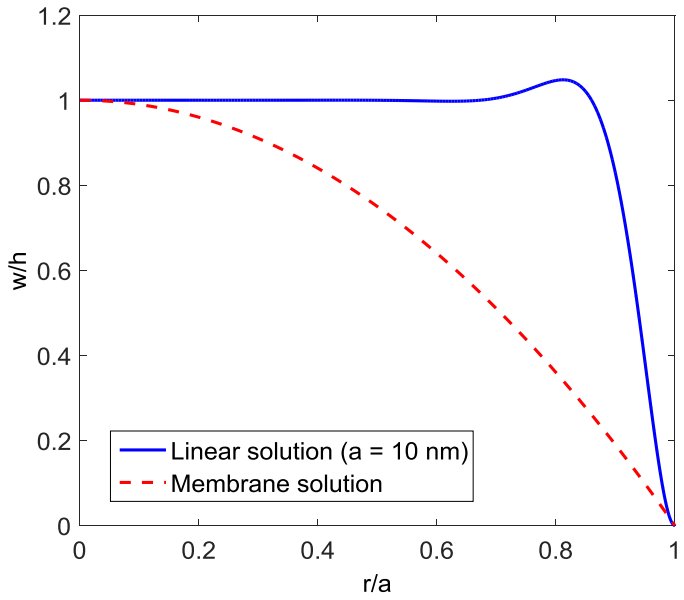

Figure 2.2: Shape functions for graphene bubble blisters.

2.3.2 A membrane solution for graphene bubble blisters

By neglecting the van der Waals forces ($\sigma_{vdW} \approx 0$), an approximate membrane solution was obtained in a previous study [103], with a deflection profile

$$w(r) = hN_2(r), \tag{2.26}$$

where the shape function is

$$N_2(r) = 1 - \frac{r^2}{a^2}, \tag{2.27}$$

and the central deflection is related to the pressure as

$$h = \left[\phi(\nu) pa^4 / E_{2D}\right]^{1/3}, \tag{2.28}$$

with $\phi(\nu) = \frac{75(1-\nu^2)}{8(23+18\nu-3\nu^2)}$. In addition, Komaragiri *et al*. [110] obtained the same approximate solution with the coefficient $\varphi(\nu) = \left(0.7179 - 0.1706\nu - 0.1495\nu^2\right)^3$ through numerical fitting. An accurate solution to the nonlinear membrane equations can only be obtained numerically [111]. As shown in Figure 2.2, the shape of the blister in this case is dome-like.

2.3.3 A membrane analysis for center-island graphene blisters

For the center-island blister, we assume a deflection profile (before snap-through)

$$w(r) = \begin{cases} 0, & 0 \le r < b \\ h\left[1 - \left(\dfrac{r - \dfrac{a+b}{2}}{\dfrac{a-b}{2}}\right)^2\right], & b \le r \le a \end{cases}, \tag{2.29}$$

where h is the maximum deflection. In addition, for the deformation to be kinematically admissible, a radial displacement is assumed:

$$u(r) = \begin{cases} 0, & 0 \le r < b \\ u_0 \dfrac{r-b}{a-b}\left[1 - \dfrac{r-b}{a-b}\right], & b \le r \le a \end{cases}, \tag{2.30}$$

where u_0 is a parameter to be determined.

Following the energy minimization method in [103], the total potential energy of the graphene blister is written as a function of the kinematic parameters: $\Pi = \Pi(h, u_0; a, b, p)$. Then, for given a, b, and p, the equilibrium values of h and u_0 are obtained by minimizing the potential energy: $\partial\Pi/\partial h = \partial\Pi/\partial u_0 = 0$. It is found that the height scales with the pressure as $h \sim p^{1/3}$.

For the graphene to delaminate from the center island, the release of the potential energy must exceed the adhesion energy. Therefore, the critical condition is set up as

$$\left(\frac{\partial\Pi}{\partial b}\right)_p = 2\pi b\Gamma_0, \tag{2.31}$$

which predicts a critical pressure as a function of the adhesion energy as $p_c = \varsigma E_{2D}^{1/4}\Gamma_0^{3/4}a^{-1}$ and ς is a dimensionless coefficient depending on the ratio b/a. For a = 1.5 μm and b = 0.25 μm, we obtain $\varsigma = 1.392$.

2.4 NUMERICAL METHOD

In this section we present a numerical method to solve the coupled nonlinear equations, (2.18) and (2.21), using Riks method. For convenience, we define an effective length scale, $h_e = \sqrt{12(1-\nu^2)D/E_{2D}}$, and normalize the equations using the dimensionless quantities: $\bar{r} = \frac{r}{h_e}$, $\bar{a} = \frac{a}{h_e}$, $\bar{u} = \frac{u}{h_e}$, $\bar{w} = \frac{w}{h_e}$, and $\bar{q} = \frac{qh_e^3}{D}$. In addition, we replace the deflection w with the angle of rotation, $\theta = \frac{dw}{dr}$, and re-write the equations as

$$g = \frac{d^2\bar{u}}{d\bar{r}^2} + \frac{1}{\bar{r}}\frac{d\bar{u}}{d\bar{r}} - \frac{\bar{u}}{\bar{r}^2} + \frac{1-\nu}{2\bar{r}}\theta^2 + \theta\frac{d\theta}{d\bar{r}} = 0 \tag{2.32}$$

and

$$f = \frac{d^2\theta}{d\bar{r}^2} + \frac{1}{\bar{r}}\frac{d\theta}{d\bar{r}} - \frac{\theta}{\bar{r}^2} - 12\theta\left(\frac{d\bar{u}}{d\bar{r}} + \nu\frac{\bar{u}}{\bar{r}} + \frac{\theta^2}{2}\right) - \frac{1}{\bar{r}}\int_0^{\bar{r}} \bar{q}\bar{r}\,d\bar{r} = 0. \tag{2.33}$$

Next we discretize the equations by the finite difference method with $\Delta\bar{r} = \frac{\bar{a}}{n}$ and $\bar{r}_k = k\Delta\bar{r}$ for $k = 0$ to n. At each internal node ($k = 1$ to n-1), we have

$$\begin{aligned} g_k = {} & \frac{n^2}{\bar{a}^2}\left(1 + \frac{1}{2k}\right)\bar{u}_{k+1} - \frac{n^2}{\bar{a}^2}\left(2 + \frac{1}{k^2}\right)\bar{u}_k + \frac{n^2}{\bar{a}^2}\left(1 - \frac{1}{2k}\right)\bar{u}_{k-1} \\ & + \frac{(1-\nu)n}{2k\bar{a}}\theta_k^2 + \frac{n}{2\bar{a}}\theta_k\left(\theta_{k+1} - \theta_{k-1}\right) \end{aligned} \tag{2.34}$$

and

$$\begin{aligned} f_k = {} & \frac{n^2}{\bar{a}^2}\left(1 + \frac{1}{2k}\right)\theta_{k+1} - \frac{n^2}{\bar{a}^2}\left(2 + \frac{1}{k^2}\right)\theta_k + \frac{n^2}{\bar{a}^2}\left(1 - \frac{1}{2k}\right)\theta_{k-1} \\ & - \frac{6n}{\bar{a}}\theta_k(\bar{u}_{k+1} - \bar{u}_{k-1}) - \frac{12\nu n}{k\bar{a}}\theta_k\bar{u}_k - 6\theta_k^3 - \xi_k \end{aligned} \tag{2.35}$$

for each internal node ($0 < r < a$) with $k = 1$ to n-1 and $\xi_k = \frac{\bar{a}}{2nk}\left(\sum_{m=1}^{k-1} 2m\bar{q}_m + k\bar{q}_k\right)$. The boundary conditions are specified for the end nodes with $k = 0$ and n: $\theta_0 = \theta_n = 0$ and $\bar{u}_0 = \bar{u}_n = 0$. Moreover, with $\bar{w}_n = 0$ at the edge of the blister ($r = a$), we calculate the deflection at each node by numerically integrating the angle of rotation:

$$\bar{w}_k = -\frac{\bar{a}}{2n}\sum_{m=k}^{n-1}\left(\theta_m + \theta_{m+1}\right), \tag{2.36}$$

for $k = 0$ to n-1, and the center deflection is then obtained as $h = w_0$.

The effect of the van der Waals force is included in the last term of Eq. (2.35), with

$$\bar{q}_k = \bar{p} - \bar{\sigma}_{vdW}\left(\bar{w}_k\right), \tag{2.37}$$

and

$$\bar{\sigma}_{vdW}\left(\bar{w}\right) = \bar{\Gamma}_0\left[\left(\frac{\bar{h}_0}{\bar{w} + \bar{h}_0}\right)^4 - \left(\frac{\bar{h}_0}{\bar{w} + \bar{h}_0}\right)^{10}\right], \tag{2.38}$$

where $\bar{p} = ph_e^3 / D$, $\bar{\sigma}_{vdW} = \sigma_{vdW} h_e^3 / D$, $\bar{h}_0 = h_0 / h_e$, and $\bar{\Gamma}_0 = 9\Gamma_0 h_e^3 / (2h_0 D)$. For the center-island and center-hole blisters, the van der Waals forces are included only in the regions interacting with the substrate underneath.

The Riks method is used to study the snap transitions of graphene blisters. The pressure p and the central deflection h are treated as two additional unknowns. The relationship between the central deflection and the angle of rotation requires that

$$\varphi_h(\boldsymbol{\theta}, \bar{h}) = \frac{\bar{a}}{n} \sum_{k=1}^{n-1} \theta_k + \bar{h} = 0. \tag{2.39}$$

To control the incremental arc length along the pressure-deflection curve, the pressure p can be related to the central deflection as:

$$\varphi_p(\bar{p}, \bar{h}) = (\bar{p} - \bar{p}_{i-1})^2 + (\bar{h} - \bar{h}_{i-1})^2 - \Delta^2 = 0, \tag{2.40}$$

where Δ is specified as the dimensionless increment, $\bar{p}_{i-1}$ and $\bar{h}_{i-1}$ are the normalized pressure and central deflection in the previous step. For computational efficiency, a regulated arc-length relation is used (except for the very first step):

$$\varphi'_p(\bar{p}, \bar{h}) = \left(\frac{\bar{p} - \bar{p}_{i-1}}{\bar{p}_{i-1}} \right)^2 + \left(\frac{\bar{h} - \bar{h}_{i-1}}{\bar{h}_{i-1}} \right)^2 - \Delta^2 = 0. \tag{2.41}$$

The Newton-Raphson method is employed to solve the system of nonlinear equations, including the discretized equilibrium equations and the two constraints in Eqs. (2.39) and (2.41). At each step, we start with a set of values as $\theta_k^{(0)}$, $\bar{u}_k^{(0)}$, $\bar{p}^{(0)}$ and $\bar{h}^{(0)}$, calculate the residual and corrections, and then iterate until a convergence condition is satisfied. At each iteration, a correction vector is calculated as

$$\begin{pmatrix} \Delta\boldsymbol{\theta} \\ \Delta\bar{\mathbf{u}} \\ \Delta\bar{p} \\ \Delta\bar{h} \end{pmatrix} = -\begin{bmatrix} \dfrac{\partial \mathbf{f}}{\partial \boldsymbol{\theta}} & \dfrac{\partial \mathbf{f}}{\partial \bar{\mathbf{u}}} & \dfrac{\partial \mathbf{f}}{\partial \bar{p}} & \mathbf{0} \\ \dfrac{\partial \mathbf{g}}{\partial \boldsymbol{\theta}} & \dfrac{\partial \mathbf{g}}{\partial \bar{\mathbf{u}}} & \mathbf{0} & \mathbf{0} \\ \dfrac{\partial \varphi_h}{\partial \boldsymbol{\theta}} & \mathbf{0} & 0 & \dfrac{\partial \varphi_h}{\partial \bar{h}} \\ 0 & 0 & \dfrac{\partial \varphi_p}{\partial \bar{p}} & \dfrac{\partial \varphi_p}{\partial \bar{h}} \end{bmatrix}^{-1} \begin{pmatrix} \mathbf{f} \\ \mathbf{g} \\ \varphi_h \\ \varphi_p \end{pmatrix}, \tag{2.42}$$

where $\Delta\boldsymbol{\theta}$ is a vector of n-1 components ($\Delta\theta_k$, k = 1 to n-1) and the same for $\Delta\bar{\mathbf{u}}$, $\mathbf{f}$, and $\mathbf{g}$. For the convergence criterion, we require that the L2-norm of the relative correction vector is smaller than a specified tolerance, namely

$$|\mathbf{R}| = \left[\sum_{k=1}^{n-1}\left(\Delta\theta_k^2/\theta_k^2 + \Delta u_k^2/u_k^2\right)\right]^{1/2} < \tau \sim 10^{-4}. \tag{2.43}$$

If not satisfied, the iteration procedure repeats with a new approximation, $\theta_k^{(i+1)} = \theta_k^{(i)} + \Delta\theta_k$, $\bar{u}_k^{(i+1)} = \bar{u}_k^{(i)} + \Delta\bar{u}_k$, $\bar{p}^{(i+1)} = \bar{p}^{(i)} + \Delta\bar{p}$ and $\bar{h}^{(i+1)} = \bar{h}^{(i)} + \Delta\bar{h}$.

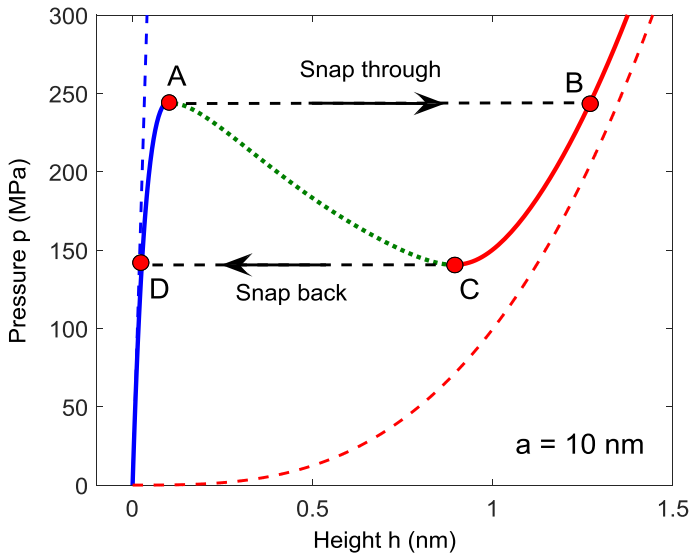

Figure 2.3: Pressure versus height for a nanoscale graphene bubble blister (a = 10 nm), showing the snap transitions from A to B and from C to D. The dotted line is the unstable branch from A to C. The linear solution and the approximate membrane solution are shown as dashed lines for comparison.

2.5 GRAPHENE BUBBLE BLISTERS

2.5.1 Nano-bubble blisters

Consider a nano-bubble graphene blister with radius a = 10 nm (Figure 2.1a). Using the numerical method (Section 2.4) with n = 300, we calculate the blister deflection and central height versus the pressure, as shown in Figure 2.3. Start with zero pressure and zero height. Subjected to increasing pressure, the central height increases until the pressure reaches a local maximum at point A (branch I). The slope of the pressure-height curve decreases and becomes zero at A, indicative of an impending instability under pressure control. Further increasing the pressure, a snap-through occurs from point A to point B along the horizontal dashed line, after which the height increases continuously along the red line (branch II). On the other hand, if the bubble blister starts with a height greater than point B on branch II and the pressure decreases, the unloading curve reaches a local minimum at point C, where the slope is again zero. Further decreasing the pressure would lead to a snap-back form point C to point D, returning to branch I. Hence, a snap-through/snap-back transition is predicted for the graphene bubble blister under the pressure-controlled loading and unloading. Between the two critical points (A and C), an unstable branch is obtained by the Riks method, where the height increases with decreasing pressure. Figure 2.4 shows the snap-through/snap-back transitions of the deflection profile and corresponding van der Waals force distributions. We note that the deflection profiles take different shapes for the two stable branches: pancake-like at points A and D (branch I) and dome-like at points B and C (branch II). Correspondingly, the distributions of the van der Waals forces are different, nearly

uniform for the pancake-like blister and concentrated near the edge for the dome-like blister.

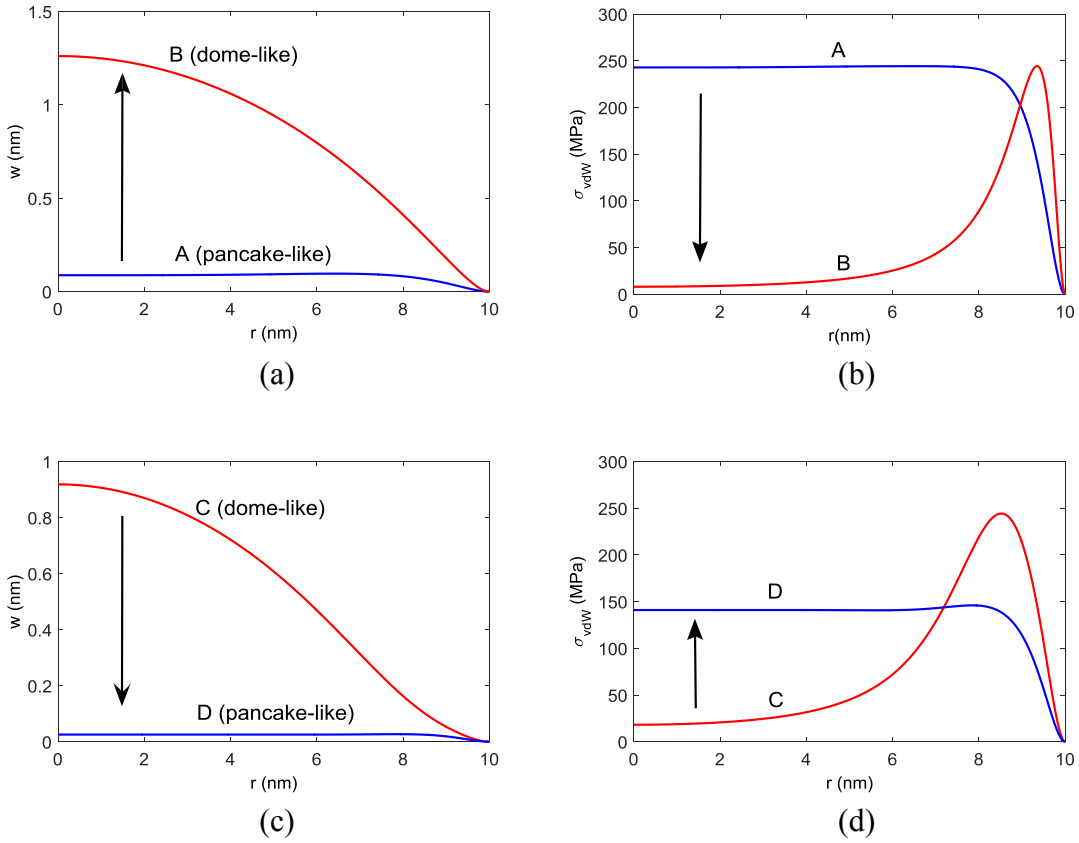

Figure 2.4: Snap transitions of a nanoscale graphene bubble blister (a = 10 nm): (a) Snap-through of the deflection profile from A to B at $p = 243$ MPa; (b) Distributions of the van der Waals force at A and B; (c) Snap-back of the deflection profile from C to D at $p = 142$ MPa; (d) Distributions of the van der Waals force at C and D. The points A-D refer to those marked in Figure 2.3.

The two blister shapes can be analyzed approximately by a linearized model and a membrane model, as presented in Section 2.3. The linearized model treats the van der Waals force as a linear spring so that the height increases linearly with the pressure, with a slope depending solely on the initial stiffness of the van der Waals interactions (

$k_s = 27\Gamma_0 / h_0^2$). As shown in Figure 2.3, the linear solution agrees with the numerical solution when the height is small (branch I). On the other hand, the approximate membrane solution ignores the van der Waals forces and compares closely with the numerical solution when the height is relatively large (branch II).

Bound by the two approximate solutions, the snap transitions in between can be understood from an energy consideration. By combining the two shape functions from the linear solution and the membrane solution, an approximate deflection profile may be written as

$$w(r) = h_1 N_1(r) + h_2 N_2(r), \tag{2.44}$$

where h_1 and h_2 are to be determined. Correspondingly, the radial displacement is

$$u(r) = \frac{2(3-\nu)h_2^2}{5a} \frac{r}{a}\left(1-\frac{r}{a}\right), \tag{2.45}$$

which is part of the membrane solution [103].

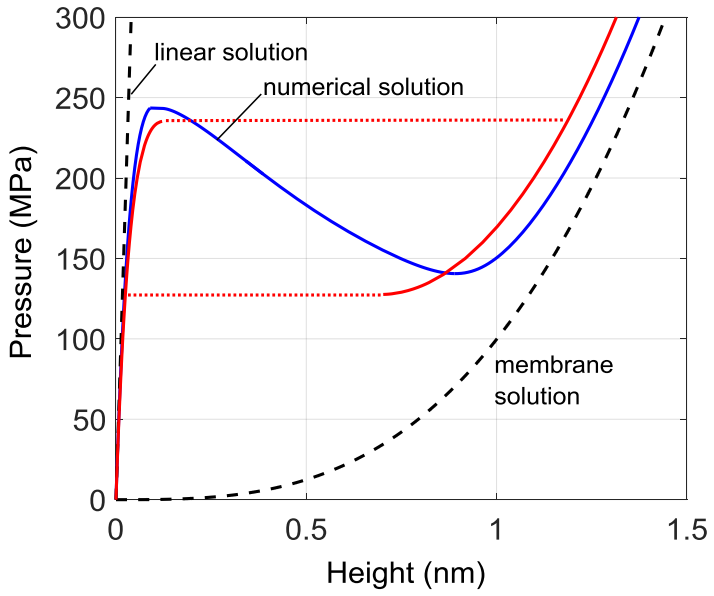

Figure 2.5: Comparison of the approximate two-state solution by energy minimization with the numerical solution for the pressure-height curve of a graphene bubble blister (a = 10 nm).

The total free energy of the blister includes the elastic strain energy of graphene, the van der Waals interaction energy, and the potential energy associated with the pressure, namely

$$\Phi(h_1, h_2; p, a) = 2\pi \int_0^a [U_b(r) + U_s(r) + U_{vdw}(r)] r dr - 2\pi p \int_0^a w(r) r dr, \qquad (2.46)$$

where the van der Waals interaction energy is given in Eq. (1.1) with $z = w + h_0$ and the elastic energy due to stretching and bending of graphene are, respectively

$$U_b(r) = \frac{D}{2}\left(\left(\frac{d^2 w}{dr^2} \right)^2 + \frac{1}{r^2}\left(\frac{dw}{dr} \right)^2 + \frac{2}{r}\frac{D - D_G}{D}\frac{dw}{dr}\frac{d^2 w}{dr^2} \right), \qquad (2.47)$$

$$U_s(r) = \frac{E_{2D}}{2(1-\nu^2)}\left(\varepsilon_r^2 + 2\nu \varepsilon_r \varepsilon_\theta + \varepsilon_\theta^2 \right). \qquad (2.48)$$

Note that the bending energy in (2.47) includes a term related to Gaussian curvature with a Gaussian curvature modulus D_G. However, it can be shown that the Gaussian curvature term drops out after integration over the area with the clamped boundary condition and hence has no influence on the result. In Eq. (2.48), the strain components are related to the displacements as usual: $\varepsilon_r = \frac{du}{dr} + \frac{1}{2}\left(\frac{dw}{dr} \right)^2$ and $\varepsilon_\theta = \frac{u}{r}$.

For a given radius a and pressure p, we minimize the free energy in (2.46) to determine the coefficients h_1 and h_2. The central height of the blister is then simply $h = h_1 + h_2$. For a = 10 nm, as shown in Figure 2.5, the result from energy minimization is in reasonable agreement with the numerical solution. Under a small pressure (e.g., p = 100 MPa), the free energy has only one minimum corresponding to a state of small deflection with a pancake-like shape. As the pressure increases (e.g., p = 200 MPa), two local minima appear in the energy landscape along with a saddle point in between. The two minima correspond to the two stable branches in the pressure-height curve, while the saddle point corresponds to the unstable branch. When p increases further (e.g., p = 300

MPa), the first local minimum disappears and the remaining minimum corresponds to the branch with a dome-like deflection profile. Thus, the snap transitions of the bubble blister can be understood as a result of energy minimization. In particular, the competition between the vdW interaction energy and the elastic energy of graphene leads to the two states with different blister shapes.

The two critical pressures for the snap transitions can be determined numerically from the pressure-height curve as shown in Figure 2.3, where the slope becomes zero ($dp/dh = 0$). Between the two critical pressures, the bubble blister is bistable, with two local minima for the free energy function. The state with the lower free energy is thermodynamically stable against any perturbation (not limited to small perturbations), while the other state is metastable. At a transition pressure ($p = p_t$), the two states have equal free energy. When $p < p_t$, the state on branch I (pancake-like blister) is thermodynamically stable; when $p > p_t$, the state on branch II (dome-like blister) is thermodynamically stable. Therefore, the snap transition of the graphene bubble blister is analogous to the first-order phase transition with a discontinuity in the central height (and volume). Similar snap transitions have been studied in other systems [112, 113].

2.5.2 Micro-bubble blisters

Next we consider microscale graphene bubble blisters, which are more commonly observed in experiments [94, 95]. With the radius $a > 1$ μm, the graphene membrane becomes highly flexible with increased nonlinearity due to relatively large deflections. Nevertheless, the problem can be solved by the same numerical method (Section 2.4) with a sufficiently large number of nodes (n). For $a = 1.5$ μm, we found that using $n = 3000$ is sufficient to avoid numerical oscillations and the numerical results do not change noticeably with more nodes. Figure 2.6a shows the central height versus pressure,

exhibiting similar snap transitions as the nano-bubble blister in Figure 2.3. The snap transitions are shown more clearly for the micro-bubble blister in a log-log plot (Figure 2.6b), where the slope is close to 1 for branch I (blue) and about 3 for branch II (red), corresponding to the linear and membrane solutions, respectively. Moreover, we plot the volume of the blister versus pressure in Figure 2.6c. Interestingly, for the unstable branch (green), as the pressure decreases, the volume underneath the blister first decreases and then increases. Such a non-monotonic behavior suggests that the blister would undergo snap transitions even if the loading/unloading is under strict volume-control.

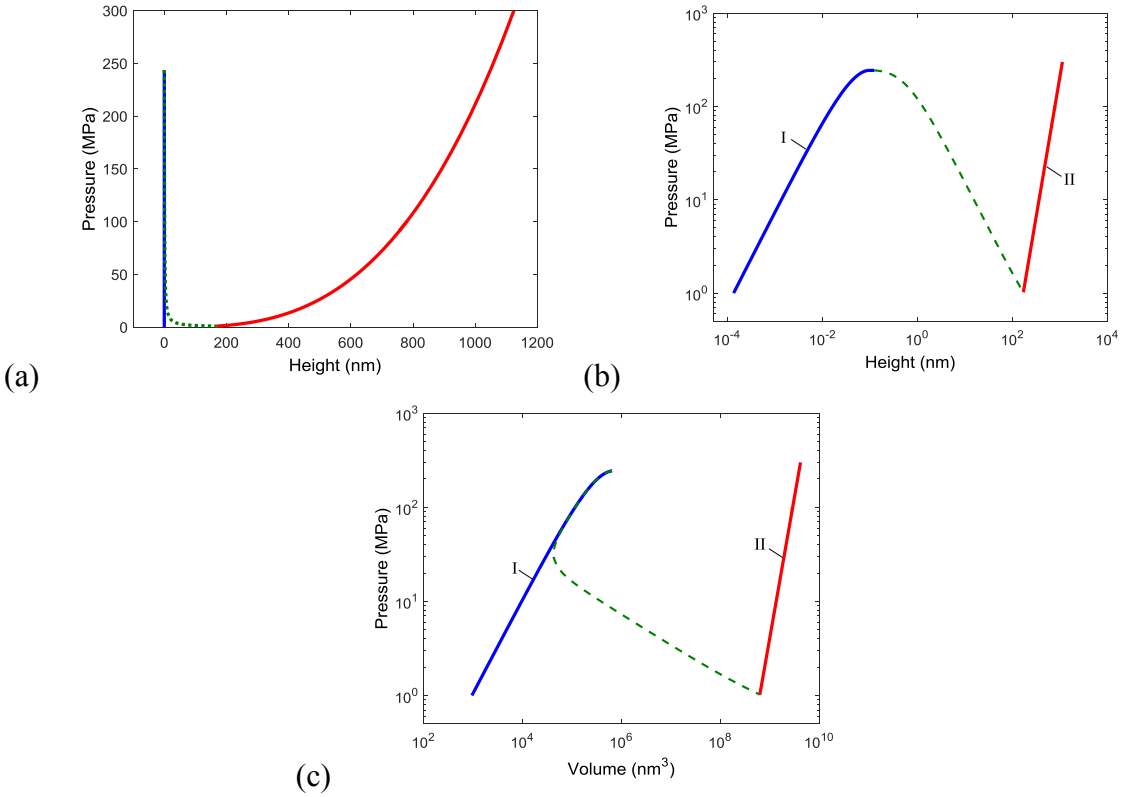

Figure 2.6: (a) Pressure versus height for a microscale graphene bubble blister (a = 1.5 μm). (b) Pressure-height in a log-log plot. (c) Pressure versus volume for the micro-bubble blister.

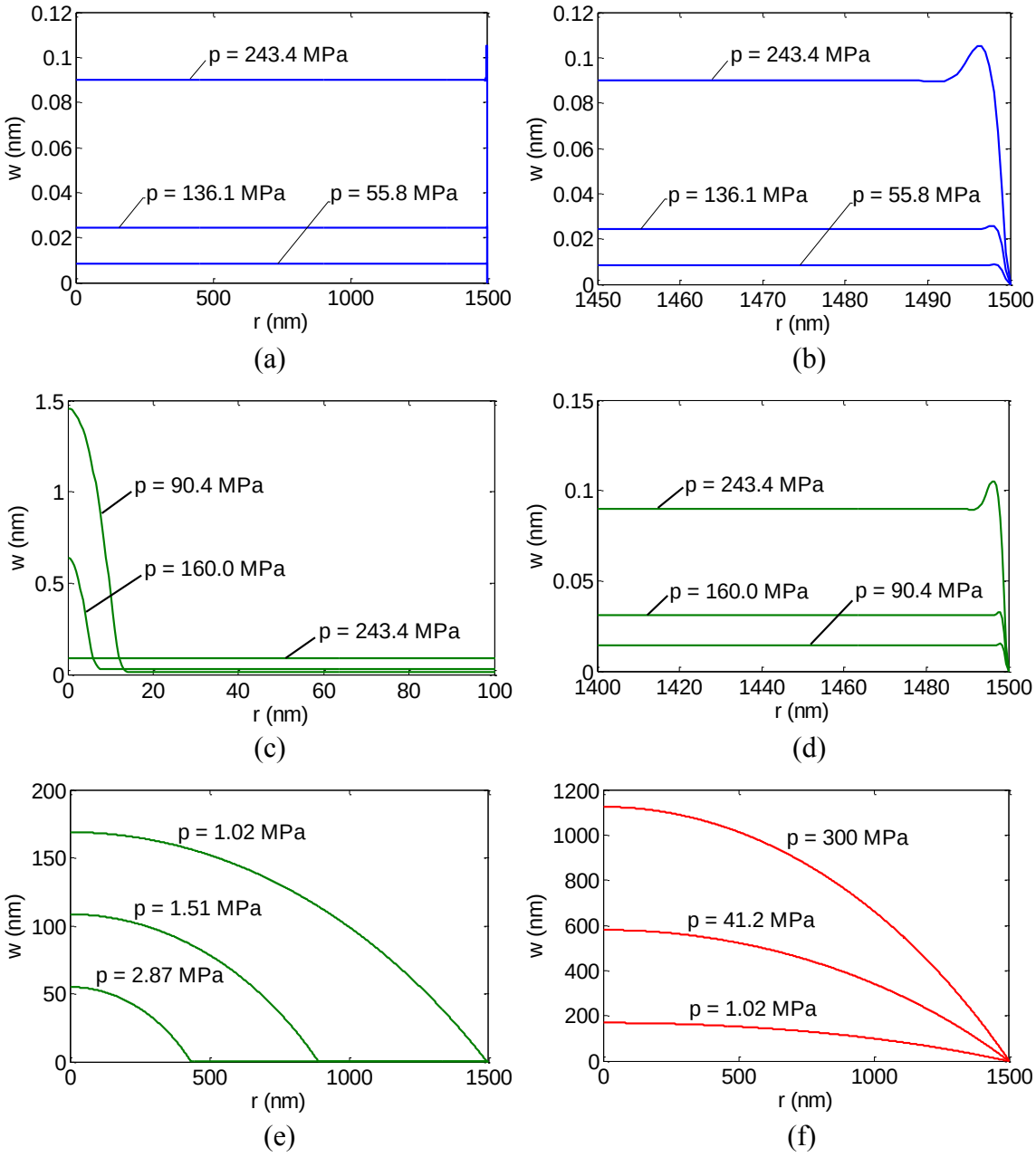

Figure 2.7: Evolution of deflection profile for a microscale graphene bubble blister (a = 1.5 μm): (a-b) for increasing pressure along branch I (stable), with (b) showing the deflection near the edge; (c-e) for decreasing pressure along the unstable branch, with (c) showing the deflection near the center and (d) showing the deflection near the edge; (f) for increasing pressure along branch II (stable).

Figure 2.7 shows the deflection profiles of the micro-bubble blister. In the first stable branch (blue) of Figure 2.6, the deflection is very small and almost uniform except near the edge (Figure 2.7, a&b). In this case, the pressure is largely balanced by the van der Waals forces. As the pressure increases, the deflection increases almost linearly. When the magnitude of the pressure becomes close to the strength of the van der Waals interactions ($\sigma_{vdW}^{\max} = 1.466\Gamma_0 / h_0$), the pancake-like blister becomes unstable with impending snap-through transition to a dome-like blister. Corresponding to the second stable branch (red) in Figure 2.6, the height of the dome-like blister decreases with decreasing pressure (Figure 2.7f) until it becomes unstable and snaps back due to the presence of the attractive van der Waals forces. Along the unstable branch (green) in Figure 2.6, the center part of graphene membrane starts to bulge up at the point of snap-through transition, forming a dome-like shape while the rest part remains flat (Figure 2.7, c&d). Such a deflection profile may be considered as a mixture of two states, dome-like center surrounded by a pancake-like annulus. The bulge expands in the radial direction with increasing central height and decreasing pressure (Figure 2.7e), similar to growth of a bubble blister with interfacial delamination. The unstable branch terminates at the point of snap-back transition, when the bulge radius reaches the prescribed bubble radius. In this section, we assume the bubble radius to be fixed. The growth of the bubble radius is considered in Section 2.7.

Notably, while the critical pressures for snap-through (from pancake-like to dome-like) are similar for both nano- and micro-bubble blisters, the critical pressure for snap-back (from dome-like to pancake-like) is much lower for the micro-bubble blister. It is found that the snap-through pressure approximately equals the strength of the van der Waals interactions, i.e., $p_{st} \sim \sigma_{vdW}^{\max} = 1.466\Gamma_0 / h_0$, at a height close to $0.165h_0$ (~0.1 nm), both insensitive to the blister radius (Figure 2.8). On the other hand, the snap-back

pressure depends sensitively on the blister radius, decreasing with increasing blister radius, as shown in Figure 2.8a. Meanwhile, the snap-back height increases almost linearly with increasing blister radius (Figure 2.8b). The linear dependence may be expected from the approximate membrane solution [103], which predicts $h \propto a$ for a given adhesion energy. Further, by the membrane solution in Eq. (2.28), $p \propto a^{-4}h^3$, and thus the critical pressure for snap-back is inversely proportional to the radius (i.e., $p_{sb} \propto a^{-1}$). Moreover, by an energy consideration, the snap-back pressure depends on the adhesion energy as $p_{sb} \propto \Gamma_0^{3/4}$ and correspondingly the snap-back height, $h_{sb} \propto \Gamma_0^{1/4}$. It should be noted that the approximate membrane solution becomes less accurate for nano-bubble blisters [47]. With the two critical pressures for the snap transitions and the corresponding heights, two phase diagrams are constructed in Figure 2.8 for the graphene bubble blisters. On the pressure-radius panel (Figure 2.8a), a bistable region is identified between the two critical pressures. On the height-radius panel (Figure 2.8b), an unstable region is identified between the two critical heights.

Dome-like graphene bubbles are commonly observed in experiments [94, 95], whereas the pancake-like bubbles are difficult to observe because of very small height (h < 1 nm). For dome-like micro-bubbles (a > 1 μm), the approximate membrane solution may be used to deduce the adhesion energy of graphene from measurements of the bubble radius and height [103]: $\Gamma_0 = \dfrac{5E_{2D}h^4}{8\varphi(\nu)a^4}$. To determine the other parameter of van der Waals interactions (i.e., h_0), additional measurements are required. For a fixed graphene bubble radius, measurement of the critical pressure for the snap-through transition would be sufficient to deduce the second parameter as $p_{st} \sim \sigma_{vdW}^{\max} = 1.466\Gamma_0/h_0$. However, it remains a challenge to design such an experiment. Instead, the center-island blister test is more suitable for this purpose, as discussed in Section 2.6.

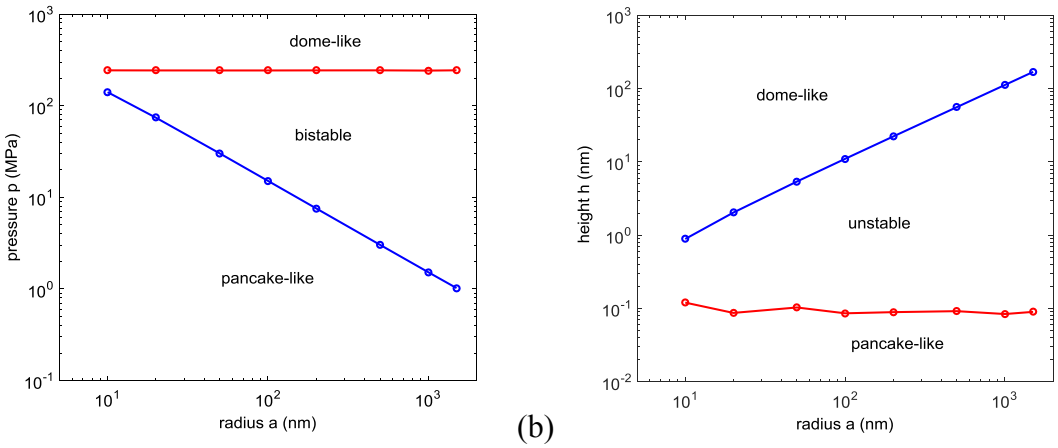

(a) (b)

Figure 2.8: Phase diagrams for graphene bubble blisters. (a) Pressure versus radius; (b) Height versus radius.

2.6 CENTER-ISLAND GRAPHENE BLISTERS

Island blister tests have been used to measure the adhesion properties of thin films or membrane materials to their substrates [90, 92]. As illustrated in Figure 2.1b, we consider a circular hole of radius a = 1.5 μm with a circular island of radius b = 0.25 μm at the center. This configuration is similar to those used in experiments for graphene [28, 29]. Here, the van der Waals forces are considered only for the center part of the graphene with $0 < r < b$. Figure 2.9 shows the numerical results in terms of the center height versus pressure and the blister volume versus pressure. The blister volume is calculated by integrating the deflection profile, without including the volume of the hole. Similar to the graphene bubble blisters, three branches are obtained, two stable branches and an unstable branch in between. Hence, snap transitions between the two stable branches are predicted during both pressurization and de-pressurization. The deflection profiles are presented in Figure 2.10. For a relative low pressure, the center deflection is nearly zero due to the presence of van der Waals forces between graphene and the island,

whereas the graphene around the island deflects, forming a donut-like shape (Figure 2.10a). The central height increases linearly with increasing pressure until it reaches the point of snap-through transition. Along the unstable branch, the deflection profiles in Figure 2.10b & c show an unstable delamination and popping process: starting from the edge of the island, the graphene delaminates progressively from the substrate and pops up as the pressure continues decreasing. The center deflection remains nearly zero before the graphene is fully delaminated from the island, thus making this part of the unstable branch indistinguishable from the first stable branch (blue) in Figure 2.9a. However, the volume underneath the blister is distinguishable, as shown in Figure 2.9b. The unstable branch terminates at the point of snap-back transition, beyond which the central height increases with increasing pressure and the blister takes a dome-like shape (Figure 2.10d). Therefore, in this case, the snap-through transition is from a donut-like blister to a dome-like blister and vice versa for the snap-back transition. Moreover, Figure 2.9b shows that the snap transitions are expected under both pressure and volume-control.

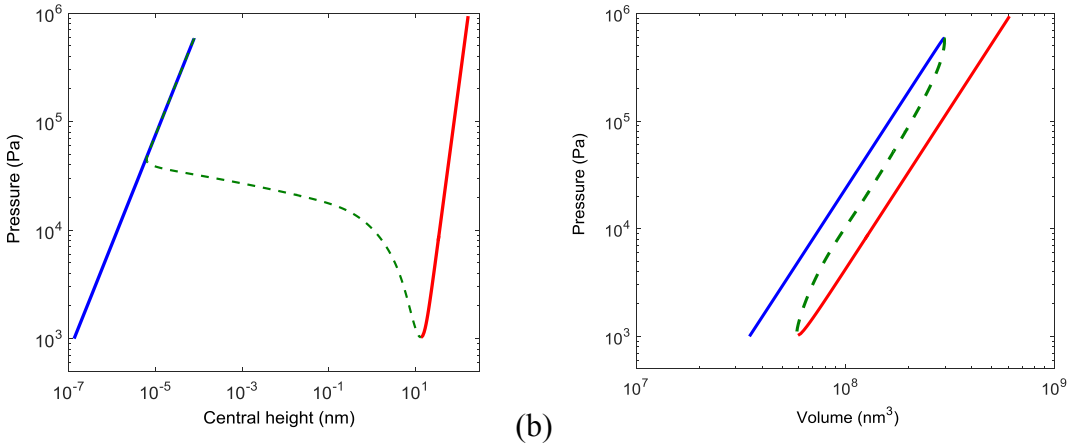

Figure 2.9: (a) Central height versus pressure and (b) Volume versus pressure for a center-island graphene blister (a = 1.5 μm and b = 0.25 μm).

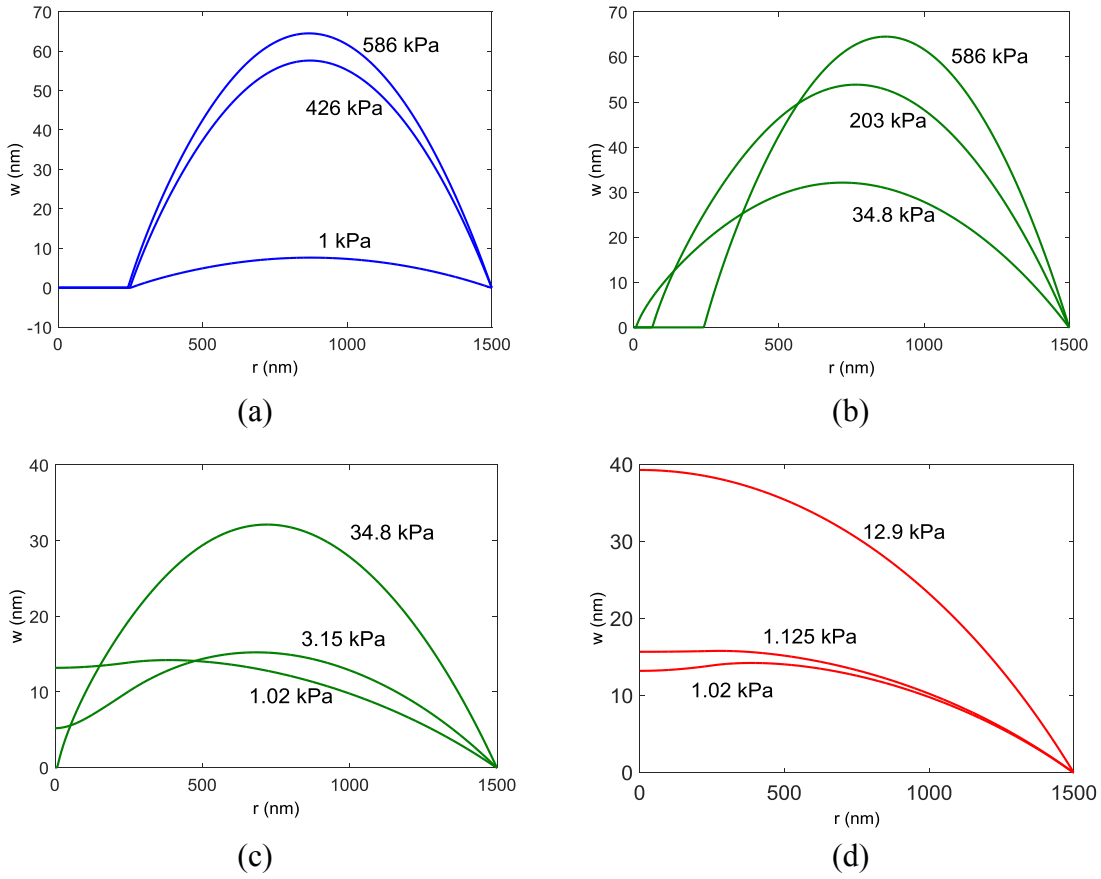

Figure 2.10: Deflection profiles of a center-island graphene blister (a = 1.5 μm and b = 0.25 μm). (a) Donut-like profiles (stable branch I); (b-c) Delamination and popping (unstable branch); (d) Dome-like profiles (stable branch II).

With the center-island configuration, it is possible to determine both parameters (adhesion energy Γ_0 and equilibrium separation h_0) for the van der Waals interactions between graphene and the substrate by measuring the critical pressures for the snap-through and snap-back transitions [28, 29]. For a fixed blister size (a and b), the critical pressure for snap-through depends primarily on the adhesion energy, while the critical pressure for snap-back depends on a combination of the two parameters. First, for the snap-back transition, we note in Figure 2.10d that the separation between graphene and

the surface of the center island is over 10 nm, much larger than the typically expected range for van der Waals interactions (< 3 nm). At such a large separation, the van der Waals interactions can be simplified by ignoring the second term in Eq. (1.2), which is for the short-ranged repulsion. With $w >> h_0$, the traction is approximately

$$\sigma_{vdW}(w) \approx \beta w^{-4}, \tag{2.49}$$

where $\beta = \frac{9}{2}\Gamma_0 h_0^3$ is the single parameter combining the effects of Γ_0 and h_0. As a result, the critical pressure for the snap-back transition depends on the interactions through the combined parameter β. The corresponding pull-in distance (i.e., the central height at the point of snap-back) also depends on β. As shown in Figure 2.11, by varying both Γ and h_0, we obtain the critical pressure and pull-in distance as functions of β. The results for different values of Γ_0 collapse onto a master curve with only dependence on β. Therefore, a measurement of the critical pressure or the pull-in distance would determine the value of β as a combination of the two parameters (Γ_0 and h_0).

The snap-through transition occurs as the graphene delaminates from the center island. As shown in Figure 2.10b, the delamination starts from the edge of the island and grows towards the center. Under a pressure control, the delamination growth is unstable and snaps through upon initiation. By a fracture mechanics consideration, assuming small-scale bridging, the critical pressure for the snap-through transition would depend on the adhesion energy Γ_0 only. As outlined in Section 2.3.3, the approximate membrane analysis predicts the critical pressure as: $p_c = \eta E_{2D}^{1/4}\Gamma_0^{3/4}a^{-1}$, which is compared to the numerical results in Figure 2.12. The numerical results for three different values of h_0 are nearly identical, in very good agreement with the membrane analysis. Therefore, the adhesion energy Γ_0 can be determined by measuring the critical pressure for snap-through transition using the center-island blister configuration. Together with measurement of the

critical pressure for snap-back or the pull-in distance, both parameters (Γ_0 and h_0) for the van der Waals interactions can be determined.

In their experiments, Liu *et al.* [28] measured pull-in distances for center-island graphene blisters, ranging from 8 nm to 10 nm for monolayer graphene. Taking 9.2 nm as the pull-in distance, we obtain from Figure 2.11b $\beta = 0.0083$ nN-nm^2. In subsequent experiments, Boddeti *et al.* [29] measured the critical pressure for snap-through to be around 1 MPa, although the island dimension is slightly different (b = 0. 35 nm). Based on these two measurements, we obtain $\Gamma_0 = 0.2$ J/m^2 and h_0 = 0.21 nm. Both of these values appear to be lower than expected. As noted by Liu *et al.* [28], the graphene membranes may have been subjected to a pretension (~0.07 N/m), and the effects of pretension could be significant for both snap-back and snap-through transitions.

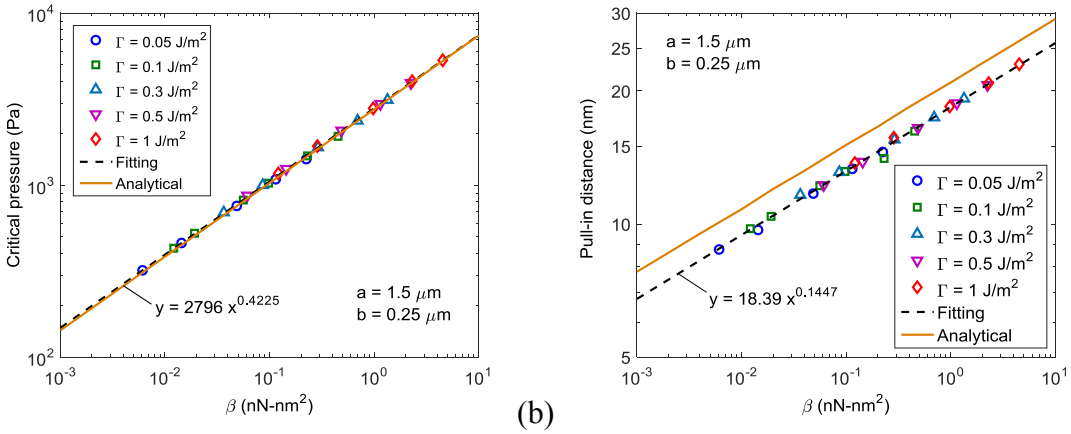

(a) (b)

Figure 2.11: Snap-back transition for a center-island graphene blister (a = 1.5 μm and b = 0.25 μm): (a) Critical pressure and (b) Pull-in distance. The analytical solutions from Liu *et al.* [28] are shown for comparison.

An analytical model was presented by Liu *et al.* [28] for the snap-back transition, assuming uniform attraction and negligible bending stiffness of graphene. As shown in Figure 2.11, the analytical model (with zero pretension) overestimates the pull-in distance compared to the numerical results, while the critical pressure agrees closely with the

numerical results. For the snap-through transition, an analytical model was also presented by Boddeti *et al.* [29], assuming a uniform radial tension and negligible circumferential strain in graphene. The predicted critical pressure has the same scaling as our analysis, i.e., $p_c \sim E_{2D}^{1/4}\Gamma_0^{3/4}a^{-1}$, but slightly lower than the numerical results as shown in Figure 2.12.

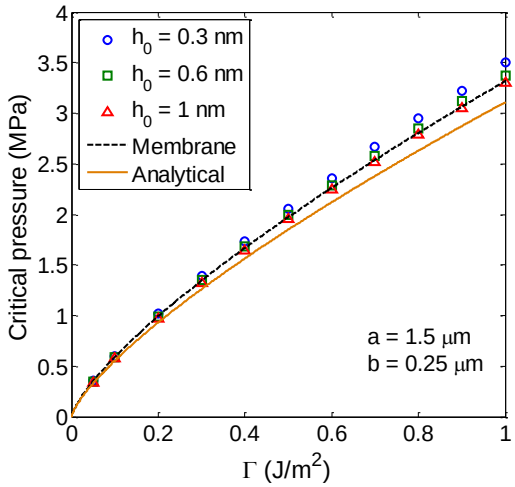

Figure 2.12: Critical pressure for snap-through transition of a center-island graphene blister (a = 1.5 μm and b = 0.25 μm), as a function of the adhesion energy Γ_0. The predictions by the membrane analysis and the analytical model in Boddeti *et al.* [29] are shown in comparison with the numerical results (symbols).

2.7 CENTER-HOLE GRAPHENE BLISTERS

Center-hole blisters are the standard configuration commonly used in experiments under either pressure or volume controlled condition [68, 93]. The gas-impermeability of graphene allowed blister tests under the condition of N-control [27, 65], where N refers to the number of trapped gas molecules. As illustrated in Figure 2.1c, we consider a circular hole of radius b = 0.25 μm, with which the graphene blister is pressurized and the radius

of the blister may grow by delamination from the substrate. The outer radius a is set to be 1.5 μm to stop the delamination. In this case, van der Waals interactions are considered only for the annular region ($a > r > b$). Figure 2.13a shows the calculated pressure-volume curve for the graphene blister. For the first segment (A to B), the blister radius remains constant and the pressure increases with volume. The approximate membrane analysis predicts that $p \propto V^3$ for a fixed blister radius [103], in good agreement with the numerical results. For the second segment (B to C), the pressure decreases and the volume increases, due to increasing blister radius. Again, by the membrane analysis, $p \propto V^{-1/3}$ is predicted for a constant energy release rate (equal to the adhesion energy). Finally, for the third segment (C to D), the blister radius is fixed at the prescribed outer radius a, and the pressure increases with volume as $p \propto V^3$. Evidently, the p-V curve of the graphene blister confirms that the growth of the blister is unstable under a pressure control but stable under a volume control. Under the N-control, we assume $pV = NkT$ by the ideal gas law, where k is the Boltzmann constant and T is temperature. As shown in Figure 2.13a, the p-V curve of the ideal gas intersects the p-V curve of the graphene blister, giving the equilibrium solution under the condition of N-control. Notably, for each value of N, only one intersection can be found, indicating a stable growth of the graphene blister under the N-controlled condition.

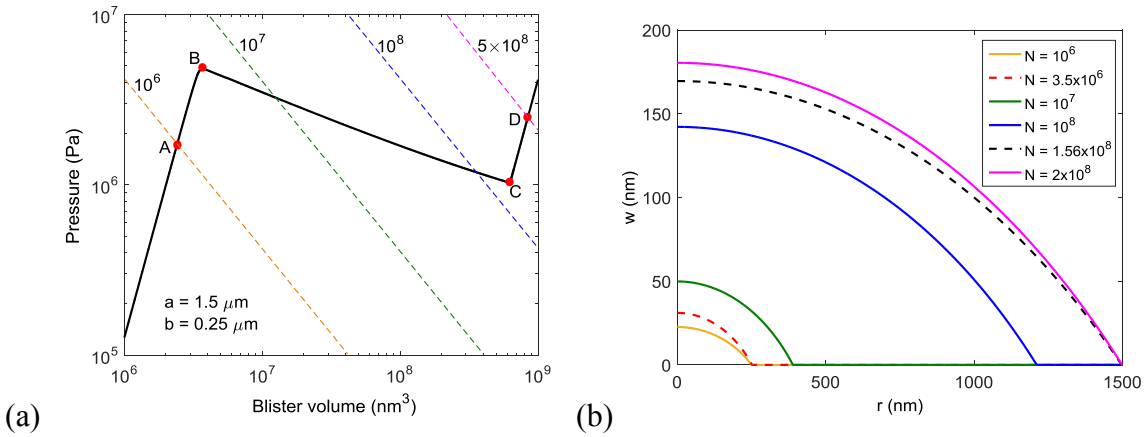

(a) (b)

Figure 2.13: (a) Pressure-volume curve for a center-hole graphene blister (a = 1.5 μm and b = 0.25 μm). The dashed lines correspond to the ideal gas law, $pV = NkT$, with different values of N as indicated (T = 300 K). (b) Deflection profiles for increasing number of gas molecules. The dashed lines correspond to the critical points B and C in (a).

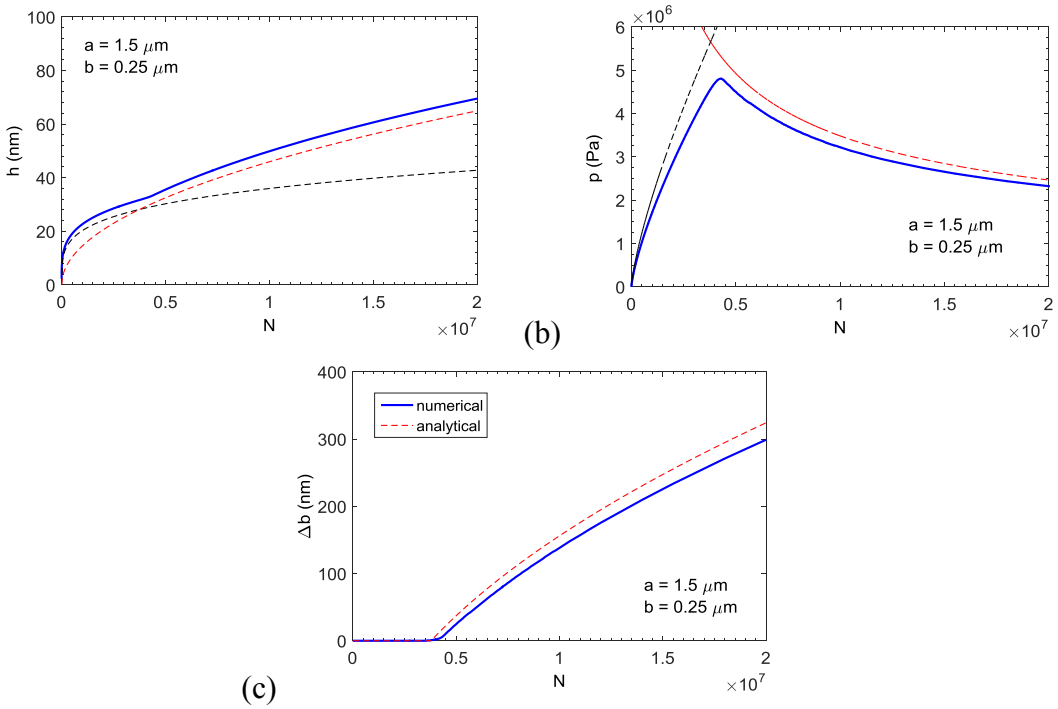

(a) (b) (c)

Figure 2.14: (a) Central height, (b) pressure, and (c) the change of radius for a center-hole graphene blister (a = 1.5 μm and b = 0.25 μm). Dashed lines show the predictions by the approximate membrane analysis.

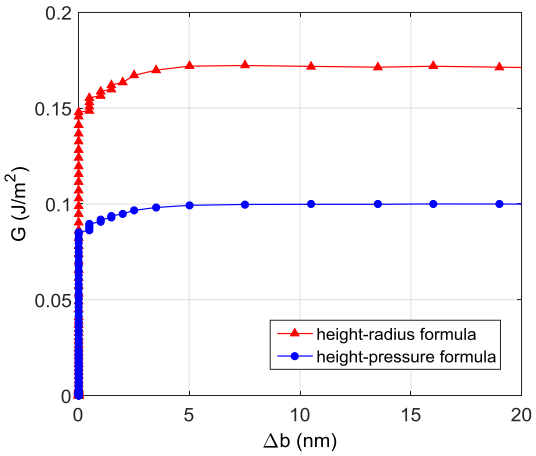

Figure 2.15: Calculated delamination resistance curves for a center-hole graphene blister (a = 1.5 μm and b = 0.25 μm) using two different formulas based on the approximate membrane analysis.

The equilibrium deflection profiles of the center-hole graphene blister are shown in Figure 2.13b for increasing N. The central height, the pressure, and the blister radius are shown in Figure 2.14 as functions of N. The numerical results are compared to the predictions by the approximate membrane analysis [103]. First, for the blister with a fixed radius (b), the central height can be obtained from Eq. (2.28) in conjunction with the ideal gas law:

$$h = \left[\frac{2\phi(\nu)}{\pi}\right]^{1/4} E_{2D}^{-1/4} b^{1/2} (NkT)^{1/4}. \tag{2.50}$$

Correspondingly, the pressure is

$$p = \left[\frac{8}{\pi^3 \phi(\nu)}\right]^{1/4} E_{2D}^{1/4} b^{-5/2} (NkT)^{3/4}. \tag{2.51}$$

Next, for a constant energy release rate (equal to the adhesion energy Γ_0), we obtain by the membrane analysis:

$$h = \left(\frac{5\varphi(\nu)}{2\pi^2}\right)^{1/4} \left(E_{2D}\Gamma_0\right)^{-1/4} \left(NkT\right)^{1/2} \tag{2.52}$$

and

$$p = \left[\frac{2^{13}\pi^2}{5^5\varphi(\nu)}\right]^{1/4} E_{2D}^{1/4}\Gamma_0^{5/4}\left(NkT\right)^{-1/2}. \tag{2.53}$$

The growth of the blister radius is predicted as

$$\Delta b = \left(\frac{5}{4\pi}\right)^{1/2} \Gamma_0^{-1/2}\left(NkT\right)^{1/2} - b, \tag{2.54}$$

where N is assumed to be greater than the critical value, $N_C = \frac{4\pi b^2\Gamma_0}{5kT}$. These predictions are in reasonable agreement with the numerical results. The discrepancy is most likely due to the approximate shape function used in the membrane analysis. A more accurate (also more complicated) shape function was used in Hencky's membrane analysis [111], which would lead to similar predictions except for the coefficient $\phi(\nu)$ and a constant shape factor for the volume. As noted in the previous studies [47, 103], the difference between the two membrane analyses is fairly small.

The presence of van der Waals interactions leads to a cohesive zone near the edge of the graphene blister. It is found that the size of the cohesive zone is relatively small (~5 nm), but depending on the two parameters (Γ_0 and h_0) used for the van der Waals interactions. In experiments, the two parameters may be determined by measuring the delamination resistance curve (R-curve) of the center-hole blister [80]. By measuring the blister height and radius, the energy release rate for delamination may be calculated based on the approximate membrane analysis [103]: $G = \frac{5E_{2D}h^4}{8\phi(\nu)a^4}$. Alternatively, if the pressure can be measured, we may calculate the energy release rate as: $G = 5ph/8$. By the numerical method, we calculate the R-curve as shown in Figure 2.15. Using the height-pressure formula, the R-curve saturates at the prescribed adhesion energy ($\Gamma_0 = 0.1$ J/m^2) for $\Delta b > 5$ nm. The height-radius formula however overestimates the adhesion energy. The shape of the R-curve depends on the traction-separation relation,

which in this case depends on the equilibrium separation h_0. Hence, both parameters (Γ_0 and h_0) may be determined from the R-curve if it can be measured with sufficient accuracy.

In their experiments, Koenig *et al.* [27] measured the height and radius of pressurized graphene blisters in a center-hole configuration. They calculated the equilibrium pressure by assuming the ideal gas law for a constant number of trapped gas molecules, with which they determined the adhesion energy of graphene based on Hencky's membrane analysis. More interestingly, in a subsequent study, Boddeti *et al.* [65] noticed that the initial growth of the graphene blister may be either stable or unstable, depending on the depth of the hole. The stability of the blister growth may be understood based on the *p*-*V* curves (Figure 2.13a). With a finite depth (*d*) for the hole and a constant outer pressure (p_{out}), the ideal gas law may be written as

$$\left(p + p_{out}\right)\left(V + \pi b^2 d\right) = NkT\,. \tag{2.55}$$

Taking $p_{out} = 0.1\,\text{MPa}$ as the outer pressure, we plot the *p*-*V* curves for two different depths in Figure 2.16. The *p*-*V* curve for the blister is the same as that in Figure 2.13a, but the *p*-*V* curves for the trapped gas depend on the hole depth (*d*). For a relatively deep hole ($d = 1\,\mu\text{m}$ in Figure 2.16a), multiple intersections become possible for some values of *N*, giving multiple solutions. This is similar to the pressure-controlled scenario, which may be considered as an extreme case with $d \to \infty$. In particular, as illustrated in Figure 2.16a, a snap transition from point B to point C is predicted for the graphene blister subjected to increasing *N*. On the other hand, for a shallow hole ($d = 0.01\,\mu\text{m}$ in Figure 2.16b), each *p*-*V* curve of the trapped gas has only one intersection with the *p*-*V* curve of the blister, similar to the case in Figure 2.13a where $d = 0$ is implied. In this case, the blister would grow stably and continuously from B to C. Therefore, by varying the hole

depth, both stable and unstable growth may be achieved with the center-hole blister configuration.

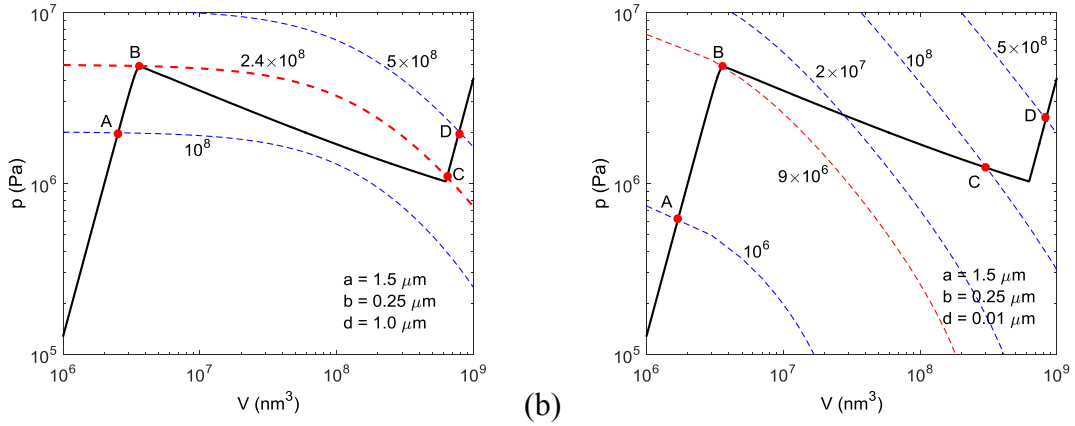

Figure 2.16: Pressure-volume curves, (a) for unstable growth of a center-hole graphene blister (d = 1.0 μm) and (b) for stable growth with d = 0.01 μm, both under N-control. The dashed lines correspond to the ideal gas law with different values of N as indicated (T = 300 K).

2.8 SUMMARY

This chapter presents a numerical study on snap transitions of pressurized graphene blisters. A continuum model is adopted combining a nonlinear plate theory for monolayer graphene with a nonlinear traction-separation relation for van der Waals interactions between graphene and the substrate. A numerical method is developed to solve the nonlinear problem with snap transitions. Three types of blister configurations are considered. For graphene bubble blisters, snap-through and snap-back transitions between pancake-like and dome-like shapes are predicted under the pressure-controlled condition. Phase diagrams are constructed for nano- to microscale bubble blisters, with bistable and unstable regions identified for the pressure and height, respectively. For center-island graphene blisters, snap transitions between donut-like and dome-like shapes

are predicted under both pressure and volume control. Finally, for the center-hole graphene blisters, unstable growth is expected under pressure control, but stable growth is predicted under the volume or *N*-control. With a finite hole depth, however, the growth may start with a snap transition (unstable growth) under *N*-control if the hole is relatively deep.

The numerical results provide a systematic understanding on the mechanics of graphene blisters, consistent with previously reported experiments. Of particular interest is the relationship between the van der Waals interactions and measurable quantities in corresponding blister tests. As a result, the adhesion energy of graphene may be determined from measurements of the radius and height of graphene bubble blisters. Both the adhesion energy and the equilibrium separation for the van der Waals interactions can be determined from measurements of the critical pressures (or critical separation) for snap-back and snap-through transitions of the center-island graphene blisters. With the standard center-hole blister configuration, measurement of the delamination resistance curve could provide sufficient information for the traction-separation relation of the interface. It is noted that, while an approximate membrane analysis may be used in most cases (especially for relatively large blisters), some quantitative discrepancies between the analytical and numerical results do exist. The more accurate numerical solutions may be used in conjunction with experiments for quantitative characterization of the interfacial properties of graphene as well as other two-dimensional membrane materials. Moreover, the numerical method may also be used to explore potential applications of the graphene blisters such as strain engineering and nano-electromechanical devices.

Chapter 3 Thermal rippling of graphene on substrate[2]

3.1 INTRODUCTION

One of the common features among these 2D materials is their monatomic thickness. As a result, they are highly flexible with extremely low flexural rigidity, compared to conventional membranes and thin film materials. At a finite temperature ($T > 0$ K), thermal fluctuations of such ultrathin membranes are expected [2, 49], similar to the ubiquitous fluctuations of biomembranes [114-116]. Indeed, experimental observations have found that suspended graphene membranes often display spontaneous ripples [2, 50, 117], likely a result of thermal fluctuations [49]. Such thermal rippling has been found to be responsible for the temperature dependent mechanical properties of graphene including elastic modulus and apparently negative coefficient of thermal expansion (CTE) at the room temperature [53, 55, 56]. In most applications, graphene membranes are supported on solid substrates, such as silicon (with an oxide surface), copper, and polymers. In addition to the intrinsic thermal rippling, the morphology of a substrate-supported graphene membrane depends on the surface roughness of the substrate as well as the interactions between graphene and the substrate. Ripples, wrinkles and folds are commonly observed in supported graphene as well as other 2D materials [118-123]. Many physical properties of graphene depend on the morphology that may be altered by the interactions with a substrate. In this chapter, we present a statistical mechanics analysis on thermal rippling of monolayer graphene supported on a rigid substrate and corresponding molecular dynamics simulations for comparison. Two main questions are to be answered: First, how would the rippling morphology depend on

[2] The content in this chapter was published in P. Wang, W. Gao, and R. Huang, *Entropic effects of thermal rippling on van der Waals interactions between monolayer graphene and a rigid substrate.* Journal of Applied Physics, 2016. **119**(7): p. 074305. Wang conducted the molecular dynamics simulation and wrote the paper. Wang, Gao and Huang developed the statistical mechanics analysis. Huang reviewed and revised the paper.

the adhesive interactions? Second, how would the statistical thermal rippling influence the graphene-substrate interactions at a finite temperature?

The mechanisms of adhesive interactions between graphene and typical substrates such as silicon oxide (SiO_2) and metals have been studied recently. Both experiments [27, 64, 68, 73, 75] and first-principle calculations [82, 107] have suggested that van der Waals interactions are the primary mechanisms in most cases, although other mechanisms may also exist in some cases [70, 80, 87]. In the present study, we assume a generic form of van der Waals interactions between graphene and the substrate at $T = 0$ K, which was derived from the Lennard-Jones (LJ) potential for pairwise particle-particle interactions [83]. Such an adhesive interaction is expected to suppress the rippling amplitude of a supported graphene membrane. However, a quantitative correlation between adhesion and rippling morphology of graphene has yet to be established. Moreover, even with temperature-independent parameters for the van der Waals interactions, the statistical nature of thermal rippling renders an entropic effect on the graphene-substrate interactions that would depend on temperature. As a result, the effective properties of the graphene-substrate interface become temperature dependent in general. Furthermore, additional effects on the morphology and adhesion of graphene may come from the fact that the graphene membrane is often subjected to an in-plane pre-strain, either unintentionally due to the growth/transfer processes or intentionally for the purpose of strain engineering [124].

The remainder of this chapter is organized as follows. Section 3.2 presents a statistical mechanics analysis based on a continuum membrane model of pre-strained graphene and the generic form of van der Waals interactions. Section 3.3 describes the MD simulations. The results are compared and discussed in Section 3.4, followed by a summary in Section 3.5.

3.2 A CONTINUUM STATISTICAL MECHANICS ANALYSIS

The graphene monolayer is modeled as a two-dimensional (2D) continuum membrane, which interacts with the substrate via an interfacial force field of van der Waals type. The presence of an interfacial force field influences thermal rippling of graphene, which in turn introduces an entropic effect on the graphene-substrate interactions at a finite temperature. The substrate is assumed to be rigid with a perfectly flat surface, whereas the effect of surface roughness is left for future studies.

The generic form of the van der Waals interaction energy function is given in Eq. (1.1). The two parameters (Γ_0 and h_0) are assumed to be independent of temperature in the present study, although they could be temperature dependent in principle (e.g., due to statistical effects of electromagnetic modes and thermal radiation [125-128]).

At a finite temperature ($T > 0$ K), the graphene membrane fluctuates out of the plane (see Figure 3.1). At a particular instance, the rippling profile of the graphene can be written as

$$z(x,y;T) = \left[\bar{z}(T) + w(x,y;T)\right]h_0, \tag{3.1}$$

where $\bar{z}$ and w are the normalized average separation and out-of-plane deflection, respectively. Correspondingly, the total interaction energy between graphene and the substrate over an area Ω is approximately

$$U_I = \iint_{\Omega} V(z)dxdy \approx \iint_{\Omega}\left[V(\bar{z}h_0) + V'(\bar{z}h_0)h_0 w + \frac{1}{2}V''(\bar{z}h_0)h_0^2 w^2\right]dxdy, \tag{3.2}$$

where $V'(z)$ and $V''(z)$ are the first and second derivatives of the interaction energy function in Eq. (1.1), and the higher order terms are neglected. Note that this approximation is valid only when $|w| << 1$ (i.e., the out-of-plane deflection is small compared to the equilibrium separation).

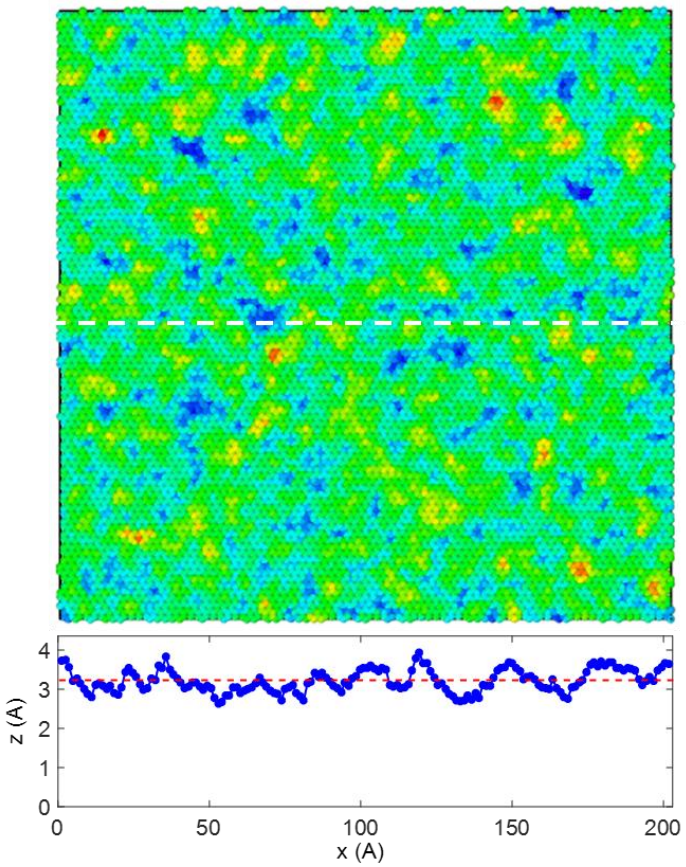

Figure 3.1: Thermal rippling of graphene on a rigid substrate by MD simulation (Γ_0 = 0.242 J/m^2, h_0 = 0.316 nm, ε_0 = 0, and T = 1000 K): a top-view snapshot with color contour for the height and a deflection profile along a line.

Following a previous work for freestanding graphene [53], we consider a graphene membrane subjected to a biaxial pre-strain ε_0, relative to the ground state at 0 K. With the rippling profile in Eq. (3.1), the elastic strain energy of graphene consists of two parts, the bending energy (U_b) and in-plane strain energy (U_s):

$$U_b \approx \frac{Dh_0^2}{2}\iint_{\Omega}\left(\frac{\partial^2 w}{\partial x^2}+\frac{\partial^2 w}{\partial y^2}\right)^2 dxdy\,, \tag{3.3}$$

$$U_s \approx \iint_{\Omega}\left\{E^*\varepsilon_0^2+\frac{E^*\varepsilon_0 h_0^2}{2}\left[\left(\frac{\partial w}{\partial x}\right)^2+\left(\frac{\partial w}{\partial y}\right)^2\right]\right\}dxdy\,, \tag{3.4}$$

where D is the bending modulus of graphene, $E^* = E_{2D}/(1-\nu)$ is the in-plane biaxial modulus, and E_{2D} and ν are the 2D Young's modulus (unit: N/m) and Poisson's ratio of graphene. Note that the bending energy due to Gaussian curvature has been ignored in Eq. (3.3) and only the quadratic terms of the deflection are retained in Eq. (3.4) for a harmonic approximation, as discussed in [53].

Assuming periodic boundary conditions in the x-y plane, the deflection $w(x, y)$ can be written in form of the Fourier series

$$w(\mathbf{r}) = \sum_k \hat{w}(\mathbf{q}_k) e^{i\mathbf{q}_k \cdot \mathbf{r}}, \tag{3.5}$$

and the corresponding Fourier coefficients are

$$\hat{w}(\mathbf{q}_k) = \frac{1}{L_0^2} \iint_\Omega w(\mathbf{r}) e^{-i\mathbf{q}_k \cdot \mathbf{r}} dxdy, \tag{3.6}$$

where $\mathbf{r}$ is the 2D position vector, $\mathbf{q}_k$ denotes the k-th wave vector in the 2D space, and L_0^2 is the area of the domain Ω. For each configuration, the mean-square amplitude of the out-of-plane fluctuation is then

$$\delta^2 = \frac{h_0^2}{L_0^2} \iint_\Omega w^2(\mathbf{r}) dxdy = h_0^2 \sum_k \left(\hat{w}_{\mathrm{Re}}^2(\mathbf{q}_k) + \hat{w}_{\mathrm{Im}}^2(\mathbf{q}_k) \right), \tag{3.7}$$

where $\hat{w}_{\mathrm{Re}}(\mathbf{q}_k)$ and $\hat{w}_{\mathrm{Im}}(\mathbf{q}_k)$ are the real and imaginary parts of $\hat{w}(\mathbf{q}_k)$, respectively. Considering the statistical nature of thermal rippling, the Fourier coefficients $\hat{w}_{\mathrm{Re}}(\mathbf{q}_k)$ and $\hat{w}_{\mathrm{Im}}(\mathbf{q}_k)$ are taken as continuous random variables. Each set of $\hat{w}_{\mathrm{Re}}(\mathbf{q}_k)$ and $\hat{w}_{\mathrm{Im}}(\mathbf{q}_k)$ constitutes a possible configuration of the membrane. All possible configurations of the membrane construct a statistical ensemble. Based on classical statistical mechanics [129, 130], the probability density function (PDF) for each configuration is given by Boltzmann distribution at thermal equilibrium

$$\rho = \frac{1}{Z} \exp\left(-\frac{U}{k_B T} \right), \tag{3.8}$$

where U is the total potential energy of the configuration, Z is the configurational partition function, and k_B is Boltzmann constant. Substituting Eq. (3.5) into Eqs. (3.2)-(3.4), the total potential energy for each configuration of the supported graphene membrane is obtained in terms of the Fourier coefficients as

$$\begin{aligned} U = U_I + U_b + U_s &\approx L_0^2 \left(V(\bar{z}h_0) + E^* \varepsilon_0^2 \right) \\ &+ L_0^2 h_0^2 \sum_{k(\mathbf{q}_k \cdot \mathbf{e}_y \geq 0)} \left(D q_k^4 + E^* \varepsilon_0 q_k^2 + V''(\bar{z}h_0) \right) \left(\hat{w}_{\mathrm{Re}}^2(\mathbf{q}_k) + \hat{w}_{\mathrm{Im}}^2(\mathbf{q}_k) \right), \end{aligned} \tag{3.9}$$

where $q_k = |\mathbf{q}_k|$ is the amplitude of the wave vector. It is important to note that the coefficients $\hat{w}(\mathbf{q}_k)$ and $\hat{w}(-\mathbf{q}_k)$ are not independent since the deflection in Eq. (3.5) must be real valued. Consequently, only those Fourier coefficients associated with the upper half-plane of the wave vectors (i.e., $\mathbf{q}_k \cdot \mathbf{e}_y \geq 0$, including only half of the x-axis) are taken as the independent random variables in Eq. (3.9).

By the equipartition theorem [130], the mean energy associated with each independent harmonic term in Eq. (3.9) equals $k_B T / 2$, and thus we obtain that

$$\left\langle \hat{w}_{\mathrm{Re}}^2(\mathbf{q}_k) \right\rangle = \left\langle \hat{w}_{\mathrm{Im}}^2(\mathbf{q}_k) \right\rangle = \frac{k_B T}{2 L_0^2 h_0^2 \left(D q_k^4 + E^* \varepsilon_0 q_k^2 + V''(\bar{z}h_0) \right)}, \tag{3.10}$$

where $\langle \cdot \rangle$ denotes the ensemble average of the enclosed quantity. The ensemble average of the mean-square amplitude in Eq. (3.7) is then

$$\left\langle \delta^2 \right\rangle = \frac{k_B T}{L_0^2} \sum_k \frac{1}{D q_k^4 + E^* \varepsilon_0 q_k^2 + V''(\bar{z}h_0)}. \tag{3.11}$$

Without the double derivative of the interaction energy function, Eq. (3.11) recovers the classical results for undulations of fluid membranes by Helfrich and Servuss [131], and the same result was obtained for a freestanding graphene membrane [53]. The additional term due to the interactions between graphene and the substrate depends on the average separation $\bar{z}h_0$, which is unknown *a priori*. As shown later, the average separation at thermal equilibrium can be determined as a function of the temperature by minimizing

the Helmholtz free energy of the graphene/substrate system under the isothermal condition. We note that, for the amplitude in Eq. (3.11) to be positive definite, it requires that $V''(\bar{z}h_0) \geq 0$ for $\varepsilon_0 \geq 0$ or $4DV''(\bar{z}h_0) > \left(E^*\varepsilon_0\right)^2$ for $\varepsilon_0 < 0$, which imposes a limitation for the harmonic approximation in the present analysis.

With Boltzmann distribution in Eq. (3.8), the configurational partition function for the statistical thermal rippling is obtained as

$$\begin{aligned} Z &\approx \int_{-\infty}^{\infty} \mathrm{L} \int_{-\infty}^{\infty} \exp\left(-\frac{U}{k_B T}\right) d\hat{w}_{\mathrm{Re}}(\mathbf{q}_1) d\hat{w}_{\mathrm{Im}}(\mathbf{q}_1) d\hat{w}_{\mathrm{Re}}(\mathbf{q}_2) d\hat{w}_{\mathrm{Im}}(\mathbf{q}_2) \mathrm{L} \\ &= \exp\left(-\frac{L_0^2}{k_B T}\left(V(\bar{z}h_0) + E^*\varepsilon_0^2\right)\right) \\ &\quad \times \prod_{k(\mathbf{q}_k \cdot \mathbf{e}_y \geq 0)} \left[\left(1 + \frac{E^*\varepsilon_0}{Dq_k^2} + \frac{V''(\bar{z}h_0)}{Dq_k^4}\right)^{-1} \left(\frac{\pi k_B T}{DL_0^2 h_0^2 q_k^4}\right)\right] \end{aligned} \quad . \tag{3.12}$$

Here the integration limits have been taken to be -∞ and ∞ for each random variable. However, the random variables should be limited within a small range ($|w| << 1$) under the harmonic approximation. Moreover, the rippling membrane should be constrained so that it does not penetrate into the substrate, which may lead to a steric effect [131-133]. Nevertheless, we proceed with Eq. (3.12) as an approximate partition function and leave the additional effects for future studies.

With the partition function in Eq. (3.12), the Helmholtz free energy of the graphene/substrate system is obtained as a function of the average separation, pre-strain and temperature:

$$\begin{aligned} A\left(\bar{z}, \varepsilon_0, T\right) &= -k_B T \ln Z \approx L_0^2 \left(V(\bar{z}h_0) + E^*\varepsilon_0^2\right) \\ &\quad - k_B T \sum_{k(\mathbf{q}_k \cdot \mathbf{e}_y \geq 0)} \left[\ln\left(\frac{\pi k_B T}{DL_0^2 h_0^2 q_k^4}\right) - \ln\left(1 + \frac{E^*\varepsilon_0}{Dq_k^2} + \frac{V''(\bar{z}h_0)}{Dq_k^4}\right)\right]. \end{aligned} \tag{3.13}$$

At a given temperature, the Helmholtz free energy can be minimized with respect to the average separation and the pre-strain for the thermomechanical equilibrium state. First, taking derivative of the free energy with respect to the average separation, we obtain the average normal traction (force per unit area) between graphene and the substrate as

$$\begin{aligned} s(\bar{z},\varepsilon_0,T) &= \frac{1}{L_0^2 h_0}\left(\frac{\partial A}{\partial \bar{z}}\right)_{T,\varepsilon_0} \\ &= V'(\bar{z}h_0) + \frac{k_B T}{L_0^2} V'''(\bar{z}h_0) \sum_{k(\mathbf{q}_k\cdot \mathbf{e}_y \geq 0)} \left[Dq_k^4 + E^*\varepsilon_0 q_k^2 + V''(\bar{z}h_0)\right]^{-1}, \end{aligned} \tag{3.14}$$

where the first term on the right-hand side is the interfacial traction at 0 K (without thermal rippling) and the second term is the entropic contribution due to thermal rippling. Hence, Eq. (3.14) predicts a temperature-dependent traction-separation relation for the interactions between graphene and the substrate. The equilibrium average separation, $\bar{z}^*(\varepsilon_0,T)$, is then obtained by setting $s=0$, namely

$$V'(\bar{z}^* h_0) + \frac{k_B T}{L_0^2} V'''(\bar{z}^* h_0) \sum_{k(\mathbf{q}_k\cdot \mathbf{e}_y \geq 0)} \left[Dq_k^4 + E^*\varepsilon_0 q_k^2 + V''(\bar{z}^* h_0)\right]^{-1} = 0. \tag{3.15}$$

In addition, it is required that $\left(\frac{\partial^2 A}{\partial \bar{z}^2}\right)_{T,\varepsilon_0} > 0$ at $\bar{z} = \bar{z}^*$ for the equilibrium separation to be stable. Interestingly, we note that, if the interaction energy is purely harmonic with $V'''(z) \equiv 0$, the entropic contribution in Eq. (3.14) vanishes and the equilibrium average separation becomes independent of temperature ($\bar{z}^* \equiv 1$). In general, however, the interaction energy as given in Eq. (1.1) is anharmonic, which leads to the entropic effect and the temperature dependence for the equilibrium separation. Therefore, despite the harmonic approximation of the interaction energy function in Eq. (3.2), the anharmonic effect of the interaction is partly taken into account in Eqs. (3.14) and (3.15).

Next, taking derivative of the Helmholtz free energy in Eq. (3.13) with respect to the pre-strain, we obtain the average in-plane stress (equi-biaxial) in the graphene membrane as

$$\begin{aligned}\sigma(\bar{z},\varepsilon_0,T) &= \frac{1}{2L_0^2}\left(\frac{\partial A}{\partial \varepsilon_0}\right)_{T,\bar{z}} \\ &= E^*\left(\varepsilon_0 + \frac{k_B T}{2L_0^2}\sum_{k(\mathbf{q}_k\cdot \mathbf{e}_y\geq 0)}\left[Dq_k^2 + E^*\varepsilon_0 + q_k^{-2}V''(\bar{z}h_0)\right]^{-1}\right).\end{aligned} \tag{3.16}$$

Taking $\bar{z} = \bar{z}^*(\varepsilon_0, T)$, the average in-plane stress at the equilibrium average separation is

$$\sigma^*(\varepsilon_0,T) = \sigma(\bar{z}^*,\varepsilon_0,T) = E^*\varepsilon_0 + \tilde{\sigma}^*(\varepsilon_0,T), \tag{3.17}$$

where the first term on the right-hand side is the pre-stress without rippling and the second term is the additional tension due to the entropic effect of thermal rippling (rippling stress)

$$\tilde{\sigma}^*(\varepsilon_0,T) = E^*\frac{k_B T}{2L_0^2}\sum_{k(\mathbf{q}_k\cdot \mathbf{e}_y\geq 0)}\left[Dq_k^2 + E^*\varepsilon_0 + q_k^{-2}V''(\bar{z}^*h_0)\right]^{-1}, \tag{3.18}$$

As noted in the previous study [53], the in-plane thermal fluctuations of the graphene lattice lead to a positive thermal expansion if the out-of-plane fluctuations are completely suppressed. Taking the in-plane thermal expansion into account, the effective in-plane stress in graphene at a finite temperature is approximately

$$\sigma^*(\varepsilon_0,T) \approx E^*(\varepsilon_0 - \alpha_{2D}T) + \tilde{\sigma}^*(\varepsilon_0,T), \tag{3.19}$$

where α_{2D} is the 2D coefficient of thermal expansion (2D-CTE) resulting from the anharmonic interactions among in-plane phonon modes and was found to be a constant, $\alpha_{2D} \sim 5.51\times10^{-6}$ K^{-1}, independent of temperature (up to 1000 K) [53]. Setting $\sigma^*(\varepsilon_0,T) = 0$ in Eq. (3.19) then leads to an equilibrium thermal strain, $\varepsilon_0^*(T)$, which gives the effective thermal expansion of the supported graphene and could be either positive or negative due to the competing effects between in-plane lattice expansion and

out-of-plane rippling, as discussed in the previous studies [53, 55, 56] for freestanding graphene.

To be specific, the predictions by the statistical mechanics analysis are illustrated and discussed for a square-shaped graphene membrane. First, the normal traction in Eq. (3.14) is evaluated by summation over discrete Fourier modes, which can be written in a dimensionless form as

$$\frac{s}{s_0} = f'(\bar{z}) + f'''(\bar{z})\frac{k_B T}{2D}\sum_{i,j=-n}^{n}\left[16\pi^4\left(\frac{h_0}{L_0}\right)^2\left(i^2+j^2\right)^2 + 4\pi^2\beta\varepsilon_0(i^2+j^2) + \eta f''(\bar{z})\left(\frac{L_0}{h_0}\right)^2\right]^{-1}, \tag{3.20}$$

where $s_0 = \Gamma_0/h_0$, $\eta = \Gamma_0 h_0^2/D$, $\beta = E^* h_0^2/D$, $f'(z)$, $f''(z)$, and $f'''(z)$ are derivatives of the normalized interaction energy function, $f(z) = \frac{1}{2}\left(z^{-9} - 3z^{-3}\right)$. The number n depends on two length scales: the domain size L_0 and a microscopic cut-off length b (e.g., the minimum wavelength of thermal rippling). For $L_0 >> b$, $n \to \infty$ and the summation in Eq. (3.20) converges to a constant. If $\varepsilon_0 = 0$, the summation in Eq. (3.20) can be calculated by an integral approximation as

$$\begin{aligned}\frac{s}{s_0} &\approx f'(\bar{z}) + f'''(\bar{z})\frac{\pi k_B T}{D}\int_{q_{\min}}^{q_{\max}}\left[16\pi^4\left(\frac{h_0}{L_0}\right)^2 q^4 + \eta f''(\bar{z})\left(\frac{L_0}{h_0}\right)^2\right]^{-1} q\,dq \\ &\approx f'(\bar{z}) + \frac{f'''(\bar{z})}{8\pi\sqrt{\eta f''(\bar{z})}}\frac{k_B T}{D}\arctan\left(\frac{4\pi^2}{\sqrt{\eta f''(\bar{z})}}\left(\frac{h_0}{b}\right)^2\right)\end{aligned}, \tag{3.21}$$

where we have taken $q_{\max} = L_0/b$ and $q_{\min} = 1$. Note that the traction is independent of the domain size L_0 as long as $L_0 >> h_0$, but weakly depends on the choice of the cut-off length b. The cut-off length is often taken as a few times of the bond length ($r_0 \sim 0.14$ nm), which is close to the typical values for h_0 (~0.3 nm). For convenience, we take

$b = h_0$ in subsequent calculations. It is found that the results from Eq. (3.21) are in close agreement with the summation in Eq. (3.20) for $L_0 / h_0 > 10$.

As shown in Figure 3.2a, the normalized traction decreases linearly with increasing temperature; the linear dependence is expected as a result of the harmonic approximation in the present analysis. For $\bar{z} > 1$, the traction is positive (attraction) at low temperatures but may become negative (repulsion) at high temperatures. Evidently, the entropic effect of thermal rippling leads to an effective repulsion in addition to the van der Waals forces. Figure 3.2b shows the predicted traction-separation relations at different temperatures. As the temperature increases, the maximum traction (a.k.a., interfacial strength) decreases. In other words, the attractive forces between graphene and substrate are weakened by the entropic repulsion due to thermal rippling. Above a critical temperature (T_c ~ 2462 K for $\eta = 0.11$), the traction becomes all repulsive (s < 0), meaning that the van der Waals forces are no longer sufficient to keep the graphene attached to the substrate. Moreover, the predicted traction-separation relation is limited by the condition, $f''(\bar{z}) > 0$ or equivalently $\bar{z} < 1.165$. For $\bar{z} > 1.165$, the integral in Eq. (3.21) is unbounded and the harmonic analysis yields no meaningful result.

By setting the traction in Eq. (3.21) to zero we obtain two equilibrium average separations, one is stable with $\left(\frac{\partial s}{\partial \bar{z}}\right)_T > 0$ at $\bar{z} = \bar{z}_0^*(T)$ and the other is unstable with $\left(\frac{\partial s}{\partial \bar{z}}\right)_T < 0$ at $\bar{z} = \bar{z}_c(T)$ (see Figure 3.2b). The latter is called the critical average separation, beyond which the traction becomes repulsive by the harmonic analysis. As shown in Figure 3.3a, the stable equilibrium average separation increases with temperature almost linearly up to 1000 K, beyond which it becomes nonlinear, and no solution can be found above the critical temperature (T_c ~ 2462 K for $\eta = 0.11$). Meanwhile, the critical average separation decreases with increasing temperature (dashed

lines in Figure 3.3a). At the critical temperature, the two average separations converge at $\bar{z}_0^*(T_c)=1.122$; hence, by Eq. (3.21), the critical temperature depends on the van der Waals interactions approximately as $k_B T_c \sim D\sqrt{\eta}$.

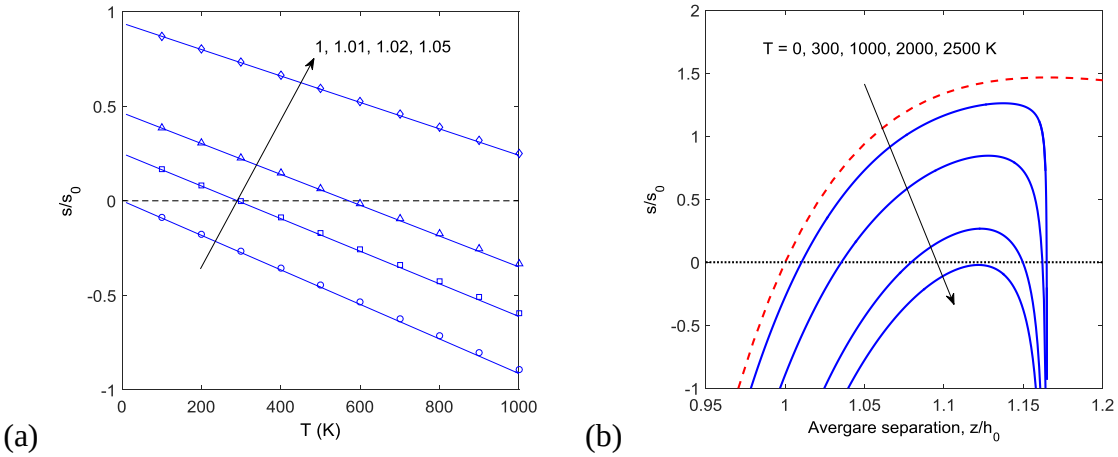

Figure 3.2: (a) Predicted normal traction as a function of temperature at different average separations, $\bar{z}=1$, 1.01, 1.02, and 1.05 (symbols by summation and lines by integral approximation); (b) Predicted traction-separation relations at different temperatures, in comparison with the relation at $T = 0$ K (dashed line). Parameters: $D = 1.4$ eV, $\Gamma_0 = 0.242$ J/m^2, $h_0 = 0.316$ nm, $\eta = 0.11$, and $\varepsilon_0 = 0$.

The increase of the stable equilibrium average separation with temperature is similar to the out-of-plane thermal expansion of graphite, with a temperature-dependent, positive coefficient of thermal expansion [58]. Quantitatively, the coefficient of out-of-plane thermal expansion (CTE) for the graphene/substrate interface may be defined as $\alpha_z = d\bar{z}_0^*/dT$, which depends on the van der Waals interactions through the dimensionless group η. As shown in Figure 3.3b, the CTE decreases as η increases. For $\eta = 0.11$ and $T < 1000$ K, we obtain $\alpha_z \approx 3.5\times10^{-5}\,\mathrm{K}^{-1}$, which is slightly larger than the measured out-of-plane CTE of graphite at around 1000 K [134]. The predicted CTE increases with increasing temperature, in qualitative agreement with the measured

CTE for graphite. However, the present prediction appears to overestimate the CTE at low temperatures ($T < 200$ K) and at very high temperatures ($T > 2000$ K).

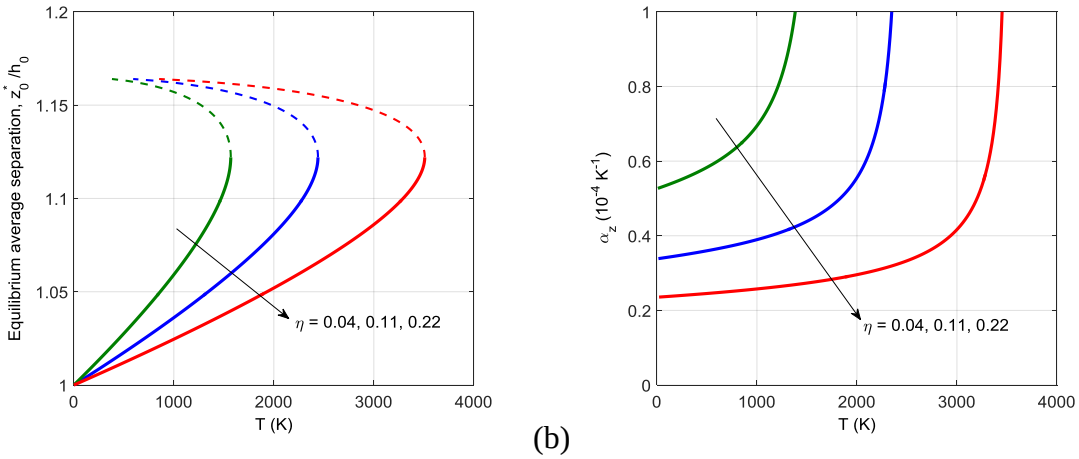

(a) (b)

Figure 3.3: (a) Predicted equilibrium average separation as a function of temperature, with an unstable branch for the critical separation (dashed lines); (b) Predicted out-of-plane coefficient of thermal expansion as a function of temperature.

At the equilibrium average separation $\bar{z}_0^*$ for $\varepsilon_0 = 0$, the average rippling amplitude can be obtained from Eq. (3.11) in form of a discrete summation as

$$\frac{\langle \delta^2 \rangle}{h_0^2} = \frac{k_B T}{D} \sum_{i,j=-n}^{n} \left[16\pi^4 (i^2 + j^2)^2 \left(\frac{h_0}{L_0} \right)^2 + \eta f''(\bar{z}_0^*) \left(\frac{L_0}{h_0} \right)^2 \right]^{-1}. \tag{3.22}$$

For $n \to \infty$, the summation can be evaluated by an integral approximation and the root-mean-square (RMS) amplitude of thermal rippling is then obtained as

$$\bar{\delta} = \sqrt{\langle \delta^2 \rangle} \approx h_0 \sqrt{\frac{k_B T}{8D}} \left[\eta f''(\bar{z}_0^*) \right]^{-1/4}. \tag{3.23}$$

For a freestanding membrane, the rippling amplitude can be obtained from Eq. (3.22) with $\eta = 0$, which recovers the result in the previous study [53]

$$\bar{\delta} \approx \frac{L_0}{4\pi^{3/2}} \sqrt{\frac{k_B T}{D}}. \tag{3.24}$$

Apparently, as a result of the harmonic approximation, the rippling amplitude of a freestanding membrane scales linearly with the domain size (L_0), although a power-law scaling was observed in MD simulations due to anharmonic effects [53]. In contrast, with the presence of van der Waals interactions ($\eta > 0$), the rippling amplitude in Eq. (3.23) is independent of the domain size (for $L_0 >> h_0$). Figure 3.4a shows the predicted rippling amplitude as a function of temperature for different values of η. Evidently, comparing to the freestanding graphene, the presence of adhesive interactions considerably suppresses the amplitude of thermal rippling, and the normalized RMS amplitude decreases with increasing η.

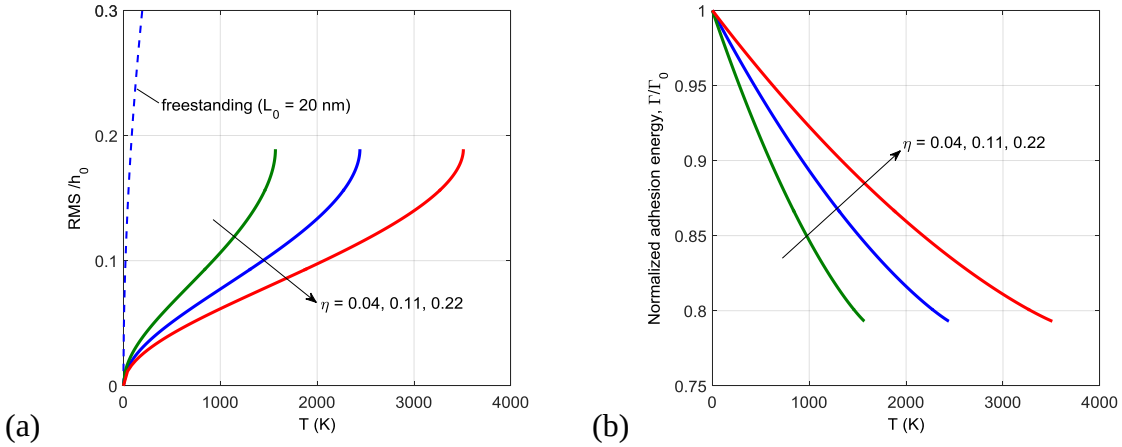

Figure 3.4: (a) Predicted RMS amplitude of thermal rippling as a function of temperature. (b) Normalized adhesion energy as a function of temperature due to the effect of thermal rippling.

The effective adhesion energy may be defined as the difference between the Helmholtz free energy at the equilibrium average separation ($\bar{z} = \bar{z}^*$) and that at infinite separation ($\bar{z} \to \infty$). For $\varepsilon_0 = 0$, we have

$$\Gamma(T) = -\frac{1}{L_0^2}\left[A(\bar{z}_0^*,0,T) - A(\infty,0,T)\right]$$
$$\approx -V(\bar{z}_0^* h_0) - \frac{k_B T}{L_0^2}\sum_{k(\mathbf{q}_k\cdot\mathbf{e}_y\geq 0)} \ln\left(1+\frac{V''(\bar{z}_0^* h_0)}{Dq_k^4}\right). \quad (3.25)$$

It can be seen that, as $T \to 0$ K, we have $\bar{z}_0^* \to 1$ and $\Gamma(T) \to \Gamma_0 = -V(h_0)$ as expected from the interaction energy function in Eq. (1.1). By integral approximation we obtain

$$\frac{\Gamma(T)}{\Gamma_0} \approx -f(\bar{z}_0^*) - \frac{k_B T}{8D}\sqrt{\frac{f''(\bar{z}_0^*)}{\eta}}. \quad (3.26)$$

As shown in Figure 3.4b, the adhesion energy decreases with increasing temperature, almost linearly up to about 1000 K. Interestingly, while the statistical effect of thermal rippling leads to an effective repulsion and hence an effectively lower adhesion energy with increasing temperature, an opposite effect was predicted by considering the electromagnetic modes and thermal radiation, where the attractive van der Waals forces increase with increasing temperature [125-128]. For the case of an atomic monolayer interacting with a solid substrate, the two effects may co-exist, leading to a more complicated dependence on temperature. Without considering the increasing attractive van der Waals forces, the entropic effect is overestimated by the thermal rippling effect alone. On the other hand, the out-of-plane CTE of graphite was underestimated by the first-principle calculations with a quasiharmonic approximaiton [58], possibly because the thermal rippling effects were not fully taken into account. Thus, the coupling of the two competing effects would be of interest for further studies.

Alternatively, the predicted traction-separation relations (see Figure 3.2b) may be used to determine the adhesion energy (or work of separation), by integrating the traction from the equilibrium average separation ($\bar{z}^*$) to the critical average separation ($\bar{z}_c$). This is equivalent to the difference in the Helmholtz free energy at the two equilibrium

separations, which would give a much lower adhesion energy due to the much shorter range of separation ($\bar{z} < \bar{z}_c < 1.165$) accessible by the harmonic analysis.

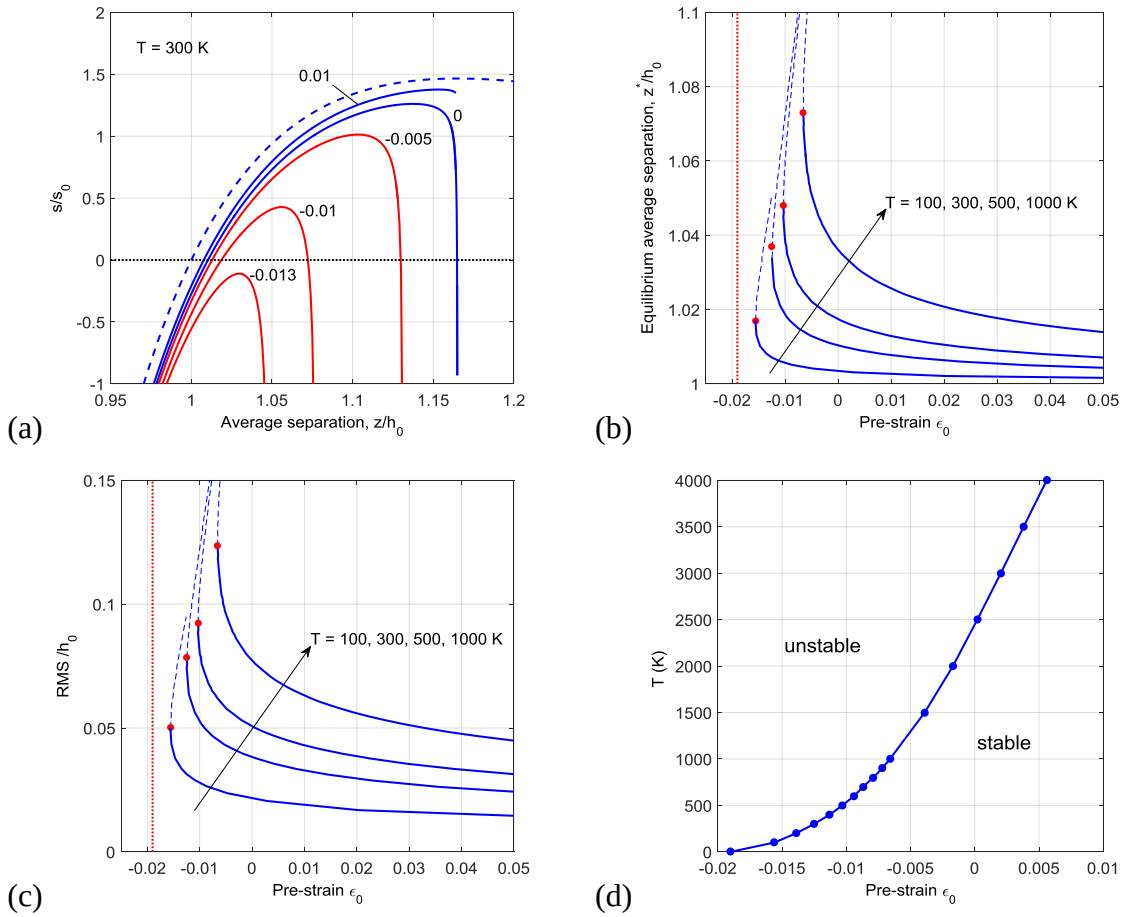

Figure 3.5: Effects of pre-strain by the statistical mechanics analysis (with parameters: $E^* = 403$ N/m, $D = 1.4$ eV, $\Gamma_0 = 0.242$ J/m^2, $h_0 = 0.316$ nm, $\eta = 0.11$). (a) Traction-separation relations at $T = 300$ K with different pre-strains as indicated. The dashed line is the traction-separation relation at $T = 0$ K, independent of the pre-strain. (b) Equilibrium average separation, with a critical strain at each temperature. (c) RMS amplitude of thermal rippling. (d) Critical strain versus temperature (a stability phase diagram).

The effect of pre-strain on the interfacial traction-separation relation is shown in Figure 3.5a, where the summation in Eq. (3.20) is calculated by an integral approximation similar to that in Eq. (3.21). When $\varepsilon_0 > 0$, we obtain

$$\frac{s}{s_0} \approx f'(\bar{z}) + \frac{k_B T}{4\pi D} \frac{f'''(\bar{z})}{\sqrt{4\eta f''(\bar{z}) - \beta^2 \varepsilon_0^2}} \left[\frac{\pi}{2} - \arctan\left(\frac{\beta \varepsilon_0}{\sqrt{4\eta f''(\bar{z}) - \beta^2 \varepsilon_0^2}} \right) \right]. \tag{3.27}$$

if $4\eta f''(\bar{z}) > \beta^2 \varepsilon_0^2$, or

$$\frac{s}{s_0} \approx f'(\bar{z}) + \frac{k_B T}{8\pi D} \frac{f'''(\bar{z})}{\sqrt{\beta^2 \varepsilon_0^2 - 4\eta f''(\bar{z})}} \ln\left(\frac{\beta \varepsilon_0 + \sqrt{\beta^2 \varepsilon_0^2 - 4\eta f''(\bar{z})}}{\beta \varepsilon_0 - \sqrt{\beta^2 \varepsilon_0^2 - 4\eta f''(\bar{z})}} \right). \tag{3.28}$$

if $4\eta f''(\bar{z}) < \beta^2 \varepsilon_0^2$. When $\varepsilon_0 < 0$, the traction is unbounded if $4\eta f''(\bar{z}) < \beta^2 \varepsilon_0^2$ and only the result for $4\eta f''(\bar{z}) > \beta^2 \varepsilon_0^2$ is meaningful. Notably, the traction-separation relation depends on the pre-strain sensitively when $\varepsilon_0 < 0$, with decreasing strength for increasingly large compressive strain. This again can be attributed to the effect of entropic repulsion due to thermal rippling that is amplified by the compressive strain. Beyond a critical compressive strain, the traction becomes all repulsive. On the other hand, when $\varepsilon_0 > 0$, the entropic repulsion is reduced so that the maximum traction increases with increasing strain, slowly approaching the limit at $T = 0$ K (dashed line).

By setting the interfacial traction to zero, we obtain the equilibrium average separation $\bar{z}^*(\varepsilon_0, T)$ as a function of the pre-strain at different temperatures, as shown in Figure 3.5b. Similar to Figure 3.3a, there are two branches for the equilibrium separation at each temperature, one stable and the other unstable (critical average separation, $\bar{z}_c(\varepsilon_0, T)$, shown as dashed lines). The two branches converge at a critical strain (ε_c), below which no solution can be found as the traction becomes all repulsive. Correspondingly, Figure 3.5c shows the effect of pre-strain on the rippling amplitude. By Eq. (3.11) and Eq. (3.14), the rippling amplitude at the equilibrium average separation is obtained as

$$\bar{\delta} = h_0 \sqrt{-\frac{2 f'(\bar{z}^*)}{f'''(\bar{z}^*)}}. \tag{3.29}$$

The rippling amplitude decreases with a tensile pre-strain and increases with a compressive strain. As a tensile strain tends to reduce the amplitude of thermal rippling, it reduces the entropic repulsion and hence the equilibrium average separation (Figure 3.5b). The opposite is true for a compressive strain until it reaches the critical strain (ε_c). The rippling amplitude increases rapidly near the critical strain, resembling a buckling instability. Beyond the critical strain ($\varepsilon_0 < \varepsilon_c$), a nonlinear analysis with anharmonic effects would be necessary for further studies. The critical strain as predicted by the present analysis depends on temperature through the dimensionless group, $k_B T / D$. In addition, it depends on the van der Waals interactions and the mechanical properties of graphene through two other dimensionless groups, $\eta = \Gamma_0 h_0^2 / D$ and $\beta = E^* h_0^2 / D$. As $T \to 0\,\mathrm{K}$, the critical strain approaches the buckling strain, $\varepsilon_B = -6\sqrt{3\eta}/\beta$; the latter was predicted previously by Aitken and Huang [83] without considering the effect of thermal rippling. At a finite temperature, with thermal rippling, the critical strain becomes less compressive, i.e., $\varepsilon_c > \varepsilon_B$, as shown in Figure 3.5d. At very high temperatures, the membrane could be unstable even under a tensile strain (e.g., $\varepsilon_c > 0$). The critical temperature noted in Figure 3.3a is simply the temperature with a zero critical strain ($\varepsilon_c = 0$). Hence, Figure 3.5d may be considered as a stability phase diagram in terms of temperature and pre-strain.

By Eq. (3.19), the average in-plane stress in graphene is obtained with an entropic contribution (the rippling stress) as

$$\begin{aligned}\tilde{\sigma}^*(\varepsilon_0, T) &= E^* \frac{k_B T}{16\pi^2 D} \sum_{i,j} \left[\left(i^2 + j^2\right) + \frac{E^* \varepsilon_0 L_0^2}{4\pi^2 D} + \frac{1}{i^2 + j^2} \frac{\eta f''(\bar{z}^*)}{16\pi^4} \frac{L_0^4}{h_0^4} \right]^{-1} \\ &\approx E^* \left[\frac{k_B T}{32\pi D} \ln\left(1 + \frac{4\pi^2}{\eta f''(\bar{z}^*)} \frac{E^* \varepsilon_0 h_0^2}{D} \left(\frac{h_0}{b}\right)^2 + \frac{16\pi^4}{\eta f''(\bar{z}^*)} \left(\frac{h_0}{b}\right)^4 \right) + \frac{E^* \varepsilon_0 h_0^2}{4D} \frac{f'(\bar{z}^*)}{f'''(\bar{z}^*)} \right] \end{aligned} \quad (3.30)$$

.

Figure 3.6a shows that the entropic rippling stress increases with increasing temperature, but decreases with increasing pre-strain, following the same trend as the rippling amplitude (Figure 3.5c). The total stress, with the effect of in-plane thermal expansion, is shown in Figure 3.6b as a function of pre-strain for T = 1000 K. Here we have assumed that the biaxial modulus E^* of graphene is independent of temperature and strain. Due to in-plane thermal expansion, the in-plane stress-strain relation simply shifts downward at a finite temperature before the rippling stress is taken into account. With thermal rippling, the total stress becomes more tensile with a slightly nonlinear dependence on the pre-strain. The effective modulus, defined as the slope of the stress-strain curve, is lower than E^* and depends on temperature, similar to the effective modulus for a freestanding graphene as discussed in the previous study [53].

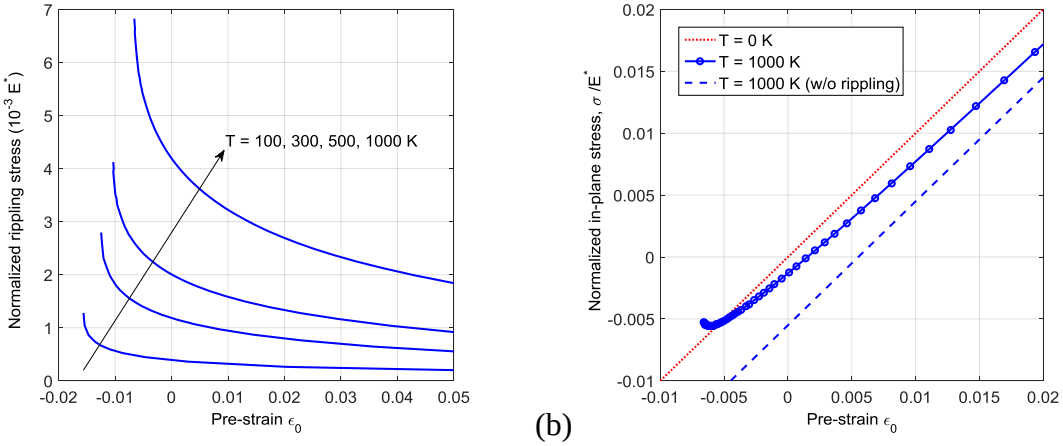

Figure 3.6: (a) Predicted rippling stress as a function of pre-strain; (b) Comparison of the average in-plane stresses at 1000 K with and without rippling.

3.3 MOLECULAR DYNAMICS SIMULATION

The theoretical predictions by the continuum statistical mechanics analysis in Section 3.2 are compared to MD simulations using LAMMPS [135]. A square-shaped

graphene membrane (L_0 ~ 20 nm) is placed on top of a flat surface as a rigid substrate. The interaction between carbon atoms of graphene and the surface was modeled by Lennard-Jones potential, specified in form of Eq. (3.31) with two parameters (ε_{CS} and δ_{CS}),

$$U_{CS} = \varepsilon_{CS}\left[\frac{2}{15}\left(\frac{\delta_{CS}}{r_{CS}}\right)^9 - \left(\frac{\delta_{CS}}{r_{CS}}\right)^3\right], \tag{3.31}$$

where r_{CS} is the distance between each carbon atom and the surface. Compared with Eq. (1.1), the equilibrium separation and adhesion energy of the graphene/substrate interface can then be obtained as

$$h_0 = \left(\frac{2}{5}\right)^{1/6}\delta_{CS}, \tag{3.32}$$

$$\Gamma_0 = \frac{4\sqrt{10}}{9\sqrt{3}}\frac{\varepsilon_{CS}}{r_0^2}, \tag{3.33}$$

where $r_0 = 0.142\,\text{nm}$ is the equilibrium bond length of graphene. The dimensionless parameter η is varied by changing the reference adhesion energy Γ_0 and equilibrium separation h_0. Here, we use two different values for h_0: 0.316 and 1.0 nm; the former is predicted by DFT calculations for graphene on SiO_2 [82], while the latter is taken as an upper bound from measurements [75, 108, 109]. The value of Γ_0 is varied between 0.05 and 1.0 J/m^2 as mentioned in Section 2.2.2.

The second-generation reactive empirical bond-order (REBO) potential [38] is used for the carbon-carbon interactions in graphene. With the REBO potential, the mechanical properties of graphene in the ground state (T = 0 K) have been predicted previously [46, 48, 104]: E_{2D} = 243 N/m, ν = 0.397, and D = 1.4 eV, as listed in Table 1.1. Although these values are different from DFT calculations [33, 34], they are used in the present study to compare the theoretical predictions with the MD simulations. Under

an equi-biaxial pre-strain (ε_0), the theoretical results depend on a dimensionless group, $\beta = E^* h_0^2 / D$. Despite the discrepancy in the 2D Young's modulus and Poisson's ratio, the biaxial modulus, $E^* = E_{2D}/(1-\nu)$, predicted by the REBO potential (E^* ~ 403 N/m) is in close agreement with DFT (E^* ~ 406 N/m). The bending modulus (D) is also in close agreement with DFT (~1.5 eV) [33, 48].

MD simulations are performed in NVT ensemble with periodic boundary conditions, where the temperature is controlled by the Nose-Hoover thermostat. The equi-biaxial pre-strain ε_0 is applied to the graphene membrane by simultaneously changing the two in-plane dimensions as $L = L_0(1+\varepsilon_0)$, where L_0 is the side length of the square-shaped membrane in the ground state (T = 0 K). It is found that the simulation results are independent of the membrane size as long as $L_0 >> h_0$, and only the simulations with $L_0 \approx 20$ nm (see Figure 3.1) are presented. Periodic boundary conditions are applied in all three directions. The thickness dimension of the simulation box is set to be 10 nm so that it is large enough to avoid interactions between periodic images. Each simulation runs up to 40 ns with a time step of 1 fs. The first 10 ns is for the system to equilibrate with the prescribed temperature and pre-strain, and the subsequent 30 ns is used for calculating the time-averaged quantities.

The normalized equilibrium average separation is calculated for each MD simulation as

$$\overline{z}^*(T, \varepsilon_0, \eta) = \frac{1}{N h_0} \left\langle \sum_{i=1}^{N} z_i \right\rangle_t, \tag{3.34}$$

where N is the total number of carbon atoms and $\langle z_i \rangle_t$ is the time-averaged z-coordinate of the i-th atom. The mean amplitude of the out-of-plane thermal rippling is calculated by a time-averaged RMS, namely

$$\bar{\delta}\left(T,\varepsilon_0,\eta\right)=\sqrt{\frac{1}{N}\left\langle\sum_{i=1}^{N}\left(z_i-\bar{z}^{*}h_0\right)^2\right\rangle_t}\ . \tag{3.35}$$

The average in-plane stress in graphene is evaluated by the time-averaged 2D virial stress:

$$\sigma=\frac{1}{L^2}\left\langle\frac{1}{2}\sum_{\substack{i,j\\ i\neq j}}\mathbf{F}_{ij}\otimes\left(\mathbf{r}_j-\mathbf{r}_i\right)-\sum_i m_i\mathbf{v}_i\otimes\mathbf{v}_i\right\rangle_t, \tag{3.36}$$

where $\mathbf{F}_{ij}$ is the interatomic force between two carbon atoms (i and j), $\mathbf{r}_i$ is the position vector of i-th atom, $\mathbf{v}_i$ is the velocity vector, and m_i is the atomic mass.

Finally, the time-averaged interaction potential energy (per unit area) is calculated, for which the corresponding ensemble average can be predicted by the statistical mechanics analysis as

$$\frac{\langle U_I\rangle}{L_0^2}\approx V(\bar{z}^{*}h_0)+\frac{1}{2}V''(\bar{z}^{*}h_0)\left\langle\delta^2\right\rangle=\Gamma_0\left(f(\bar{z}^{*})-\frac{f'\left(\bar{z}^{*}\right)f''(\bar{z}^{*})}{f'''\left(\bar{z}^{*}\right)}\right). \tag{3.37}$$

We note that the average interaction energy differs from the effective adhesion energy defined by the Helmholtz free energy (Eq. (3.25)). The latter may be calculated by the steered MD simulations [136], which is left for future studies.

3.4 RESULTS AND DISCUSSION

In this section we compare the theoretical predictions by the statistical mechanics analysis in Section 3.2 with the MD simulations in Section 3.3. First, we compare the RMS amplitude of thermal rippling (Figure 3.7a) and the equilibrium average separation (Figure 3.7b) for cases with zero pre-strain ($\varepsilon_0 = 0$). Both increase with increasing temperature as a result of the entropic effect. Increasing the adhesion energy (η) reduces the rippling amplitude and hence the entropic repulsion, leading to less expansion in the

equilibrium separation. The results from MD simulations agree reasonably well with the theoretical predictions at relatively low temperatures. At high temperatures the statistical mechanics analysis over-predicts the amplitude of thermal rippling, possibly due to the harmonic approximation. The predicted critical temperature is not observed in the MD simulations. It is possible that the anharmonic effects not considered in the present analysis are substantial at high temperatures, suppressing the rippling amplitude and delaying the critical temperature behavior. Figure 3.7c shows the average interaction energy between graphene and substrate, decreasing with increasing temperature. The same trend is predicted for the effective adhesion energy (Figure 3.4b). By Eq. (3.37), the normalized interaction energy with $U_0 = -\Gamma_0 L_0^2$ depends on the rippling amplitude and the average separation. Again, the theoretical prediction agrees with the MD simulations at relatively low temperatures.

Constrained at zero pre-strain (relative to the ground state at 0 K), a thermal stress is induced in graphene at a finite temperature. By Eq. (3.19), the amplitude of thermal stress would increase linearly with temperature if the out-of-plane rippling is completely suppressed, as shown by the dashed line in Figure 3.7d. While the positive 2D-CTE ($\alpha_{2D} > 0$) leads to a compressive thermal stress, the rippling stress $\tilde{\sigma}^*$ is tensile, as predicted by Eq. (3.30) and shown in Figure 3.6a. As a result, the average thermal stress in graphene becomes less compressive and depends on the adhesive interactions with the substrate. In contrast, for a freestanding graphene the thermal stress was found to be tensile due to significantly larger rippling stress [53]. Figure 3.7d shows that the thermal stresses obtained from MD simulations agree reasonably well with the theoretical prediction up to moderately high temperatures (~1000 K).

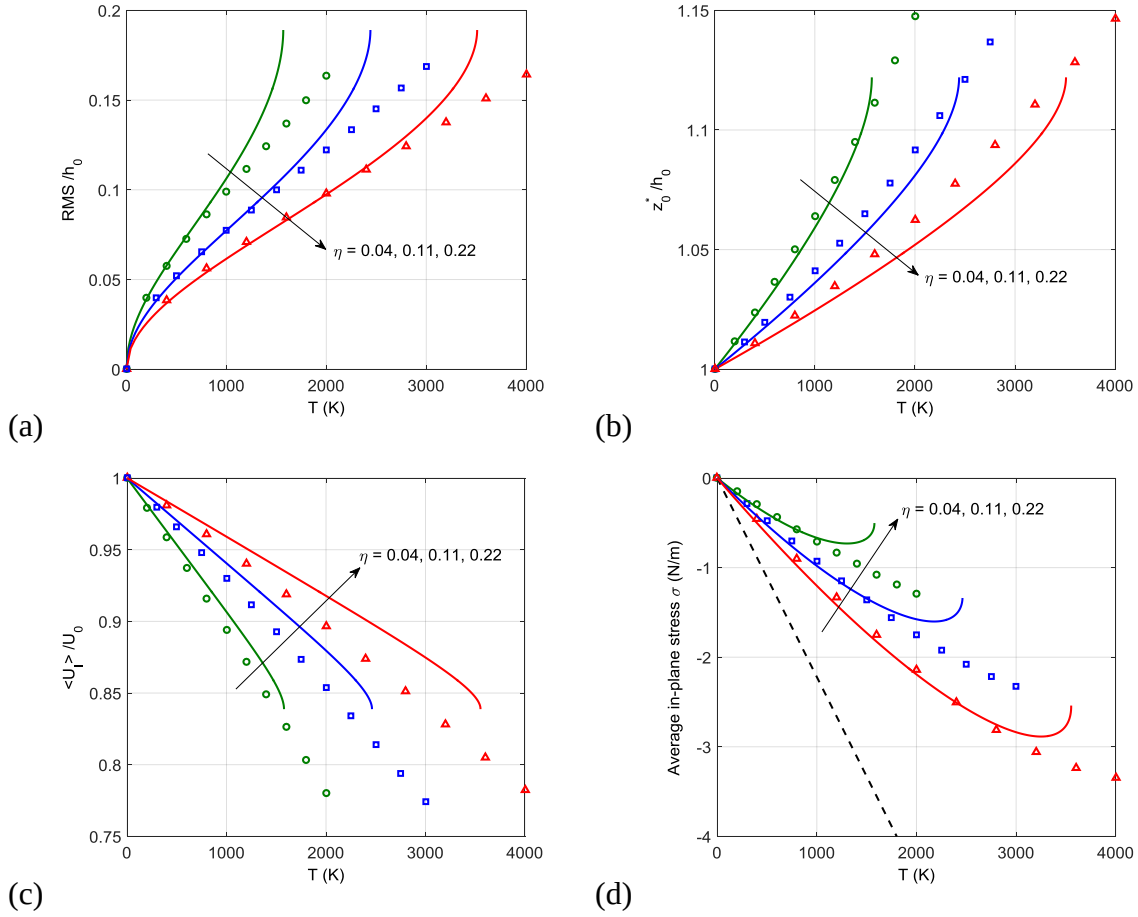

Figure 3.7: Comparison between theoretical predictions and MD ($\varepsilon_0 = 0$): (a) RMS amplitude of thermal rippling as a function of temperature for different η. (b) Equilibrium average separation as a function of temperature. (c) Average interaction energy between graphene and substrate. (d) Average in-plane stress in graphene (dashed line for the case of no rippling). All symbols are from MD simulations and lines by the theoretical predictions.

The effects of pre-strain are compared in Figure 3.8. First, the rippling amplitudes at four different temperatures are shown with pre-strains ranging from -0.02 to 0.06 (Figure 3.8a). The results from MD simulations agree well with the predictions for the cases with a tensile pre-strain ($\varepsilon_0 > 0$). The statistical mechanics analysis predicts a temperature dependent critical strain (Figure 3.5d), beyond which the harmonic

approximation yields no meaningful result. The RMS amplitude of thermal rippling from MD simulations increases dramatically as the pre-strain changes from -0.01 to -0.02, indicating a critical strain in between. Figure 3.9 shows the morphology of the supported graphene at 300 K with a pre-strain of -0.02, where a zigzag buckling pattern is observed. Similar buckling patterns are observed at other temperatures. Such a buckling phenomenon resembles the telephone cord blistering in thin films as a result of biaxial compression and interfacial delamination [137]. Apparently, the largest separation shown in Figure 3.9 is greater than 1 nm (~$3h_0$), for which the van der Waals interactions with the substrate become negligible and the graphene may be considered as delaminated locally from the substrate. A few recent studies have also simulated buckling of substrate-supported graphene with a variety of morphological patterns such as wrinkles, folds, and crumpling [138-140]. However, the transition from thermal rippling to buckling is noted for the first time in the present study. The critical strain for this transition and its dependence on the interfacial adhesion and temperature will be studied in Chapter 4.

Figure 3.8d compares the normalized in-plane stress of graphene. As noted in Figure 3.6b, the average in-plane stress is subject to two competing effects. Relative to the stress-strain relation at 0 K, the stress becomes more compressive at a finite temperature ($T > 0$ K) due to the positive lattice expansion but becomes less compressive due to thermal rippling. The two effects combine to give a weak temperature dependence for the in-plane stress-strain relation of the supported graphene. The results from MD simulations agree with the theoretical predictions when the strain is small ($-0.01 < \varepsilon_0 < 0.01$) for temperatures up to 1000 K. At larger tensile strains ($\varepsilon_0 > 0.01$), the stresses from MD simulations are lower because of the intrinsic elastic nonlinearity of graphene as discussed in previous studies [34, 48, 53]. At larger compressive strains (e.g.,

$\varepsilon_0 = -0.02$), the compressive stress is largely relaxed due to buckling and becomes nearly independent of temperature.

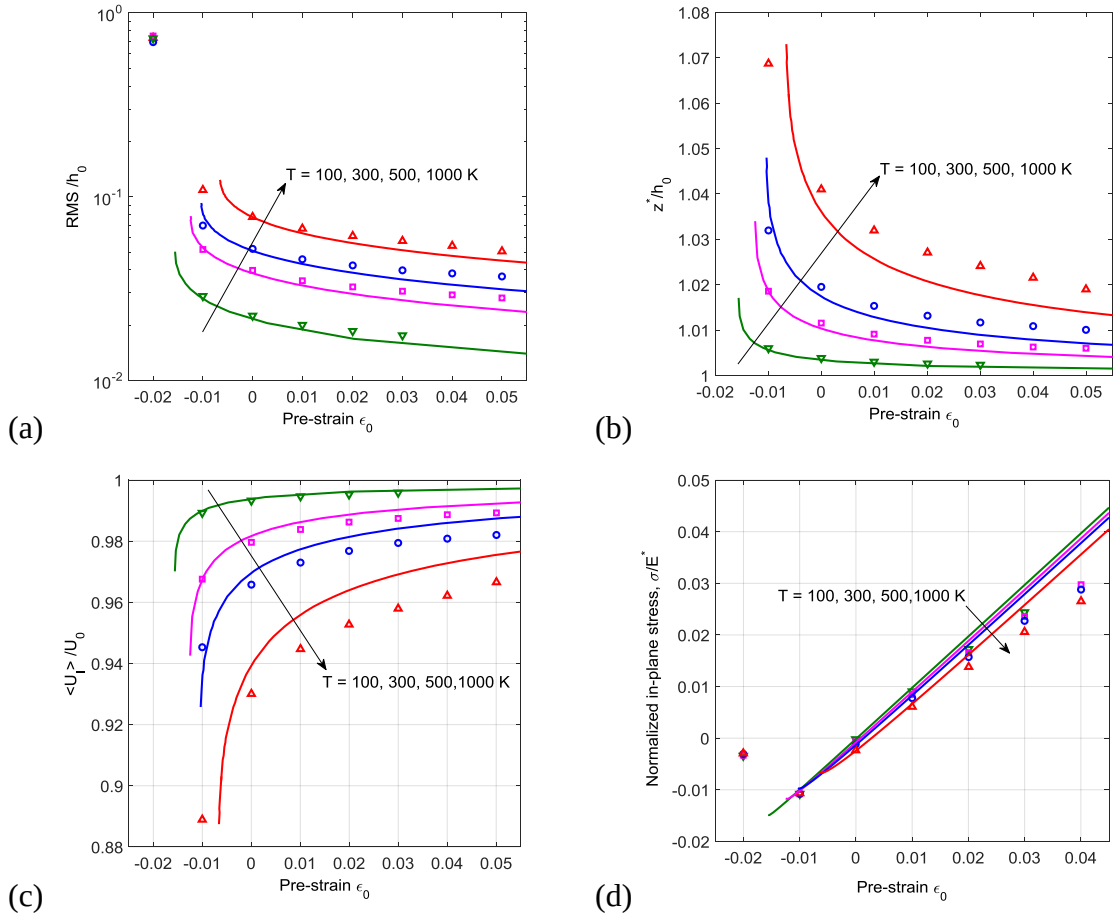

Figure 3.8: Effects of pre-strain by MD ($\Gamma_0 = 0.242$ J/m^2, $h_0 = 0.316$ nm, and $\eta = 0.11$). (a) RMS amplitude of thermal rippling as a function of strain at different temperatures. (b) Equilibrium average separation as a function of strain. (c) Average interaction energy between graphene and substrate. (d) Average in-plane stress in graphene. All symbols are from MD simulations and lines by the theoretical predictions.

We close this section by commenting on the major differences between substrate-supported graphene and freestanding graphene. For freestanding graphene ($\eta = 0$), as shown in the previous study [53], the rippling amplitudes from MD simulations are

considerably lower than the predictions by the harmonic analysis (even at low temperatures) and depend on the size of the graphene membrane by a power law instead of the linear scaling predicted by the harmonic approximation. For supported graphene with adhesive interactions ($\eta > 0$), the rippling amplitudes are independent of the membrane size as long as $L_0 >> h_0$, and the harmonic approximation becomes more applicable since the rippling amplitude is much smaller than freestanding graphene. The comparisons in Figure 3.7 and Figure 3.8 suggest that the theoretical predictions by the harmonic approximations are reasonable as long as the rippling amplitude is relatively small (e.g., $\bar{\delta} / h_0 < 0.1$). For the case with $\eta = 0.11$, the applicable temperature range is up to 1000 K with the pre-strain $\varepsilon_0 > -0.01$.

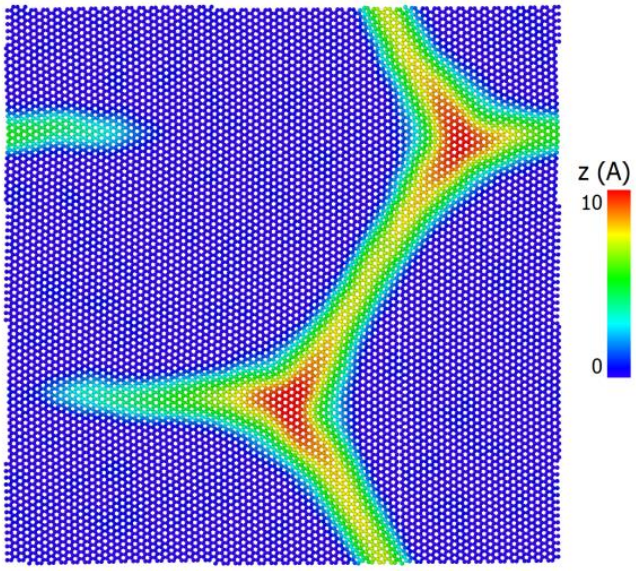

Figure 3.9: Buckling of a substrate-supported graphene by MD simulation at 300 K with a biaxial pre-strain of -0.02. The side length of the graphene membrane as shown is about 20 nm, and the interfacial properties are: Γ_0 = 0.242 J/m^2 and h_0 = 0.316 nm.

3.5 SUMMARY

Thermal rippling of a substrate-supported graphene depends on the adhesive interactions between graphene and the substrate, and the statistical nature of thermal rippling leads to an entropic effect on the graphene-substrate interactions. This inter-relationship between thermal rippling and adhesion is theoretically analyzed by a continuum statistical mechanics analysis under harmonic approximations. Comparisons with MD simulations show that the theoretical predictions on the rippling amplitude, the equilibrium average separation, and the average interaction energy are reasonable up to moderately high temperatures, when the rippling amplitude is relatively small. Of particular interest is the entropic effects of thermal rippling that lead to an effective repulsion, and as a result, the equilibrium average separation increases and the effective adhesion energy decreases with increasing temperature. Moreover, the presence of a biaxial pre-strain in graphene could either reduce or amplify the thermal rippling and the entropic effects, depending on the sign of strain (tensile or compressive). A rippling-to-buckling transition is predicted and observed in MD simulations beyond a critical compressive strain. These theoretical and numerical results shed light on the commonly observed morphological features (wrinkles, buckles, and folds) in substrate-supported graphene and other 2D materials, and in particular, on the effects of adhesive interactions and temperature. Further studies would extend the statistical mechanics analysis to account for the anharmonic effects and consider more realistic substrate surfaces with roughness.

Chapter 4 Buckling of monolayer graphene on a substrate

4.1 INTRODUCTION

Due to its high flexibility with extremely low flexural rigidity, graphene thin membranes are unstable to boundary or substrate-induced compressive loads: moderate compression results in regular wrinkling [141-143], while further confinement can lead to crumpling [138, 144, 145]. One- and two-dimensional periodic wrinkles in suspended graphene sheets are observed by using both spontaneously and thermally generated strains [141]. The wrinkle orientation, wavelength and amplitude are controlled by boundary conditions and graphene's negative thermal expansion coefficient (TEC). When synthesizing large-area graphene layers on poly-nickel substrate by chemical vapor deposition (CVD), Chae *et al.* [5] also observed the wrinkles are formed by two processes: i) nucleation of defect lines on step edges between Ni terraces and ii) thermal-stress-induced formation of wrinkles around step edges and defect lines. The rippling, wrinkling, buckling and crumpling morphologies of graphene have important impacts on its electrical, mechanical, and electromechanical properties. The ability to control morphological structure in graphene could allow device design based on local strain and selective bandgap engineering [146]. Graphene is transferred to pre-stretched PDMS films to form spontaneously nanoscale periodical buckling. This controllable process of buckled graphene provides a feasible fabrication for graphene flexible electronic devices and strain sensors [143]. Zhang *et al.* [138] report an approach to reversibly control the crumpling and unfolding of large-area graphene sheets, which enables to fabricate large-area conductive coatings and electrodes showing superhydrophobicity, high transparency, and tunable wettability and transmittance. In the present study, we consider a monolayer graphene placed on substrate subjected to compressive strain. Wrinkling and buckling analysis are performed to predict to critical transition strain as well as buckling height

and width. Molecular dynamics simulations are conducted to study the evolution of instability morphology.

The remainder of this chapter is organized as follows. Section 4.2 describes the analytically approximate solution for both regular wrinkling and buckling. Section 4.3 presents the details for molecular dynamics simulations. The results are discussed in Section 4.4, followed by a summary in Section 4.5.

4.2 ANALYTICAL PREDICTIONS

Consider a monolayer graphene on a rigid substrate with a flat surface. Subject to an in-plane uniaxial compression, the graphene membrane may buckle to relax the in-plane stress, but the adhesive interactions would keep the membrane close to the substrate. The competition may lead to formation of sinusoidal wrinkles or localized buckles (see Figure 3.9). To determine which buckling mode would take place, we first consider each of the two modes separately and then compare the critical conditions.

Here, graphene monolayer is modeled as an elastic membrane with a 2D plane-strain modulus $\overline{E} = \frac{E_{2D}}{1-\nu^2}$ and a bending modulus D. We model the adhesive interactions between graphene and substrate by the van der Waals interaction with potential energy function given in Eq. (1.1) and the traction-separation relation given in Eq. (1.2).

4.2.1 Sinusoidal wrinkling

Based on previous studies [83, 138], we assume a sinusoidal wrinkle deflection with wavelength λ_w and amplitude A_w as

$$w = A_w \sin\left(\frac{2\pi x}{\lambda_w}\right), \tag{4.1}$$

plotted in Figure 4.1a. The elastic strain energy (to the leading orders of amplitude) of wrinkled graphene per unit area of graphene is

$$U_w^e \approx \frac{1}{2}\bar{E}\varepsilon_0^2 + \frac{A_w^2}{4}\left[-\bar{E}\varepsilon_0\left(\frac{2\pi}{\lambda_w}\right)^2 + D\left(\frac{2\pi}{\lambda_w}\right)^4\right] + \frac{\bar{E}A_w^4}{16}\left(\frac{2\pi}{\lambda_w}\right)^4, \tag{4.2}$$

where ε_0 is the in-plane uniaxial strain of the membrane before buckling, which is taken to be positive for compression. For a relatively long corrugation wavelength, compared to the C−C bond length (0.142 nm) in graphene, the average interaction energy per unit area is approximately

$$U_w^{vdW} = \frac{1}{\lambda_w}\int_0^{\lambda_w} V\left(w+h_0\right)dx \approx \Gamma_0\left(-1+\frac{27A_w^2}{4h_0^2}+\frac{675A_w^4}{4h_0^4}\right). \tag{4.3}$$

Combine Eq. (4.2) and (4.3) to obtain the total free energy and then minimize it with respect to A_w and λ_w, we obtain a nonlinear equation for the wrinkle wavelength

$$\frac{200D}{\bar{E}h_0^2}\frac{\varepsilon_0}{\varepsilon_c^w}\left(\frac{\lambda_w}{\lambda_c}\right)^6 + \left(1-\frac{200D}{\bar{E}h_0^2}\right)\left(\frac{\lambda_w}{\lambda_c}\right)^4 - 1 = 0, \tag{4.4}$$

where the critical strain is

$$\varepsilon_c^w = \frac{6\sqrt{3\Gamma_0 D}}{\bar{E}h_0}, \tag{4.5}$$

and

$$\lambda_c = 2\pi\left(\frac{Dh_0^2}{27\Gamma_0}\right)^{1/4}. \tag{4.6}$$

It is noted that the critical strain for onset of wrinkling is independent of the size of graphene membrane. Then the corresponding amplitude is calculated from

$$\frac{A_w}{h_0} = \sqrt{\frac{\frac{\bar{E}\varepsilon_0}{\Gamma_0}\left(\frac{2\pi h_0}{\lambda_w}\right)^2 - \frac{D}{\Gamma_0 h_0^2}\left(\frac{2\pi h_0}{\lambda_w}\right)^4 - 27}{\frac{\bar{E}}{4\Gamma_0}\left(\frac{2\pi h_0}{\lambda_w}\right)^4 + 675}}. \tag{4.7}$$

When $\varepsilon_0 > \varepsilon_c$, the wrinkling wavelength decreases and the amplitude increases with the magnitude of the compressive strain, similar to wrinkling of an elastic thin film on a hyperelastic substrate [147].

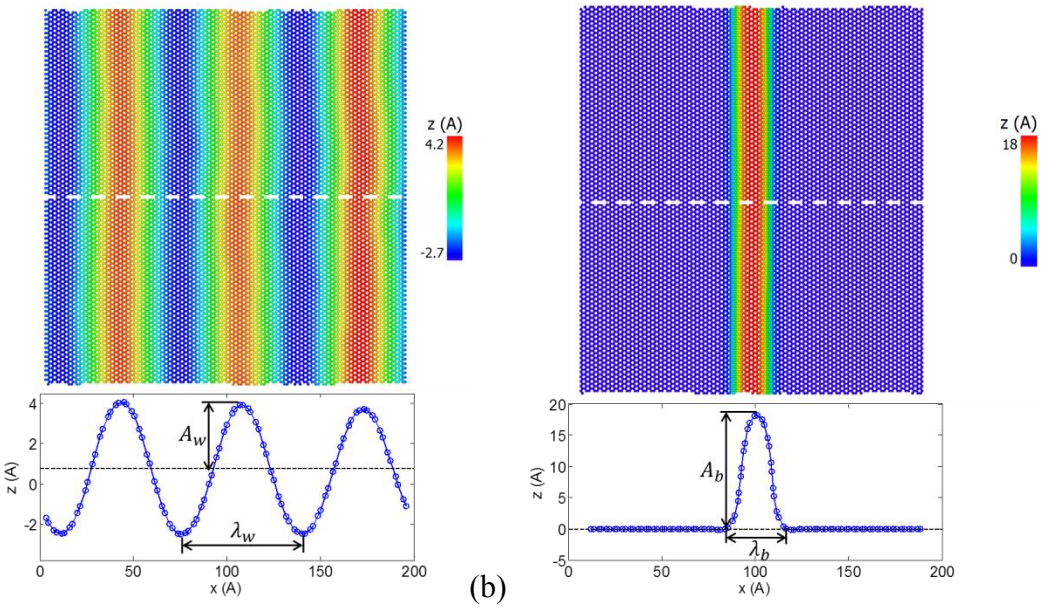

Figure 4.1: (a) Wrinkling profile of top view (Top) and cross-sectional view (Bottom) from MD simulation for a square graphene membrane with length and width around 20 nm under compressive strain $\varepsilon_0 = 0.025$ at $T = 1$ K and the interfacial properties $\Gamma_0 = 0.242$ J/m^2 and $h_0 = 6$ nm. (b) Buckling profile of top view (Top) and cross-sectional view (Bottom) from MD simulation for a square graphene membrane with length and width around 20 nm under compressive strain $\varepsilon_0 = 0.1$ at $T = 1$ K and the interfacial properties $\Gamma_0 = 0.242$ J/m^2 and $h_0 = 0.316$ nm. Cross-sectional profile is extracted by a line scan at the middle of graphene membrane.

In the limiting case when $\bar{E}h_0^2 >> D$, the critical strain in Eq. (4.5) approaches zero, and Eq. (4.7) becomes approximately

$$\left(\frac{\pi A_w}{\lambda_w}\right)^2 = \varepsilon_0 . \tag{4.8}$$

This is the case of an inextensible membrane where the in-plane strain is fully relaxed by wrinkling. As a result, Eq. (4.4) simply leads to a constant wrinkle wavelength, $\lambda_w = \lambda_{wc}$, and the wrinkle amplitude increases with the compressive strain as $A_w \sim \lambda_{wc}\varepsilon_0^{1/2}$.

4.2.2 Localized buckling

By following previous work on buckle delamination of elastic thin films [148, 149], we assume a cosine function for the buckling deflection (Figure 4.1b) as

$$w = \begin{cases} \frac{1}{2}A_b\left(1+\cos\frac{2\pi x}{\lambda_b}\right) & |x| \le \lambda_b/2 \\ 0 & \lambda_b/2 < |x| \le L/2 \end{cases}, \tag{4.9}$$

where λ_b and A_b are the width and height of the buckle, respectively, and L is the length of the graphene membrane. The width and height of the buckle can be related by assuming that the in-plane strain is fully relaxed by buckling [148, 149], namely

$$\frac{\pi^2 A_b^2}{4\lambda_b} = \Delta, \tag{4.10}$$

where $\Delta = \varepsilon_0 L$ is the applied compressive displacement. As a result, the in-plane strain energy is zero after buckling. On the other hand, both the potential energy of the adhesive interactions and the elastic bending energy of the graphene increase with compressive displacement. The total energy of the buckled graphene is approximately,

$$U_b \approx \frac{\pi^4 D A_b^2}{\lambda_b^3} - \Gamma_0\left(L-\lambda_b\right), \tag{4.11}$$

where the membrane in the buckled region ($|x| < \lambda_b/2$) is assumed to be fully delaminated from the substrate.

With the inextensibility condition in Eq. (4.10), the total energy U_b is minimized at an equilibrium buckle width

$$\frac{\lambda_b}{l_b} = 2\pi^{2/3}\left(\frac{\Delta}{l_b}\right)^{1/3}, \tag{4.12}$$

where $l_b = \sqrt{D/\Gamma_0}$ is a characteristic length as a result of the competition between bending and adhesion. Correspondingly, the buckle height is obtained as

$$\frac{A_b}{l_b} = 2^{3/2}\pi^{-2/3}\left(\frac{\Delta}{l_b}\right)^{2/3}. \tag{4.13}$$

It is noted that both the buckling width and height as predicted depend on the compressive displacement Δ. In contrast, the wrinkle wavelength and amplitude by Eqs. (4.4) and (4.7) depend on the compressive strain ε_0.

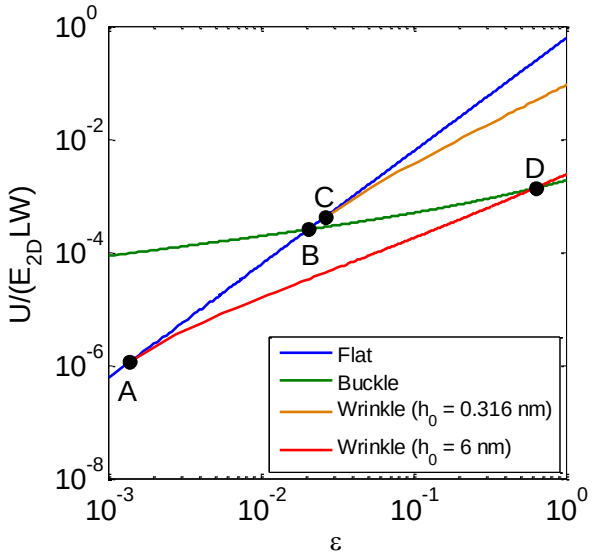

Figure 4.2: Potential energies for flat, wrinkled and buckled graphene at various strain level. The initial length of graphene is 20 nm and the adhesion energy Γ_0 is 0.242 J/m^2. The wrinkle energies are calculated for both h_0 = 0.316 nm and h_0 = 6 nm.

4.2.3 Buckling transitions

The wrinkling analysis predicts a critical strain for onset of sinusoidal wrinkling. To predict a critical strain for onset of local buckling, we may compare the potential energies before and after buckling. Before buckling, the graphene membrane is

compressed but remains flat with no delamination, for which the total energy (per unit area) is

$$U_{flat} \approx \frac{1}{2}\overline{E}\varepsilon_0^2 - \Gamma_0, \tag{4.14}$$

Upon buckling, with the equilibrium buckle width in Eq. (4.12) and height in Eq. (4.13), the total potential energy in Eq. (4.11) can be re-written as

$$U_b \approx \left(3\pi^{2/3} l_b^{2/3} \Delta^{1/3} L^{-1} - 1\right)\Gamma_0. \tag{4.15}$$

The potential energies as a function of compressive strain are plotted in Figure 4.2. From thermodynamics point of view, the state with lower potential energy would be more stable and likely to occur. Initially graphene membrane remains perfectly flat when subjected to relative small compression, as shown by the blue curve on the left of point A in Figure 4.2. At the critical buckling point B, the potential energy for the flat state and buckled state equal to each other, i.e., $U_{\text{buckle}} = U_{\text{flat}}$. Thus the critical buckling strain can be obtained by as

$$\varepsilon_{\text{cb}} = -\left(6\frac{\Gamma_0}{\overline{E}}\right)^{\frac{3}{5}}\left(\pi\frac{l_{\text{b}}}{L}\right)^{\frac{2}{5}}. \tag{4.16}$$

We notice that the whole buckling analysis is independent of h_0. However, since the critical compressive strain for wrinkling depends on the value of h_0, two scenarios become possible as compressive strain increases. For the case of small equilibrium separation (h_0 = 0.316 nm), the threshold for wrinkling is relative large, indicated by point C, which is larger than the critical buckling strain (point B). Thus transition from flat to buckling occurs at point B as a consequence of energy relaxation, and the buckling state will remain as compressive strain keeps increasing. Note that the sinusoidal wrinkling doesn't appear for small h_0 because it is energetically unpreferable. For the case of large equilibrium (h_0 = 6 nm), the critical wrinkling strain calculated by Eq. (4.5) becomes much lower, which now is located below critical buckling point B. The

wrinkling initiates at point A and keeps growing with strain until reached point D, where the wrinkling energy and buckling energy becomes equal. The transition from wrinkling to buckling occurs at point D, and similarly the critical strain this transition can be calculated implicitly by comparing the potential energy, i.e., $U_{\text{buckle}} = U_{\text{wrinkle}}$. Beyond point D, the buckling state is expected to remain since it has the lowest energy compared to other states.

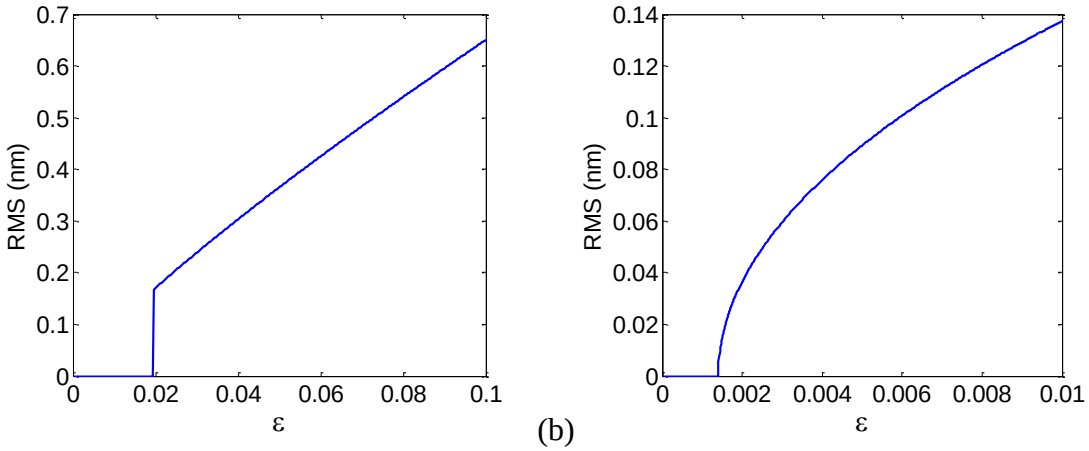

Figure 4.3: (a) RMS amplitude for $h_0 = 0.316$ nm indicating flat to buckling transition. (b) RMS amplitude for $h_0 = 6$ nm indicating flat to wrinkling transition.

The root mean square amplitude (RMS) is commonly measured in both experiments and simulations. For both wrinkling and buckling, the RMS can be calculated by the formula

$$A_{RMS} = \frac{1}{\Omega}\iint_{\Omega} w^2 d\Omega. \tag{4.17}$$

where Ω is the area of undeformed graphene, w is the assumed deflection for wrinkling and buckling in Eqs. (4.1) and (4.9). The RMS amplitudes are plotted in Figure 4.3. As discussed above, transition from planar state to buckling occurs for small value of h_0. The buckling transition leads to discontinuity in RMS amplitude as shown in Figure 4.3a,

resembling the first-order transition with critical transition strain depending on the graphene length. On the contrary, the wrinkling transition, occurs at relative large value of h_0, results in smoothly increase of RMS amplitude, resembling the second-order transition with critical transition strain depending on the equilibrium separation h_0 of the interface. For commonly used graphene/substrate interface, the h_0 value measured in experiment and predicted from simulation is typically smaller than 1 nm. Thus the wrinkling transition is rarely observed while the buckling transition is more common.

4.3 MOLECULAR DYNAMICS SIMULATIONS

The MD simulation set up is nearly identical as used in Chapter 3. In this chapter we use a rectangular-shaped graphene membrane with length L and width W in the ground state (T = 0 K) on top of a flat surface as a rigid substrate, and apply uniaxial compressive strain ε, to the graphene membrane by changing x in-plane dimension as $L' = L(1+\varepsilon)$. MD simulations are carried out at T = 1 K to compare with theoretical predictions, and then at T > 1 K to investigate the effect of temperature. The adhesion energy Γ_0 varies from 0.05 and 1.0 J/m^2 and the equilibrium separation h_0 varies from 0.3 nm to 1.0 nm unless specified otherwise.

When the compressive strain is beyond critical value, the graphene membrane buckles out of the plane as shown in Figure 4.1b. A nearly uniform buckle appears in the vertical direction, and the buckling height is several nanometers while the rippling amplitude from thermal fluctuation is negligible. To capture the buckling features of graphene, time-averaged RMS over the entire graphene membrane is calculated by Eq. (3.35). Buckling profiles are extracted by line scan in x direction at the middle of graphene membrane. Buckling height A_b is measured as the maximum deflection and

buckling width is taken as the projected length from buckled profile to ground state plane ($z = h_0$).

4.4 Results and Discussion

4.4.1 Buckling height and width

Based on the buckling analysis, the buckling characteristics depends the adhesion energy Γ_0 through characteristic length l_b and the length of graphene L through compressive displacement Δ, as shown in Eqs. (4.12) and (4.13). Thus we perform MD simulations for various graphene/substrate interfacial adhesions and various lengths of graphene, and measure the buckle height and width during continuous compressive loading. Here, we use $h_0 = 0.316$ nm for the equilibrium separation, which is predicted by DFT calculations for graphene on SiO_2 [82]. The length of graphene membrane L varies from 5 nm to 80 nm, as limited by the computational resource. The buckling amplitudes and widths for adhesion energy Γ_0 at the graphene/substrate interface and different length of graphene membrane are shown in Figure 4.4 and Figure 4.5. The buckling amplitude and width as a function of normalized compressive displacement Δ/l_b from MD simulation collapse into master curves, which are consistent with buckling analysis in Eqs. (4.12) and (4.13). The buckling analysis slightly overestimates the buckling heights as shown in Figure 4.4a and Figure 4.5a. The discrepancies between MD simulation and analytical results increase with the compression Δ/l_b. However, the buckling width initially increases with loading displacement Δ/l_b and then decreases after it reaches a peak, in contrast with the monotonically increasing buckling width from analytical prediction.

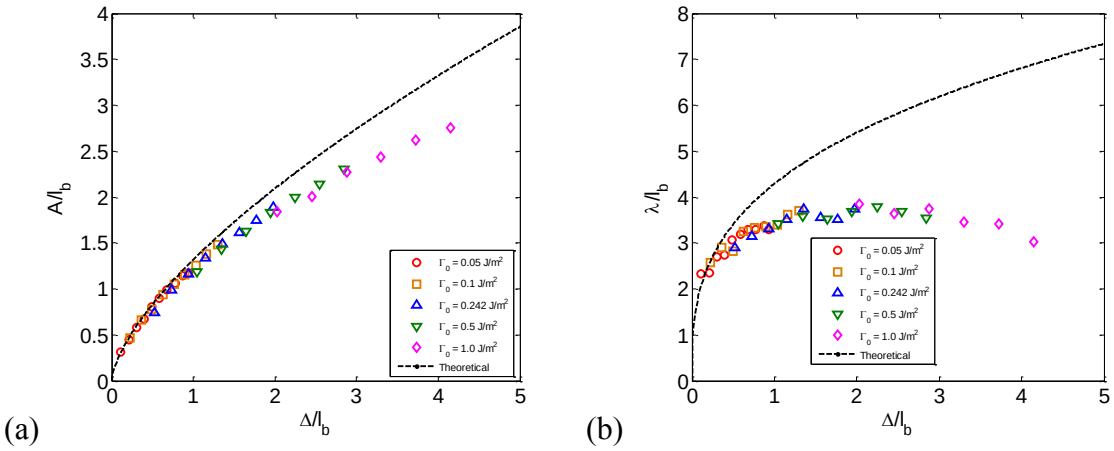

Figure 4.4: (a) Normalized buckle height and (b) normalized buckle width as a function of normalized compressive displacement Δ/l_b for different adhesion energy Γ_0 (l_b). Here we use $h_0 = 0.316$ nm, $L = 20$ nm and $W = 5$ nm. All symbols are from MD simulations and dashed lines by the buckling analysis.

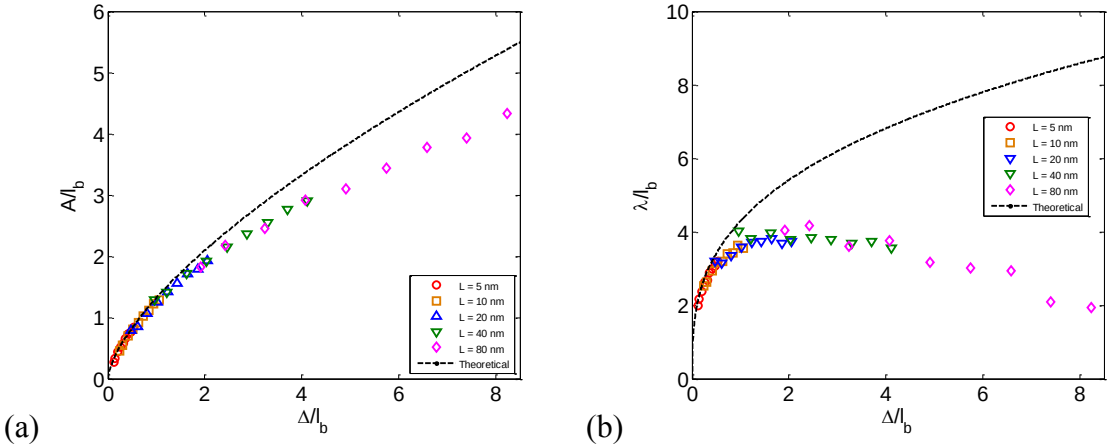

Figure 4.5: (a) Normalized buckle height and (b) normalized buckle width as a function of normalized compressive displacement Δ/l_b for different length of graphene membrane L. Here we use $h_0 = 0.316$ nm, $W = 5$ nm and $\Gamma_0 = 0.242$ J/m^2. All symbols are from MD simulations and dashed lines by buckling analysis.

We notice that the theoretical predictions only limit to small compression amplitude ($\Delta/l_b < 1$). The discrepancy for large Δ/l_b may come from the profile assumption in Eq. (4.9), which is only accurate for membrane under small compression Δ

and with large l_b. The characteristic length of l_b plays an important role in the prediction on the height and width of buckle. $l_b=(D/\Gamma_0)^{1/2}$ captures the competition between bending of the membrane and adhesion at the interface. For conventional thin membrane with adhesion energy of $\Gamma_0 \sim 2$ J/m^2 in macroscale, l_b is approximately 6×10^5 nm by assuming $E \sim 1$ GPa, $t \sim 20$ μm and $v = 0.3$. However, graphene is only one-atom-thickness membrane with very small bending rigidity (~1.4 eV), thus the characteristic length l_b is only 0.96 nm for the adhesion energy of $\Gamma_0 = 0.242$ J/m^2, nearly six orders lower than that of conventional membrane. The small characteristic length l_b of graphene, corresponds to $\Delta/l_b > 1$ for the same range of compression amplitude Δ as shown in Figure 4.4 and Figure 4.5, leads to the discrepancy between theoretical prediction and MD simulation. To validate this argument and further investigate the effect of l_b, we consider a much weak graphene/substrate interface with fictitiously small adhesion energy 2.42×10^{-3} J/m^2, corresponding to a characteristic length $l_b = 9.62$ nm, much larger than previous cases. A larger width of the buckle is expected for the much lower adhesion energy ($\Gamma_0 = 2.42\times10^{-3}$ J/m^2) at the interface, thus we perform MD simulation for a larger graphene membrane with length $L = 80$ nm to accommodate the buckle and eliminate the restriction of periodic boundary conditions. The buckle height and width from both theoretical prediction and MD simulation are shown in Figure 4.6a and Figure 4.6b. The theoretical predictions and MD results are in a good agreement for the same range of compression amplitude Δ. The buckle profile keeps the same cosine shape assumed in buckling analysis in Eq. (4.9) during entire compression process as shown in Figure 4.6c. This comparison further elucidates the discrepancy in Figure 4.4 and Figure 4.5 originates from the inaccurate cosine shape assumption, which is caused by the intrinsic low rigidity of monolayer graphene. Nevertheless, the theoretical buckling analysis can be applicable and have a good prediction for other 2D materials as well as

conventional membrane which have large bending rigidity and small interfacial adhesion energy.

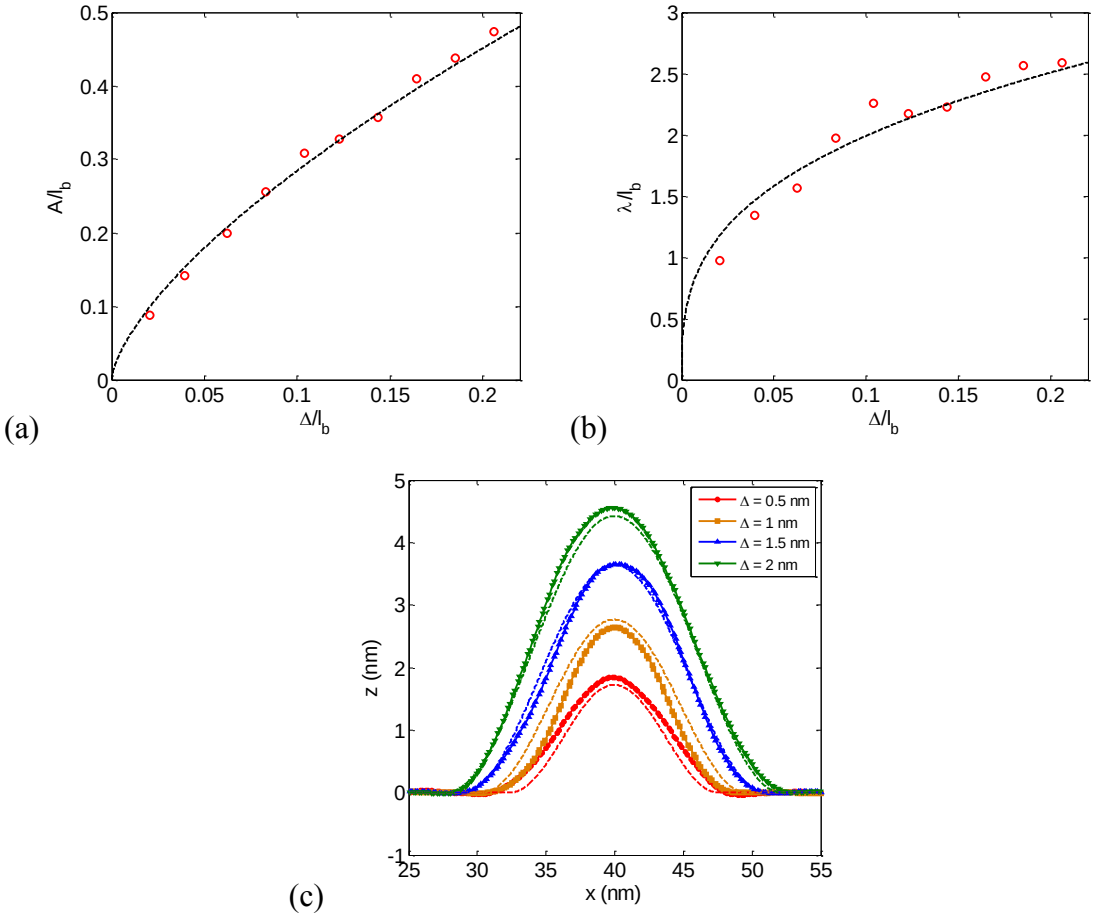

Figure 4.6: (a) Normalized buckle height and (b) normalized buckle width as a function of normalized compressive displacement Δ/l_b for $\Gamma_0 = 2.42 \times 10^{-3}$ J/m^2. (c) Buckling profiles of graphene membrane for different compressive displacement from MD simulation. Here we use $h_0 = 0.316$ nm, $L = 80$ nm and $W = 5$ nm. All symbols are from MD simulations and dashed lines by buckling analysis.

4.4.2 Folding

As the compression keeps increasing, the buckle gradually transits to a fold and the profile deviates the cosine-shape assumed in (4.9). We define the transition point from buckling to folding as the critical point where the width starts to decrease with

increasing compressive loading. To better demonstrate folding morphology, we further compress the buckled graphene membrane until the compressive displacement Δ reaches $L/2$. Profiles of graphene membrane under different compression are shown in Figure 4.7. For small compression (Δ < 2 nm), buckled profiles with approximate cosine shape are observed and both the amplitude and width increases with compressive loading. As the compression further increases, a fold configuration appears with increasing height but decreasing width with respect to the compressive displacement. The cosine function is no longer valid for folding shape while curvilinear coordinates needs to be established to describe it.

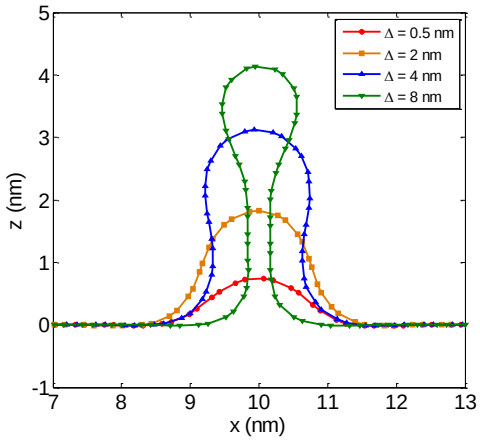

Figure 4.7: Profiles of graphene membrane under different compressive displacement from MD simulation with L = 10 nm, W = 5 nm, h_0 = 0.316 nm and adhesion energy Γ_0 = 0.242 J/m^2.

In our MD simulation, the van der Waals interaction between carbon and carbon atoms is included. As the compressive displacement continues increasing, the width of the fold decreases and the carbon atoms at the neck park of the fold approach each other. When the distance between carbon atoms decreases below a critical value, the neck of fold snaps in to form a flat double-layer structure with carbon atoms aligning on two parallel vertical planes. The average spacing between the double-layers of the fold is

around 0.336 nm, which is close to interlayer distance of double-layer graphene and graphite, and the distance between the layers in double-layer graphene is determined by the thickness of the dielectric spacer [150]. This fold shape of graphene membrane was observed in experiment and analyzed by linear elastic continuum model to derive the bending rigidities of 2D membranes [151].

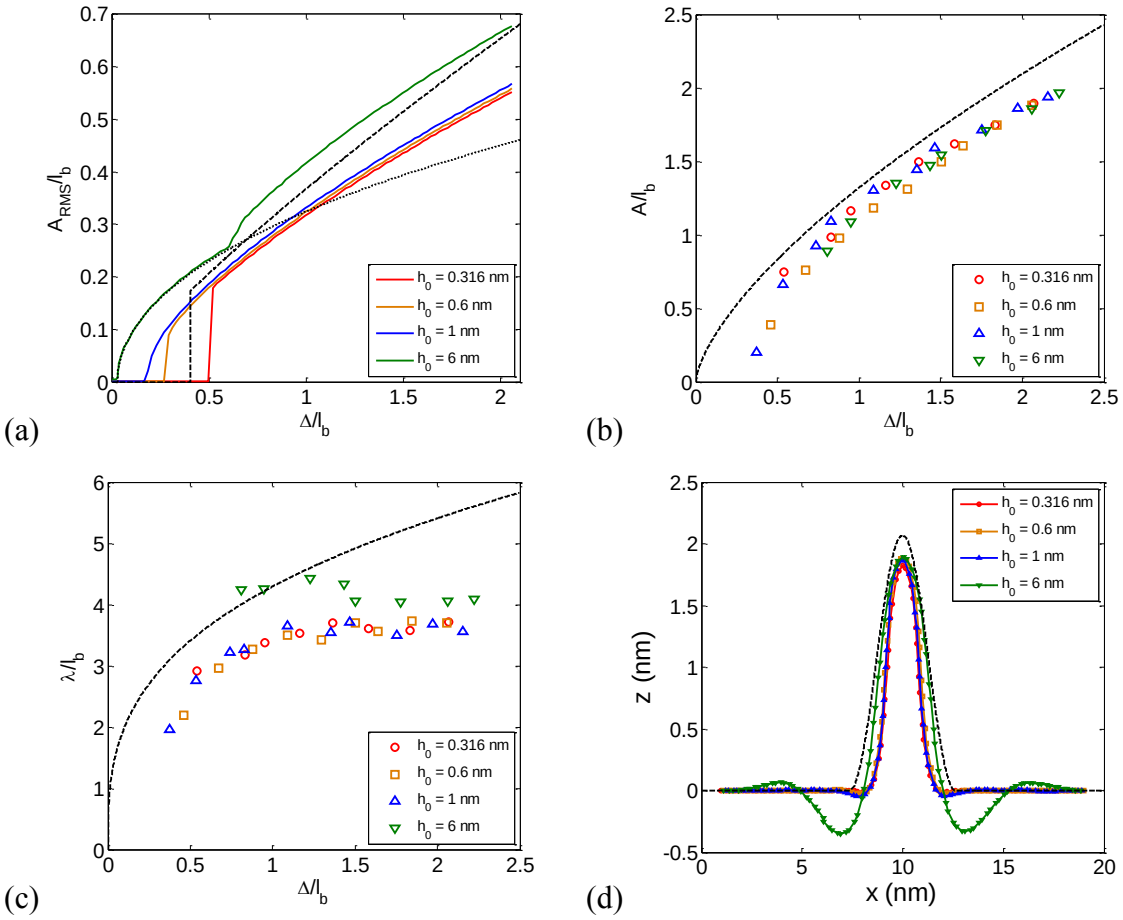

Figure 4.8: (a) Normalized RMS amplitude, (b) normalized buckle height and (c) normalized buckle width as a function of normalized compressive displacement Δ/l_b for different equilibrium separation h_0. (d) Buckling profiles of graphene membrane under the same compression $\Delta = 2$ nm for different equilibrium separation h_0. Here we use $L = 20$ nm, $W = 5$ nm and $\Gamma_0 = 0.242$ J/m^2. All symbols are from MD simulations and dashed lines by buckling analysis. The dotted line in (a) are calculated by wrinkling analysis.

4.4.3 Effect of h_0

As discussed in Section 4.3, buckling is a snap transition (first-order) with a critical strain depending on the length L of graphene membrane, while wrinkling is a second-order transition with a critical strain depending on the equilibrium separation h_0 of the interface. We vary the value of h_0 from 0.316 to 1.0 nm and also include the case of artificially large equilibrium separation (h_0 = 6 nm), where the wrinkling occurs first and then transits to buckling with gradual increasing compression. The normalized RMS amplitudes are nearly the same after buckling for h_0 < 1.0 nm, while the critical compressive displacement for buckling transition decreases as h_0 becomes larger, as shown in Figure 4.8a. We attribute this dependence to the thermal fluctuation in MD simulations since the buckling analysis is independent h_0 of as discussed in Section 4.2.2. As h_0 becomes larger, the stiffness of the van der Waals interaction at the interface becomes smaller. As a result, carbon atoms of graphene membrane become easier to deviate from their equilibrium positions due to thermal fluctuation, resulting in a smaller critical compressive displacement for the onset of buckling. For larger large equilibrium separation (h_0 = 6 nm), sinusoidal wrinkling occurs first and the RMS amplitude of wrinkling is in a good agreement with wrinkling analysis. The buckling heights and width for different h_0 are nearly the same as shown in Figure 4.8a and Figure 4.8b, except that the width for h_0 = 6 nm is higher than other cases and is nearly independent of compressive loading. It verifies that the characteristics after buckling are invariant with respect to equilibrium separation h_0 (h_0 <= 1 nm), in agreement with buckling analysis in Eqs. (4.12) and (4.13). The buckling analysis predicts higher RMS amplitude, buckling height and width compared to MD simulation, and we similarly attribute this discrepancy to the extreme small l_b value of graphene membrane on substrate. Finally, we take a closer look on the buckling profiles for different h_0 presented in Figure 4.8d. Profiles for

$h_0 < 1$ nm are nearly identical with a slight smaller amplitude and width compared with the cosine shape assume in buckling analysis in Eq. (4.9). In contrast for $h_0 = 6$ nm, the buckling profile has significant undulations beside the buckle, as a result of smaller stiffness and larger spacing of the graphene/substrate interface. The buckling height isn't affected by the undulation while the buckling width becomes slight larger compared with profiles with $h_0 < 1$ nm.

4.4.4 Effect of temperature

MD simulations involve temperature dependent dynamic effect, while analytical method only provides static solutions. Spontaneous rippling due to thermal fluctuations is observed in freestanding graphene [53] and substrate-supported graphene [152]. The effect of temperature dependent thermal rippling on regular wrinkling and buckling delamination of monolayer graphene is studied by performing MD simulation at three different temperatures, 1 K, 300 K and 1000 K, as shown in Figure 4.9. Since higher temperature leads to more significant thermal fluctuation or thermal rippling [53, 152], the RMD amplitude and the buckling height slight increase with temperature, and in a good agreement with buckling analysis at higher temperature ($T = 1000$ K). The buckling widths are scattered and lower than the theoretical prediction from buckling analysis due to extreme small l_b value of graphene membrane on substrate. The buckling profiles at various temperatures are presented in Figure 4.9d. A slight larger height and more significant thermal fluctuation beside the buckled part are observed for higher temperature. The in-plane stress is greatly relaxed after buckling, thus causing the buckling profiles insensitive to temperature. Buckling shapes are in close agreement except the analytical shape is slightly wider.

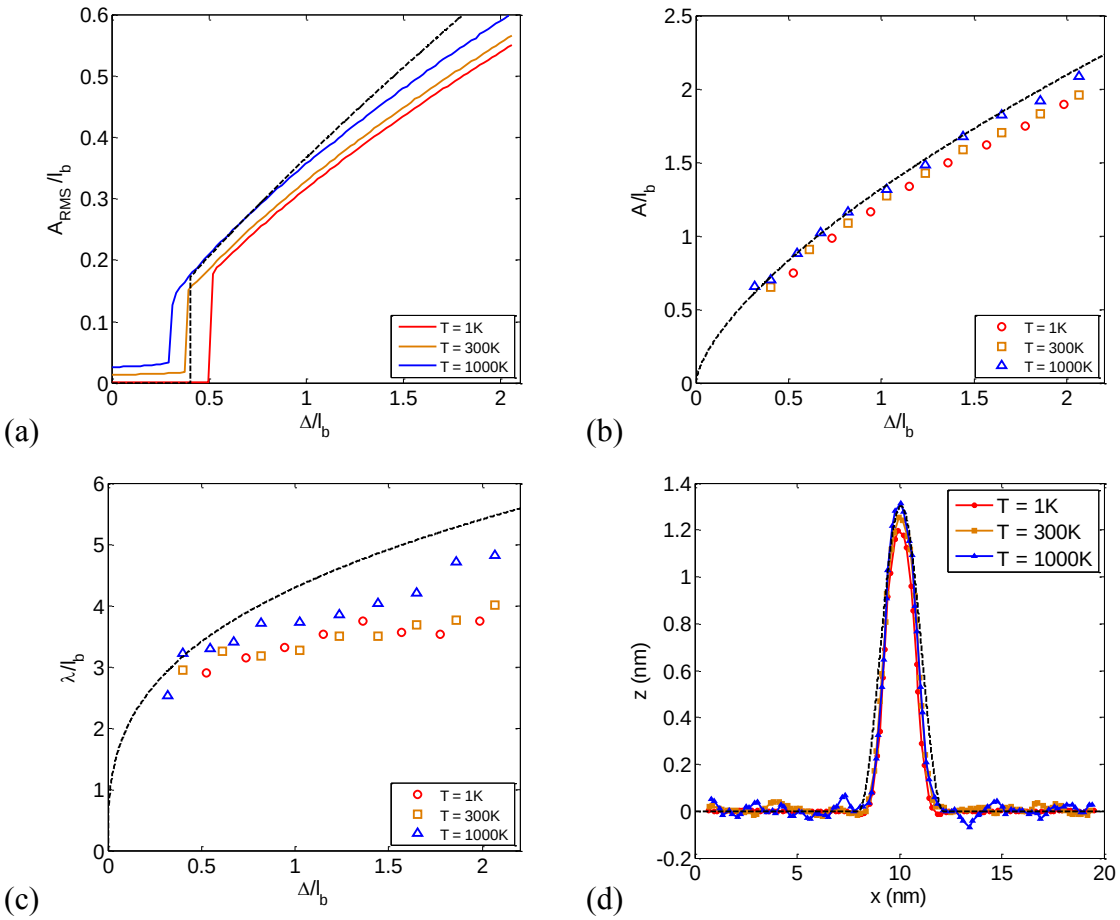

Figure 4.9: (a) Normalized RMS amplitude, (b) normalized buckle height and (c) normalized buckle width as a function of normalized compressive displacement Δ/l_b for different temperature T. (d) Buckling profiles of graphene membrane under the same compression $\Delta = 1$ nm for different temperature T. Here we use $L = 20$ nm, $W = 5$ nm, $h_0 = 0.316$ nm and $\Gamma_0 = 0.242$ J/m^2. All symbols are from MD simulations and dashed lines by buckling analysis.

Thermal fluctuation acts as large amplitude imperfection to trigger buckling between graphene and substrate, thus a relatively smaller compressive strain is needed for the onset of buckling at larger temperatures. The critical strain for different temperatures is plotted in Figure 4.10, together with the harmonic analysis similar to Figure 3.5d. Here we use plane strain modulus $\overline{E} = E_{2D}/\left(1-\nu^2\right)$ for uniaxial compression instead of

biaxial modulus used in Chapter 3. While the critical compressive strain for buckling both decreases with temperature, the harmonic analysis underestimates the critical strain at high temperature since the anharmonic effect is significant at high temperature. Moreover, the effective adhesion energy drops as temperature increases due to the entropic repulsion effect from thermal rippling (Figure 3.5b), leading to smaller compressive critical strain by the buckling analysis in Eq. (4.16), qualitatively interpreting the decrease of critical strain with temperature by MD simulation. In all, the critical compressive strain or displacement for the onset of buckling is determined by the stiffness of the interface (related to adhesion Γ_0 and equilibrium separation h_0) and thermal fluctuation of the membrane (related to the temperature T).

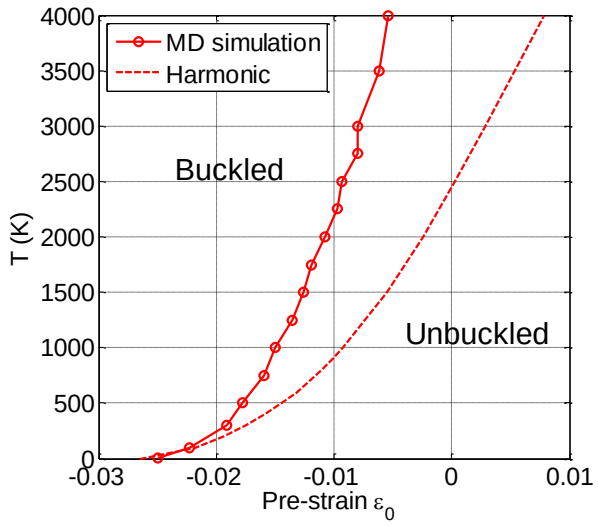

Figure 4.10: Critical pre-strain for the onset of buckling versus temperature T (a stability phase diagram) from both MD simulations and statistical harmonic analysis.

4.5 SUMMARY

In this chapter, we present a comprehensive study for monolayer graphene on substrate under uniaxial compressive strain, including analytical method and molecular dynamics simulation. Various instability morphologies are observed and the transitions between them are analyzed. Sinusoidal wrinkling only occurs for large equilibrium separation (h_0 > 1 nm), followed by localized buckling-delamination. Folding appears upon further compression, where the width decreases with compressive loading. The buckling analysis slightly overestimates the buckling height and width due to the low bending rigidity of graphene membrane compared with the adhesion energy at the graphene/substrate interface. The buckling characteristics are insensitive to the equilibrium separation (for h_0 < 1 nm) and the temperature, while the critical compression for the onset of buckling is affected by the stiffness of the interface and the thermal fluctuation of the membrane.

Chapter 5 Wet adhesion of graphene

5.1 INTRODUCTION

To date, most of the studies on adhesion of graphene have assumed dry adhesion of van der Waals type [82, 83, 153-155]. However, measurements of the adhesion energy of graphene are often performed in ambient conditions [27, 64, 65, 68, 73, 80], not in high vacuum. The results are likely influenced by the presence of water at the interfaces, depending on relative humidity of the environment. In the case of wet-transferred graphene [80, 156], both the graphene membrane and its substrate are directly exposed to liquid water during fabrication. Experiment reported ultra-long-range interactions between wet-transferred graphene and a silicon substrate [80], calling for further studies on other mechanisms of interfacial adhesion of graphene. Molecular dynamics (MD) simulations were conducted to investigate the separation process with a sequence of morphological transitions of water between graphene and a-SiO_2 substrate [87]. In this chapter we follow pervious work [87] to continue study the wet adhesion of graphene. We consider a relative simple system with a graphene monolayer on a highly hydrophilic fictitious substrate (such as amorphous silicon oxide), where a thin layer of water is sandwiched in between (see Figure 5.1a).

Graphene is generally considered to be hydrophobic, with a contact angle of ~90^o [157-161]. However, some other studies have found that the contact angle of water on graphene could vary over a wide range, depending on airborne contamination [162, 163], defects [158], roughness [164], and the substrate on which it has been deposited [165, 166]. In principle, the contact angle can be related to the interactions between graphene and water. Lee *et al.* [19] showed that water could diffuse between monolayer graphene and SiO_2 substrates under high humidity conditions. A double ice-like water layer was formed as a result of water diffusion, which is quite stable, even under ambient

conditions. Additional highly mobile and volatile liquid phase water can further diffuse between graphene and the ice-like layer on the SiO_2 substrate. In this chapter, we conduct molecular dynamics (MD) simulation to investigate the traction-separation relation as well as the separation process with a sequence of morphological transitions of water between graphene and a hydrophilic fictitious substrate. Approximate continuum analyses are developed to help understand the MD results. The effect of water contact angle of graphene and the thickness of water film are investigated. When the amount of water molecules is small, discrete layered structure of water is observed in MD simulations and the double-peak traction-separation behavior is studied for monolayer water. Section 5.2 presents the model and method for MD simulations, and the force fields are described in Section 5.3. A modified nucleation theory is proposed in Section 5.4 by taking into account the nonlinear elastic compressibility of liquid water and the water contact angle of graphene membrane. The full traction-separation relation and morphological evolution of water from cavitation to capillary bridging, together with a simple continuum model are provided in Section 5.5. The results are discussed in Section 5.6, followed by a summary in Section 5.7.

5.2 MOLECULAR DYNAMICS SIMULATION

We performed classical MD simulations using LAMMPS [135]. A square-shaped graphene membrane ($L \sim 10$ nm) was placed on top of a flat substrate surface, with water molecules in between. MD simulations were carried out in NVT ensemble with periodic boundary conditions at 300K, where the temperature was controlled by a Nose-Hoover thermostat. The integration time step was 1 fs. The in-plane dimension of the periodic box was set by the size of the graphene sheet ($L \sim 10$ nm), and the thickness of the

periodic box was 20 nm so as to keep periodic images in the thickness direction from interacting with each other. Here, we use $h_{GS} = 0.316$ nm for the equilibrium separation between graphene and substrate, which is predicted by DFT calculations for graphene on SiO_2 [82]. The substrate was modeled as a rigid surface placed at z^s = -0.316 nm so that the average position of the carbon atoms in the graphene would be around z = 0 if no water molecules are trapped in between. Initially, a number of water molecules were placed as a block between the substrate and the graphene sheet. Then, the system was relaxed for 1 ns under NVT to reach equilibrium. Figure 5.1a shows a snapshot of graphene membrane on wet substrate with 14580 water molecules. The equilibrium position of graphene during relaxation $\overline{z}_r^g$ is calculated by averaging all carbon atoms for the last 0.5 ns as described in Chapter 3. The thickness of water film t_w is calculated by subtracting the equilibrium average separation between graphene and substrate with the absence of water molecules from the one when water is present. Obviously, the thickness of water film depends on the number of water molecules (N) input in the simulation. For instance, the simulation with N = 14580 water molecules in Figure 5.1a corresponds to the thickness of 4.19 nm.

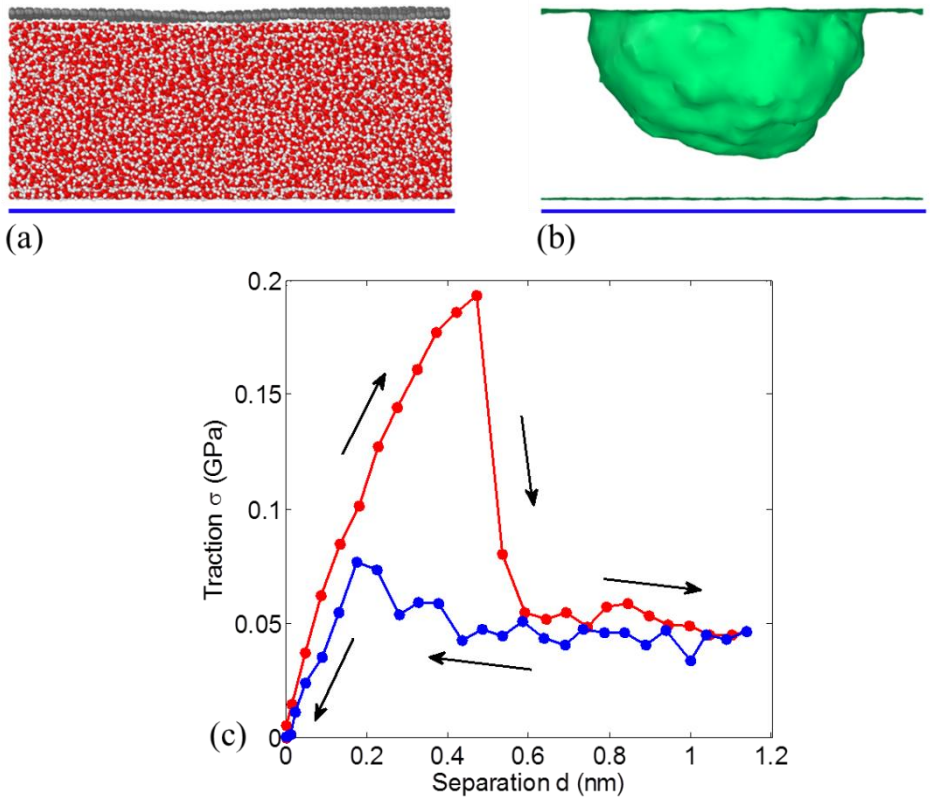

Figure 5.1: MD simulation of a graphene membrane on wet substrate with 14580 water molecules (t_w = 4.19 nm). The water contact angles are 60°and 5° for graphene and the substrate, respectively.(a) A side view snapshot after relaxation, showing the water molecules (oxygen in red and hydrogen in white) between graphene (carbon in gray) and the substrate surface (blue line). (b) Cavity surface at d = 1.12 nm, constructed by the alpha-shape method [167] with a virtual probe sphere of radius 0.4 nm using OVITO [168]. (c) Calculated traction separation relation, subjected to a loading−unloading cycle at T = 300 K.

Then, a fictitious planar indenter is placed beneath graphene membrane. The interaction force field between each carbon atom of graphene and the indenter is specified as (in the positive z direction)

$$f_i(z_i) = \begin{cases} K\left(z_i^g - z^p\right)^2 & z_i^g < z^p \\ 0 & z_i^g \geq z^p \end{cases}, \tag{5.1}$$

where the z_i^g is the position of each carbon atom in the z direction, z^p is the position of planar indenter and K is the specified force constant. In the current study, we choose $K = 10\ eV/A^3$ for all simulations to generate smooth separation process. To avoid continuous ramping loading, we displace the position of planar indenter stepwisely in a form of

$$z_p = \overline{z}_e^g + \Delta z^p \times \left\lfloor \frac{n_{total}}{n_{relax}} \right\rfloor, \tag{5.2}$$

where $\overline{z}_e^g$ is the equilibrium of graphene membrane at the end of relaxation, Δz^p is the increment distance of planar indenter between loading stages, n_{total} is the total running steps and n_{relax} is relax steps at each loading stage. The Δz^p and n_{relax} together determine the loading rate of planar indenter applied on the graphene membrane. We have tested that using different Δz^p and n_{relax} values while keeping identical loading rate yields very close traction-separation results. It is found that the critical strain and stress for cavitation depends on the loading rate while the stress–strain behavior before cavitation and during unloading remains unaffected by changing the relaxation time [169]. For consistency, we used $\Delta z^p = 0.01$ nm and $n_{relax} = 10000$(corresponds to a relaxation time $\tau_r = 0.01$ ns) in our current simulations. We keep moving the fictitious indenter as constant rate determined by Δz^p and $\mathrm{n_{relax}}$ until graphene is fully separated from the wet substrate. The equilibrium position of graphene during loading $\overline{z}_l^g$ is calculated by averaging all carbon atoms for n_{relax} steps. The separation d is defined as the difference between $\overline{z}_l^g$ and $\overline{z}_r^g$. At each loading stage, we assume equilibrium is reached during n_{relax} steps. Then the traction between graphene and wet substrate can be extracted from the reaction force acting on the fictitious indenter by a simple force balance. The total reaction force acting on the indenter is calculated as

$$F^p = \sum_{i=1}^{N} f_i^p \ . \tag{5.3}$$

Then the average traction at each loading stage is obtained as

$$\bar{\sigma}(d) = \frac{\left\langle F^p \right\rangle_t}{\Omega}, \tag{5.4}$$

where Ω is the area of undeformed graphene membrane.

As shown in Figure 5.1c, the traction is nearly zero after relaxation. As the displacement loading increases, the traction first increases and then drops abruptly. The initial stiffness is obtained from the slope of the traction-separation relation at small strain, which is 0.719 GPa/nm. As the separation increases, the tangent stiffness decreases, indicating a nonlinear traction-separation behavior of graphene/wet-substrate interface. The traction reaches a maximum of 193.2 MPa at d = 0.472 nm, after which the traction drops abruptly. It is found that the sudden traction drop is associated with onset of cavitation in the water film, which leads to a nearly spherical-cap cavity as shown in Fig. 1b. Hence, the MD simulation predicts the strength of graphene/wet-substrate interface to be around 193.2 MPa at 300 K. Subsequently, as the separation increases further, the cavity grows larger in size and the traction decreases slowly. Before the spherical-cap cavity reaches the boundary of simulation box, we reverse the movement of the fictitious indent to unload the system. Upon unloading by decreasing the separation d, the cavity shrinks and the traction increases. Eventually, the cavity disappears at a lower critical traction (~76.9 MPa), and further unloading follows the loading curve back to the initial state at zero strain. A hysteresis loop is thus observed in the traction-separation diagram after the loading/unloading cycle, indicating energy dissipation associated with the cavitation process.

5.3 FORCE FIELDS

This section presents the empirical force fields used in MD simulation. The second-generation reactive empirical bond-order (REBO) potential [38] was used for the carbon-carbon interactions in graphene as described in Chapter 3. A fictitious surface interacting with both graphene and water molecules was used to represent the rigid substrate [152]. As discussed in Section 3.3, the interaction between graphene and substrate is captured by Lennard-Jones potential. Here we use δ_{CS}= 0.368 nm so that h_{GS} = 0.316 nm, and ε_{CS}= 0.0376 *e*V so that the adhesion energy between graphene and substrate Γ_{GS} is 0.242 J/m^2. This interaction decays very fast with respect to the separation between graphene and substrate and become negligible when thickness of water film is greater than 1 nm.

5.3.1 Water model

Many different empirical potentials have been proposed for water, such as ST2 [170], SPC/E [171], TIP4P [172], TIP5P [173], TIP4P/2005 [174], and polarizable AMOEBA [175, 176] models. In this study we use the TIP4P/2005 model, which accurately describes the surface tension of water over the whole range of temperatures from the triple point to the critical temperature [177]. In the TIP4P/2005 model, each water molecule has four interaction sites, including a massless M-site located coplanar with the oxygen (O) and hydrogen (H) sites on the bisector of the H-O-H bond angle. The O-H bond length and the H-O-H bond angle are fixed as 0.9572 Å and 104.52°, respectively. The intermolecular pair potential has two contributions, a Lennard-Jones (LJ) term and an electrostatic part. The oxygen site carries no charge, but contributes to the LJ term:

$$U_{LJ} = 4E_{OO}\left[\left(\frac{L_{OO}}{r_{OO}}\right)^{12} - \left(\frac{L_{OO}}{r_{OO}}\right)^{6}\right], \tag{5.5}$$

where r_{OO} is the distance between the oxygen sites of two water molecules, $L_{OO} = 3.1589$ Å and $E_{OO} = 0.00803$ eV. The H and M sites are charged ($q_H = 0.5564\ e$ and $q_M = -2q_H = -1.1128\ e$), but do not contribute to the LJ term. The electrostatic part of the interaction potential between two water molecules is

$$U_e = \sum_{i,j(i\neq j)} \frac{k_e q_i q_j}{r_{ij}}, \tag{5.6}$$

where the summation is taken over all pairs of charged sites, r_{ij} is the distance between two charged sites, and k_e is the electrostatic constant. The total potential energy of the system is the sum of the pair potentials between all molecules. The cutoff distance is set to be 13 Å for both the LJ and electrostatic interactions. The electrostatic interactions are computed by using the particle-particle particle-mesh (PPPM) algorithm [178] as implemented in LAMMPS.

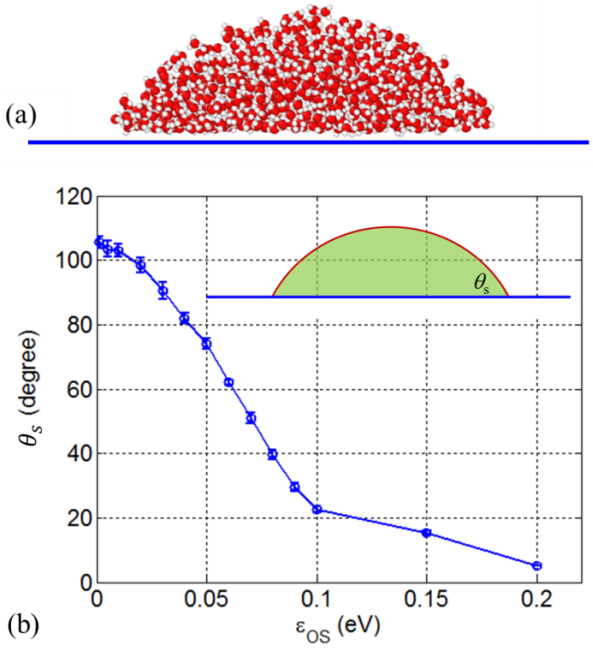

Figure 5.2: (a) A snapshot of a water droplet on a substrate surface with $N = 900$ and $\varepsilon_{OS} = 0.08$ eV, where the contact angle is around 40°. (b) Water contact angle of substrate as a function of ε_{OS} .

ε_{CO}(meV)	7.50	6.00	3.75	2.50
Contact angle(°)	30	60	90	100

Table 5.1: The ε_{CO} parameters and corresponding water contact angles for graphene used in the MD simulations in Chapter 5.

5.3.2 Interaction between water and substrate

The interactions between water molecules and the substrate surface were modeled similarly by a LJ potential function with two parameters (ε_{OS} and δ_{OS}) for the interactions between the oxygen atoms of water and the surface as

$$U_{WS} = \varepsilon_{OS}\left[\frac{2}{15}\left(\frac{\delta_{OS}}{r_{OS}}\right)^9 - \left(\frac{\delta_{OS}}{r_{OS}}\right)^3\right], \tag{5.7}$$

while the interactions between the hydrogen atoms of water and the surface were ignored. We also let $\delta_{OS} = 0.368$ nm so that the equilibrium separation between the water molecules and the surface is identical to the graphene/substrate interface. The parameter ε_{OS} can be varied to yield different water contact angles for the substrate. We performed MD simulations of a water droplet on the surface to determine the contact angle as a function of ε_{OS} (Figure 5.2). For this purpose, the water surface was re-constructed at 10 snapshots of the simulation by the alpha-shape method [167] with a virtual probe sphere of radius 0.4 nm using OVITO [168]. The surface area and the water volume were calculated, with which the averaged contact angle (θ_s) was calculated by assuming a spherical cap shape for the droplet. The effect of the number of water molecules on the contact angle was examined and found to be insignificant in the range from N = 100 to N

= 4500. Based on this result, we chose $\varepsilon_{OS} = 0.2\,\text{eV}$ to have a water contact angle of ~5^0, indicating a strong hydrophilic substrate.

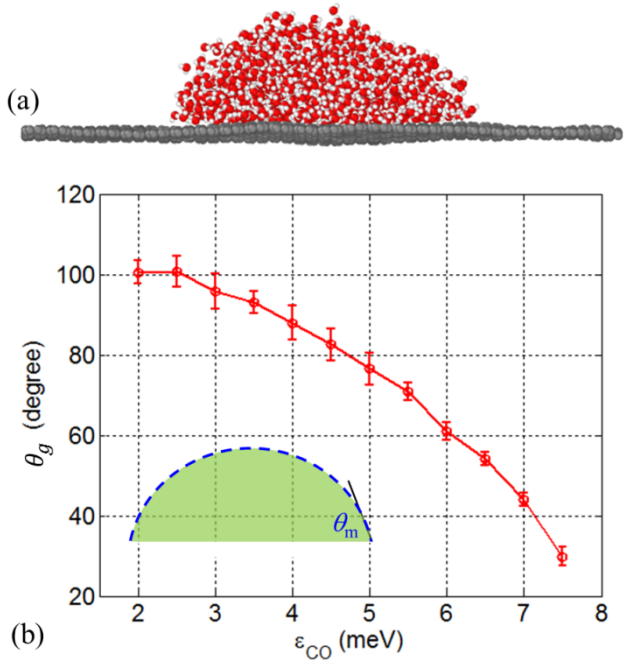

Figure 5.3: (a) A snapshot of a water droplet on graphene with $N = 1000$ and $\varepsilon_{CO} = 6.0$ meV, where the contact angle is around 60°. (b) Water contact angle of graphene as a function of ε_{CO} by MD simulations.

5.3.3 Interaction between water and graphene

Next, for the interactions between water and graphene, previous first-principle calculations [87, 179] have shown that the interactions between graphene and water are dominated by dispersion interactions. Werder *et al.* [180] calibrated a set of parameters for the interactions between the oxygen atoms of water and the carbon atoms of graphene using the LJ potential in its standard form:

$$U_{GW} = 4\varepsilon_{CO}\left[\left(\frac{\delta_{CO}}{r_{CO}}\right)^{12} - \left(\frac{\delta_{CO}}{r_{CO}}\right)^{6}\right], \tag{5.8}$$

With fitted parameters $\delta_{CO} = 0.319\text{nm}$ and $\varepsilon_{CO} = 4.07\text{meV}$, they obtained a water contact angle of around 90^0 for graphene [180, 181]. However, recent studies found that the water contact angle is around 60^0 for pristine graphene without air-borne contamination [182]. In order to study the effect of contact angle of graphene on wet adhesion, we use four ε_{CO} parameters which correspond to water contact angle from 30° to 100° for graphene as indicated in Table 5.1. Figure 5.3a shows a snapshot of a water droplet on graphene by MD simulations, and Figure 5.3b shows the water contact angle as a function of ε_{CO} based on the MD simulations.

5.4 MODIFIED NUCLEATION THEORY

From previous study [87], cavitation was observed inside liquid water while separating graphene from wet substrate. Motivated by the study in [169], we propose a modified nucleation theory to predict cavitation and traction-separation relation. In this chapter, we consider separating graphene membrane from wet substrate under displacement control, i.e., by specifying the position of fictitious indenter in MD simulation. In particular, we take into account the finite compressibility of liquid water under volume-controlled condition (instead of pressure control). In this way, the separation process is stabilized, which allows the prediction of traction-separation relation after cavitation as well as the critical cavitation point. The initial volume of the liquid water V_0 in its stable phase between graphene membrane and substrate at $T = 300$ K is $L^2 t_w$. Stretch the water volume to $V = L^2(t_w + d)$ by displacing the graphene membrane away from wet substrate under isothermal condition. Assuming a cavity with a spherical cap shape of radius R in water ($R = 0$ if no cavity) and θ_g for

water contact angle of graphene membrane as shown in Figure 5.4, the area of cavity surface and the volume of the cavity can be calculated as

$$S_c = 2\pi R^2 \left(1+\cos\theta_g\right), \tag{5.9}$$

and

$$V_c = \frac{1}{3}\pi R^3 \left(2+3\cos\theta_g - \cos^3\theta_g\right). \tag{5.10}$$

The free energy of the system can be written as

$$\Phi = V_0 U_L\left(\varepsilon\right) + \Delta\gamma - V_c p_0, \tag{5.11}$$

where $U_L(\varepsilon)$ is the elastic strain energy density of the liquid as a function of the volumetric strain ε, $\Delta\gamma$ is the change of adhesion energy per unit area to form a spherical-cap cavity and p_0 is the equilibrium vapor pressure in the cavity. We only keep the first two terms in Eq. (5.11) by assuming the vapor pressure is negligibly small compared to the tension inside water. The stress-strain relation for water can be written as

$$\sigma = K_1\varepsilon + K_2\varepsilon^2, \tag{5.12}$$

where $K_1 = 2.09\,\text{GPa}$ is the linear bulk modulus and $K_2 = -4.62\,\text{GPa}$ is the second-order modulus for the nonlinear behavior at relatively large strains T = 300 K [169]. Since liquid water spreads out the entire simulation box and no cavity penetration during the entire separation process, the hydrostatic tension (σ in Eq. (5.12)) inside water equals the traction for the graphene/wet-substrate system. By integrating Eq. (5.12) with respect to the strain, we obtain the strain energy density function as

$$U_L\left(\varepsilon\right) = \frac{1}{2}K_1\varepsilon^2 + \frac{1}{3}K_2\varepsilon^3, \tag{5.13}$$

Let $\varepsilon_V = V/V_0 - 1 = d/t_w$ be the nominal strain. With a spherical-cap cavity of radius R and contact angle θ_g in V, the volume of liquid water is $V - V_c$ and hence the volumetric strain in the liquid is

$$\varepsilon = \frac{V - V_c - V_0}{V_0} = \frac{d}{t_w} - \frac{V_c}{V_0}. \tag{5.14}$$

For a spherical-cap cavity, the Young–Dupré equation [165, 183] leads to

$$\gamma_w \cos\theta_g = \gamma_g - \gamma_{gw}, \tag{5.15}$$

where γ_w, γ_g, and γ_{gw} are the surface energy for water, graphene and graphene/water interface, respectively. Then the change of adhesion energy per unit area to form a spherical-cap cavity can be written as

$$\Delta\gamma = \gamma_w S_c + \left(\gamma_g - \gamma_{gw}\right) A_c, \tag{5.16}$$

where

$$A_c = \pi R^2 \sin^2\theta_g, \tag{5.17}$$

is the projected area of the cavity onto graphene membrane. Plug Eqs. (5.15) and (5.17) into (5.16), we obtain

$$\Delta\gamma = \gamma_w \pi R^2 \left[2 + 3\cos\left(\theta_g\right) - \cos^3\left(\theta_g\right)\right]. \tag{5.18}$$

Substituting Eqs. (5.13), (5.14) and (5.18) into Eq. (5.11), we obtain

$$\Phi = V_0 U_L\left(\varepsilon_V\right) + \Delta\Phi\left(R, \varepsilon_V\right), \tag{5.19}$$

where

$$\begin{aligned}\Delta\Phi\left(R; d, t_w\right) = \eta\pi R^2\gamma\Bigg[1 - \frac{1}{3}\left(\frac{d}{t_w} + \frac{K_2 d^2}{K_1 t_w^2}\right)\frac{R}{l} \\ + \frac{\eta\pi l^3}{18L^2 t_w}\left(1 + \frac{2K_2 d}{K_1 t_w}\right)\left(\frac{R}{l}\right)^4 - \frac{\eta^2\pi^2 l^6 K_2}{81L^4 t_w^2 K_1}\left(\frac{R}{l}\right)^7\Bigg],\end{aligned} \tag{5.20}$$

with a length scale $l = \gamma / K_1$ and a shape factor $\eta = 2 + 3\cos\theta_g - \cos^3\theta_g$ for spherical-cap cavity. The first term on the right-hand side of Eq. (5.19) gives the free energy without cavitation, while the second term is the change of free energy with cavitation in the same total volume of water. It is noted that the liquid water outside the cavity is assumed to be in a state of constant pressure for static equilibrium (i.e., no

viscous flow), whereas the pressure inside the cavity is different and the pressure difference is balanced by the surface tension.

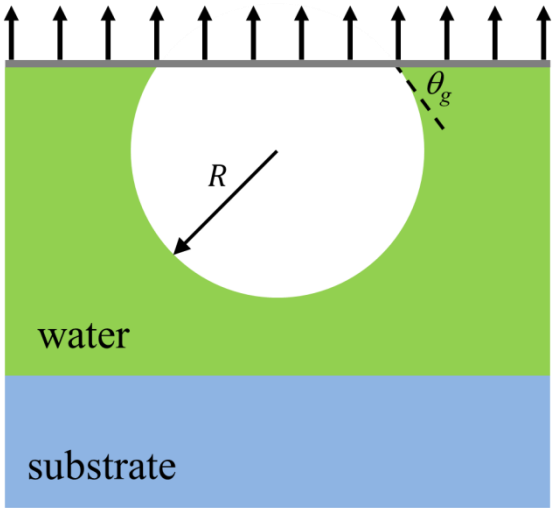

Figure 5.4: A schematic illustration for a cavity with a spherical cap shape in water without penetrating the substrate. The radius of the cavity is *R* and the water contact angle of graphene is θ_g.

Consider a graphene/wet-substrate interface with the thickness of water film $t_w = 4.19$ nm and contact angle of graphene $\theta_g = 60°$ at *T* = 300 K (same as the MD simulation in Figure 5.1). Stretch graphene away from the substrate to a separation *d*, the change of free energy in Eq. (5.20), normalized by $\eta\pi l^2\gamma$, is plotted as a function of the dimensionless cavity size R/l in Figure 5.5b. Here, we take $\gamma = 0.0693$ N/m as the surface tension of water at 300 K as predicted by the TIP4P/2005 model [177], along with the bulk moduli for water in Eq. (5.12), $K_1 = 2.09$ GPa and $K_2 = -4.62$ GPa; the vapor pressure (p_0) is negligible and thus ignored hereafter. When the separation is small ($d < 0.323$ nm), the free energy function has a single minimum at $R = 0$, and thus the liquid water is uniformly stretched without any cavity when separating graphene membrane away from the substrate. When the separation exceeds a threshold value

($\sim 0.323\,\text{nm}$), a local minimum of the free energy function appears at a finite cavity radius ($R > 0$). The free energy at the local minimum decreases with increasing separation. When the nominal strain exceeds a critical value ($\sim 0.376\,\text{nm}$), the free energy at the second minimum ($R > 0$) becomes lower than the free energy at the first minimum ($R = 0$). As a result, the uniformly stretched liquid water becomes metastable with respect to formation of a cavity, whereas the state with a finite cavity ($R > 0$) is stable under displacement control for graphene membrane. Therefore, by displacement control loading, cavitation in water is predicted as a first-order phase transition from the homogeneous liquid phase (stretched but no cavity) to the cavitated state with coexisting liquid and vapor phases within the volume.

The critical separation for cavitation can be predicted by setting the free energy values at the two minima to be equal. First, the radius of cavity is obtained as a function of separation (Figure 5.5c) by setting $\partial\Phi/\partial R = 0$ and $\partial^2\Phi/\partial R^2 > 0$ for the energy minimum. It can be shown that the cavity radius thus obtained satisfies the Young-Laplace equation as expected, namely

$$R(d) = \frac{2\gamma}{\sigma}, \tag{5.21}$$

where σ is the hydrostatic tension in liquid water (after cavitation) and can be obtained from Eq. (5.12) with the strain in Eq. (5.14). Next, by inserting $R(d)$ into Eq. (5.20) and setting $\Delta\Phi = 0$, we obtain an equation that can be solved to predict the critical strain for cavitation. As shown in Figure 5.5c, a discontinuous transition (from point A to point B) is predicted at the critical separation ($d \sim 0.376\,\text{nm}$), whereas the radius for the metastable cavity is obtained before the critical strain ($0.323\,\text{nm} < \varepsilon < 0.376\,\text{nm}$). Also shown in Figure 5.5c is an unstable branch (dashed line) corresponding to the maximum

free energy between the two energy minima in Figure 5.5b, which may be considered as the critical cavity radius ($R = R_c$) under the displacement control separation.

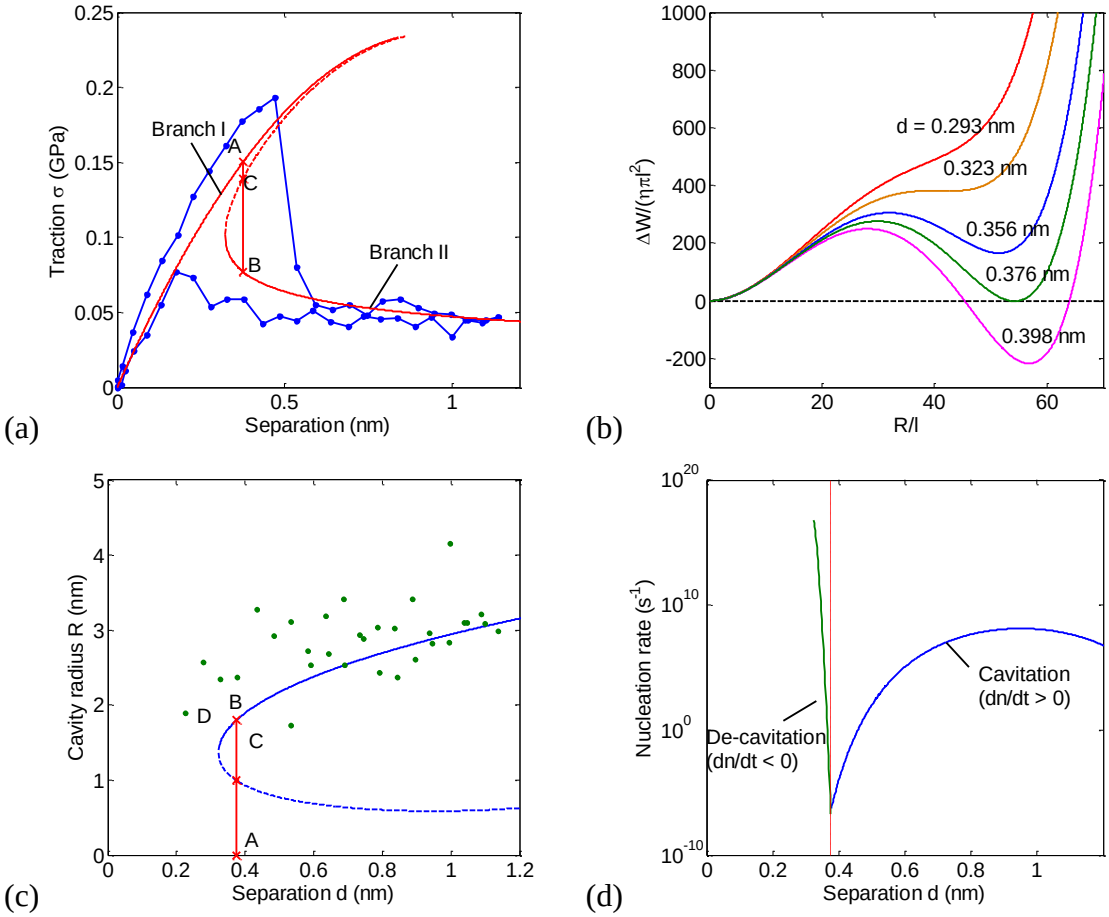

Figure 5.5: Prediction of traction-separation relation and cavitation by a modified nucleation theory: (a) Traction-separation relation diagram, in comparison with MD simulation (filled symbols). (b) Free energy function under different separation d. (c) Cavity radius as a function of separation, in comparison with MD simulation (filled symbols). (d) Nucleation rate for cavitation and de-cavitation. The dashed lines in (a) and (c) are the unstable branches. The vertical lines in (a) and (c) indicate the transition (from A to B) at the critical strain.

At the critical separation ($d_c \sim 0.376\,\text{nm}$), the traction changes abruptly before and after cavitation (from A to B in Figure 5.5a). Before cavitation, the hydrostatic stress

can be obtained directly from Eq. (5.12) with $\varepsilon = \frac{d_c}{t_w}$. This gives a critical stress of 150 MPa, slightly lower than that from the MD simulation. After cavitation, the volumetric strain in liquid is less than the nominal strain as given in Eq. (5.14), with which the traction can be calculated. Alternatively, the stress after cavitation can also be calculated by Eq. (5.21).

As shown in Figure 5.5a, the traction-separation diagram consists of two branches. Before cavitation (branch I), the traction is higher in MD simulation compared with stress-strain relation for bulk water in Eq. (5.12). Therefore, the elastic behavior of the water film between graphene and substrate is stiffened by the graphene/water and water/substrate interfaces. There is a hysteresis during unloading for branch I, indicating the stiffening effect is non-recoverable after cavity appears at the graphene/water interface. After cavitation (branch II), the stress calculated by the modified nucleation theory compares closely with the MD results. In addition, an unstable branch (dashed line) is shown in between, corresponding to the critical cavity radius (dashed line in Figure 5.5c). The unstable branch connects with branch II at a threshold separation ($\sim 0.323\,\text{nm}$) with infinite slope and approaches branch I asymptotically at increasingly large separation. With Eq. (5.21), the cavity radius in the MD simulation can be estimated by the measured traction. As shown in Figure 5.5c, the estimated radius agrees with the prediction reasonably well despite the fluctuation.

Furthermore, we note that in the MD simulation cavitation occurs at a strain greater than the predicted critical strain and disappears at a smaller strain during unloading. This may be qualitatively understood by a kinetic theory of nucleation [184]. Under constant volume condition for liquid water, the free energy function has two local

minima when the separation is greater than a threshold value (~ 0.323 nm) as shown in Figure 5.5b. In this case, the net rate of cavity formation can be written as:

$$\frac{dn}{dt} = \Gamma\left[\exp\left(-\frac{\Delta\Phi_{\max}}{k_B T}\right) - \exp\left(-\frac{\Delta\Phi_{\max} - \Delta\Phi_{\min}}{k_B T}\right)\right], \tag{5.22}$$

where $\Delta\Phi_{\max}$ is the energy difference between the homogeneous state ($R = 0$) and the state with the locally maximum free energy ($R = R_c$) and $\Delta\Phi_{\min}$ is the energy difference between the two energy minima. Thus, $\Delta\Phi_{\max}$ is the energy barrier to form a cavity and $\Delta\Phi_{\max} - \Delta\Phi_{\min}$ is the energy barrier for the cavity to disappear, both varying with the separation as shown in Figure 5.5b. The kinetic pre-factor Γ is not known precisely. Nevertheless, we plot the nucleation rate as a function of the separation in Fig. Figure 5.5d by taking $\Gamma = Nk_B T / h$, where N is the number of water molecules in the MD simulation (N = 14580). At the critical separation ($d_c \sim 0.376$ nm), the net nucleation rate is zero. When $d < d_c$, $\Delta\Phi_{\min} > 0$ and the nucleation rate is negative. On the other hand, when $\varepsilon > \varepsilon_c$, $\Delta\Phi_{\min} < 0$ and the nucleation rate is positive. For cavitation to occur within a finite time, a positive nucleation rate is required and hence the cavitation separation observed in the MD simulation is larger than the critical separation. Similarly, during unloading, the nucleation rate must be negative for the cavity to disappear and hence the de-cavitation separation is lower than the critical separation. Quantitatively, however, the nucleation rate by Eq. (5.22) is too low for a cavity to form within the relaxation time (0.01 ns) at each strain level, possibly due to the rough estimate of the pre-factor Γ. For unloading, the MD simulation shows that the cavity remains at separation levels below the threshold (~ 0.323 nm), which may suggest that the relaxation time was too short for the cavity to disappear. However, the negative nucleation rate by Eq. (5.22) for $d < d_c$ is very high in magnitude and thus the relaxation time should be sufficient. Therefore, the kinetic theory of nucleation, while

qualitatively consistent with the MD simulation, is not quantitatively accurate in predicting the cavitation/de-cavitation separations. An alternative approach to account for the rate effect may be developed by considering the transient evolution of the cavity with viscous flow of the liquid water, which is left for future studies.

5.5 FULL SEPARATION

We further increases the displacement of graphene membrane until it was fully separated from the substrate. Three stages of the traction-separation relations are observed and analyzed by a simple continuum model, similar to previous work [87]. The traction-separation relation obtained from MD simulation and continuum model is shown in Figure 5.6. The traction – separation relations and the associated morphological evolution of water can be divided into four stages: (I) increasing traction with continuous water film, (II) decreasing traction with interfacial cavitation, (III) decreasing traction with parallel ridge capillary bridging and (IV) island capillary bridging. The first stage is already discussed in Section 5.4 and the traction-separation relation can be obtained from the constitutive law of water by Eq. (5.12). For other three stages, we have the volume relation for water

$$L^2\left(t_w+d\right)-V_c^i=L^2t_w\left(1+\varepsilon\right), \tag{5.23}$$

where V_c^i is the volume of cavity in *i*-th stage. The left-hand side calculates the current volume of water by subtracting the volume of cavity from the total volume beneath graphene membrane, while the right-hand side calculates the volume of water through the volumetric strain ε, which is related to the stress in water by Eq. (5.12). For each stage, distinct geometric shapes are assumed for the cavity, leadings to different formulas for V_c^i; the relation between the stress in water and the surface tension of water can also be

retrieved distinctly by a simple force balance. In the following we discuss the last three stages in detail with associated continuum analyses.

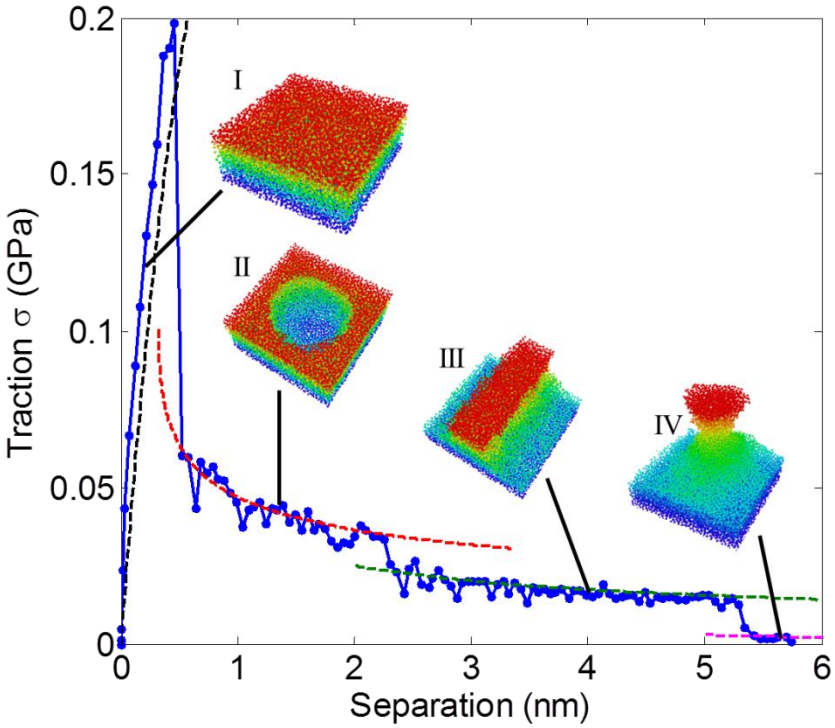

Figure 5.6: Full traction separation relation from both MD simulation and continuum model. The initial thickness of water film t_w is 4.19 nm and the water contact angle of graphene membrane θ_g is 60°.

5.5.1 Spherical-cap cavitation

As discussed in Section 5.4, the radius of the spherical-cap cavity can be related to the surface tension of water and the traction by force balance in Eq. (5.21). By taking the volume for the cavity V_c^{II} from Eq. (5.10) and plug into Eq. (5.23), the traction-separation relation at this water cavitation stage can be written as

$$d = \frac{8\pi\eta\gamma^3}{3L^2\sigma^3} - t_w\left(\frac{K_1}{2K_2} + \sqrt{\frac{K_1^2}{4K_2^2} + \frac{\sigma}{K_2}}\right), \tag{5.24}$$

plotted as red dashed line in Figure 5.6. It is noted that this traction-separation relation is exactly same as the one derived in Section 5.4. We note that first term, without taking into account the volume change of water and the thermodynamics of evaporation/condensation [185], has the simple scaling, $d \sim \sigma^{-3}$.

The lower bound of separation for Stage II is the critical separation ($d_l^{II} = 0.376$ nm), and the initial radius of the cavity obtained from Figure 5.5c is around 1.80 nm, which defines a minimum thickness for the water film with a hemispherical cavity. The growth of a spherical-cap cavity is limited by the size of the periodic box in the MD simulations, i.e., $R \le L/2$. When $R = L/2$, the neighboring cavities come into contact and coalesce, entering the next stage. The transition however often occurs when the neighboring cavities are sufficiently close but before contacting. Apparently, the size of the periodic box is arbitrarily set in the MD simulations, with no physical significance. A more realistic scenario may be that multiple cavities are nucleated over a large area and they grow independently until coalescence. The phenomenon is thus more complicated, beyond the scope of the present study. By plugging it and Eq. (5.21) into Eq. (5.24), we obtain the upper bound for separation in Stage II as

$$d_u^{II} = \frac{\pi \eta L}{24} - t_w \left(\frac{K_1}{2K_2} + \sqrt{\frac{K_1^2}{4K_2^2} + \frac{4\gamma}{K_2 L}} \right), \tag{5.25}$$

which is around 4.475 nm. However, we notice that the cavity already penetrate the substrate before the cavity coalesces with its periodic neighbors, when the assumption of spherical-cap shape of the cavity no long holds. Thus the separation for the transition to the next stage is lower than the upper bound d_u^{II}. Spherical-cap cavity is observed in the MD simulation when the separation is around 0.5 to 2.5 nm, as shown in Figure 5.6.

5.5.2 Parallel ridge capillary bridging

Cavitation growth in Stage II eventually leads to coalescence of neighboring cavities and the formation of capillary bridges. As shown in Figure 5.6, we see parallel ridges form on top of a continuous water layer covering the substrate surface. It is possible to study the capillary bridging by numerical simulations based on continuum models [186, 187]. In the present study, we consider simple models by assuming geometric shapes for parallel water ridges.

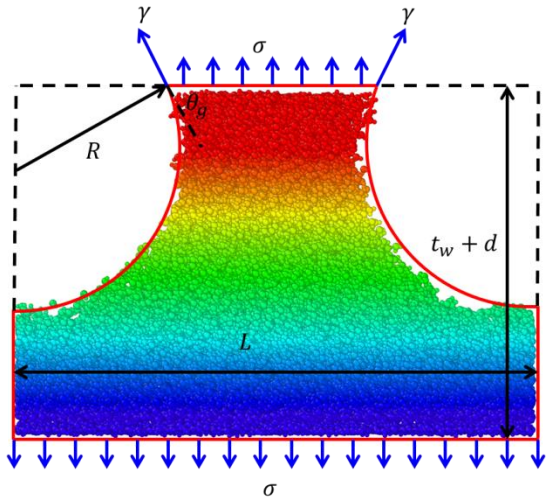

Figure 5.7: Cross section of a water bridging between graphene and substrate, comparing the continuum model (red lines) with MD simulation (t_w = 4.19 nm, θ_g = 60° and σ = 24.2 MPa).

The water bridging morphology in Stage III can be described as parallel ridges on top of a blanket layer of water. Figure 5.7 shows a cross-sectional view, where the side faces of the water ridge are approximately cylindrical with a radius R and the contact angle of θ_g on the ridge top. The force balance requires that

$$R = \frac{\gamma}{\sigma}, \tag{5.26}$$

With $\sigma = 24.2$ MPa, $\theta_g = 60°$ and $L = 10$ nm in Figure 5.7, the radius of the cylindrical side surface can be determined by Eq. (5.26), giving $R = 2.86$ nm. The volume of the cavity can be calculated by a simple geometric analysis as

$$V_c^{III} = \left(\pi - \theta + \sin\theta\cos\theta\right) LR^2 . \tag{5.27}$$

Again, by plugging Eq. (5.26) and Eq. (5.26) into Eq. (5.23), the separation is obtained as a function of the traction as

$$d = \frac{\left(\pi - \theta + \sin\theta\cos\theta\right)\gamma^2}{L\sigma^2} - t_w\left(\frac{K_1}{2K_2} + \sqrt{\frac{K_1^2}{4K_2^2} + \frac{\sigma}{K_2}}\right), \tag{5.28}$$

plotted as green dashed line in Figure 5.6. As the separation d increases, the first term, without considering the volume change of water, decreases with a scaling relation, $d \sim \sigma^{-2}$; note that this scaling is different from that in Eq. (5.24) for cavitation growth in Stage II. Eventually, when $R = L/2$, the narrowest part of the ridge shrinks to a line. By taking $R = L/2$ into Eq. (5.26) and Eq. (5.28), the upper limit for the separation is calculated as

$$d_u^{III} = \frac{\left(\pi - \theta + \sin\theta\cos\theta\right)L}{4} - t_w\left(\frac{K_1}{2K_2} + \sqrt{\frac{K_1^2}{4K_2^2} + \frac{4\gamma}{K_2 L}}\right), \tag{5.29}$$

giving $d_u^{III} = 6.38$ nm. Parallel ridge is observed in the MD simulation when the separation is around 2.5 to 5.5 nm. The parallel water ridges become unstable before the smallest width of water ridge shrinks to zero, transitioning to water islands as shown in Figure 5.6. This transition is similar to break-up of a liquid jet as a result of the Rayleigh instability [188, 189], but with additional complexity due to the water-graphene interactions in the present case.

5.5.3 Island capillary bridging

In the last stage of the separation process, the parallel water ridges break up to form water islands, similar to Rayleigh instability [188, 189]. An approximate continuum

analysis assuming an array of axisymmetric water islands on a continuous water film was performed [190]. As shown in Figure 5.6, we see nearly axisymmetric water island form on top of a continuous water layer covering the substrate surface. Here we assume the water island takes axisymmetric shape with the same cross-sectional view through the axis in Figure 5.7. We notice that the base of water island takes a circular shape of radius $L/2$ in our continuum model while it takes a square shape of length L. Besides, the mean curvature is nonuniform across the water island, which is contradictory to the constant stress assumed in the analytical model. Nevertheless, we ignore those inconsistencies and force balance condition gives

$$R = \frac{2L}{\sin\theta} + \frac{\gamma}{\sigma} - \sqrt{\left(\frac{\gamma}{\sigma}\right)^2 + \frac{1}{\pi}\left(\frac{L}{\sin\theta}\right)^2}. \tag{5.30}$$

The volume of the water island can be calculated by axisymmetric volume integral thus the volume of the cavity can be written explicitly by taking $\theta_g = 60°$ as

$$V_c^{IV} = \frac{3}{2}\pi R^3 - \frac{\pi R}{24}\left[9L^2 - \left(3\sqrt{3}+8\pi\right)LR + 27R^2\right]. \tag{5.31}$$

Again, the traction-separation can be obtained by plugging Eq. (5.30) and Eq. (5.31) into Eq. (5.23), plotted as magenta dashed line in Figure 5.6. The traction-separation formula is too complicated thus will not be presented here. We don't see a clear scaling relation between d and σ because the V_c^{IV} has a complicate dependence on *R* in Eq. (5.31). Finally, when *R* = *L*/2, the narrowest part of the ridge shrinks to a point. By taking *R* = *L*/2 into Eq. (5.31) and Eq. (5.23), the upper limit for the separation in Stage IV is calculated as

$$d_u^{IV} = \frac{\left(6\sqrt{3}+16\pi-27\right)\pi L}{192} - t_w\left(\frac{K_1}{2K_2} + \sqrt{\frac{K_1^2}{4K_2^2} + \frac{4\gamma}{K_2 L}}\right), \tag{5.32}$$

giving $d_u^{IV} = 5.56\,\text{nm}$. Island bridging is observed in the MD simulation when the separation is around 5.5 to 6 nm, suggesting that graphene is fully separated from the

substrate soon after the formation of water islands. We notice the narrowest part of the water island is not necessarily the top part of the bridging contact with graphene membrane, i.e., for the case when $\theta_g < 90°$. Thus the breaking point of water bridging occurs at the narrowest part of water island, leaving the majority of water molecules on the substrate while few water molecules are sticky on the graphene membrane when fully separated from wet substrate.

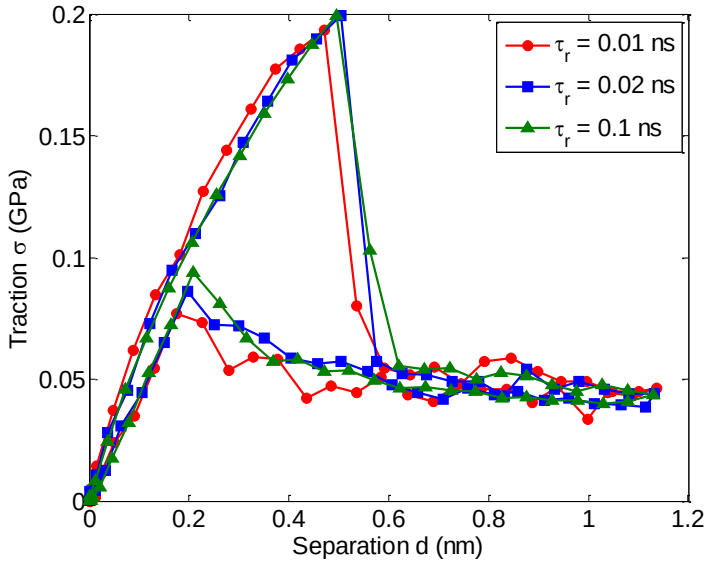

Figure 5.8: Traction-separation relation by MD simulations with different relaxation times (t_w = 4.19 nm and θ_g = 60°).

5.6 RESULTS AND DISCUSSION

5.6.1 Effect of relaxation time

MD simulations are often limited by computational cost to the cases with unrealistically high loading rates or short relaxation time. With a linear displacement increment $\Delta z_p = 0.01$ nm and a relaxation time $\tau_r = 0.01$ ns of the planar indenter at

each loading stage, the loading rate is 1 m/s. By increasing the relaxation time to 0.02 and 0.1 ns in MD simulations, thus reducing the loading rate by a factor of 2 and 10, the traction-separation diagrams show little difference (Figure 5.8), while the one with longer relaxation time has smaller fluctuation in traction. Based on our modified nucleation theory, the traction-separation relation before cavitation and during unloading remains unaffected by changing the relaxation time. However, the relaxation time may be related to the nucleation rate that is required for a cavity to form, roughly, $dn/dt \sim 1/\tau_R$. Thus, a longer relaxation time requires a lower nucleation rate and correspondingly a smaller critical separation as shown in Figure 5.5d. The MD simulations show a nearly identical critical separation for all cases with different relaxation time. We attribute this discrepancy to that the final equilibrium of the whole system is not fully reached due to the relative small relaxation times used in our current MD simulations.

5.6.2 Effect of water contact angle of graphene

Since a wide range of water contact angle of graphene is measured and calculated, we vary the contact angle θ_g as indicated in Table 5.1 and study its effect on the traction-separation relation. The traction-separation relation for different water contact angles of graphene θ_g from MD simulations are shown in Figure 5.9a and Figure 5.9b. A smaller θ_g, corresponding to stronger water/graphene interaction, leads to longer separation range and higher traction for the entire separation process, including a larger initial stiffness, a higher strength and a higher traction after cavitation for the traction-separation relation.

The water contact angle of graphene θ_g affects the modified nucleation theory through the cavity shape factor η in the total free energy (See Eq. (5.20)). The shape factor η monotonically decreases with respect to θ_g: when θ_g equals 0°, the shape

factor $\eta = 4$ representing a full spherical cavity inside liquid water; when θ_g equals 180°, shape factor $\eta = 0$ indicating the graphene/water system is unstable due to super-hydrophobicity of graphene. For higher shape factor value η, corresponding to smaller water contact angle of graphene θ_g or greater hydrophilicity of graphene membrane, a larger separation *d* is predicted under the same traction from the force balance Eq. (5.24). Equivalently, larger contact angle θ_g leads to smaller traction after cavitation from the modified nucleation theory, as shown in Figure 5.9c. As written in Eq. (5.11), formation of a cavity increases the surface energy but decreases the elastic strain energy in the liquid water. The competition leads to a critical separation d_c for cavitation that depends on the water contact angle θ_g: a larger contact angle leads to a lower critical separation (Figure 5.9c) as well as lower critical traction for the onset of cavitation. Moreover, the radius of the cavity increases with the water contact angle θ_g from the force balance Eq. (5.21), as shown in Figure 5.9d. The traction-separation relation predicted by the modified nucleation theory agrees reasonably with MD simulations. However, MD results show a stronger dependence on the contact angle θ_g for the traction before and after cavitation. Besides, the tangential stiffness increases with decreasing contact angle θ_g for the traction-separation relation from MD simulations, in contrast to the same tangential stiffness for all θ_g from the modified nucleation theory. We attribute those discrepancies to the inaccurate description of elastic behavior of water film by simply taking the constitutive relation from bulk water in Eq. (5.12), since the interaction between water and substrate and the interaction between water and graphene have an impact on the stress-strain behavior of water film. Moreover, the modified nucleation theory assumes a perfect spherical-cap shape of the cavity while the cavity shape is distorted in the MD simulations due to the restriction of finite thickness of water film (t_w) and the no cavity penetration condition of the fictitious substrate.

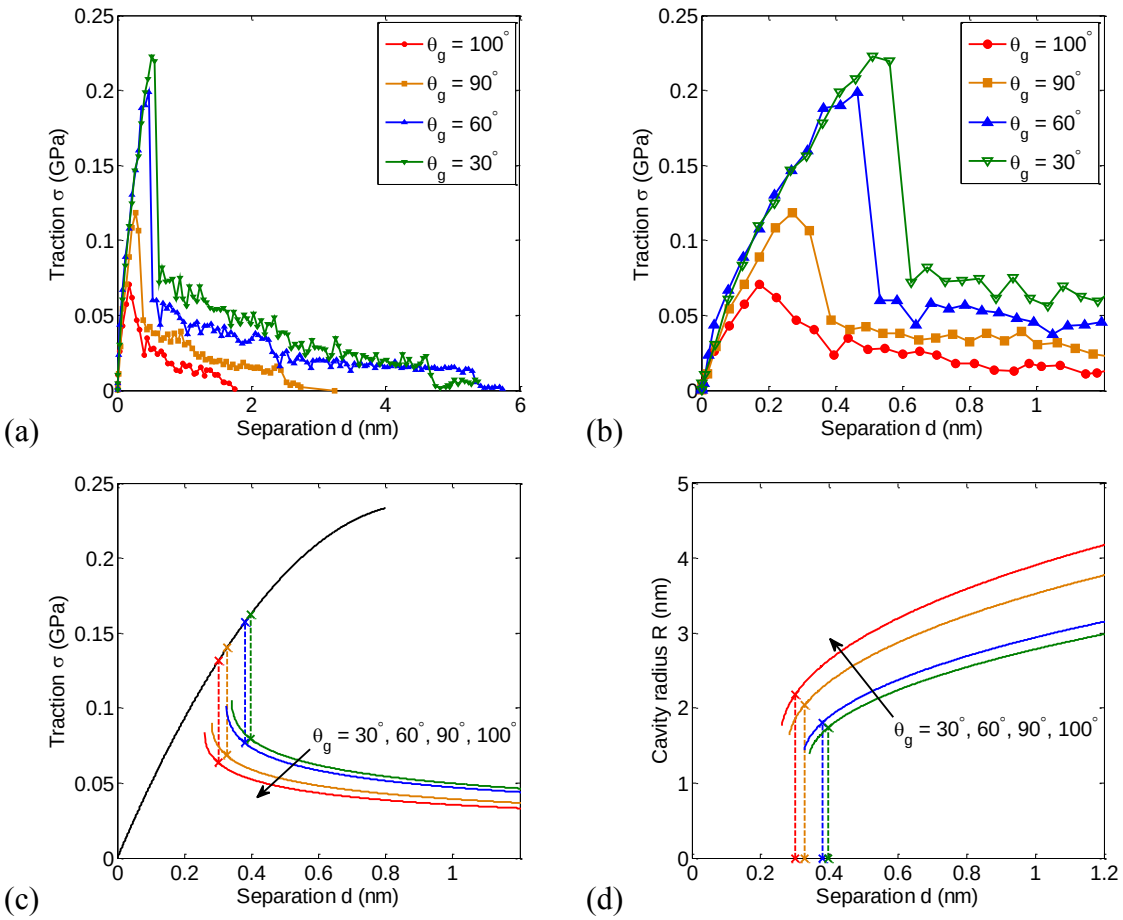

Figure 5.9: Traction-separation relation by MD simulations and analytical prediction with different water contact angle of graphene θ_g ($t_w = 4.19$ nm). (a) Full traction-separation diagram by MD simulations. (b) Zoom in of (a) near the cavitation point. (c) Traction-separation relation and (d) radius of cavity predicted by the modified nucleation theory, with the vertical dashed lines for onset of cavitation.

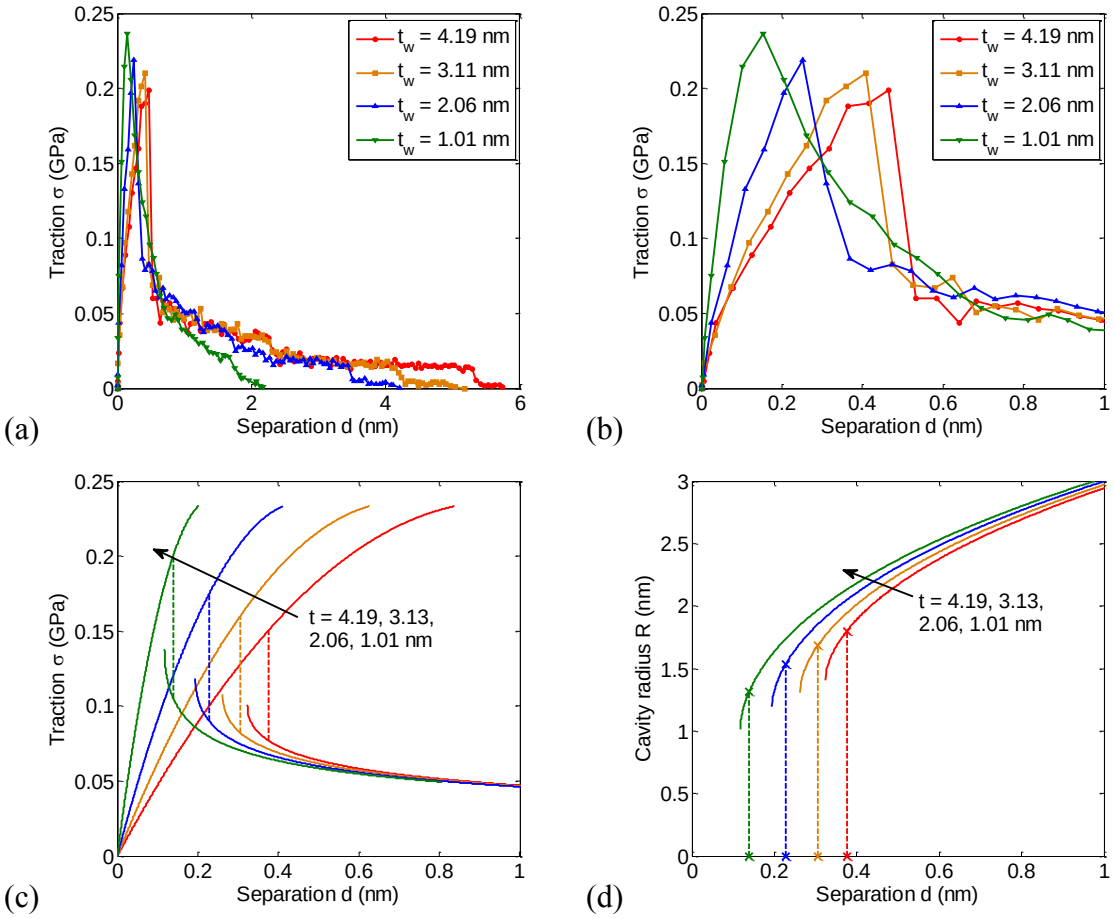

Figure 5.10: Traction-separation relation by MD simulations and analytical prediction with different thicknesses of water film (θ_g = 60°). (a) Full traction-separation diagram by MD simulations. (b) Zoom in of (a) near the cavitation point. (c) Traction-separation relation and (d) radius of cavity predicted by the modified nucleation theory, with the vertical dashed lines for onset of cavitation.

5.6.3 Effect of the thickness of water film

Due to the limitation of computational resources, we used a small simulation box and a thin water film between graphene and substrate. Previous study shows a strong dependence of the critical strain and stress for cavitation on the initial liquid volume [169]. Therefore, we fix the in-plane length L of the simulation box around 10 nm and vary the number of water molecules to investigate the effect of initial thickness of water

film t_w on the traction separation relation as well as cavitation behavior. Here we perform MD simulations with four different numbers of water molecules, corresponding to four different thicknesses of water film as shown in Table 5.2. As the thickness of water film decreases, the initial stiffness, maximum traction and critical separation for cavitation increase as shown in Figure 5.10a and Figure 5.10b. In contrast, the interaction range becomes shorter for thinner water film and is only around 2 nm for case of $t_w = 1.01$ nm. This trend is expected to continue until the thickness researches zero, where the van der Waals interactions for dry adhesion of graphene dominates with the maximum traction above 1 GPa and the range of interaction lower than 1 nm.

By classical nucleation theory, the initial volume of liquid water or the thickness of water film for our current study affects the cavitation pressure through the nucleation rate only, which has been found to be insignificant for the prediction of cavitation pressure [169, 191-193]. In contrast, the modified nucleation theory in Section 5.4 predicts a more significant effect, not only on the nucleation rate but also on the free energy through Eq. (5.20). As a result, a smaller thickness leads to a smaller critical separation for cavitation as shown in Figure 5.10c. While the stress-strain relation remains unchanged from Eq. (5.12), a smaller separation is expected for thinner water film under the same traction, thus resulting in a higher stiffness and correspondingly slight higher cavitation stress. As the separation keeps increasing after cavitation, the tractions continuously decrease and merge into a master curve for all thickness. This can be explained by the traction-separation relation in Eq. (5.24): when the traction becomes small, the first term in Eq. (5.24) dominates, which is independent of the thickness. Interestingly, the radius of cavity slightly increases as the initial thickness increases, leading to slight lower traction after cavitation as dictated by Eq. (5.21). Note that the critical cavity radius is even larger than the thickness of water film for small values of

t_w, indicating the cavity penetrates the substrate. The critical condition for cavity touching the substrate can be written as

$$\left(1+\cos\theta_g\right)R_c = t_r, \tag{5.33}$$

where $R_c = R_c(\theta_g, t_r)$ is the critical cavity radius and t_r is the threshold thickness of water film, only above which the modified nucleation theory holds. By taking the water contact angle $\theta_g = 60°$, we obtained the threshold thickness $t_r = 2.378$ nm, inferring the modified nucleation model become inaccurate for $t_w = 1.01$ nm and $t_w = 2.06$ nm. Nevertheless, the modified nucleation theory and MD simulations are in a reasonable agreement except the stiffnesses before cavitation from MD simulation is slightly larger than the predicted values, which may be explained by the inaccurate elastic behavior of water film as discussed in Section 5.6.2.

N	3645	7290	10935	14580
t_w (nm)	1.01	2.06	3.11	4.19

Table 5.2: The number of water molecules *N* and corresponding initial thickness of water film t_w after relaxation for MD simulations with in-plane dimension *L* ~ 10 nm and $\theta_g = 60°$.

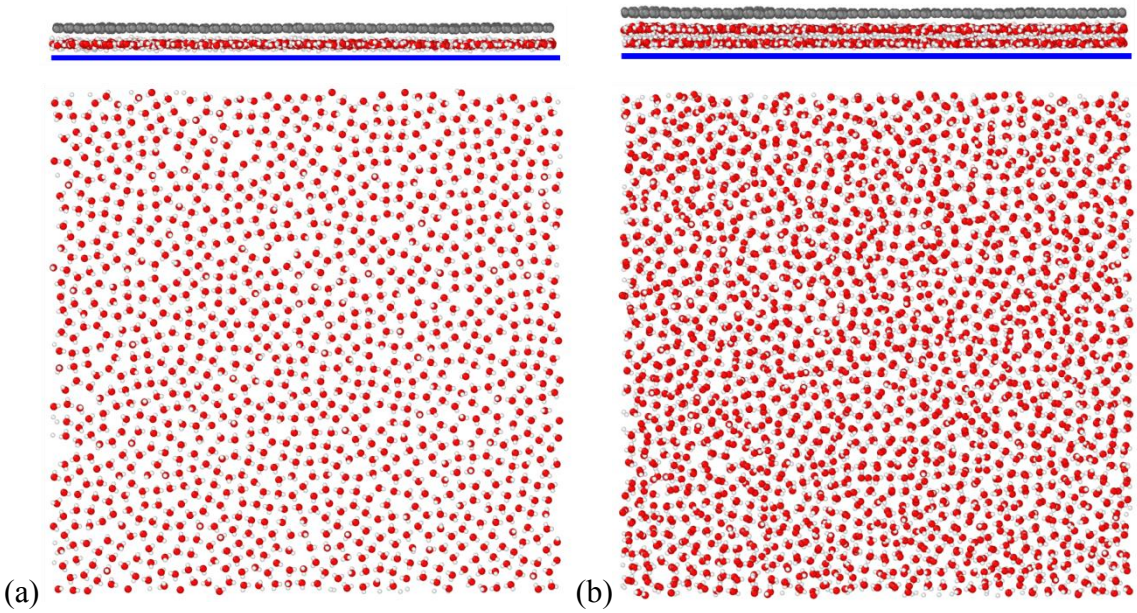

Figure 5.11: Side view snapshots (top) and top view snapshots (bottom) of (a) monolayer water structure with $N = 1156$ and (b) bilayer water structure with $N = 2312$ from MD simulations with water contact angle of graphene $\theta_g = 60°$. Top view snapshots of water layers are shown by removing graphene on top of them.

5.6.4 Discrete layered water structures

When water is absorbed and confined at the interface, an discrete monolayer and bilayer structure were observed in experiments at room temperature [88, 89]. Water adlayers grew epitaxially on the mica substrate to form a monolayer and bilayer of ice, while thicker layers appear liquid-like [88]. Moreover, two-layer crystalline ice films forms on a hydrophobic substrate, graphene on Pt(111), even at zero pressure without confinement [194]. In this section we tune the number of water molecules in our MD simulations to form discrete layered structure and study its traction-separation behavior. Since the thickness of the layered water is smaller than 1 nm, we take into account the interaction between graphene membrane and substrate in our MD simulations. For simulation box with in-plane length L around 10 nm, a monolayer and bilayer structures

of water are formed corresponding to the number of water molecules N = 1156 and 2312, as shown in Figure 5.11. The thicknesses are measured as 0.328 nm and 0.602 nm for monolayer and bilayer water, respectively. We didn't observer any square ice structure in our simulation as mentioned in [89], which may be caused by the fictitious substrate without any crystal ordering used in our simulation. Next, we detach the graphene membrane from the substrate with discrete layered water in between and obtain the traction-separation relation for monolayer water in Figure 5.12. It is interesting to note that a double peak traction-separation relation is observed for monolayer water, in contrast to all single peak traction-separation relations we obtained before.

By extracting a series of top view snapshots during the whole separation process, we take a closer look on the morphological change of water film as well as the corresponding traction-separation relation. Initially the monolayer water is uniformly stretched as the graphene is detached away from the substrate until reach the peak point A in Figure 5.12. Thereafter, when the separation further increases, vacancies and overlayers appear and coalesce inside layered water and the traction monotonically reduces to the minimum point B, where a perfect bilayer structure forms with a nearly circular cavity in the middle due to the constant number of water molecules used in our simulation. This cavitated bilayer structure is self-equilibrated thus the traction on the graphene membrane is mainly contributed from the interaction between graphene and substrate. Upon further separating graphene from the substrate, the cavitated bilayer water structure is stretched and the traction increases to reach the second peak, which is much lower than the first peak. Afterwards, the cavity in the bottom layer shrinks and the cavity in the top layer enlarges, corresponding to monotone drop in traction. Finally, as the graphene is separated far away from the substrate, the top layer of discrete water

structure disappears, leaving continuum water film on top of substrate, and the traction on graphene membrane approaches zero.

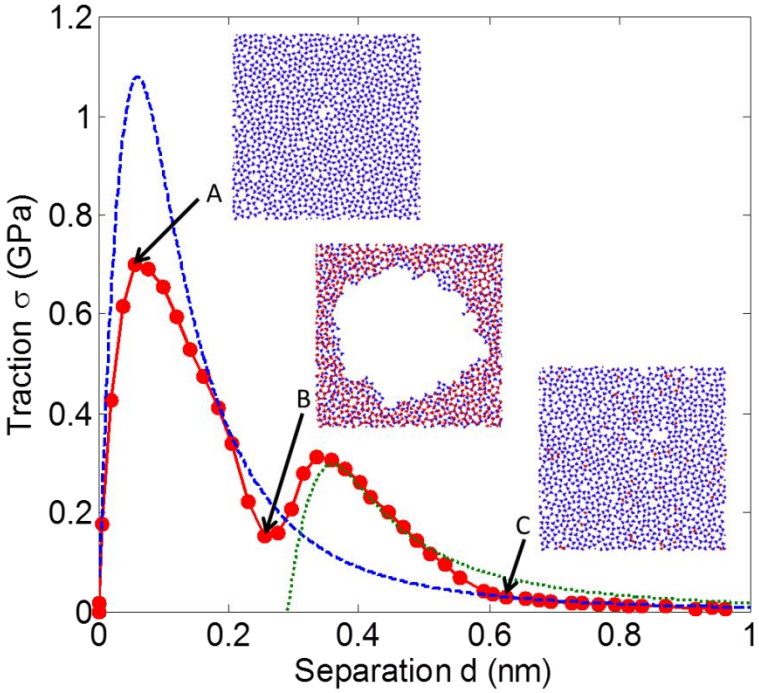

Figure 5.12: Traction-separation relation from both MD simulation and analytical prediction for monolayer water. Top view snapshots at critical points from MD simulation are inserted. The water contact angle of graphene membrane θ_g is 60°. The blue dashed line and green dotted line are predicted by analytical monolayer and bilayer model, respectively.

Based on the potential used in the MD simulations as described in Section 5.3, we present a simple continuum model to predict the traction-separation relation for monolayer water. Consider monolayer water as a flat plate with number density of water molecules $\rho_w = \frac{N}{L^2} = 11.21\ \text{nm}^{-2}$, then the interaction potential per unit area between graphene membrane and monolayer water can be calculated from the LJ potential used in MD simulation in Eq. (5.8). By taking first derivative of interaction potential, the interaction force is obtained as

$$\sigma^{gw}(z)=\frac{20}{3}\frac{\Gamma_0^{gw}}{h_0^{gw}}\left[\left(\frac{h_0^{gw}}{z}\right)^5-\left(\frac{h_0^{gw}}{z}\right)^{11}\right], \tag{5.34}$$

where $h_0^{gw}=\delta_{CO}$ is the equilibrium separation and $\Gamma_0^{gw}=\frac{8\pi\rho_w\varepsilon_{CO}\delta_{CO}^2}{5\sqrt{3}r_0^2}$ is the adhesion energy between graphene membrane and layered water. Here $r_0=0.142$ nm is the bond length of graphene. Similarly, the interaction force between layered water and substrate can be obtained from the LJ potential in Eq. (5.7) as

$$\sigma^{ws}(z)=\frac{9}{2}\frac{\Gamma_0^{ws}}{h_0^{ws}}\left[\left(\frac{h_0^{ws}}{z}\right)^4-\left(\frac{h_0^{ws}}{z}\right)^{10}\right], \tag{5.35}$$

where $h_0^{ws}=\left(\frac{2}{5}\right)^{1/6}\delta_{OS}$ is the equilibrium separation and $\Gamma_0^{ws}=\frac{\sqrt{10}}{3}\rho_w\varepsilon_{OS}$ is the adhesion energy between water layered and substrate. Note that the interaction force between graphene membrane and substrate is already described by Eq. (1.2) with the equilibrium separation h_0^{gs} and adhesion energy Γ_0^{gs} given in Eq. (3.32) and Eq. (3.33). Then consider a monolayer model: a graphene membrane on top of substrate with a water layer sandwiched in between, including interaction forces between any two of them. The whole system is in equilibrium when the forces acting on graphene membrane and water layer are balanced, i.e.,

$$\sigma^{gw}\left(a_e^{gw}\right)+\sigma^{gs}\left(a_e^{gw}+a_e^{ws}\right)=0 \tag{5.36}$$

and

$$\sigma^{gw}\left(a_e^{gw}\right)-\sigma^{ws}\left(a_e^{ws}\right)=0, \tag{5.37}$$

where a_e^{gw} and a_e^{ws} are the equilibrium interface spacings at the graphene/water interface and water/substrate interface, respectively. By solving the equilibrium Eqs. (5.36) and (5.37), we obtain a_e^{gw} = 0.3156 nm and a_e^{ws} = 0.3138 nm, respectively. Then as the graphene membrane is detached from the substrate, we have the condition for the total separation as

$$d = a^{gw} + a^{ws} - a_e^{gw} - a_e^{ws}, \tag{5.38}$$

where a^{gw} and a^{ws} are interface spacings for any given separation d. The force equilibrium on layered water is slightly different from Eq. (5.37) as

$$\sigma^{gw}\left(a^{gw}\right) - \sigma^{ws}\left(a^{ws}\right) = 0. \tag{5.39}$$

The force balance Eq. (5.37) on layered water still holds and the total traction acting on graphene membrane is

$$\sigma = \sigma^{gw}\left(a^{gw}\right) + \sigma^{gs}\left(a^{gw} + a^{ws}\right). \tag{5.40}$$

For given separation d, the traction can be solve by combing Eq. (5.38), Eq. (5.39) and Eq. (5.40), plotted as blue dashed line in Figure 5.12. The MD simulation shows the same interaction range with the analytical prediction, but the traction from MD simulation is much smaller. Since MD simulation is performed at finite temperature (T = 300 K) while theoretical model considers the mechanical behavior at ground state (T = 0 K), we attribute this discrepancy in traction to the entropic repulsion of thermal rippling at the interfaces.

Next we consider the cavitated bilayer structure between point B and point C in Figure 5.12, including a graphene membrane, two water layers and a substrate, as well as interaction forces between any two of them. We assume each water layer as neural rigid plate and the dipole of water molecules can be ignored, thus only LJ potential in Eq. (5.5) contributes to the interaction force between water layers, i.e.,

$$\sigma^{ww}\left(z\right) = \frac{20}{3}\frac{\Gamma_0^{ww}}{h_0^{ww}}\left[\left(\frac{h_0^{ww}}{z}\right)^5 - \left(\frac{h_0^{ww}}{z}\right)^{11}\right], \tag{5.41}$$

where $h_0^{ww} = \delta_{OO}$ is the equilibrium separation and $\Gamma_0^{ww} = \frac{6\pi\rho_w^2\varepsilon_{OO}\delta_{OO}}{5}$ is the adhesion energy between two water layers. Since the same size cavities appear in both water layers, we assume each layer has the averaged number density of water molecules $\rho_w = \frac{N}{2L^2} = 5.61\ \mathrm{nm}^{-2}$. Similarly, the total separation can be written as

$$d = b^{gw} + b^{ww} + b^{ws} - a_e^{gw} - a_e^{ws}, \tag{5.42}$$

where b^{gw}, b^{ww} and b^{ws} are interface spacings at the graphene/water, water/water and water substrate interface for any given separation *d*. Then the traction acting on graphene membrane can be obtained by solving the equilibrium equations

$$\sigma^{gw}\left(b^{gw}\right) - \sigma^{ww}\left(b^{ww}\right) - \sigma^{ws}\left(b^{ww} + b^{ws}\right) = 0, \tag{5.43}$$

$$\sigma^{gw}\left(b^{gw} + b^{ww}\right) + \sigma^{gw}\left(b^{gw}\right) - \sigma^{ws}\left(b^{ws}\right) = 0 \tag{5.44}$$

and

$$\sigma = \sigma^{gw}\left(b^{gw}\right) + \sigma^{gw}\left(b^{gw} + b^{ww}\right) + \sigma^{gs}\left(b^{gw} + b^{ww} + b^{ws}\right), \tag{5.45}$$

plotted as green dotted line in Figure 5.12. The analytical prediction and MD simulation are in good agreement in both traction amplitude and interaction range, despite the temperature effect is not included in the analytical bilayer model. After point C when graphene membrane is far enough away from the wet substrate, the bilayer structure disappears, leaving a continuum water film on top of substrate. Therefore, the analytical monolayer model can be approximately used to predict the traction-separation relation in this range.

Then we vary the water contact angle of graphene θ_g and study its effect on the traction-separation relation for discrete layered water structures. Based on the MD result for monolayer structure in Figure 5.1a, the double peak traction-separation only occurs for small water contact angle θ_g, corresponding to strong interactions between water and graphene membrane. This is because the water/graphene interface will break apart before the formation of cavitated bilayer for weak water/graphene interface (or large θ_g). The double peak traction-separation relation doesn't occur for bilayer structure, as shown in Figure 5.1b. In all our MD simulations, we didn't observe discrete layered structure with more than two layers. Therefore, when bilayer structure is further stretched by detaching graphene membrane away from the substrate, it becomes continuum water film instead of

forming a cavitated discrete layered structure with more layers, which is responsible for the double peak traction-separation behavior.

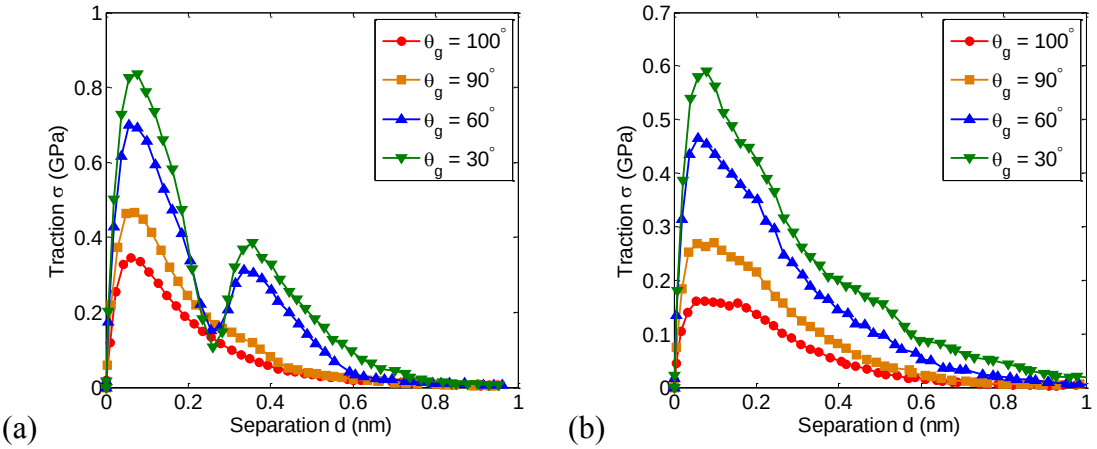

Figure 5.13: Traction-separation relation of (a) monolayer water structure and (b) bilayer water structure for different water contact angles.

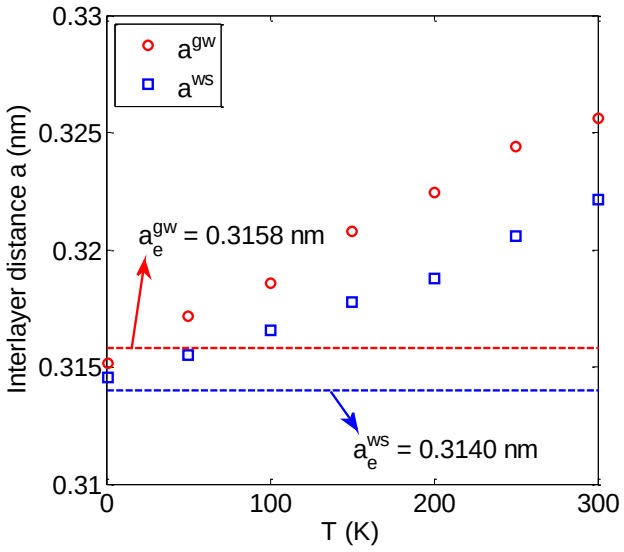

Figure 5.14: Interface spacings at graphene/water interface a^{gw} and water/substrate interface a^{ws} from MD simulations (all dots) for monolayer water structure at different temperatures. The dashed lines are equilibrium interlayer separations predicted by theoretical model at $T = 0$ K.

Finally, we briefly explore the entropic effects of thermal rippling on the interface spacing for monolayer water structure. As mentioned in Chapter 3, the equilibrium separation between graphene and substrate increases with temperature due to the thermal rippling of graphene membrane. Here we conduct MD simulations for different temperatures ranging from 1K to 300K, and measure the position of graphene membrane $\overline{z}_r^g$ by averaging all carbon atoms and the position of layered water $\overline{z}_r^w$ by averaging all oxygen atoms. The interface spacings for different temperatures at the graphene/water interface and water/substrate interface are calculated by $a^{gw} = \overline{z}_r^g - \overline{z}_r^w$ and $a^{ws} = \overline{z}_r^w - z^s$, respectively. The equilibrium interface spacings from analytical monolayer model, which is derived at ground state (T = 0), are very close to the MD result at 1K in Figure 5.14. Both interface spacings increase with temperature in an approximately linear trend. Similar to Figure 3.7b, the entropic repulsion is caused by the thermal rippling of graphene membrane and water layer.

5.6.5 Comparison

With the MD simulation results for various water contact angles of graphene θ_g and initial thicknesses of water film t_w, including both continuum water film and discrete layered structure, we extract the main characteristics from the traction-separation relation and compare them with properties of dry adhesion (graphene membrane directly placed on top of substrate as discussed in Chapter 3 and Chapter 4). The strengths or maximum tractions as a function of initial thickness of water film for different contact angles are plotted in Figure 5.15a. The strength decreases with the thickness for the discrete layered structures and becomes nearly constant in the continuum region ($t_w >$ 1 nm), both of which are lower than the strength of dry adhesion. For discrete layered structures ($t_w < 1$ nm), the interaction between graphene and substrate has a significant

contribution to relative high strength, and this contribution decays as the thickness increases. In contrast, for continuum water film ($t_w > 1$ nm), the interaction between graphene and substrate becomes negligible, thus the strength is determined by the occurrence of cavitation. It is also noted that for all thicknesses, the strength becomes higher for smaller water contact angle of graphene θ_g, corresponding to stronger graphene/water interaction. Thus the strength is also affected by the interaction between graphene and water. Next, we fit the traction-separation relation with a quadratic function, motivated by the nonlinear stress-strain relation for bulk water in Eq. (5.12), and extract the coefficient in front of the linear term as the initial stiffness, plotted in Figure 5.15b. The initial stiffness decreases with increasing thickness and contact angle. A significant drop in initial stiffness is observed during the transition from discrete layered structure to continuum water film, suggesting the elastic behavior of discrete layered water is totally distinct from the continuum water film. Finally, we use numerical integration to calculate the area under the traction-separation relation to obtain the adhesion energy, or the work of separation, as shown in Figure 5.15c. The total adhesion energy sums up two parts: the adhesion energy between graphene and substrate (the dashed line in Figure 5.15c) and the adhesion energy between graphene and water film. By integrating the atom-atom interaction potential function in Eq. (5.8) with respect to all oxygen atoms in bulk water, the potential energy between graphene and the static bulk water can be obtained in Table 5.3 [83, 190]. For discrete layered structures with small thicknesses ($t_w < 1$ nm), the total adhesion energy decreases with $\mathrm{t_w}$ because the interaction between graphene and substrate decays dramatically. In the region of continuum water film ($t_w > 1$ nm), where the interaction between graphene and substrate becomes negligible, the total adhesion energies are larger than the potential energies in Table 5.3. Several snap transitions or sudden drops in traction occur during

the entire separation process (see Figure 5.6), leading to energy dissipations at these snapping points. For large water contact angles of graphene, the snapping is very small and can be ignored from Figure 5.9, thus the adhesion energy is nearly constant with respect to initial thickness and close to the theoretical potential energy. In contrast, for small water contact angles of graphene ($\theta_g = 60°$ and $\theta_g = 30°$), significant snapping is observed especially for larger initial thickness (see Figure 5.9 and Figure 5.10), thus the adhesion energy increases with thickness and is much higher than the theoretical potential energy. The adhesion energy or the work of separation is found to be in the range 0.03 ~ 0.25 J/m^2, in a good agreement with typical both experiments and theoretical calculations [27, 64, 65, 68, 73, 75, 82, 107]. The interaction range for $t_w > 1$ nm are compared in Figure 5.15d, while the interaction range for thin water films ($t_w < 1$ nm) is assumed to be ~ 1 nm, as the typical interaction range for van der Waals type dry adhesion. For smaller water contact angle of graphene and a thicker water film, a longer interaction range up to 6 nm is observed before the graphene is fully separated from the substrate. However, an exception is observed for the case $t_w = 4.2$ nm and $\theta_g = 30°$, where a thin water film residual is left on the graphene side after full separation, as a result of strong graphene/water interaction. The strength and interaction range depends on the initial volume of water film through the thickness t_w and in-plane dimension L in Eq. (5.20), similar to the case of bulk water [169]. Extrapolate to much larger initial thickness t_w or in-plane dimension L of water film beyond the MD simulations, the strength can be reduced to several mega pascals and the interaction can be extended to micrometer range, which may offer a possible explanation for the ultra long-range interactions between large area graphene and silicon observed in experiment [80].

Contact angle(°)	30	60	90	100
Adhesion energy (J/m^2)	0.109	0.0872	0.0545	0.0363

Table 5.3: The adhesion energy between graphene membrane and bulk water for different water contact angle of graphene θ_g.

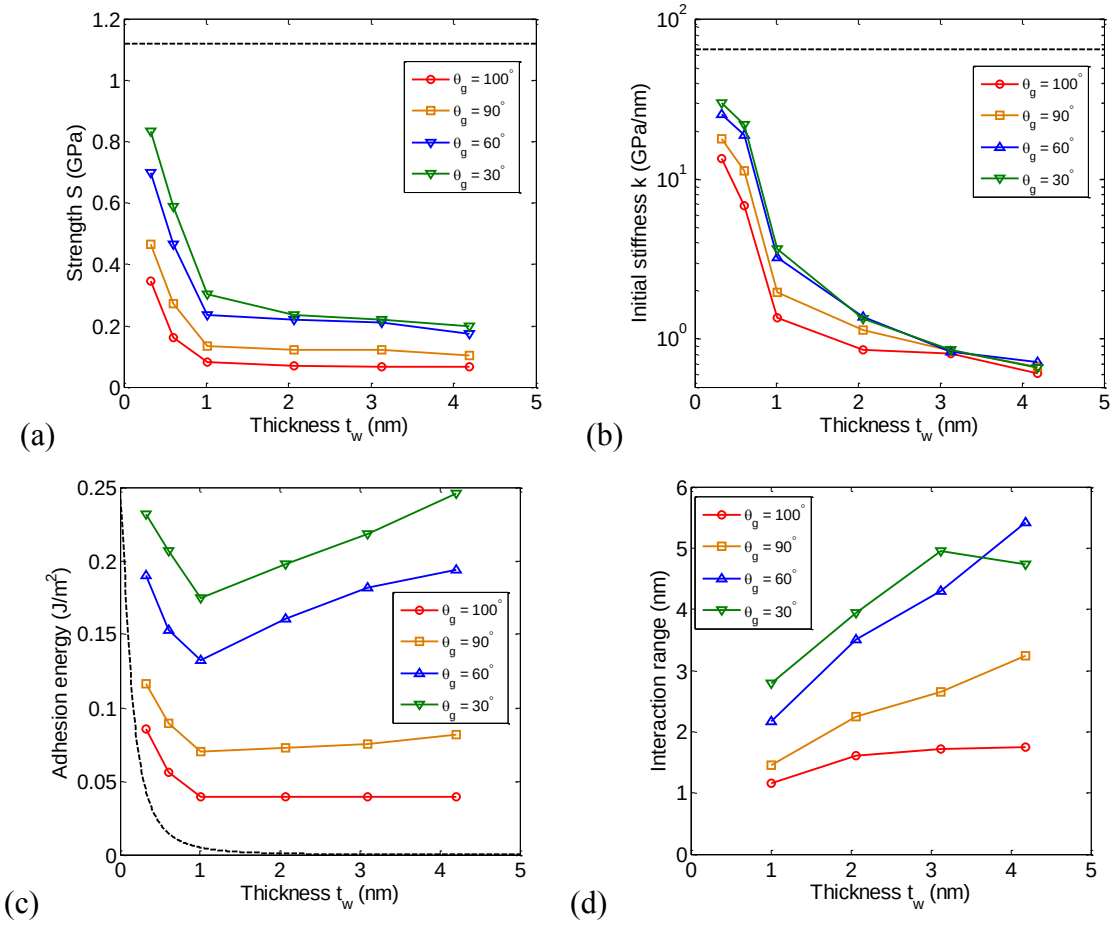

Figure 5.15: (a) Strength, (b) initial stiffness, (c) adhesion energy and (d) interaction range of the traction-separation relation for graphene on wet substrate. All symbols are from MD simulations and dashed lines represent the graphene/substrate system without any water (dry adhesion).

5.7 SUMMARY

MD simulations are conducted to study the traction-separation relations for wet adhesion between graphene and substrate. By taking into account the nonlinear elasticity of water and water contact angle of graphene, a modified nucleation theory for cavitation was proposed. Four stages of the full traction-separation relations are identified and they are analyzed approximately by simple continuum models. The numerical and theoretical results are compared and discussed to elucidate the effects of water contact angle of graphene and initial thickness of water film on cavitation and traction-separation relation. When the thickness of water film is small, monolayer and bilayer water structures are observed and traction-separation behaviors are measured for layered structures. Motivated by the double peak behavior in the traction-separation relation of monolayer water structure, we propose a simple continuum model to compare with MD results. Entropic repulsions at graphene/water and water/substrate interfaces are observed at finite temperatures, as a result of thermal rippling of graphene membrane and layered water. By comparing the strength, initial stiffness and adhesion energy for different water contact angles of graphene and initial thicknesses of water film, we found a significant distinction between discrete layered water structures and continuum water films. The range of interaction can extend up to 6 nm and the adhesion energy measured in our MD simulations is between 0.03 and 0.25 J/m^2, in a good agreement with typical both experiments and theoretical calculations.

Chapter 6 Liquid-filled graphene blisters

6.1 Introduction

Many studies have been carried out recently to explore various aspects of nanoblisters, including the effects of heat [195], blister content [196], humidity dependence [197], and their shape characteristics [198]. Although there is no consensus on whether the blisters are filled with air, liquid, or solid [199, 200], adhesion is one of the well-accepted governing parameters for the formation of blisters. In fact, interfacial blisters have been used as indicators of good adhesion between the constituents of vdW heterostructures [201], since blisters are energetically favorable only when the adhesion between layers is relatively high. Mechanics models have been developed and widely used to relate gas-filled blister profiles to interfacial adhesion [103, 196, 197, 202, 203]. However, the subtle nature of the content of the blisters may render the assumption of a gas content inappropriate. Direct application of this *ad hoc* model had led to unrealistically small adhesion values for graphene interfaces when compared to well-established adhesion measurements [197].

In this chapter, we studied the mechanical and adhesive properties of liquid-filled graphene blisters on substrates, in contrast to the gas-filled graphene blister discussed in Chapter 2. Molecular dynamics simulations were performed for water-filled graphene blisters on a fictitious substrate. The shape characteristics of the blister were measured and discrete layered structure was observed. A continuum model based on simple membrane theory was developed for liquid-filled nanoblisters. Compared with gas-filled blisters assuming ideal gas law for the content in Chapter 2, the liquid blister theory assumes that the liquid inside the blister is nearly incompressible. Like the gas blister theory, our liquid blister theory can also be utilized to quantitatively characterize the adhesion properties for graphene or other 2D materials based on the measured blister

profiles. Alternatively, the blister shape, strain, and pressure characteristics could be controlled by tuning adhesion properties and trapped contents, which provides a viable guideline for the design of 2D material blisters for various applications.

6.2 MOLECULAR DYNAMICS SIMULATION

We performed classical MD simulations using LAMMPS [135]. A square-shaped graphene membrane ($L \sim 30$ nm) was placed on top of a flat substrate surface, with water molecules in between. MD simulations were carried out in NVT ensemble with periodic boundary conditions at 300K, where the temperature was controlled by a Nose-Hoover thermostat. The integration time step was 1 fs. The in-plane dimension of the periodic box was set by the size of the graphene sheet (~30 nm), and the thickness of the periodic box was 20 nm so as to keep periodic images in the thickness direction from interacting with each other. Here, we fix the equilibrium separation between graphene and substrate to be 0.316 nm. The substrate was modeled as a rigid surface placed at z = -0.316 nm so that the average position of the carbon atoms in the graphene would be around z = 0 if no water molecules are trapped in between. Initially, a number of water molecules were placed as a block between the substrate and the graphene sheet. Then, the system was relaxed for 2 ns to form a bubble. Figure 6.1 shows a snapshot of a graphene bubble with 2700 water molecules, shaped like a spherical cap as viewed from the top and side. We retrieved the bubble configuration by sampling 10 snapshots evenly after 1 ns relaxation. The bubble height (h) was measured as the difference between the largest z positon of the carbon atoms and the average z position (~0) outside the bubble edge (see Figure 6.1B). The bubble diameter ($2a$) was measured as the maximum span distance for the carbon

atoms with $z > 0.1$ nm. The height-radius ratio (h/a) was calculated by averaging over the 10 snapshots with an error bar for the standard deviation.

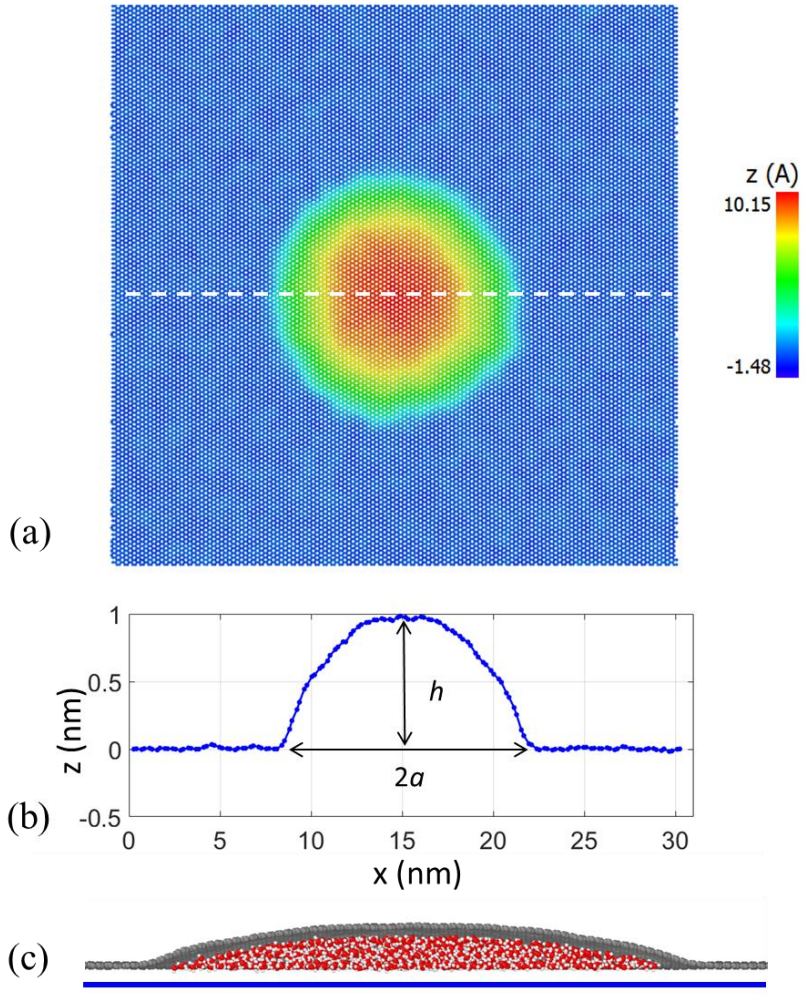

Figure 6.1: MD simulation of a graphene bubble with 2700 water molecules. The adhesion energy $\Gamma_0 = 0.242$ J/m^2, while the water contact angles are 60° and 40° for graphene and the substrate, respectively. (a) A top view snapshot of the bubble, with color contour for the z-position of the carbon atoms in graphene; (b) A height profile along a line scan (dashed line in (a)) across the bubble; (c) A cross-sectional view of the bubble, showing the water molecules (oxygen in red and hydrogen in white) between graphene (carbon in gray) and the substrate surface (blue line).

The force field used in the simulation is the same as described in Chapter 5. The second-generation reactive empirical bond-order (REBO) potential [38] was used for the carbon-carbon interactions in graphene as described in Chapter 3. The TIP4P/2005 model [174] was used for interactions between water molecules. A fictitious surface interacting with both graphene and water molecules was used to represent the rigid substrate [152]. Lennard-Jones potential was adopted to describe the interaction between graphene and substrate, water and substrate, and graphene and water. In this chapter, we vary the interaction parameters between graphene and the substrate to simulate graphene blisters with different aspect ratios as a result of different adhesion energies Γ_0 ranging from 0.05 to 0.5 J/m^2, as the typical range mentioned in Section 2.2.2; we chose $\varepsilon_{OS} = 0.08$ eV to have a water contact angle of ~40^0 for the substrate, the typical water contact angle for SiO_2 [204]; We used $\varepsilon_{CO} = 6.0$ meV so that the predicted water contact angle is 60^o for pristine graphene without air-borne contamination [182].

By a simple force balance analysis of the graphene membrane, the pressure of the water can be estimated by summing up all forces between each carbon atom and substrate and then divided by the projected area of water droplet. The interaction force σ_{CS} between carbon atoms and substrate is already obtained in Eq. (1.2). The projected area of the water droplet can be estimated from the radius a. Thus the pressure of the water can be written as

$$p = \frac{\sum \sigma_{CS}}{\pi a^2}. \tag{6.1}$$

For each snapshot, we record the position of each carbon atom and calculate the force between carbon atom and substrate from Eq. (1.2), and the bubble radius can also be obtained as mentioned above. Similarly, we calculate the pressure at each snapshot and average it over 10 snapshots.

6.3 A SIMPLE MEMBRANE ANALYSIS

6.3.1 Aspect ratio of bubble

As in previous studies [47, 103, 205], in this simple membrane analysis, the deflection profile of the membrane for is assumed to be:

$$w(r) = h\left(1 - \frac{r^2}{a^2}\right), \tag{6.2}$$

where the height h is relatively small compared to the blister radius a. For a liquid-filled blister, the liquid within the blister is assumed to be incompressible so that the blister volume,

$$V = \frac{\pi}{2} a^2 h, \tag{6.3}$$

remains a constant. The area of the bulged surface $A' = \pi(a^2 + h^2) \approx \pi a^2$ for small h/a ratio. For a given liquid volume, the aspect ratio (h/a) of the blister is determined by the competition between the elastic strain energy of the membrane and the interfacial energy.

Based on the scaling analysis in [86], the aspect ratio for a liquid-filled bubble can be written as

$$\frac{h}{a} = \left(\phi \frac{\Gamma_0 - \gamma_w\left(\cos\theta_g + \cos\theta_s\right)}{E_{2D}}\right)^{\frac{1}{4}}, \tag{6.4}$$

where Γ_0 is the work of adhesion (or adhesion energy) of the graphene/substrate interface, γ_w is the surface tension of water (~0.0693 J/m^2 in our current MD simulations [177]) and $\theta_s = 40°$ and $\theta_g = 60°$ are the water contact angles of the substrate and the graphene respectively. The dimensionless coefficient ϕ has to be determined by a detailed simple membrane analysis [86]. For the strong shear limit,

where the membrane outside the bubble edge is not deformed, we have $\phi = \frac{24(1-\nu)}{5(7-\nu)}$; while for the weak shear limit, where the membrane in the annular region outside of the bubble edge ($r > a$) slides inward as the liquid pressure pushes up the membrane to form a bubble, we have $\phi = \frac{6}{5}$. To compare with MD simulations (Section 6.2), where the graphene/substrate interface is frictionless and periodic boundary conditions are applied with a finite-sized graphene membrane, the analysis for the weak shear limit is modified so that the radial displacement is zero at $r = L/2$, for the square-shaped membrane with length of L in MD simulations. As a result, we obtain $\phi = \frac{6L^2(1-\nu)}{5L^2(1-\nu)+12a^2(1+\nu)}$. Note that, in this case, ϕ depends on the ratio L/a. The liquid volume can be related to the number of water molecules as

$$V = \frac{N}{\rho}, \tag{6.5}$$

where ρ is the number density of water, which equals $33.2\ \mathrm{nm}^{-3}$ at $T = 300\mathrm{K}$ from the TIP4P/2005 model [169]. For a specific number of water molecules (N) used in MD simulations, the coefficient ϕ can be determined by solving a nonlinear algebraic equation as

$$\phi + \frac{3(1+\nu)}{5(1-\nu)}\left(\frac{16N}{\pi\rho L^3}\right)^{\frac{2}{3}}\left(\frac{E_{2D}}{\Delta\gamma}\right)^{\frac{1}{6}}\phi^{\frac{5}{6}} = \frac{6}{5}, \tag{6.6}$$

where $\Delta\gamma = \Gamma_0 - \gamma_w\left(\cos\theta_g + \cos\theta_s\right)$ is the change of the interfacial energy per unit area required to form the liquid-filled blister. Apparently in this case, the height-to-radius ratio of the blister depends on the size of the membrane through the ratio $\rho L^3/N$ or L^3/V. As $L^3/V \to \infty$, the coefficient ϕ approaches the weak shear limit ($\phi = \frac{6}{5}$). When $a = L/2$, the edge of the blister is fixed with no sliding, and the solution reduces to the strong shear limit $\phi = \frac{24(1-\nu)}{5(7-\nu)}$. As a result, the aspect ratio of bubble in MD simulation is bounded by the strong and weak limits.

6.3.2 Pressure inside bubble

The confining pressure across the membrane takes the following form

$$\Delta p = \frac{1}{a}\left(\lambda E_{2D}\frac{h^3}{a^3}\right), \tag{6.7}$$

where λ is $\frac{2}{1-\nu}$ and 1 for strong and weak shear limits and λ is $\frac{L^2(1-\nu)+4a^2(1+\nu)}{L^2(1-\nu)}$ for the modified weak shear limit in MD simulations [86]. Notice that the radius a in λ can be related to the number of water molecules and the aspect ratio by combining Eq. (6.3) and Eq. (6.5) as

$$a = \left(\frac{2N}{\pi\rho}\right)^{1/3}\left(\frac{h}{a}\right)^{-1/3}. \tag{6.8}$$

Therefore, the liquid pressure inside the bubble may be estimated by Eq. (6.7) in terms of the number of molecules and aspect ratio. This could be of interest for applications using bubbles of 2D materials for the study of interface-confined high-pressure chemistry [206-208].

6.4 RESULTS AND DISCUSSION

6.4.1 Aspect ratio of bubbles

Figure 6.2 plots the MD results in comparison with the analytical predictions, along with three snapshots for the trapped water molecules (N = 2700). When the adhesion energy is relatively large (Γ_0 > 0.2 J/m^2), the water molecules take the shape of a spherical cap as assumed in the continuum model. In this case, the aspect ratio h/a increases with increasing adhesion energy, in close agreement with the analytical prediction assuming a frictionless interface. As expected, the results are bounded by the strong shear limit ($\phi = \frac{24(1-\nu)}{5(7-\nu)}$) and the weak shear limit ($\phi = \frac{6}{5}$) for an infinitely large membrane. The weak shear limit overestimates the aspect ratio in MD due to the periodic

boundary conditions employed in the MD simulations, and the strong shear limit underestimates the aspect ratio due to the assumption of no sliding. Interestingly, for lower adhesion energies ($\Gamma_0 < 0.2$ J/m^2), the top of the blister is nearly flat, and the water molecules form a distinct bilayer structure instead of a spherical cap. As a result, the continuum assumption breaks down, and the aspect ratio becomes nearly independent of the adhesion energy for the same number of water molecules ($N = 2700$). Nevertheless, the analytical prediction based on the continuum model is in close agreement with the MD simulations for the cases when the adhesion energy and the number of water molecules combine to yield a blister in the shape of a spherical cap, such as $\Gamma_0 > 0.2$ J/m^2 and $N = 2700$ in Figure 6.2.

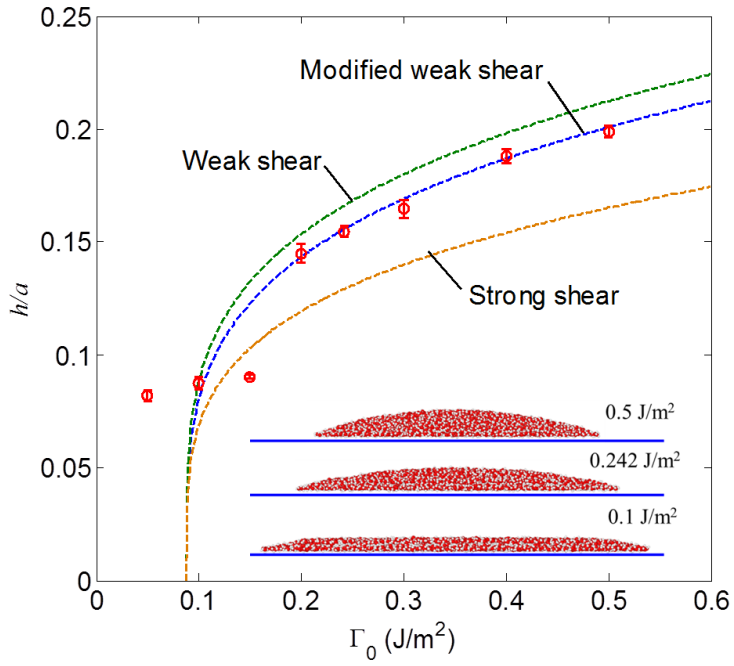

Figure 6.2: Analytical solution and MD simulations of water-filled blisters. Comparing simulation results (circular markers) with our simplified model assuming frictionless, sliding interface. The deviations, especially under small height or aspect ratio, are attributed to the size limitation of MD, which can induce discrete behaviors. The inset figure demonstrates how the shape of the blister changes for different values of the work of adhesion.

6.4.2 Pressure inside bubble

The pressure of the liquid as a function of aspect ratio was plotted in Figure 6.3 from both MD simulations and continuum modeling for relatively large (Γ_0 > 0.2 J/m^2) graphene/substrate adhesion, where water molecules take the shape of a spherical cap as assumed in the continuum model. Similarly, the pressures are bounded by the strong shear limit ($\lambda = \frac{2}{1-\nu}$) and the weak shear limit ($\lambda = 1$) for an infinitely large membrane, but do not align with the modified weak shear solution. The pressures obtained from MD simulations remain nearly constant while analytical predictions monotonically increase with aspect ratio for all types of shear conditions. The discrepancy may come from the approximate pressure measurement by force balance in MD simulation as described in Section 6.3.

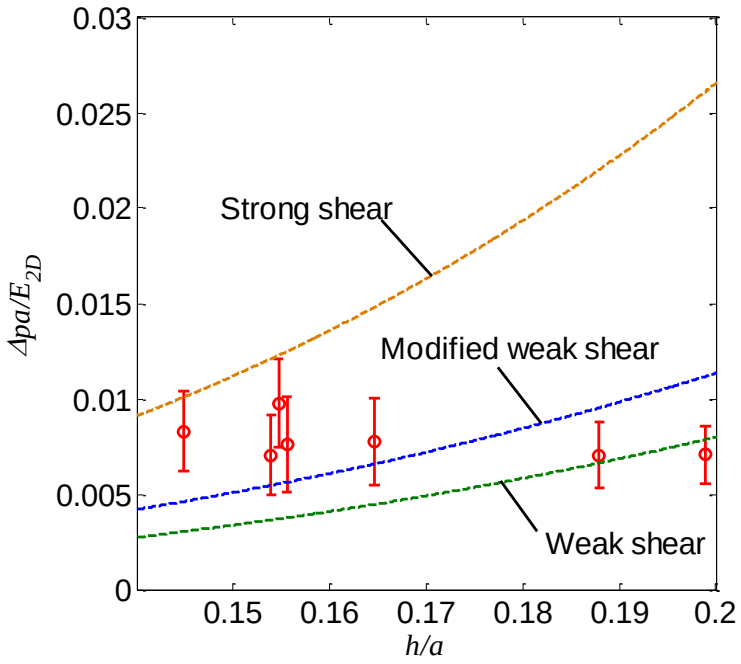

Figure 6.3: Normalized pressure for different aspect ratio *h*/*a*. The dots represent result from MD simulations while the dashed lines represent three types of analytical solutions.

6.4.3 Breakdown of the continuum model

By assuming the trapped water in the blister as a continuum liquid, the model predicts that the shape of the blister is close to a spherical cap. However, our MD simulations showed that the blister may take a different shape when the membrane/substrate adhesion energy was relatively low and the number of water molecules was small. Instead of a spherical cap, the top of the blister was flat, indicating that the water molecules formed discrete layers, similar to the simulation results in Chapter 5. In this case, the continuum model breaks down because the trapped water cannot be treated as a continuum liquid. It is found that the breakdown occurs when the height of the blister predicted by the continuum model drops below the thickness of three water monolayers. A simple analysis is presented below to predict the breakdown condition in terms of the adhesion energy and the number of water molecules.

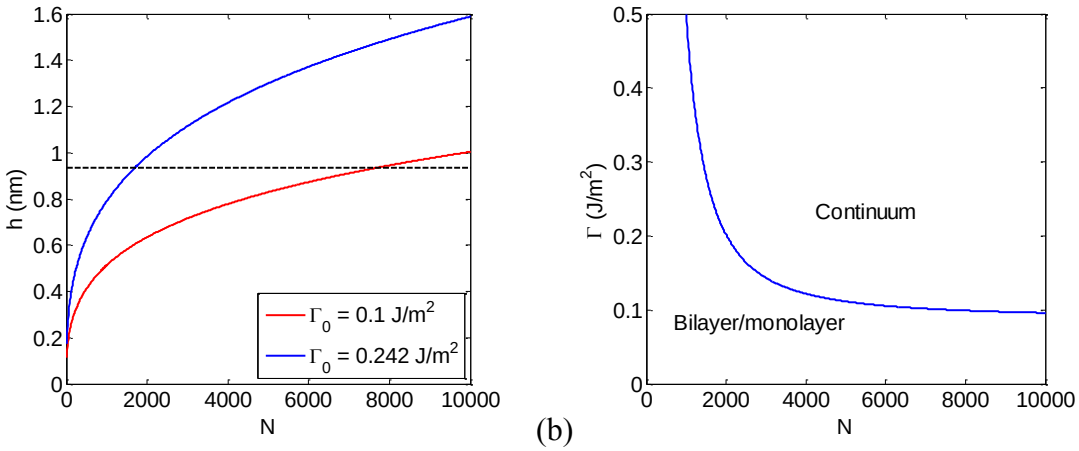

Figure 6.4: (a) The height of graphene blister as a function of the number of water molecules, predicted by the continuum model for Γ_0 = 0.1 J/m^2 and 0.242 J/m^2, where the dashed line indicates the critical height for the continuum model. (b) The breakdown limit for the continuum model, in terms of the adhesion energy Γ_0 and the number of water molecules N with the water contact angles being 60° and 40° for graphene and the substrate, respectively.

By combining Eq. (6.4) and Eq. (6.8), the height of the blister can be written as

$$h = \left(\frac{2N}{\pi\rho}\right)^{1/3}\left(\frac{h}{a}\right)^{2/3} = \left(\frac{2N}{\pi\rho}\right)^{1/3}\left(\phi\frac{\Gamma_0 - \gamma_w\left(\cos\theta_g + \cos\theta_s\right)}{E_{2D}}\right)^{1/6}. \quad (6.9)$$

Note that, under the condition of MD simulations, the parameter ϕ is given by Eq. (6.6) as a function of Γ_0 and N (or V). For a given adhesion energy Γ_0 and the water contact angles, the blister height decreases with decreasing number of water molecules as shown in Figure 6.4a. When the height drops below a critical level, the continuum model breaks down and the water molecules form discrete layers instead. The critical height is roughly three times the thickness of a water monolayer, which is estimated as $h_c = 3\rho^{-1/3} = 0.93$ nm. Thus, the continuum model holds only when $h > h_c$. For Γ_0 = 0.242 J/m^2, the continuum model breaks down when the number of water molecules N < 1690, while for Γ_0 = 0.1 J/m^2 the breakdown occurs for N < 7640. By setting $h = h_c$, we obtain the critical condition in terms of Γ_0 and N shown as the blue curve in Figure 6.4b. Furthermore, when the number of water molecules drops below a second critical level ($\sim 2\rho^{-1/3} = 0.62$ nm), we may expect the water molecules to form a single monolayer. However, since the continuum model has already broken down, it is not possible to predict exactly when the water monolayer would form.

The formation of layered water molecules was observed in MD simulations. We conducted MD simulations with different number of water molecules ranging from N = 50 to N = 4500 for different values of the adhesion energy Γ_0. The *h/a* ratio varying with respect to the number of water molecules is plotted in Figure 6.5, along with analytical predictions by the modified weak shear continuum model. For Γ_0 = 0.242 J/m^2, the MD results are in close agreement with the continuum prediction for N > 1600, below which the continuum model breaks down. The water molecules form a bilayer structure for 400 < N < 1600 and form a monolayer for N < 400. At each transition, from continuum to

bilayer or from bilayer to monolayer, the ratio *h/a* drops abruptly and then increases with decreasing *N*. This can be understood as the blister height changes discontinuously at the transition, whereas the blister radius decreases almost continuously with decreasing *N*. For Γ_0 = 0.1 J/m^2, however, the continuum regime was not reached for the limited number of water molecules in the MD simulations ($N < 5000$). In this case, the water molecules form a bilayer structure for $N > 400$ and transition to a monolayer for $N < 400$.

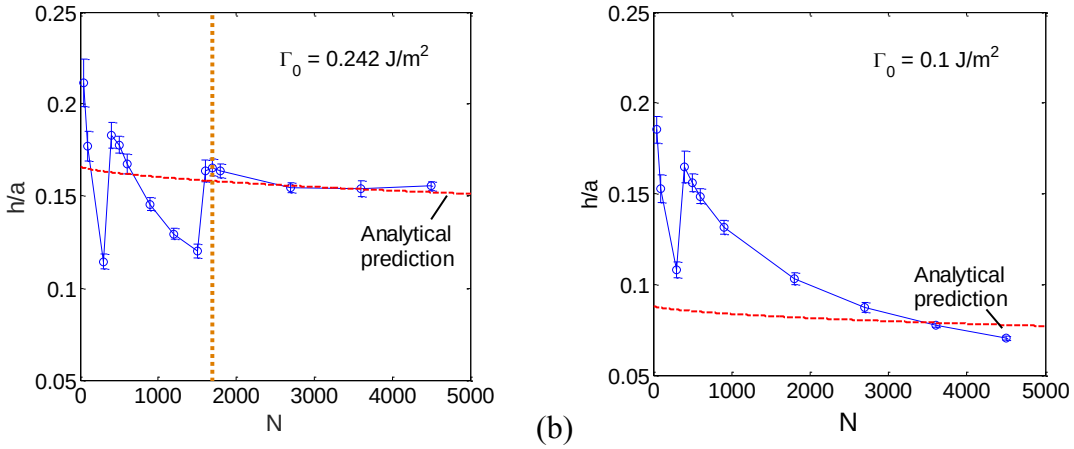

Figure 6.5: Blister aspect ratio for different numbers of water molecules, for (a) Γ_0 = 0.242 J/m^2 and (b) 0.1 J/m^2 with water contact angles being 60° and 40° for graphene and the substrate, respectively. The dashed line is predicted by the continuum model. The breakdown of the continuum model is predicted at N = 1690 for Γ_0 = 0.242 J/m^2 (dotted vertical line in (a)) and N = 7640 for Γ_0 = 0.1 J/m^2.

6.4.4 Profile of bubble

Then we take a closer look at the height profile of the bubble with various shapes with N = 2700, including both continuum spherical cap and discrete layers. A line scan is performed across the bubble to extract the height profiles of graphene membrane for different adhesion energy levels shown in Figure 6.6. As discussed above, a liquid bubble with spherical cap shape is observed for relatively large adhesion energies ($\Gamma_0 > 0.2$ J/m^2). With larger Γ_0, graphene membrane tends to squeeze the water molecules to form

a bubble with smaller in-plane radius and a larger height in order to reduce the adhesion energy at the graphene/substrate interface. Therefore, the height decreases and the radius increases with decreasing Γ_0, leading to smaller aspect ratio h/a. As the bubble height becomes smaller than h_c, a discrete double layer structure forms with a height h_2 close to 0.62 nm. The height and the radius of bilayer structure remain invariant for different adhesion energies. Due to the in-plane size limitation (~30 nm), monolayer structure doesn't appear for any small adhesion energies for $N = 2700$. Thus the height profile for a smaller number of water molecules ($N = 300$) is added in Figure 6.6. For small adhesion energy ($\Gamma_0 = 0.242$ J/m^2), monolayer structure is observed with a height h_1 around 0.35 nm. As discussed in Chapter 5, the graphene/substrate adhesion tends to compress water layers, leading to smaller interlayer distance; while the entropic repulsions of both graphene membrane and layered water, tend to increase the interlayer distance. Thus the heights h_1 and h_2 are the results of a combination of those two effects. The height h_1, which represents the interlayer distance between graphene membrane and layered water, is slightly larger than the expected distance $\delta_{CO} = 0.319$, indicating that the entropic repulsion effect is dominant between graphene membrane and layered water. The interlayer distance between water layers, represented by $h_2 - h_1 = 0.27$ nm, is slight smaller equilibrium thickness $\rho^{-1/3} = 0.31$ nm, indicating that the adhesive compression effect is dominant between water layers.

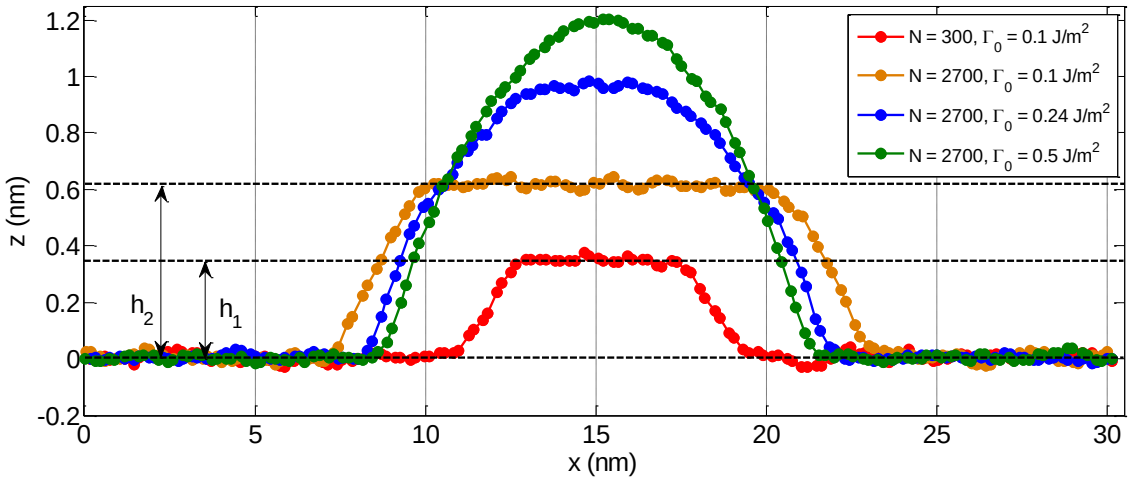

Figure 6.6: Height profiles of the bubble with $N = 2700$ for different adhesion energies from 0.1 J/m^2 to 0.5 J/m^2. Dots represent carbon atoms. The height profile with $N = 300$ and $\Gamma_0 = 0.1$ J/m^2 was added to show the monolayer structure.

6.5 APPLICATIONS OF 2D MATERIAL BLISTERS

Having validated our theoretical analysis with MD simulations, the model can be applied to experimentally measured aspect ratio data to extract the adhesion energy for graphene/substrate interfaces, as well as a variety of 2D material interfaces. Based on the present study, we propose that adhesion energy of a 2D material interface can be readily estimated by measuring the aspect ratio of spontaneously formed liquid-filled nanoblisters (if present). To calculate the adhesion energy, Eq. (6.4) is rewritten as

$$\Gamma_0 = \frac{E_{2D}h^4}{\phi a^4} + \gamma_w\left(\cos\theta_m + \cos\theta_s\right), \tag{6.10}$$

where θ_m is the water contact angle of 2D crystal membrane. It suggests that once the relevant material properties are available, the adhesion energy can be determined by just measuring the aspect ratio of a blister. By using the measurements in experiments and taking $\phi = 1.2$ for the weak interface model due to the typically weak interfacial shear

resistance for most of 2D material interfaces [86], we calculated the adhesion energy for graphene/SiO_2 interface is around 0.093 J/m^2, which is in reasonable agreement with values determined in similar systems via alternative methods (0.1-0.4 J/m^2)[29, 64].

If the affinity between the 2D crystal and its substrate is smaller than the affinity of the 2D crystal to the entrapped liquid, then the energetically favorable configuration should be the one that maximizes the contact between the 2D crystal and the liquid. To achieve this configuration, the liquid would spread out and form a monolayer or bilayer water structure as shown in our MD simulation. Our model can hence predict an upper limit for the adhesion energy of these 2D material interfaces as $\Gamma_0 \leq \gamma_w(\cos\theta_m + \cos\theta_s)$. This simple relation also quantitatively offers a criterion for the interesting observation of room temperature ice formation in a 2D nanochannel [88, 209-214]. This formula can also help explain the so called self-cleansing mechanism (formation of blisters) which is typically observed at atomically smooth, hydrophobic 2D heterostructure interfaces such as graphene/V_2O_5 [215].

Knowing the adhesion values of various van der Waals interfaces of 2D crystals is very beneficial to the fabrication of 2D crystal based devices. The fabrication typically involves either exfoliation of 2D layers from bulk crystal or transfer of synthesized 2D crystals from a donor substrate to a target substrate. Such processes rely on the competing adhesion energies between the 2D crystal and its "stamp", and the various surfaces that it contacts.

In addition to adhesion energy, our liquid-filled blister model can also predict the confinement pressure, Δp, inside the blisters and the strain distribution in the 2D membrane. The confinement pressure was previously estimated by capturing the pressure-sensitive molecules trapped inside the blister, studying the molecular structural and conformational changes, and observing the specific chemistry inside the blister [206,

208]. Now our model offers a direct relation between the confinement pressure, Δp and the geometry of the blisters (Section 6.3.2). The confining pressure across the membrane can be calculated from Eq. (6.7) with $\lambda \simeq 3.1$ for a graphene blister with a strong shear interface and $\lambda \simeq 1.6$ for a weak shear interface based on a more accurate Hencky's solution [86]. Note that unlike the interface adhesion, which only depends on the aspect ratio of the blister, the confinement pressure given in Eq. (6.7) has to be estimated with both the height and radius known. Note that the strain distribution in the blisters can also be estimated based on the membrane analysis [86].

Besides, in applications of 2D material blisters, it is vital that the blister shape and confinement conditions can be controlled. Equation (6.4) provides a direct guidance to the aspect ratio of the blisters. For a given interface with fixed adhesion, trapping different types of liquid with different surface energy and contact angles can tune the blister shape and membrane strain. In fact, a recent study by Neek-Amal *et al.* [196] demostrated the dependence of the shape of graphene nanoblisters on trapped substance. Our proposed strategies are also consistent with our MD simulations in Figure 6.2.

6.6 SUMMARY

In this chapter, liquid-filled graphene nanoblisters were studied by molecular dynamics simulations and a continuum membrane analysis. The aspect ratios of the blister and pressure across the membrane were calculated and compared. Discrete layered structures (monolayer and bilayer) were observed in our MD simulation for relatively small adhesion energy Γ_0 and few numbers of molecules *N*. The breakdown of continuum model and the transition to discrete layered structure were investigated. The liquid blister model can also be utilized to quantitatively characterize the adhesion

properties for graphene and other 2D materials based on the measured blister profiles. Alternatively, the blister shape, strain, and pressure characteristics could be controlled by tuning adhesion properties and trapped contents, which provides a viable guideline for the design of 2D material blisters for various applications.

Chapter 7 Conclusions

This dissertation presents a set of theoretical and numerical studies on adhesive interactions between monolayer graphene membranes and their substrates based on continuum mechanics models and molecular dynamics simulations.

7.1 SUMMARY

First, a numerical study on snap transitions of gas-filled graphene blisters is presented, based on a continuum model combining a nonlinear plate theory with a nonlinear traction-separation relation. Three types of blister configurations are considered. The numerical results provide a systematic understanding on the mechanics of graphene blisters, consistent with previously reported experiments. Of particular interest is that the numerical results may be used in conjunction with experiments for quantitative characterization of the interfacial properties of graphene and other two-dimensional (2D) membrane materials.

Next, a statistical mechanics analysis on thermal rippling of monolayer graphene supported on a rigid substrate was presented and compared with molecular dynamics simulations to reveal the entropic effects of thermal rippling on van der Waals interactions between graphene and the substrate. While the amplitude of thermal rippling is reduced by the adhesive interactions, the entropic contribution of thermal rippling leads to an effective repulsion. As a result, the equilibrium average separation increases and the effective adhesion energy decreases with increasing temperature. Moreover, the effect of a biaxial pre-strain in graphene is considered, and a buckling instability is predicted at a critical compressive strain that depends on both the temperature and the adhesive interactions. This motivated a systematic study on morphological transitions of

monolayer graphene on a substrate under uniaxial compressive strain, from rippling to wrinkling/buckling and to folding. Sinusoidal wrinkling occurs only for large equilibrium separation ($h_0 > 1$ nm), followed by localized buckling-delamination. Typically, with $h_0 <$ 1 nm, a rippling to buckling transition is predicted. High-aspect-ratio folding appears upon further compression.

Molecular dynamics simulations were performed to investigate wet adhesion of graphene on a wet substrate that is covered by a thin layer of water. Four stages of the traction-separation relations were identified and they were analyzed approximately by simple continuum models. Motivated by the MD simulations, we propose a modified nucleation theory for cavitation, taking into account the nonlinear elasticity of water and water contact angle of graphene. The results are compared and discussed to elucidate the effects of water contact angle of graphene and initial thickness of water film on cavitation and traction-separation relation. When the thickness of water layer is below 1 nm, the water molecules form discrete monolayer or bilayer structures, leading to different traction-separation behaviors. Finally, with a finite number of water molecules trapped between a monolayer graphene and its substrate, water-filled graphene blisters form spontaneously. Unlike gas-filled graphene blisters in previous studies, the shape and size of the water-filled graphene blister depend on the wetting properties of graphene and the substrate. Based on molecular dynamics simulations and a simple continuum model, the work of adhesion for the graphene/substrate interface may be estimated by measuring the aspect ratios of the graphene blisters. Moreover, the pressure inside the nanoblisters can also be estimated with both the radius and height of water-filled graphene blisters known. The results on wet adhesion and water-filled blisters can be readily extended to other 2D materials, which provide important implications for the fabrication and deformability of 2D heterostructures and devices.

7.2 FUTURE WORK

Since blister behavior depends sensitively on the pre-tension of graphene membrane, we can extend our analysis to take into account the effect of pretension for both gas-filled and liquid filled blisters. Recently, Lloyd *et al.* [66] observed adhesion hysteresis during inflation and deflation of pressurized bubbles. We can further extend our numerical models and simulations to explore the mechanism underlying the adhesion hysteresis, and predict the work of separation and work of adhesion between graphene membrane and substrate.

The present statistical mechanics analysis is limited by the harmonic approximation, while the anharmonic effect has been revealed from MD simulations. Thus it is worthwhile to extend current statistical mechanics analysis to include the anharmonic effect. The study of in-plane anharmonic effect may explain the in-plane intrinsic thermal expansion of graphene membranes, and the study of out-of-plane anharmonic effect may improve the prediction from harmonic analysis, especially for free standing graphene membrane at high temperature. In fact, by utilizing statistical mechanics of the fully coupled nonlinear system including all the coupling and anharmonic terms in the total elastic energy, Ahmadpoor *et al*. [62] studied the thermal rippling of freestanding graphene membranes. Using a variational perturbation method, Ahmadpoor *et al*. showed a power law dependency of the rippling amplitude on the temperature and the size of the sheet, in a good agreement with the MD simulations. Their derivations provide a transparent approach that can be extended to include effect of the substrate, multi-field couplings and anisotropy for other 2D materials. Besides, we have compared the potential energy between statistical mechanics analysis and MD

simulation. By separating the graphene from the substrate, we can extract the traction-separation relation and then integrate to obtain the adhesion energy. Or by performing steered MD simulations, it is possible to compare the adhesion energy instead of potential energy.

We have investigated the morphological transitions between various instabilities. A more detailed instability phase diagram can be constructed by conducting more simulations to determine the boundaries between unstable phases. A loading-unloading full cycle can be performed to explore the hysteresis between onset and disappearance of buckling instability. Moreover, similar to the wet adhesion in Chapter 5, water molecules can be sandwiched between graphene and substrate in MD simulations, to study the effect of water on the morphological transitions between various instabilities.

For the wet adhesion of graphene membrane, firstly, it is possible to reversely attach the graphene membrane to the wet substrate and measure the traction-separation relation during the full adhesion process, thus obtaining the work of adhesion. It would be interesting to compare the work of separation and work of adhesion, as well as to investigate the hysteresis in the traction-separation relation during separation and adhesion. Secondly, we can construct a realistic substrate with atoms arranged in a specific pattern instead of using a fictitious substrate in MD simulation. In a MD analysis of realistic substrate, the cavity is likely to penetrate the substrate under certain initial water thickness, yielding a different morphological evolution and traction-separation relation. Thirdly, a more appropriate water model, which accurately predicts the phase transitions of water, can be used to identify the phase for monolayer and bilayer water structures observed in our MD simulations.

For the current study, we mainly used the van der Waals formula to describe the interaction at graphene/substrate interface, which only captures the normal traction. This

can be further extended to consider the effects of interfacial friction and shear force on. Besides, because graphene can conform more closely to a substrate surface than conventional materials due to its high flexibility [63], the effect of surface roughness can also be included in future studies. Finally, our theoretical and numerical studies on adhesive interactions between graphene and substrate can be easily generalized to study other 2D materials on substrate, such as transition metal-dichalcogenides (TMDs, e.g., MoS2), hexagonal boron-nitride (h-BN), and black phosphorous or phosphorene, or extended to investigate the adhesive interactions between 2D materials.

References

1. Novoselov, K.S., et al., *Electric field effect in atomically thin carbon films.* science, 2004. **306**(5696): p. 666-669.
2. Meyer, J.C., et al., *The structure of suspended graphene sheets.* Nature, 2007. **446**(7131): p. 60.
3. Li, X., et al., *Large-area synthesis of high-quality and uniform graphene films on copper foils.* Science, 2009. **324**(5932): p. 1312-1314.
4. Tao, L., et al., *Synthesis of high quality monolayer graphene at reduced temperature on hydrogen-enriched evaporated copper (111) films.* Acs Nano, 2012. **6**(3): p. 2319-2325.
5. Chae, S.J., et al., *Synthesis of large‐area graphene layers on poly‐nickel substrate by chemical vapor deposition: wrinkle formation.* Advanced Materials, 2009. **21**(22): p. 2328-2333.
6. Kim, K.S., et al., *Large-scale pattern growth of graphene films for stretchable transparent electrodes.* nature, 2009. **457**(7230): p. 706.
7. Obraztsov, A.N., *Chemical vapour deposition: making graphene on a large scale.* Nature nanotechnology, 2009. **4**(4): p. 212.
8. Sutter, P.W., J.-I. Flege, and E.A. Sutter, *Epitaxial graphene on ruthenium.* Nature materials, 2008. **7**(5): p. 406.
9. Pan, Y., et al., *Highly ordered, millimeter‐scale, continuous, single‐crystalline graphene monolayer formed on Ru (0001).* Advanced Materials, 2009. **21**(27): p. 2777-2780.
10. Kwon, S.-Y., et al., *Growth of semiconducting graphene on palladium.* Nano letters, 2009. **9**(12): p. 3985-3990.
11. Gao, L., et al., *Repeated growth and bubbling transfer of graphene with millimetre-size single-crystal grains using platinum.* Nature communications, 2012. **3**: p. 699.
12. Sun, J., et al., *Large-area uniform graphene-like thin films grown by chemical vapor deposition directly on silicon nitride.* Applied Physics Letters, 2011. **98**(25): p. 252107.
13. Zhang, Y., et al., *Experimental observation of the quantum Hall effect and Berry's phase in graphene.* nature, 2005. **438**(7065): p. 201.
14. Bolotin, K.I., et al., *Ultrahigh electron mobility in suspended graphene.* Solid State Communications, 2008. **146**(9-10): p. 351-355.
15. Mayorov, A.S., et al., *Micrometer-scale ballistic transport in encapsulated graphene at room temperature.* Nano letters, 2011. **11**(6): p. 2396-2399.
16. Neugebauer, P., et al., *How perfect can graphene be?* Physical review letters, 2009. **103**(13): p. 136403.
17. Fratini, S. and F. Guinea, *Substrate-limited electron dynamics in graphene.* Physical Review B, 2008. **77**(19): p. 195415.
18. Qu, L., et al., *Nitrogen-doped graphene as efficient metal-free electrocatalyst for oxygen reduction in fuel cells.* ACS nano, 2010. **4**(3): p. 1321-1326.

19. Panchakarla, L., et al., *Synthesis, Structure, and Properties of Boron‐and Nitrogen‐Doped Graphene.* Advanced Materials, 2009. **21**(46): p. 4726-4730.
20. Balandin, A.A., et al., *Superior thermal conductivity of single-layer graphene.* Nano letters, 2008. **8**(3): p. 902-907.
21. Mak, K.F., et al., *Measurement of the optical conductivity of graphene.* Physical review letters, 2008. **101**(19): p. 196405.
22. Nair, R.R., et al., *Fine structure constant defines visual transparency of graphene.* Science, 2008. **320**(5881): p. 1308-1308.
23. Li, Z., et al., *Dirac charge dynamics in graphene by infrared spectroscopy.* Nature Physics, 2008. **4**(7): p. 532.
24. Wang, F., et al., *Gate-variable optical transitions in graphene.* science, 2008. **320**(5873): p. 206-209.
25. Bhimanapati, G.R., et al., *Recent advances in two-dimensional materials beyond graphene.* Acs Nano, 2015. **9**(12): p. 11509-11539.
26. Butler, S.Z., et al., *Progress, challenges, and opportunities in two-dimensional materials beyond graphene.* ACS nano, 2013. **7**(4): p. 2898-2926.
27. Koenig, S.P., et al., *Ultrastrong adhesion of graphene membranes.* Nature nanotechnology, 2011. **6**(9): p. 543.
28. Liu, X., et al., *Observation of pull-in instability in graphene membranes under interfacial forces.* Nano letters, 2013. **13**(5): p. 2309-2313.
29. Boddeti, N.G., et al., *Graphene blisters with switchable shapes controlled by pressure and adhesion.* Nano letters, 2013. **13**(12): p. 6216-6221.
30. Lee, C., et al., *Measurement of the elastic properties and intrinsic strength of monolayer graphene.* science, 2008. **321**(5887): p. 385-388.
31. Freund, L.B. and S. Suresh, *Thin film materials: stress, defect formation and surface evolution*. 2004: Cambridge University Press.
32. Nicklow, R., N. Wakabayashi, and H. Smith, *Lattice dynamics of pyrolytic graphite.* Physical Review B, 1972. **5**(12): p. 4951.
33. Kudin, K.N., G.E. Scuseria, and B.I. Yakobson, *C 2 F, BN, and C nanoshell elasticity from ab initio computations.* Physical Review B, 2001. **64**(23): p. 235406.
34. Wei, X., et al., *Nonlinear elastic behavior of graphene: Ab initio calculations to continuum description.* Physical Review B, 2009. **80**(20): p. 205407.
35. Koskinen, P. and O.O. Kit, *Approximate modeling of spherical membranes.* Physical Review B, 2010. **82**(23): p. 235420.
36. Wei, Y., et al., *Bending rigidity and Gaussian bending stiffness of single-layered graphene.* Nano letters, 2012. **13**(1): p. 26-30.
37. Brenner, D.W., *Empirical potential for hydrocarbons for use in simulating the chemical vapor deposition of diamond films.* Physical review B, 1990. **42**(15): p. 9458.
38. Brenner, D.W., et al., *A second-generation reactive empirical bond order (REBO) potential energy expression for hydrocarbons.* Journal of Physics: Condensed Matter, 2002. **14**(4): p. 783.

39. Stuart, S.J., A.B. Tutein, and J.A. Harrison, *A reactive potential for hydrocarbons with intermolecular interactions.* The Journal of chemical physics, 2000. **112**(14): p. 6472-6486.
40. Lindsay, L. and D. Broido, *Optimized Tersoff and Brenner empirical potential parameters for lattice dynamics and phonon thermal transport in carbon nanotubes and graphene.* Physical Review B, 2010. **81**(20): p. 205441.
41. Los, J.H., et al., *Improved long-range reactive bond-order potential for carbon. I. Construction.* Physical Review B, 2005. **72**(21): p. 214102.
42. Liu, F., P. Ming, and J. Li, *Ab initio calculation of ideal strength and phonon instability of graphene under tension.* Physical Review B, 2007. **76**(6): p. 064120.
43. Akinwande, D., et al., *A review on mechanics and mechanical properties of 2D materials—Graphene and beyond.* Extreme Mechanics Letters, 2017. **13**: p. 42-77.
44. Arroyo, M. and T. Belytschko, *Finite crystal elasticity of carbon nanotubes based on the exponential Cauchy-Born rule.* Physical Review B, 2004. **69**(11): p. 115415.
45. Huang, Y., J. Wu, and K.-C. Hwang, *Thickness of graphene and single-wall carbon nanotubes.* Physical review B, 2006. **74**(24): p. 245413.
46. Lu, Q. and R. Huang, *Nonlinear mechanics of single-atomic-layer graphene sheets.* International Journal of Applied Mechanics, 2009. **1**(03): p. 443-467.
47. Wang, P., et al., *Numerical analysis of circular graphene bubbles.* Journal of Applied Mechanics, 2013. **80**(4): p. 040905.
48. Lu, Q., M. Arroyo, and R. Huang, *Elastic bending modulus of monolayer graphene.* Journal of Physics D: Applied Physics, 2009. **42**(10): p. 102002.
49. Fasolino, A., J. Los, and M.I. Katsnelson, *Intrinsic ripples in graphene.* Nature materials, 2007. **6**(11): p. 858.
50. Bangert, U., et al., *Manifestation of ripples in free-standing graphene in lattice images obtained in an aberration-corrected scanning transmission electron microscope.* physica status solidi (a), 2009. **206**(6): p. 1117-1122.
51. Xu, P., et al., *Unusual ultra-low-frequency fluctuations in freestanding graphene.* Nature communications, 2014. **5**: p. 3720.
52. Košmrlj, A. and D.R. Nelson, *Response of thermalized ribbons to pulling and bending.* Physical Review B, 2016. **93**(12): p. 125431.
53. Gao, W. and R. Huang, *Thermomechanics of monolayer graphene: Rippling, thermal expansion and elasticity.* Journal of the Mechanics and Physics of Solids, 2014. **66**: p. 42-58.
54. Zhao, H. and N. Aluru, *Temperature and strain-rate dependent fracture strength of graphene.* Journal of Applied Physics, 2010. **108**(6): p. 064321.
55. Zakharchenko, K., M. Katsnelson, and A. Fasolino, *Finite temperature lattice properties of graphene beyond the quasiharmonic approximation.* Physical review letters, 2009. **102**(4): p. 046808.
56. Chen, S. and D. Chrzan, *Monte Carlo simulation of temperature-dependent elastic properties of graphene.* Physical Review B, 2011. **84**(19): p. 195409.

57. Los, J., A. Fasolino, and M. Katsnelson, *Scaling behavior and strain dependence of in-plane elastic properties of graphene.* Physical review letters, 2016. **116**(1): p. 015901.
58. Mounet, N. and N. Marzari, *First-principles determination of the structural, vibrational and thermodynamic properties of diamond, graphite, and derivatives.* Physical Review B, 2005. **71**(20): p. 205214.
59. Jiang, J.-W., J.-S. Wang, and B. Li, *Thermal expansion in single-walled carbon nanotubes and graphene: Nonequilibrium Green's function approach.* Physical Review B, 2009. **80**(20): p. 205429.
60. Pozzo, M., et al., *Thermal Expansion of Supported and Freestanding Graphene: Lattice Constant versus Interatomic Distance.* Physical Review Letters, 2011. **106**(13): p. 135501.
61. Blees, M.K., et al., *Graphene kirigami.* Nature, 2015. **524**(7564): p. 204.
62. Ahmadpoor, F., et al., *Thermal fluctuations and effective bending stiffness of elastic thin sheets and graphene: A nonlinear analysis.* Journal of the Mechanics and Physics of Solids, 2017. **107**: p. 294-319.
63. Lui, C.H., et al., *Ultraflat graphene.* Nature, 2009. **462**(7271): p. 339.
64. Zong, Z., et al., *Direct measurement of graphene adhesion on silicon surface by intercalation of nanoparticles*. 2010, AIP.
65. Boddeti, N.G., et al., *Mechanics of adhered, pressurized graphene blisters.* Journal of Applied Mechanics, 2013. **80**(4): p. 040909.
66. Lloyd, D., et al., *Adhesion, Stiffness, and Instability in Atomically Thin MoS2 Bubbles.* Nano letters, 2017. **17**(9): p. 5329-5334.
67. Wang, P., K.M. Liechti, and R. Huang, *Snap transitions of pressurized graphene blisters.* Journal of Applied Mechanics, 2016. **83**(7): p. 071002.
68. Cao, Z., et al., *A blister test for interfacial adhesion of large-scale transferred graphene.* Carbon, 2014. **69**: p. 390-400.
69. Jensen, H.M., *Analysis of mode mixity in blister tests.* International journal of fracture, 1998. **94**(1): p. 79.
70. Cao, Z., et al., *Mixed-mode interactions between graphene and substrates by blister tests.* Journal of Applied Mechanics, 2015. **82**(8): p. 081008.
71. Evans, A.G. and J.W. Hutchinson, *Effects of non-planarity on the mixed mode fracture resistance of bimaterial interfaces.* Acta Metallurgica, 1989. **37**(3): p. 909-916.
72. Na, S.R., et al., *Selective mechanical transfer of graphene from seed copper foil using rate effects.* ACS nano, 2015. **9**(2): p. 1325-1335.
73. Yoon, T., et al., *Direct measurement of adhesion energy of monolayer graphene as-grown on copper and its application to renewable transfer process.* Nano letters, 2012. **12**(3): p. 1448-1452.
74. Na, S., et al., *Clean graphene interfaces by selective dry transfer for large area silicon integration.* Nanoscale, 2016. **8**(14): p. 7523-7533.
75. Ishigami, M., et al., *Atomic structure of graphene on SiO2.* Nano letters, 2007. **7**(6): p. 1643-1648.

76. Jiang, T. and Y. Zhu, *Measuring graphene adhesion using atomic force microscopy with a microsphere tip.* Nanoscale, 2015. **7**(24): p. 10760-10766.
77. Suk, J.W., et al., *Probing the adhesion interactions of graphene on silicon oxide by nanoindentation.* Carbon, 2016. **103**: p. 63-72.
78. Hutchinson, J. and A. Evans, *Mechanics of materials: top-down approaches to fracture.* Acta materialia, 2000. **48**(1): p. 125-135.
79. Bao, G. and Z. Suo, *Remarks on crack-bridging concepts.* Applied Mechanics Reviews, 1992. **45**(8): p. 355-366.
80. Na, S.R., et al., *Ultra long-range interactions between large area graphene and silicon.* ACS nano, 2014. **8**(11): p. 11234-11242.
81. Rudenko, A., et al., *Graphene adhesion on mica: Role of surface morphology.* Physical Review B, 2011. **83**(4): p. 045409.
82. Gao, W., et al., *Interfacial adhesion between graphene and silicon dioxide by density functional theory with van der Waals corrections.* Journal of Physics D: Applied Physics, 2014. **47**(25): p. 255301.
83. Aitken, Z.H. and R. Huang, *Effects of mismatch strain and substrate surface corrugation on morphology of supported monolayer graphene.* Journal of Applied Physics, 2010. **107**(12): p. 123531.
84. Kumar, S., D. Parks, and K. Kamrin, *Mechanistic origin of the ultrastrong adhesion between graphene and a-SiO2: beyond van der Waals.* ACS nano, 2016. **10**(7): p. 6552-6562.
85. Gao, W. and R. Huang, *Effect of surface roughness on adhesion of graphene membranes.* Journal of Physics D: Applied Physics, 2011. **44**(45): p. 452001.
86. Sanchez, D.A., et al., *Mechanics of Spontaneously Formed Nanoblisters Trapped by Transferred 2D Crystals.* Under review, 2018.
87. Gao, W., K.M. Liechti, and R. Huang, *Wet adhesion of graphene.* Extreme Mechanics Letters, 2015. **3**: p. 130-140.
88. Xu, K., P. Cao, and J.R. Heath, *Graphene visualizes the first water adlayers on mica at ambient conditions.* Science, 2010. **329**(5996): p. 1188-1191.
89. Algara-Siller, G., et al., *Square ice in graphene nanocapillaries.* Nature, 2015. **519**(7544): p. 443.
90. Allen, M.G. and S.D. Senturia, *Application of the island blister test for thin film adhesion measurement.* The Journal of Adhesion, 1989. **29**(1-4): p. 219-231.
91. Jensen, H.M., *The blister test for interface toughness measurement.* Engineering Fracture Mechanics, 1991. **40**(3): p. 475-486.
92. Lai, Y.-H. and D.A. Dillard, *A study of the fracture efficiency parameter of blister tests for films and coatings.* Journal of adhesion science and technology, 1994. **8**(6): p. 663-678.
93. Xu, D. and K. Liechti, *Bulge testing transparent thin films with moiré deflectometry.* Experimental mechanics, 2010. **50**(2): p. 217-225.
94. Stolyarova, E., et al., *Observation of graphene bubbles and effective mass transport under graphene films.* Nano letters, 2008. **9**(1): p. 332-337.

95. Georgiou, T., et al., *Graphene bubbles with controllable curvature.* Applied Physics Letters, 2011. **99**(9): p. 093103.
96. Bunch, J.S., et al., *Impermeable atomic membranes from graphene sheets.* Nano letters, 2008. **8**(8): p. 2458-2462.
97. Herbig, C., et al., *Xe irradiation of graphene on Ir (111): From trapping to blistering.* Physical Review B, 2015. **92**(8): p. 085429.
98. Levy, N., et al., *Strain-induced pseudo–magnetic fields greater than 300 tesla in graphene nanobubbles.* Science, 2010. **329**(5991): p. 544-547.
99. Lu, J., A.C. Neto, and K.P. Loh, *Transforming moiré blisters into geometric graphene nano-bubbles.* Nature Communications, 2012. **3**: p. 823.
100. Pan, W., et al., *Biaxial compressive strain engineering in graphene/boron nitride heterostructures.* Scientific reports, 2012. **2**: p. 893.
101. Qi, Z., et al., *Pseudomagnetic fields in graphene nanobubbles of constrained geometry: A molecular dynamics study.* Physical Review B, 2014. **90**(12): p. 125419.
102. Zabel, J., et al., *Raman spectroscopy of graphene and bilayer under biaxial strain: bubbles and balloons.* Nano letters, 2012. **12**(2): p. 617-621.
103. Yue, K., et al., *Analytical methods for the mechanics of graphene bubbles.* Journal of Applied Physics, 2012. **112**(8): p. 083512.
104. Lu, Q., W. Gao, and R. Huang, *Atomistic simulation and continuum modeling of graphene nanoribbons under uniaxial tension.* Modelling and Simulation in Materials Science and Engineering, 2011. **19**(5): p. 054006.
105. Helfrich, W., *Elastic properties of lipid bilayers: theory and possible experiments.* Zeitschrift für Naturforschung C, 1973. **28**(11-12): p. 693-703.
106. Timoshenko, S.P. and S. Woinowsky-Krieger, *Theory of plates and shells*. 1959: McGraw-hill.
107. Vanin, M., et al., *Graphene on metals: A van der Waals density functional study.* Physical Review B, 2010. **81**(8): p. 081408.
108. Gupta, A., et al., *Raman scattering from high-frequency phonons in supported n-graphene layer films.* Nano letters, 2006. **6**(12): p. 2667-2673.
109. Sonde, S., et al., *Dielectric thickness dependence of capacitive behavior in graphene deposited on silicon dioxide.* Journal of Vacuum Science & Technology B: Microelectronics and Nanometer Structures Processing, Measurement, and Phenomena, 2009. **27**(2): p. 868-873.
110. Komaragiri, U., M. Begley, and J. Simmonds, *The mechanical response of freestanding circular elastic films under point and pressure loads.* Journal of applied mechanics, 2005. **72**(2): p. 203-212.
111. Hencky, H., *On the stress state in circular plates with vanishing bending stiffness.* Z. Math. Phys, 1915. **63**: p. 311-317.
112. Springman, R.M. and J.L. Bassani, *Snap transitions in adhesion.* Journal of the Mechanics and Physics of Solids, 2008. **56**(6): p. 2358-2380.
113. Li, T. and Z. Zhang, *Snap-through instability of graphene on substrates.* Nanoscale research letters, 2010. **5**(1): p. 169.

114. Nelson, D. and L. Peliti, *Fluctuations in membranes with crystalline and hexatic order.* Journal de physique, 1987. **48**(7): p. 1085-1092.
115. Aronovitz, J.A. and T.C. Lubensky, *Fluctuations of solid membranes.* Physical review letters, 1988. **60**(25): p. 2634.
116. Los, J., et al., *Scaling properties of flexible membranes from atomistic simulations: application to graphene.* Physical Review B, 2009. **80**(12): p. 121405.
117. Zan, R., et al., *Scanning tunnelling microscopy of suspended graphene.* Nanoscale, 2012. **4**(10): p. 3065-3068.
118. Stolyarova, E., et al., *High-resolution scanning tunneling microscopy imaging of mesoscopic graphene sheets on an insulating surface.* Proceedings of the National Academy of Sciences, 2007. **104**(22): p. 9209-9212.
119. Xu, K., P. Cao, and J.R. Heath, *Scanning tunneling microscopy characterization of the electrical properties of wrinkles in exfoliated graphene monolayers.* Nano letters, 2009. **9**(12): p. 4446-4451.
120. Ni, G.-X., et al., *Quasi-periodic nanoripples in graphene grown by chemical vapor deposition and its impact on charge transport.* ACS nano, 2012. **6**(2): p. 1158-1164.
121. Zhu, W., et al., *Structure and electronic transport in graphene wrinkles.* Nano letters, 2012. **12**(7): p. 3431-3436.
122. Jiang, T., R. Huang, and Y. Zhu, *Interfacial sliding and buckling of monolayer graphene on a stretchable substrate.* Advanced Functional Materials, 2014. **24**(3): p. 396-402.
123. Brennan, C.J., et al., *Interface adhesion between 2D materials and elastomers measured by buckle delaminations.* Advanced Materials Interfaces, 2015. **2**(16).
124. Amorim, B., et al., *Novel effects of strains in graphene and other two dimensional materials.* Physics Reports, 2016. **617**: p. 1-54.
125. Ninham, B.W., V.A. Parsegian, and G.H. Weiss, *On the macroscopic theory of temperature-dependent van der Waals forces.* Journal of Statistical Physics, 1970. **2**(4): p. 323-328.
126. Boyer, T.H., *Temperature dependence of Van der Waals forces in classical electrodynamics with classical electromagnetic zero-point radiation.* Physical Review A, 1975. **11**(5): p. 1650.
127. Wennerström, H., J. Daicic, and B. Ninham, *Temperature dependence of atom-atom interactions.* Physical Review A, 1999. **60**(3): p. 2581.
128. Berman, P., G. Ford, and P. Milonni, *Nonperturbative calculation of the London–van der Waals interaction potential.* Physical Review A, 2014. **89**(2): p. 022127.
129. Weiner, J., *Statistical Mechanics of Elasticity*. 2002: Courier Corporation.
130. Pathria, R. and P.D. Beale, *Statistical mechanics.* Butter worth, 1996.
131. Helfrich, W. and R.-M. Servuss, *Undulations, steric interaction and cohesion of fluid membranes.* Il Nuovo Cimento D, 1984. **3**(1): p. 137-151.

132. Freund, L., *Entropic pressure between biomembranes in a periodic stack due to thermal fluctuations.* Proceedings of the National Academy of Sciences, 2013. **110**(6): p. 2047-2051.
133. Hanlumyuang, Y., L. Liu, and P. Sharma, *Revisiting the entropic force between fluctuating biological membranes.* Journal of the Mechanics and Physics of Solids, 2014. **63**: p. 179-186.
134. Pierson, H.O., *Handbook of carbon, graphite, diamond, and fullerenes*. 1993, Noyes Publications. p. 59-60.
135. Plimpton, S., *Fast parallel algorithms for short-range molecular dynamics.* Journal of computational physics, 1995. **117**(1): p. 1-19.
136. Park, S., et al., *Free energy calculation from steered molecular dynamics simulations using Jarzynski's equality.* The Journal of chemical physics, 2003. **119**(6): p. 3559-3566.
137. Moon, M.-W., et al., *An experimental study of the influence of imperfections on the buckling of compressed thin films.* Acta Materialia, 2002. **50**(5): p. 1219-1227.
138. Zhang, K. and M. Arroyo, *Adhesion and friction control localized folding in supported graphene.* Journal of Applied Physics, 2013. **113**(19): p. 193501.
139. Zhang, K. and M. Arroyo, *Understanding and strain-engineering wrinkle networks in supported graphene through simulations.* Journal of the Mechanics and Physics of Solids, 2014. **72**: p. 61-74.
140. Al-Mulla, T., Z. Qin, and M.J. Buehler, *Crumpling deformation regimes of monolayer graphene on substrate: a molecular mechanics study.* Journal of Physics: Condensed Matter, 2015. **27**(34): p. 345401.
141. Bao, W., et al., *Controlled ripple texturing of suspended graphene and ultrathin graphite membranes.* Nature nanotechnology, 2009. **4**(9): p. 562.
142. Li, Z., et al., *Deformation of wrinkled graphene.* Acs Nano, 2015. **9**(4): p. 3917-3925.
143. Wang, Y., et al., *Super-elastic graphene ripples for flexible strain sensors.* ACS nano, 2011. **5**(5): p. 3645-3650.
144. Zang, J., et al., *Multifunctionality and control of the crumpling and unfolding of large-area graphene.* Nature materials, 2013. **12**(4): p. 321.
145. Guo, F., et al., *Hydration-responsive folding and unfolding in graphene oxide liquid crystal phases.* Acs Nano, 2011. **5**(10): p. 8019-8025.
146. Elias, D.C., et al., *Control of graphene's properties by reversible hydrogenation: evidence for graphane.* Science, 2009. **323**(5914): p. 610-613.
147. Jiang, H., et al., *Finite deformation mechanics in buckled thin films on compliant supports.* Proceedings of the National Academy of Sciences, 2007. **104**(40): p. 15607-15612.
148. Vella, D., et al., *The macroscopic delamination of thin films from elastic substrates.* Proceedings of the National Academy of Sciences, 2009. **106**(27): p. 10901-10906.

149. Pan, K., et al., *Nonlinear analysis of compressed elastic thin films on elastic substrates: From wrinkling to buckle-delamination.* International Journal of Solids and Structures, 2014. **51**(21-22): p. 3715-3726.
150. Popov, A.M., et al., *AA stacking, tribological and electronic properties of double-layer graphene with krypton spacer.* The Journal of chemical physics, 2013. **139**(15): p. 154705.
151. Zhao, J., et al., *Two-dimensional membrane as elastic shell with proof on the folds revealed by three-dimensional atomic mapping.* Nature communications, 2015. **6**: p. 8935.
152. Wang, P., W. Gao, and R. Huang, *Entropic effects of thermal rippling on van der Waals interactions between monolayer graphene and a rigid substrate.* Journal of Applied Physics, 2016. **119**(7): p. 074305.
153. Huang, R., *Graphene: Show of adhesive strength.* Nature nanotechnology, 2011. **6**(9): p. 537.
154. Lu, Z. and M.L. Dunn, *van der Waals adhesion of graphene membranes.* Journal of Applied Physics, 2010. **107**(4): p. 044301.
155. Li, T. and Z. Zhang, *Substrate-regulated morphology of graphene.* Journal of Physics D: Applied Physics, 2010. **43**(7): p. 075303.
156. Li, X., et al., *Transfer of Large-Area Graphene Films for High-Performance Transparent Conductive Electrodes.* Nano Letters, 2009. **9**(12): p. 4359-4363.
157. Wang, S., et al., *Wettability and surface free energy of graphene films.* Langmuir, 2009. **25**(18): p. 11078-11081.
158. Shin, Y.J., et al., *Surface-energy engineering of graphene.* Langmuir, 2010. **26**(6): p. 3798-3802.
159. Kim, K.-S., et al., *Chemical vapor deposition-grown graphene: the thinnest solid lubricant.* ACS nano, 2011. **5**(6): p. 5107-5114.
160. Raj, R., S.C. Maroo, and E.N. Wang, *Wettability of graphene.* Nano letters, 2013. **13**(4): p. 1509-1515.
161. Taherian, F., et al., *What is the contact angle of water on graphene?* Langmuir, 2013. **29**(5): p. 1457-1465.
162. Li, Z., et al., *Effect of airborne contaminants on the wettability of supported graphene and graphite.* Nature materials, 2013. **12**(10): p. 925.
163. Kozbial, A., et al., *Study on the surface energy of graphene by contact angle measurements.* Langmuir, 2014. **30**(28): p. 8598-8606.
164. Dong, J. and X. Li, *Rainbow connection number, bridges and radius.* Graphs and Combinatorics, 2013. **29**(6): p. 1733-1739.
165. Rafiee, J., et al., *Wetting transparency of graphene.* Nature materials, 2012. **11**(3): p. 217.
166. Shih, C.-J., et al., *Breakdown in the wetting transparency of graphene.* Physical review letters, 2012. **109**(17): p. 176101.
167. Edelsbrunner, H. and E.P. Mücke, *Three-dimensional alpha shapes.* ACM Transactions on Graphics (TOG), 1994. **13**(1): p. 43-72.

168. Stukowski, A., *Visualization and analysis of atomistic simulation data with OVITO–the Open Visualization Tool.* Modelling and Simulation in Materials Science and Engineering, 2009. **18**(1): p. 015012.
169. Wang, P., et al., *Cavitation of water by volume-controlled stretching.* Extreme Mechanics Letters, 2017. **11**: p. 59-67.
170. Stillinger, F.H. and A. Rahman, *Improved simulation of liquid water by molecular dynamics.* The Journal of Chemical Physics, 1974. **60**(4): p. 1545-1557.
171. Berendsen, H., J. Grigera, and T. Straatsma, *The missing term in effective pair potentials.* Journal of Physical Chemistry, 1987. **91**(24): p. 6269-6271.
172. Jorgensen, W.L., et al., *Comparison of simple potential functions for simulating liquid water.* The Journal of chemical physics, 1983. **79**(2): p. 926-935.
173. Mahoney, M.W. and W.L. Jorgensen, *A five-site model for liquid water and the reproduction of the density anomaly by rigid, nonpolarizable potential functions.* The Journal of Chemical Physics, 2000. **112**(20): p. 8910-8922.
174. Abascal, J.L. and C. Vega, *A general purpose model for the condensed phases of water: TIP4P/2005.* The Journal of chemical physics, 2005. **123**(23): p. 234505.
175. Ren, P. and J.W. Ponder, *Polarizable atomic multipole water model for molecular mechanics simulation.* The Journal of Physical Chemistry B, 2003. **107**(24): p. 5933-5947.
176. Laury, M.L., et al., *Revised parameters for the AMOEBA polarizable atomic multipole water model.* The Journal of Physical Chemistry B, 2015. **119**(29): p. 9423-9437.
177. Vega, C. and E. De Miguel, *Surface tension of the most popular models of water by using the test-area simulation method.* The Journal of chemical physics, 2007. **126**(15): p. 154707.
178. Hockney, R.W. and J.W. Eastwood, *Computer simulation using particles*. 1988: crc Press.
179. Ma, J., et al., *Adsorption and diffusion of water on graphene from first principles.* Physical Review B, 2011. **84**(3): p. 033402.
180. Werder, T., et al., *On the water− carbon interaction for use in molecular dynamics simulations of graphite and carbon nanotubes.* The Journal of Physical Chemistry B, 2003. **107**(6): p. 1345-1352.
181. Werder, T., J. Walther, and P. Koumoutsakos. *Hydrodynamics of Carbon Nanotubes-Contact Angle and Hydrophobic Hydration*. in *Technical Proceedings of the Second International Conference on Computational Nanoscience and Nanotechnology-ICCN*. 2002.
182. Kozbial, A., et al., *Understanding the intrinsic water wettability of graphite.* Carbon, 2014. **74**: p. 218-225.
183. Israelachvili, J., *Intermolecular and Surface Forces 2nd edn (New York: Academic)*. 1992.
184. Debenedetti, P.G., *Metastable liquids: concepts and principles*. 1996: Princeton University Press.

185. Butt, H.-J. and M. Kappl, *Normal capillary forces.* Advances in colloid and interface science, 2009. **146**(1-2): p. 48-60.
186. Orr, F., L. Scriven, and A.P. Rivas, *Pendular rings between solids: meniscus properties and capillary force.* Journal of Fluid Mechanics, 1975. **67**(4): p. 723-742.
187. Qian, J. and H. Gao, *Scaling effects of wet adhesion in biological attachment systems.* Acta biomaterialia, 2006. **2**(1): p. 51-58.
188. Rayleigh, L., *On the instability of jets.* Proceedings of the London mathematical society, 1878. **1**(1): p. 4-13.
189. Eggers, J., *Nonlinear dynamics and breakup of free-surface flows.* Reviews of Modern Physics, 1997. **69**(3): p. 865-929.
190. Gao, W., *Thermomechanical and interfacial properties of monolayer graphene*. 2014.
191. Caupin, F. and E. Herbert, *Cavitation in water: a review.* Comptes Rendus Physique, 2006. **7**(9-10): p. 1000-1017.
192. Fisher, J.C., *The fracture of liquids.* Journal of applied Physics, 1948. **19**(11): p. 1062-1067.
193. Caupin, F., et al., *Exploring water and other liquids at negative pressure.* Journal of Physics: Condensed Matter, 2012. **24**(28): p. 284110.
194. Kimmel, G.A., et al., *No confinement needed: Observation of a metastable hydrophobic wetting two-layer ice on graphene.* Journal of the American Chemical Society, 2009. **131**(35): p. 12838-12844.
195. Pizzocchero, F., et al., *The hot pick-up technique for batch assembly of van der Waals heterostructures.* Nature communications, 2016. **7**: p. 11894.
196. Ghorbanfekr-Kalashami, H., et al., *Dependence of the shape of graphene nanobubbles on trapped substance.* Nature communications, 2017. **8**: p. 15844.
197. Bampoulis, P., et al., *Hydrophobic ice confined between graphene and mos2.* The Journal of Physical Chemistry C, 2016. **120**(47): p. 27079-27084.
198. Khestanova, E., et al., *Universal shape and pressure inside bubbles appearing in van der Waals heterostructures.* Nature communications, 2016. **7**: p. 12587.
199. Haigh, S., et al., *Cross-sectional imaging of individual layers and buried interfaces of graphene-based heterostructures and superlattices.* Nature materials, 2012. **11**(9): p. 764.
200. Cao, P., et al., *The microscopic structure of adsorbed water on hydrophobic surfaces under ambient conditions.* Nano letters, 2011. **11**(12): p. 5581-5586.
201. Novoselov, K., et al., *2D materials and van der Waals heterostructures.* Science, 2016. **353**(6298): p. aac9439.
202. An, H., et al., *Graphene nanobubbles produced by water splitting.* Nano letters, 2017. **17**(5): p. 2833-2838.
203. Falin, A., et al., *Mechanical properties of atomically thin boron nitride and the role of interlayer interactions.* Nature communications, 2017. **8**: p. 15815.
204. Alam, A., M. Howlader, and M. Deen, *The effects of oxygen plasma and humidity on surface roughness, water contact angle and hardness of silicon, silicon dioxide*

and glass. Journal of Micromechanics and Microengineering, 2014. **24**(3): p. 035010.
205. Zhang, K. and M. Arroyo, *Coexistence of wrinkles and blisters in supported graphene.* Extreme Mechanics Letters, 2016.
206. Lim, C.H.Y.X., M. Nesladek, and K.P. Loh, *Observing High-Pressure Chemistry in Graphene Bubbles.* Angewandte Chemie International Edition, 2014. **53**(1): p. 215-219.
207. Lim, C.H.Y.X., et al., *A hydrothermal anvil made of graphene nanobubbles on diamond.* Nature communications, 2013. **4**: p. 1556.
208. Vasu, K., et al., *Van der Waals pressure and its effect on trapped interlayer molecules.* Nature communications, 2016. **7**: p. ncomms12168.
209. Gowthami, T., et al., *The role of ambient ice-like water adlayers formed at the interfaces of graphene on hydrophobic and hydrophilic substrates probed using scanning probe microscopy.* Physical Chemistry Chemical Physics, 2015. **17**(21): p. 13964-13972.
210. He, K.T., et al., *Scanning tunneling microscopy study and nanomanipulation of graphene-coated water on mica.* Nano letters, 2012. **12**(6): p. 2665-2672.
211. Kazakova, O., V. Panchal, and T.L. Burnett, *Epitaxial graphene and graphene–based devices studied by electrical scanning probe microscopy.* Crystals, 2013. **3**(1): p. 191-233.
212. Komurasaki, H., et al., *Layered structures of interfacial water and their effects on Raman spectra in graphene-on-sapphire systems.* The Journal of Physical Chemistry C, 2012. **116**(18): p. 10084-10089.
213. Ochedowski, O., B.K. Bussmann, and M. Schleberger, *Graphene on mica-intercalated water trapped for life.* Scientific reports, 2014. **4**: p. 6003.
214. Shim, J., et al., *Water-gated charge doping of graphene induced by mica substrates.* Nano letters, 2012. **12**(2): p. 648-654.
215. Kretinin, A., et al., *Electronic properties of graphene encapsulated with different two-dimensional atomic crystals.* Nano letters, 2014. **14**(6): p. 3270-3276.

Vita

Peng Wang was born in Suining, Sichuan Province, China. In 2008, he entered Department of Modern Mechanics at University of Science and Technology of China. He received the National Scholarship from Ministry of Education of China in 2011, and received his B.S. degree in 2012. In August 2012, he joined the University of Texas at Austin pursuing a Ph.D. degree in Engineering Mechanics.

Permanent email: pengwang@utexas.edu

This dissertation was typed by Peng Wang.